

THE UNIVERSITY
of EDINBURGH

This thesis has been submitted in fulfilment of the requirements for a postgraduate degree (e.g. PhD, MPhil, DClinPsychol) at the University of Edinburgh. Please note the following terms and conditions of use:

This work is protected by copyright and other intellectual property rights, which are retained by the thesis author, unless otherwise stated.
A copy can be downloaded for personal non-commercial research or study, without prior permission or charge.
This thesis cannot be reproduced or quoted extensively from without first obtaining permission in writing from the author.
The content must not be changed in any way or sold commercially in any format or medium without the formal permission of the author.
When referring to this work, full bibliographic details including the author, title, awarding institution and date of the thesis must be given.

Reconstructing the late-Quaternary glacial history of northeastern Patagonia (43°S, 71°W): new insights from geomorphology, geochronology and numerical glacier modelling

Tancrède P. M. Leger



THE UNIVERSITY
of EDINBURGH

Thesis submitted in fulfilment of the requirements for the degree of
Doctor of Philosophy
to the
University of Edinburgh
2022

Declaration

"I here confirm that the work presented within this Ph.D. thesis is original and my own, unless specified clearly as part of collaborative peer-reviewed publications. I moreover confirm that this thesis, either in whole or in part, has not been submitted for any other degree in this or any other University."

Tancrède P. M. Leger

June 2022

Abstract

Former investigations conducting geomorphological mapping of Patagonia, a region formerly covered by an extensive ice sheet, have revealed a uniquely rich record of Quaternary glacial sediment-landform assemblages. Patagonia is located in the ocean-dominated southern mid-latitudes and in the pathway of major southern hemisphere circulation systems including the precipitation-bearing southern westerly winds, and the Antarctic circumpolar current. For these reasons, Quaternary glacier reconstructions from Patagonia can help identify the main drivers of climate and glacial events in the Southern Hemisphere. However, in northeastern Patagonia (39-46°S), geochronological data addressing the precise timing of Quaternary glacial events during Pleistocene glacial cycles are lacking. Indeed, in this region, little is known about the magnitude and timing of the Patagonian Ice Sheet's response to climate events such as, for instance, the local Last Glacial Maximum (lLGM) and the last glacial termination. This Ph.D investigation attempted to fill in this knowledge gap, by producing a robust geochronological reconstruction that would describe the extent, stratigraphic relationship, characteristics and precise timing of most Quaternary glacial events preserved in a key valley system formerly host to major outlet glaciers of the northern Patagonian Ice Sheet.

Firstly, this thesis presents the first detailed glacial geomorphological map of the Río Corcovado, Río Huemul and Lago Palena/General Vintter valleys (43°S; 71°W). This mapping effort enabled the identification of 25 distinct categories of sediment-landform assemblages related to the glaciogenic, glaciofluvial and glaciolacustrine activity of the former Patagonian Ice Sheet. This work revealed the preservation of at least eight distinct moraine-outwash complexes at the study site, each indicative of a former outlet-glacier advance/still-stand. Secondly, this thesis provides a new terrestrial cosmogenic nuclide exposure age (n = 38) chronology that establishes the precise timing of the local Last Glacial Maximum resurgences of the Patagonian Ice Sheet. In total, five distinct advances/still-stands of the Río Corcovado outlet glacier occurred over a 6-7 ka period, at 26.4 ± 1.4 ka, 22.4 ± 1.15 ka, 21.7 ± 0.9 ka, 20.7 ± 1.0 ka and 19.9 ± 1.1 ka. Additionally, this work reveals the onset of local deglaciation and the timing of final ice-sheet disintegration occurred at 20-19 ka and 16.3 ± 0.3 ka, respectively. Furthermore, evidences for the likely formation and drainage of three distinct glaciolacustrine phases at the study site were established. Dating revealed that the first phase occurred from 26.4 ± 1.4 ka, the second between ~21 and ~19 ka and the third between ~19 ka and ~16.3 ka.

Thirdly, this thesis presents a separate reconstruction of an independent mountain-glacier advance dated to approximately ~18 ka using surface exposure dating. A series of numerical model simulations quantitatively reconstruct the geometry of this late-LGM glacier resurgence, and enable to estimate the local climate conditions at the time. This work for instance suggests that local precipitation must have been significantly higher than today during the late-LGM (~18 ka) glacial event, thus implying an equatorward migration of the Southern Westerly Winds at the time. Finally, this Ph.D. thesis features an additional terrestrial cosmogenic nuclide exposure-age chronology from the study site (n = 25) that focuses on dating the deposition of proglacial outwash plains and moraines formed during three extensive middle Pleistocene expansions of the Patagonian Ice Sheet. This dataset reveals, for the first time, that major glaciations occurred during the marine isotope stage eight and six intervals in northeastern Patagonia, while no prominent advances seem to have occurred during marine isotope stages four and three locally, in contrast with other Patagonian regions.

This thesis's findings enable us to draw hypotheses on the likely paleoclimate forcing mechanisms responsible for the timing of major middle-to-late Pleistocene glaciations at the southern mid-latitudes. This investigation also entails implications for better comprehending whether the former Patagonian Ice Sheet's different sectors responded to major climate events synchronosuly or asynchronously during the late Quaternary.

Lay summary

Scientific efforts to study the present-day landscape of Patagonia, the southernmost region of South America, have revealed that this region displays ample evidence for the former existence of an extensive continental-scale ice sheet during the Quaternary period; the past 2.6 million years of Earth's history. Glaciers and ice sheets are highly sensitive to changes in climate, and reconstructing their former behaviour can therefore serve as a proxy to better understand the mechanisms that naturally forced past climate fluctuations. Patagonia is a key location to conduct such investigations, as it is located within the ocean-dominated middle latitudes of the Southern Hemisphere, a region that is highly influenced by important oceanic and atmospheric circulation systems such as the Antarctic Circumpolar Current and the Southern Westerly Winds. These circulation systems control local ocean surface and atmospheric temperatures, and control the pathways of storms which bring precipitation to the Patagonian Andes. Local glaciers are sensitive to these variables such that lower atmospheric temperatures and increased snowfall will cause them to build up and expand, and vice versa. Due to Earth's natural climate cycles, the intensity and location of these circulation systems varies through time. Being able to better reconstruct and understand these past variations is both a major scientific challenge and a highly valuable endeavour to improve our understanding of the Earth's climate system. Producing detailed reconstructions of the former behaviour of Patagonian glaciers can thus help identify the main drivers of Quaternary climate change in the Southern Hemisphere. However, in the northeastern region of Patagonia (between latitude 39°S and longitude 46°S), such investigations are lacking. Consequently, little is known about the magnitude and timing of the Patagonian Ice Sheet's response to climate events such as, for instance, the local Last Glacial Maximum, which globally occurred approximately between 18,000 and 26,000 years before present. This Ph.D investigation attempted to fill in this knowledge gap, by producing a robust reconstruction that describes the extent, order, characteristics and precise timing of most Quaternary glacial events preserved in a key valley system formerly host to major glaciers flowing out from the Patagonian Ice Sheet.

This thesis first presents a novel detailed map, drawn from both field analyses and satellite-derived data, of the different preserved landforms depicting the former glacial activity at the chosen study site: the Río Corcovado, Río Huemul and Lago Palena/General Vintter valleys

(latitude 43°S; longitude 71°W). This map revealed, for instance, the preservation of eight distinct units of terminal moraine deposits at the study site. Such sediments are deposited at the margins of glaciers, and thus indicate that a minimum of eight different expansions of the Patagonian Ice Sheet occurred locally. Secondly, using a state-of-the-art absolute dating technique, this thesis then presents a novel chronology that establishes the timing of five glacier advances associated with the local Last Glacial Maximum. These occurred over a 6-7 thousand-year period, at 26.4 ± 1.4, 22.4 ± 1.2, 21.7 ± 0.9, 20.7 ± 1.0 and 19.9 ± 1.1 thousand years before present. Additionally, this work reveals the local Patagonian Ice Sheet outlets started deglaciating between 20 and 19 thousand years before present, while full ice-sheet disintegration had occurred by 16.3 ± 0.3 thousand years before present. Furthermore, this work provides evidence for the formation of three distinct ice-dammed glacial lakes during the different phases of most recent ice-sheet retreat, which occurred from 26.4 ± 1.4 thousand years before present, between ~21 and ~19 thousand years before present and between ~19 and ~16.3 thousand years before present, respectively. Thirdly, this thesis presents a separate reconstruction of an independent mountain-glacier advance at the study site, dated to approximately ~18 thousand years before present using surface exposure dating. Using a numerical model, this work also reconstructs the former geometry of this glacier resurgence, and provides an estimation of local climate conditions at the time. The results for instance suggest that local precipitation must have been significantly higher than today during this glacier advance, thus implying a northward migration of the Southern Westerly Winds around 18 thousand years before present. Finally, this Ph.D. thesis features an additional chronology from the study site that focuses on dating the deposition of glacier sediment units formed during three distinct and extensive expansions of the Patagonian Ice Sheet that occurred prior to the Last Glacial Maximum, during older glaciations and global cooling events of the Quaternary.

Overall, this thesis's findings enable to better understand the dynamics of the Patagonian Ice Sheet during the Quaternary by bridging an important geographical knowledge gap. Furthermore, the investigation's results allow us to draw hypotheses on the likely past-climate forcing mechanisms responsible for the timing of major Southern Hemisphere glaciations. Such information can be vital to parameterise ice-sheet and climate models and better assess the significance of current and predicted global environmental change.

Acknowledgments

I wish to express my most sincere gratitude towards my main supervisor, Dr. Andrew Hein. His precious advice and guidance have represented a tremendous help for all aspects of this Ph.D. research, from finding my way through fieldwork, including some rather unimaginable mishaps involving flat tires and hungry camp mates, to presenting at international conferences and writing grant applications and scientific articles. I am thankful for his controlled attitude and patience, which have enabled many intense work phases to run as smoothly as one could hope. I also wish to thank Professor Robert Bingham, my second supervisor, for his precious help and company in the field, and for his guidance in the final stages of writing my Ph.D. research under the form of scientific articles. His remarkable sense of humour have made this process highly enjoyable, moreover. I thank Dr. Daniel Goldberg for his help working with coding languages and his numerical ice flow model, and for putting up with my initial incompetence in this field. I want to thank Dr. Irene Schimmelpfennig for providing me with a post-COVID working environment to work at CEREGE during a Professional Internship Programme and then as a research visitor for the last few months of my thesis. My time there has promoted numerous research opportunities that I would have never anticipated.

I would like to thank the numerous local landowners (Chubut province, Argentina) for authorizing us to access, study, and sample on their land. I am grateful to Dr. Ángel Rodés, Alan Davidson, Dr. Derek Fabel and Dr. Irene Schimmelpfennig for having had the patience to teach me the laboratory tasks involved in cosmogenic nuclide analyses. I wish to express my gratitude towards all those who provided me with precious scientific and/or logistical help and advice with my work, including all individuals who contributed to the crowdfunding campaign I organised to raise fieldwork money (https://crowd.science/crowdfunding), but also including Dr. Robert McCulloch, Dr. Juan Luis García, Pablo Tapia Gonzalez, Dr. Oscar Martínez, Professor Neil Glasser, María Paz Lira-Bahamonde, Dr. Mateo Martini, Dr. Rodrigo Soteres, Maxime Vergez, and Emeritus professor David E. Sugden. Finally, I am grateful to the members of the Edinburgh cryosphere research group and to the fellow Ph.D. students of CEREGE who provided dynamic and fun working environments enabling to socialise and share knowledge between colleagues.

Finally, I would like to thank the public and private organisations that funded my Ph.D. and made this work possible, namely, the UK Natural Environment Research Council (E3 DTP PhD award NE/L002558/1; CIAF award 9196-0419; NEIF award 2245-0320), the University of Edinburgh School of GeoSciences (E3 DTP PhD award), the Scottish Alliance for Geoscience Environment and Society (Small Grant Scheme grant awarded in 08/2020), the UK Quaternary Research Association (New Research Worker's grant awarded in 06/2019), and the British Society for Geomorphology (Postgraduate Research grant awarded in 10/2019).

List of Contents

Declaration 3

Abstract 5

Lay summary 7

Acknowledgements 9

1 Introduction 24

1.1 Background……..……... 25

1.2 Rationale…….……... 29

1.2.1 Patagonia: a key location to study and reconstruct palaeo-climate dynamics in the Southern Hemisphere……. 29

1.2.2 The northeastern Patagonian knowledge gap …….. 31

1.2.3 The preservation of glacial geomorphological records in eastern Patagonia…… 35

1.2.4 The potential of TCN surface exposure dating for reconstructing the timing of glacial events in northeastern Patagonia……. 36

1.2.5 The conundrums on latitudinal and longitudinal asynchronies in the timing of the local LGM across Patagonia…… 37

1.3 Aims…….. 39

1.4 Research objectives……... 40

1.4.1 Objective 1: Establishing a geomorphological and morphostratigraphic reconstruction of glacial dynamics at the study site……... 40

1.4.2 Objective 2: Establishing a detailed geochronological reconstruction of local glacial and proglacial events during the LGM and last deglaciation...……..…… 40

1.4.3 Objective 3: Establishing a reconstruction of paleoclimate dynamics by combining geochronology and glacier numerical modelling..…… 41
1.4.4 Objective 4: Establishing a reconstruction of major pre-LGM and pre-Last Glacial Cycle glaciations at the study site and assess the palaeo-climatic context…….…… 41

1.5 Thesis structure……..…….... 42

1.5.1 Chapter 2 ……...…….……... 42
1.5.2 Chapter 3 ……...…….……... 43
1.5.3 Chapter 4 ……...…….……... 44
1.5.4 Chapter 5 ……...…….……... 45

2 The glacial geomorphology of the Río Corcovado, Río Huemul and Lago Palena/General Vintter valleys, northeastern Patagonia (43°S, 71°W) 47

2.1 Introduction……..... 50

2.2 Study location and previous work……..……..... 51

2.3 Methods ……...……..……..... 54

2.3.1 Remote sensing ……..…… 54
2.3.2 Field mapping ……..…….. 54

2.4 Results ……...……..……..... 56

2.4.1 Glacial geomorphology ……...…… 56
2.4.2 Ice-contact glaciogenic landforms ……...…… 56
2.4.2.1 Moraine complexes and kettle-kame topography……..……. 56
2.4.2.2 Moraine ridges…….……...…… 58
2.4.2.3 Hummocks and hummocky ridges …….……...…… 61
2.4.2.4 Kettle holes ……...……...……. 61
2.4.3 Glaciofluvial landforms ……...……...…… 65
2.4.3.1 Proglacial outwash plains ……..……..…… 65
2.4.3.2 Meltwater channels ……..……..…… 65
2.4.3.3 Fluvial incision scarps ……..……..…… 68
2.4.3.4 Glacial lake outburst flood deposits……..…..……..…… 68

2.4.4 Glaciolacustrine landforms ……..……..…… 69
2.4.4.1 Glaciolacustrine deposits ……..……..…… 69
2.4.4.2 Palaeo-shorelines ……..……..…… 69
2.4.4.3 Raised deltas ……..……..…… 73
2.4.5 Subglacial landforms ……...……...…… 73
2.4.5.1 Glacial lineations, flutings, drumlinoid forms and ice-moulded bedrock
…….. 73

2.5 Summary and conclusions ……....…….. 76

2.6 Additional methods (not included in publication) ..…….. 77

2.6.1 Digital mapping ……..…… 77
2.6.2 Field surveys ……..…… 78

3 Geomorphology and ^{10}Be chronology of the Last Glacial Maximum and deglaciation in northeastern Patagonia, 43°S - 71°W

80

3.1 Introduction……..... 83

3.2 Study location and physical setting ……...……..... 87

3.2.1 Geographical setting ……..…… 87
3.2.2 Geologic setting ……..……..…….. 88
3.2.3 Climatic setting ……..……..…….. 88
3.2.4 Previous work in study area ……...……..…….. 89

3.3 Methods ……...……..……..... 87

3.3.1 Geomorphological mapping …… 90
3.3.2 Moraine morphology/sedimentology analyses …….. 92
3.3.3 Dating approach and sampling ……..…….. 92
3.3.4 Sample preparation and wet chemistry ……..…….. 96
3.3.5 Age calculations ……..…….. 96

3.4 Results ……...……..…….... 100

3.4.1 Geomorphology/Sedimentology ……....……...… 100

3.4.1.1 The RC III-VII moraines geomorphology ……..……..…... 100
3.4.1.2 The RH and RC former glaciolacustrine phases ……..……. 103
3.4.2 Dating results ……...……...……...…….. 105
3.4.2.1 Cosmogenic ^{10}Be exposure ages ……..……. 105
3.4.2.2 Bayesian age modelling results ……..…112

3.5 Discussion ……..…….. 114
3.5.1 Style of glaciation ……...……....…….. 114
3.5.2 Chronological and geomorphological results interpretation …….. 114
3.5.2.1 The local LGM (RC III) and proglacial lake phase one (Figure 9a) …. 117
3.5.2.2 The RC IV-RC VII advances and proglacial lake phase two (Figure 9b-e) ..
…….....…… 119
3.5.2.3 The onset of local deglaciation and proglacial lake phase three (Figure 9f)
……. 122
3.5.2.4 The timing of ice-sheet disintegration and Atlantic/Pacific drainage reversal
(Figure 9G, H) …… 125
3.5.3 Palaeoclimate ……..... 126
3.5.3.1 The timing of local LGM expansions …… 126
3.5.3.2 The onset of local deglaciation …… 130

3.6 Conclusions …….. 133

4 Northeastern Patagonian glacier advances (43°S) reflect northward migration of the Southern Westerlies towards the end of the last glaciation 135

4.1 Introduction……... 138

4.2 Study location ……...……... 141

4.3 Materials and methods ……..……... 143
4.3.1 Geomorphological mapping ……..…..……... 143
4.3.2 ^{10}Be Terrestrial Cosmogenic Nuclide dating ……..……. 146
4.3.2.1 Dating approach and sampling ……..…… 146
4.3.2.2 Sample preparation, wet chemistry and exposure-age calculations ..… 146
4.3.3 GIA-related uplift estimates ……..……...……..149
4.3.4 Numerical modelling of the EL and RCO palaeo-glaciers ...……. 150
4.3.4.1 Ice flux ……..……..……..……150

4.3.4.2 Surface mass balance ……151
4.3.4.3 Modern climate ……152
4.3.4.4 Model simulations ……155
4.3.4.5 Model sensitivity tests ……156

4.4 Results ……160
4.4.1 Geomorphology ……160
4.4.1.1 Valley geomorphology ……160
4.4.1.2 Glacial moraines ……160
4.4.2 ^{10}Be surface exposure ages ……163
4.4.3 GIA-related uplift ……165
4.4.4 Numerical modelling results ……167
4.4.4.1 Glacier geometry ……167
4.4.4.2 Palaeo-temperature ……168
4.4.4.3 Palaeo-precipitation ……169

4.5 Discussion ……173
4.5.1 Geomorphological considerations and age interpretation ……173
4.5.2 Palaeo-climate ……175
4.5.2.1 PIS context and the late-LGM cold/wet episode ……175
4.5.2.2 Palaeo-precipitation ……177
4.5.2.3 Palaeo-temperatures ……178
4.5.2.4 Younger late-glacial advances/still-stands ……180
4.5.3 Positive degree-day melt factor variability ……182
4.5.4 Limitations and future work ……182

4.6 Conclusion ……185

5 A cosmogenic nuclide-derived chronology of pre-Last-Glacial-Cycle glaciations during MIS 8 and MIS 6 in northern Patagonia 188

5.1 Introduction……191

5.2 Setting ……194

5.3 Methods ……197

5.4 Results ……202

5.4.1 Geomorphology ……. 202
5.4.2 TCN exposure-age chronology ……..…….. 205
5.4.2 TCN exposure-age scatter sources …….…….. 208

5.5 Discussion ……...…….....…….……....211
5.5.1 TCN exposure-age interpretations …….. 211
5.5.1.1 The Tecka/RC 0 outwash cobble exposure ages ……..….211
5.5.1.2 The RC I outwash cobbles and timing of the RC I outermost advance ...214
5.5.1.3 The RC I-II bedrock surface and timing of innermost RC I advances 215
5.5.1.4 The RC II outwash cobble and moraine boulder exposure ages ……....217
5.5.2 Comparisons with palaeo-climate and global cryosphere contexts 220
5.5.2.1 The MIS 8 glaciations ……...…….…..… 220
5.5.2.2 The MIS 7 glaciation ……..……...…….…..…224
5.5.2.3 The penultimate MIS 6 glaciation ……...…….…..… 225
5.5.2.4 Synthesis: The timing of Patagonian glaciations …….…..….226
5.5.3 Climatic and orbital drivers of SH glaciations - hypotheses …….....229

5.6 Conclusions …...……...232

6 Conclusions **235**

6.1 Main conclusions and implications …...……... 236
6.1.1 Objective 1 …….…….. 236
6.1.2 Objective 2 …….…….. 237
6.1.3 Objective 3 …….……..238
6.1.4 Objective 4 …….……...240

6.2 Future work ……...……....244
6.2.1 Empirical ice thickness constraints in Patagonia …...…….…….. 244
6.2.2 Numerical modelling of the PIS ….....……. 244
6.2.3 Dating pre-LGC glacial deposits in Patagonia ….....…….…….. 245
6.2.4 The study of glaciolacustrine deposits in the Río Corcovado valley system ...…….. 245
6.2.5 The deglacial Pacific/Atlantic drainage reversal event in the Palena region ……...…….…….. 246

Reference list **248**

7 Appendix **275**

7.1 Chapter 2 supplementary materials …...……....276

7.2 Chapter 3 supplementary materials …...……....278

7.2.1 Study site former glaciolacustrine phases: additional geomorphological evidence and interpretation …...…….…….. 278

7.2.1.1 Glaciolacustrine phase one …….…….……..….278

7.2.1.2 Glaciolacustrine phase two …….…….……..…278

7.2.1.3 Glaciolacustrine phase three …….……...…..….280

7.2.2 OSL dating samples details and lab methodology ……..…….. 288

7.2.3 ^{10}Be TCN dating wet chemistry lab methodology ……..…….. 291

7.2.4 Vertical plot of published LGM TCN exposure ages from glacial deposits in Patagonia ……...…….. 292

7.2.5 ^{10}Be TCN exposure dating kernel density plots per landform …..…. 294

7.2.6 Cosmo-Ages Sequence Calculator (CASC) - Bayesian age model 295

7.3 Chapter 4 supplementary materials …...……....296

7.3.1 Ice-flow model output comparison with GlaRe flowline model 296

7.3.1.1 GlaRe methods …….……...…….……...….296

7.3.1.2 GlaRe results and comparisons ……...…….……...….297

7.3.2 Ice-flow model source code ……..... 297

7.3.3 Supplementary Figures and Tables …….…..... 298

7.3.3.1 Supplementary Figures ……..……...…….……...….298

7.4 Chapter 5 supplementary materials …...……....300

7.4.1 Rock sample preparation, wet chemistry and exposure-age calculations ……..... 300

7.4.1.1 SUERC cosmogenic isotopes analysis laboratory methodology ……....300

7.4.1.2 CEREGE LN_2C laboratory methodology ……..……..……...…301

7.4.1.3 University of Edinburgh Cosmogenic Nuclide Laboratory methodology ……...….302

7.4.2 ^{10}Be and ^{26}Al concentrations ratio analysis ……..…….....303

7.4.3 Sample location maps ……..……..... 304

7.4.3.1 RC II moraine-outwash complex samples & RC I-II ice-moulded bedrock sample …….. 304

7.4.3.2 RC I moraine-outwash complex samples ……..305

7.4.3.3 Tecka / RC 0 outwash samples …….……..306

7.4.4 Sample photographs ……..……..…….....307

7.4.5 Method: estimating potential impact of outwash-cobble exhumation on exposure-age scatter …… 311

List of Figures

Chapter 1

Figure 1.1 Satellite image of Patagonia and location of study site ……..... 26
Figure 1.2 Geographical and climatic context of thesis study area ……..... 28
Figure 1.3 Area in context of other Patagonian glacier chronologies …..... 33
Figure 1.4 Area in context of other chronological data ……..... 34

Chapter 2

Figure 2.1 Study area within wider geographical context …..…..…..…..... 53
Figure 2.2 Study area and location of subsequent figures/maps …....…..... 55
Figure 2.3 Imagery/geomorphology: moraine belt ……..…..... 57
Figure 2.4 Imagery/geomorphology: hummocky terrain ……..... 58
Figure 2.5 Imagery/photos/geomorphology: morainic landforms ……..... 60
Figure 2.6 Imagery/photos/geomorphology: glaciofluvial landforms 67
Figure 2.7 Imagery/photos/geomorphology: glaciolacustrine landforms ... 71
Figure 2.8 Imagery/geomorphological map comparisons 5 ……....…... 75

Chapter 3

Figure 3.1 Study area within wider geographical context …..…..…..…..... 85
Figure 3.2 Geomorphological map of study area …..…..... 91
Figure 3.3 Field photographs of moraines and sampled boulders …..…..... 95
Figure 3.4 Field photographs of palaeo-shorelines and cobbles 98
Figure 3.5 Map and field photographs of bedrock samples 99
Figure 3.6 Map and ages of individual TCN dating samples 102
Figure 3.7 Geomorphological and sedimentological data 104
Figure 3.8 Probability density diagrams for each landforms dated 113
Figure 3.9 Palaeoglacial and palaeolake reconstructions …….....116
Figure 3.10 Vertical plot of palaeoclimate record comparisons ….....129

Chapter 4

Figure 4.1 Study area and wider geographical context …...……..…...140
Figure 4.2 Geomorphological map of study area …...……...144
Figure 4.3 Field photographs of EL valley, moraines, boulders …..….....148
Figure 4.4 A sample of Surface Mass Balance profiles …..…….....154
Figure 4.5 Kernel density plot of TCN exposure ages …..……..….....164
Figure 4.6 Ice-flow model output figures …..……...……..….....168
Figure 4.7 Elevation profile graphs of simulated glaciers …..…….....170
Figure 4.8 Ice-flow model parameter combinations …..…….....172
Figure 4.9 Model parameter combinations / simulations combined 184

Chapter 5

Figure 5.1 Study area and wider geographical context …...……..…...196
Figure 5.2 Field photographs of outwash plains and cobbles ..……....200
Figure 5.3 Field photographs of moraine boulders ……...……....201
Figure 5.4 Kernel density plots for exposure dating outputs ..……....210
Figure 5.5 Illustration of sources of exposure-age scatter ..……....213
Figure 5.6 Geomorphology/exposure ages/profile graphs ..……....219
Figure 5.7 Palaeo-glacial reconstructions of studied valleys ..…….....223
Figure 5.8 Vertical plot of palaeoclimate record comparisons ..…….....228

Chapter 6

Figure 6.1 Geomorphology and all TCN exposure ages produced .....…....241
Figure 6.2 All palaeoglacial and palaeolake reconstructions .....…...242

List of Tables

Chapter 2

Table 2.1 Summary of mapped landform morphologies, mapping criteria, and mapping uncertainties ……. 63

Chapter 3

Table 3.1 Sample details and nuclide concentrations ….....……...106

Table 3.2 Exposure ages and summary statistics ….....…….....109

Chapter 4

Table 4.1 Sample details and nuclide concentrations ….....……...159

Table 4.2 Ice-flow and PDD model input parameters ….....…..……...163

Table 4.3 Exposure ages and summary statistics ….....……..……...163

Table 4.4 gFlex GIA-related surface elevation change ….....……..……..166

Table 4.5 Numerical model output statistics and ranges …..……...……...179

Chapter 5

Table 5.1 TCN dating sample details and nuclide concentrations …...…...204

Table 5.2 TCN exposure ages and summary statistics ……....…..207

List of Abbreviations

AAR	Accumulation Area Ratio
ACC	Antarctic Circumpolar Current
ACR	Antarctic Cold Reversal
ALR	Adiabatic Lapse Rate
AMS	Accelerator Mass Spectrometer
A/P reversal	Atlantic/Pacific reversal
AW3D30	ALOS world 3D – 30 m DEM
BI	Bahía Inútil (outlet glacier)
BV	Bella Vista (outlet glacier)
CDI	Cordillera Darwin Icefield
DEM	Digital Elevation Model
DG	Digital Globe
EDC	EPICA Dome C (ice core)
EDML	EPICA Dronning Maud Land
ELA	Equilibrium Line Altitude
EL	El Loro (river, valley and glacier)
EL-out	El Loro outermost advance
EL-mid	El Loro intermediate advance
EM	Estrecho de Magallanes (outlet glacier)
GIA	Glacial Isostatic Adjustment
GLOF	Glacial Lake Outburst Flood
GPS	Global Positioning System
LA	Lago Argentino (outlet glacier)
LBA	Lago Buenos Aires (outlet glacier)
LC/P	Lago Cochrane/Pueyrredón (outlet glacier)
LGC	Last Glacial Cycle
lLGM	local Last Glacial Maximum
gLGM	global Last Glacial Maximum
LGT	Last Glacial Termination
LN_2C	French National Laboratory for Cosmogenic Nuclides
LP/LGV	Lago Palena/Lago General Vintter (glacier)
LV	Lago Viedma (outlet glacier)
MIS	Marine Isotope Stage
MODIS	Moderate Resolution Imaging Spectroradiometer
MSWD	Mean Squared Weighted Deviation
m a.s.l.	meters above sea level (present-day sea level)
mm w.e.	millimetre water equivalent
NERC	Natural Environment Research Council
NERC-CIAF	NERC-Cosmogenic Isotope Analysis Facility
NPI	North Patagonian Icefield

ODP	Ocean Drilling Program
PDD	Positive Degree-Day
PF	Polar Front
PIS	Patagonian Ice Sheet
Pr_{EL}	Precipitation in El Loro glacier catchment
Pr_{RCO}	Precipitation in Río Comisario glacier catchment
Qtz	Quartz
RC	Río Corcovado (river, valley, and outlet glacier)
RCO	Río Comisario (river, valley, and outlet glacier)
RF	Río Frío (river, valley, and outlet glacier)
RH	Río Huemul (river, valley, and outlet glacier)
SAF	Sub-Antarctic Front
SIA	Shallow Ice Approximation
SMB	Surface Mass Balance
SPI	South Patagonian Icefield
SS	Seno Skyring (outlet glacier)
SST	Sea Surface Temperature
STD	Standard Deviation
STF	Sub-tropical Front
SUERC	Scottish Universities Environmental Research Centre
SWW	Southern Westerly Winds
TCN	Terrestrial Cosmogenic Nuclide
TDP	Torres del Paine (outlet glacier)
TSL	Temperature at sea level
UE	Última Esperanza (outlet glacier)
UTM	Universal Transverse Mercator (coordinate system)
WAIS Divide and WDC	West Antarctic Ice Sheet Divide (ice core)
WC2	WorldClim version 2 (climate dataset)
YD	Younger Dryas

Chapter I

|

Introduction



1.1. Background

The region of Patagonia, located in southern South America, is host to the largest extra-polar ice masses in the southern hemisphere (Mouginot and Rignot, 2015; Millan *et al*., 2022; Fig. 1.1). During major Quaternary glaciations, including the Last Glacial Maximum (LGM), the former Patagonian Ice Sheet (PIS) stretched for more than 2000 km from ~38°S to 55°S along the spine of the Andes (Rabassa and Clapperton, 1990). To the east of the Patagonian Andes, large land-terminating glaciers advanced towards the semi-arid Argentine foreland during Quaternary glacial maxima, and terminated into large proglacial lakes during retreat phases (Clapperton, 1993). The numerous waxing and waning cycles of these eastern outlet glaciers greatly modified the landscape through glacial erosion (Kaplan *et al*., 2009) and left remarkably well-preserved glacial geomorphological records near their former margins. These records provide a unique opportunity to reconstruct the former Quaternary glacial, glaciofluvial and glaciolacustrine activity associated with the former PIS (Mercer, 1976). On the western side of the Andes, the PIS is thought to have reached the present submarine continental shelf, which causes any record of previous glacial activity to be less preserved or accessible, and thus less studied (Davies *et al*., 2020). The broad latitudinal range of the former PIS is unique in the ocean-dominated southern mid-latitudes. Robust and detailed reconstructions of its former evolution enable us to gain invaluable insights into past cryospheric, but also climatic change, due to the climate-sensitive nature of the temperate Patagonian ice masses that evolved at relatively low-elevations (Denton *et al*., 1999). Indeed, in Patagonia, local glaciers and ice-sheets are and were highly influenced by southern circum-hemispheric oceanic and atmospheric circulation, which controls both local temperature and precipitation variations and features important components of the global climate system. Such variations in local climate variables are tied to fluctuations in glacier surface mass balance, and this link can be studied by reconstructing the extent, the timing and the surface mass balance dynamics of specific glacier and ice-sheet expansion and retreat events. The study of Quaternary Patagonian glaciations can thus act as powerful proxies of former climate change during the late Quaternary.

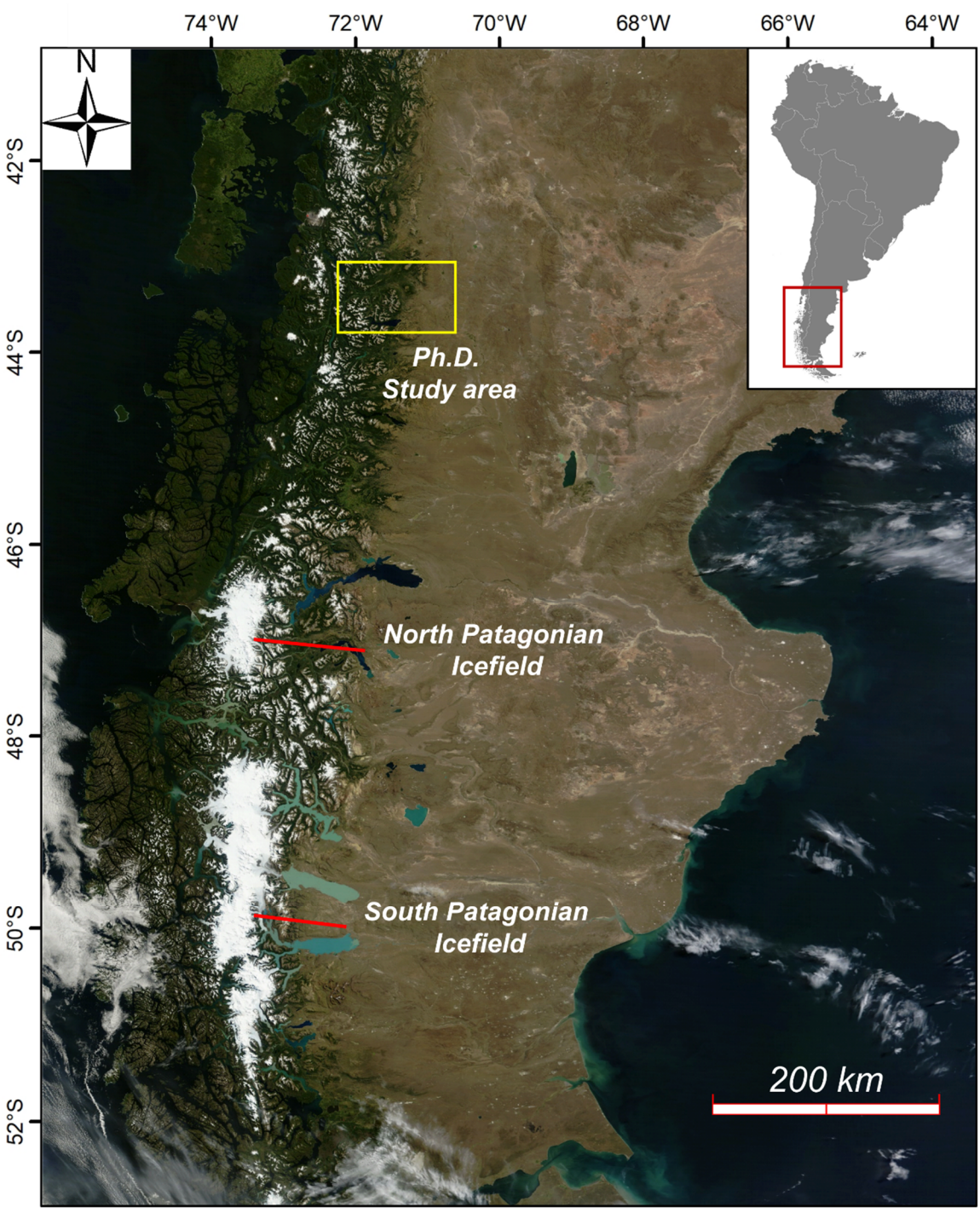

Figure 1.1. Natural colour image of cloud-free Patagonia, southern South America, from the moderate resolution imaging spectroradiometer (MODIS) instrument aboard the Terra satellite (NASA). The image was captured on February 19th, 2011. The denoted North and South Patagonian Icefields are currently the largest extra-polar ice masses in the southern hemisphere. The study-site location of this Ph.D. investigation, located in northeastern Patagonia, is here highlighted in yellow.

Scientific research focused on reconstructing the Quaternary glacial history of Patagonia was pioneered by Carl Caldenius, who first mapped and described the preserved morphostratigraphic sequences of former glacier margins along the PIS (Caldenius, 1932). Since then, investigations focusing on understanding past ice sheet extent and the timing of major glaciations in Patagonia have multiplied. These studies have relied on the development of numerical dating techniques such as radiocarbon dating (*e.g.* Mercer, 1970; Denton, 1999), $^{40}Ar/^{39}Ar$ and K-Ar dating of interbedded glacial till and lava flows (*e.g.* Singer et al., 2004), and more recently varve chronologies (*e.g.* Bendle *et al.*, 2017a), optically stimulated luminescence dating (*e.g.* Smedley *et al.*, 2016) and Terrestrial Cosmogenic Nuclide surface exposure and depth profile dating (*e.g.* Kaplan *et al.*, 2005; Hein *et al.*, 2009; 2011). However, large formerly glaciated regions of Patagonia are still under-studied, and numerous geomorphological records of former glacier events are currently unmapped and undated (Davies *et al.*, 2020). Consequently, there remains important research questions regarding the synchronous or asynchronous nature of numerous glacier events in Patagonia and across the southern mid-latitudes, regarding the forcing factors responsible for southern mid-latitude glaciations, and regarding inter-hemispheric linkages of Quaternary climate change (Darvill *et al.*, 2016; Mendelova *et al.*, 2017; Davies *et al.*, 2020; Denton *et al.*, 2021).

This Ph.D. thesis aims at contributing to the growing body of research attempting to solve some of these key conundrums, by producing a detailed reconstruction of Quaternary glacial landscape evolution in the understudied region of northeastern Patagonia. More detailed justifications and presentations of the chosen research project, methodology, aims and objectives, and study site, are presented in the following sections.

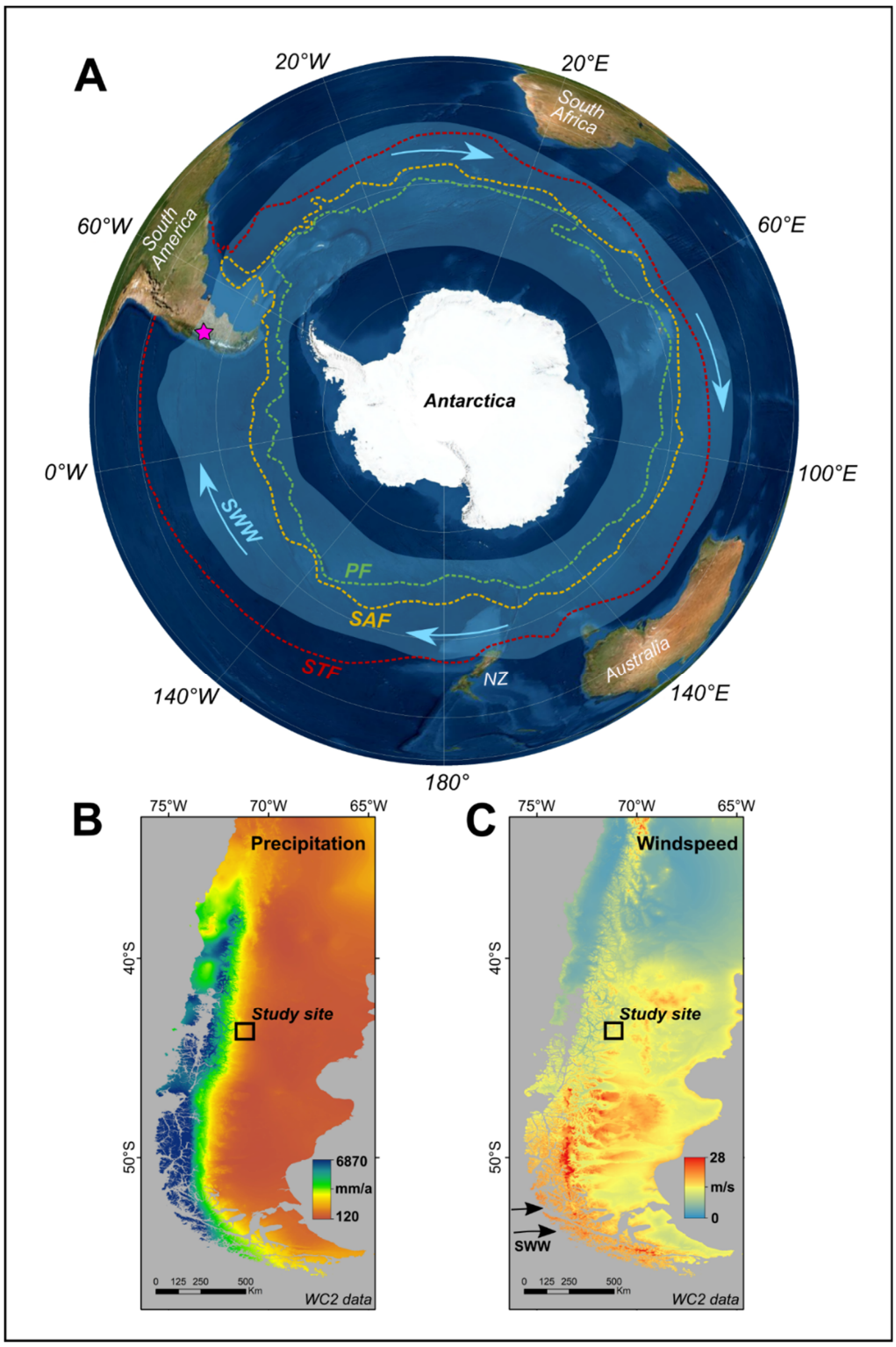

Figure 1.2. Geographical and climatic context of the Ph.D. thesis study area. **A**: Orthographic-view map of the Southern Hemisphere highlighting the approximate contemporary positions of the Southern Westerly Winds (SWW: after Sime *et al*., 2013) belt (light blue), the Polar Front (PF: green), the Sub-Antarctic Front (SAF: orange), and the Sub-Tropical-Front (STF: red), adapted from Darvill *et al*. (2016) and based on Orsi *et al*. (1995) and Carter *et al*. (2008). The map also highlights the location of the Ph.D. study site in northern Patagonia (purple star). 1-km spatial resolution total annual precipitation (mm a^{-1}) (**B**) and mean windspeed (m s^{-1}) (**C**) land data from the WorldClim 2 dataset (Fick and Hijmans, 2017) are shown, overlaying maps of southernmost South America with location of Ph.D. study area highlighted by black rectangle.

1.2. Rationale

This section describes the five primary justifications for the chosen research aims and objectives, study site and methodology employed within the context of this Ph.D. investigation. Where relevant, sets of key research questions that arise from these justifications are also provided in this section.

1.2.1. Patagonia: a key location to study and reconstruct palaeo-climate dynamics in the Southern Hemisphere

The southern Hemisphere mid-latitudes are ocean dominated, with an ocean earth-surface cover of 98% between 40°S and 60°S. Patagonia represents the only continental landmass that fully covers this latitudinal expanse and therefore provides a rare opportunity to use terrestrial palaeoclimate proxies to investigate former climate evolution in this part of the world. The mid-latitude Patagonian glaciers and icefields occur at relatively low elevations and thus in relatively warm environments (Clapperton, 1993). They are sustained by significant volumes of snowfall precipitated over the Patagonian Andes due to the orographic effect. This causes these ice masses to be highly temperate, warm based, and some of the most climate-sensitive ice masses on Earth (Oerlemans and Fortuin, 1992; Carrivick *et al*., 2016). For instance, due to present-day climate change, Patagonian Icefields experience highly negative mass balances and currently represent the greatest contribution to sea level rise per unit area in the world, with a sea level-equivalent contribution of 0.067 ± 0.004 mm yr^{-1} between 2000 and 2012, a notable acceleration compared to the rate of 0.042 ± 0.002 mm yr^{-1} estimated for the 1975-2000 period (Mouginot *et al*., 2015; Carrivick *et al*., 2016). The significant moisture delivery that influences Patagonian glacier surface mass balance is and was primarily controlled by the circumpolar Southern Westerly Winds (SWW), which blow from west to east between the subtropical high-pressure and polar low-pressure zones (Toggweiler, 2009; Fig. 1.2) and bring precipitation from the Pacific Ocean to Patagonia (Garreaud *et al*., 2013; Lamy *et al*., 2015). The wind stress associated with the SWW drives the Antarctic Circumpolar Current (ACC) (Toggweiler, 2009; Fig. 1.2). Together, these key ocean-atmosphere energy redistribution mechanisms play a crucial role in controlling southern mid-latitude and global climate (Sime *et al*., 2013), through critical climate feedback mechanisms such as, for instance, oceanic carbon

sequestration through Southern Ocean ventilation or North Atlantic Deep Water formation through Agulhas Leakage modulation (Denton *et al*., 2021). Therefore, understanding the former latitudinal shifts and strength variations of the SWW and oceanic Subtropical Front (STF) is crucial to better comprehend and reconstruct Earth's Quaternary climate history (Sime *et al*., 2013). Northern Patagonian climate is particularly sensitive to latitudinal shifts in the SWW as this region is located towards the northern edge of the wind belt in its present configuration (Moreno *et al*., 2018; Fig. 1.2). The important latitudinal cover of the former PIS may thus be useful in testing existing scientific hypotheses regarding possible asynchronies in the pattern of millennial-scale glacier stages throughout Patagonia. For instance, Sugden *et al*. (2005) hypothesised that while southern Patagonia presents some evidence of glacier expansions during the Antarctic Cold Reversal (14.7-13 ka) associated with a southern climatic signal, northern Patagonian glacier records may instead indicate more sensitivity to northern climatic signals and cooling during the Younger Dryas. Consequently, studying glacial geomorphological records and establishing a geochronological reconstruction of former PIS evolution in northern Patagonia has important implications for recording former SWW behaviour and thus may represent a key palaeo-climate proxy record for the southern mid-latitudes.

Consequently, the high-climate sensitivity of contemporary and former Patagonian glaciers enables us to ask the following set of research questions:

Research question set 1:

What are the complex environmental and climatic mechanisms responsible for the timing of ice-sheet waxing and waning cycles in Patagonia and at the southern mid-latitudes? Is there an agreement between the timing of northeastern PIS advances and patterns of orbitally-controlled local summer and/or winter insolation intensity? Did the timing of major PIS advances coincide with observations of former cold and high precipitation phases observed through other proximal palaeoclimate proxy records, such as pollen, ocean, and ice-core records for instance? Is there a link between the behaviour of the PIS in its northeastern sector and former variations in the intensity and position of the coupled SWW and ACC system?

1.2.2. The northeastern Patagonian knowledge gap

As well as representing a region that holds a significant palaeo-climate reconstruction potential, the northeastern sector of the former PIS features a major geographical knowledge gap on the Quaternary behaviour of palaeo-glaciers. The geographical coverage of published investigations providing geochronological reconstructions of PIS evolution can be analysed through the review studies of Darvill *et al*. (2015; 2016), Mendelová *et al*. (2017) and the latest database compiled by the PATICE project (Davies *et al*., 2020). Datasets and maps produced within the context of these scientific reviews, along with the most recent online terrestrial cosmogenic nuclide (TCN) exposure-age datasets from Expage[1] and ICE-D Alpine[2], demonstrate a clear lack of palaeo-glacial geochronological data for the northeastern sector of the former PIS, between 41°S and 46°S (Fig. 1.3). At the start of this Ph.D. investigation (10/2018), only four TCN exposure ages from glacial moraine boulders had been published within this region that covers approximately 710 km of latitudinal expanse, by Zech *et al*. (2017). In that study, two separate advances of the Nahuel Huapi outlet glacier (41°S) were dated using only two exposure ages respectively, a number generally considered too low to provide numerical dating that can be interpreted with confidence (Heyman *et al*., 2011). Following this, García *et al*. (2019) produced four supplementary TCN exposure ages from moraine boulders which complement an organic ^{14}C- and Optically-Stimulated Luminescene (OSL)- derived late-LGM and deglacial chronology of the former Río Cisnes (44°3'S – 44°4'S) and Lago Fontana outlet glaciers (44°5'S) (Fig. 1.3, 1.4). The only other organic ^{14}C ages informing palaeo-glacial dynamics from the eastern Patagonian Andes and located north of the well-studied Lago Buenos Aires valley (46°S: Kaplan *et al*., 2004; Douglass *et al*., 2006; Hein *et al*., 2017) were published by Van Daele *et al*., (2016) (Fig. 1.4). With regards to former PIS behaviour, this study determines when Lago Castor (45°3'S, 71°5'W) was last free of glacier ice (~28 ka). Therefore, before this Ph.D. research project, no investigation had attempted to conduct a detailed geochronological reconstruction featuring direct, numerical dating of the numerous glacial margins preserved within the several glacially-carved valleys of this vast northeastern Patagonian region. In fact, this region was formerly host to dozens of large PIS outlet glaciers which, in many cases, emplaced remarkably well-preserved glacial geomorphological records (Glasser and Jansson, 2008, Davies *et al*., 2020). This knowledge

[1] Link: https://expage.github.io/index.html
[2] Link : http://alpine.ice-d.org/

gap impedes our ability to compare the timing and relative extent of PIS outlet glacier expansion events in its northeastern sector, to such events occurring in more western and southern sectors of the former PIS. Such regional comparisons of ice-sheet behaviour are essential for testing hypotheses regarding the variations and former latitudinal migrations of local atmospheric and oceanic circulation during climate transitional phases. Northeastern Patagonia thus provides many opportunities to produce detailed palaeo-glacial investigations, address former glacier-climate interactions, and better understand local climatic processes during the late Quaternary.

The observation of this knowledge gap raises the following set of research questions.

Research question set 2:

How extensive were the former PIS outlet glaciers during their numerous preserved late-Quaternary expansion events? What was the precise timing of these ice-sheet expansion events? Did the timing of these major advances coincide with observations of former cold and high precipitation phases observed in other palaeoclimate proxy records? Did ice-sheet retreat following these advances lead to meltwater drainage re-arrangement and to the formation of large proglacial lakes as observed in other eastern Patagonian basins?

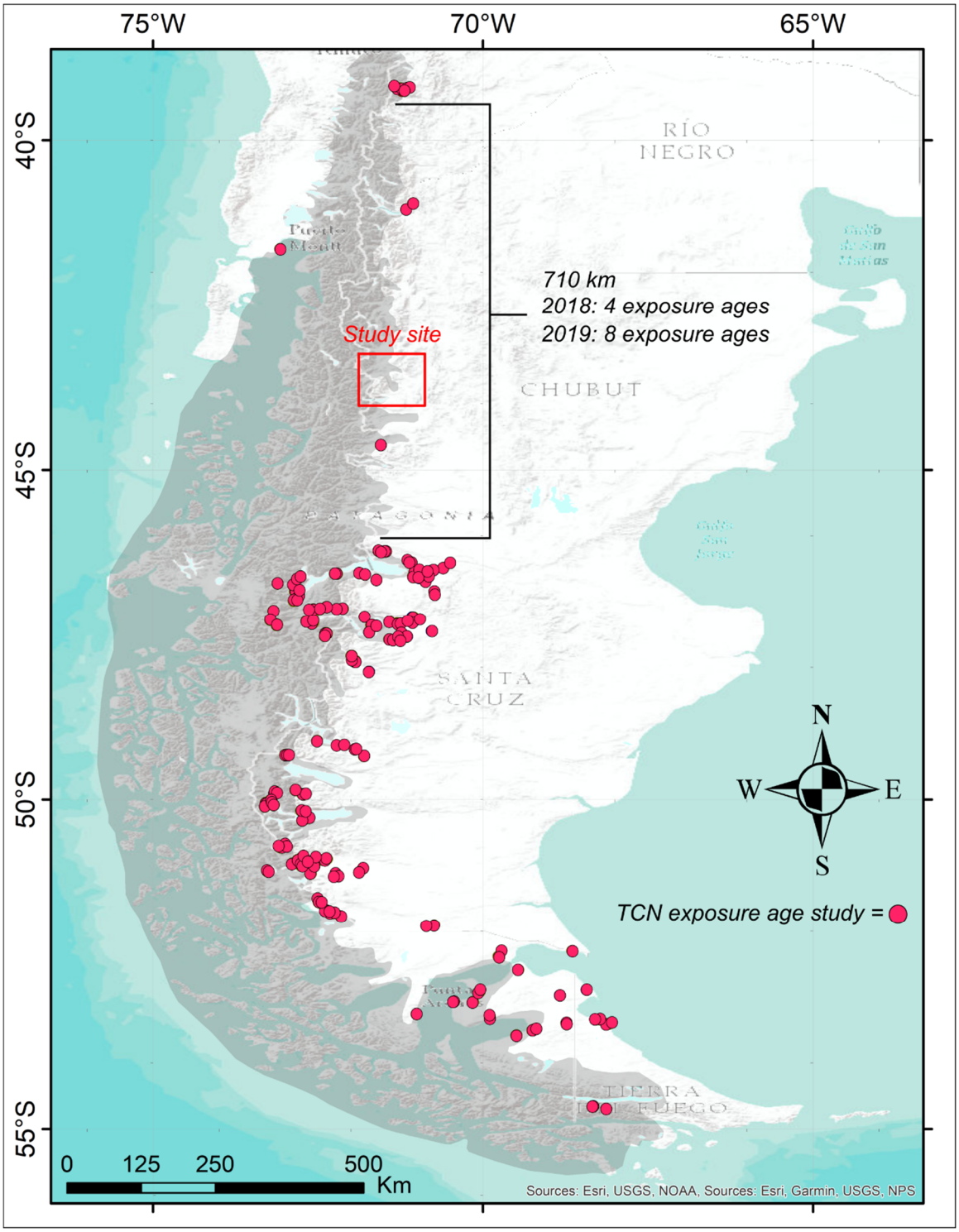

Figure 1.3. Geographical context of the Ph.D. thesis study area with regards to previous TCN exposure-age glacier chronologies produced in Patagonia. The approximate former extent of the PIS at the LGM is represented by the light grey polygon, redrawn after Glasser *et al*. (2008) and Glasser and Jansson (2008). Topographic and bathymetric spatial data from ESRI. Location of previous TCN exposure age datasets was obtained from the *Expage* online global dataset compiled by Jakob Heyman (https://expage.github.io/index.html). At the onset of the Ph.D. project: the 710 km-long northeastern sector of the PIS only featured 4 exposure ages informing glacier advance timing (Zech *et al*., 2017).

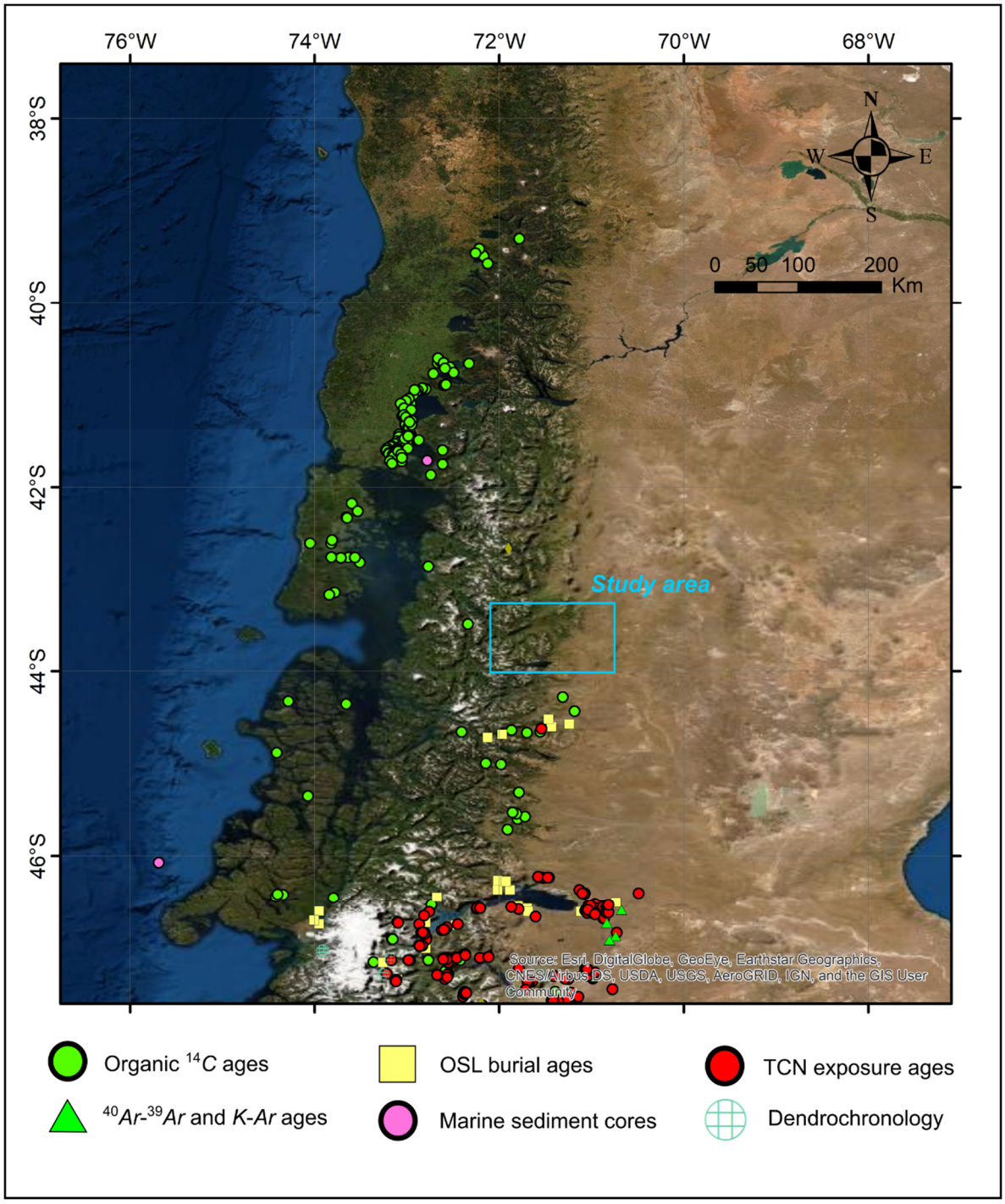

Figure 1.4. Location of the chosen study area in relation to other chronological data published within the context of palaeo-glacial and/or palaeo-climatological investigations. These data were obtained from the PATICE compilation (Davies *et al*., 2020). The underlying remotely-sensed imagery data was obtained from ESRI™ and is characterised by 1 m - resolution images from DigitalGlobe (GeoEye, IKONOS, 2000–2011) at the study site. Note that the TCN exposure ages produced by Zech *et al*. (2017) from this region are intentionally not included within this compilation under the justification that the number of exposure ages per landform was too low to produce a robust chronology. Note also that not all organic ^{14}C ages compiled here relate to reconstructions investigating palaeo-glacial processes.

1.2.3. The preservation of glacial geomorphological records in eastern Patagonia

The East-Patagonian foreland is classified as a semi-arid climate zone and is described as a steppe ecoregion characterized by sparse shrubby and herbaceous vegetation covers (Heusser, 1989). Throughout the Quaternary, these characteristics, combined with the persistently windy conditions and low population densities, has promoted the excellent preservation and low post-depositional disturbance of glaciogenic deposits and landforms associated with the waxing and waning cycles of the former PIS. Indeed, as first observed by the pioneering geographers Francisco Moreno (Moreno, 1899), Otto Nordenskjöld (Nordenskjöld, 1897; 1899) and Carl Caldenius (Caldenius, 1932), these sediment-landform assemblages, usually described as fragile and easily erodible due to their unconsolidated and unsorted nature, can in some cases be preserved over several Quaternary glacial cycles in eastern Patagonia (Auer, 1956). The lack of steep topography diagnostic of the eastern Patagonian plains reduces the potential for erosion of glacial sediment deposits via down-wasting events, and contributes to their preservation. Moreover, major eastern Patagonian outlet glaciers formerly advanced up against retrograde, westward-sloping basal topographies, such that the Atlantic/Pacific drainage divide is located tens of kilometres to the east of the mountain front in most glacial troughs (Clapperton, 1993). Such topographic characteristics, combined with the high subglacial erosion rate of the temperate PIS (Kaplan, 2009) causing relative bed-elevation lowering at a given location during each major glaciation, can promote each subsequent glacier advance to terminate inboard of older glacial deposits and thus preserve them. This setting is quite unique as in most downward-sloping mountain valleys, older glaciogenic deposits are often removed, or partially eroded, by either younger glacier advances associated with the LGM, or by the glaciofluvial activity associated with them. The combination of these aforementioned factors results in the glacial geomorphological record of eastern Patagonia to being remarkably well preserved and well suited to establishing detailed, multi-glacial-cycle reconstructions of Quaternary ice-sheet behaviour (Mercer, 1976). Moreover, direct access to these records is made viable due to local transport links and the lack of dense vegetation cover. In some locations, the preservation of the glacial geomorphology enables to map and date distinct series of PIS-related glacial deposits that cover the entirety of the last glacial cycle (LGC) and older Quaternary glacial cycles. Consequently, as well as being under-studied, the Argentine foreland of Patagonia's northeastern sector is highly suitable to investigations aiming to

reconstruct the former glacial history, as it displays a remarkable preservation of the local glacial geomorphology.

1.2.4. The potential of TCN surface exposure dating for reconstructing the timing of glacial events in northeastern Patagonia

As well as being under-studied and well preserved, the glacial geomorphological record in northeastern Patagonia presents characteristics that make it highly suitable to robust numerical dating of former glacier events. Indeed, the local proximity of the Patagonian Batholith and other igneous felsic lithologies (Hervé *et al*., 2017) allows quartz-bearing rocks to be found in relatively high concentration within the glaciogenic deposits of interest to this investigation, such as glacial moraines and proglacial outwash-plain deposits. This enables to calculate exposure ages from the determination of *in situ* cosmogenic ^{10}Be concentration (in atoms g^{-1} yr^{-1}), which accumulates mostly in quartz (Dunai, 2010). For the timescales of interest to this work (10^3 - 10^5 yr), ^{10}Be is the most commonly used cosmogenic nuclide (Balco, 2011). This radionuclide is characterised by relatively well-constrained production pathways featuring a high dominance of spallation-derived production (~96.4%; Dunai, 2010) and a relatively well-constrained half-life constant of 1.387 ± 0.0012 x10^6 years (Chmeleff *et al*., 2010; Korschinek *et al*., 2010). Such characteristics enable the analysis of *in situ* ^{10}Be concentration in quartz to produce exposure ages with the lowest currently possible analytical uncertainties associated with Accelerator Mass Spectrometer (AMS) measurements (typically around 3%; Balco, 2011). Moreover, Kaplan *et al*. (2011) were able to better estimate the site-specific production rate of ^{10}Be in quartz in central Patagonia (Lago Argentino; 50°S), using independent ^{14}C age constraints for several glacier advances. Using this local production rate and the most up-to-date time-dependent scaling schemes (LSDn: Lifton *et al*., 2014), one can determine a more realistic ^{10}Be production rate for our sample locations. This enables us to reduce scaling uncertainties and produce more accurate exposure ages than when using a global average production rate (*e.g*. Borchers *et al*., 2016).

The contemporary Patagonian Icefields and former PIS are characterised by low elevation, temperate and climate-sensitive outlet glaciers (Mouginot *et al*., 2015). In many valleys across Patagonia, ample geomorphological evidence of striated and ice-moulded bedrock surfaces, as well as large-scale lineations, indicate that major palaeo-outlet glaciers of the PIS were sliding

and warm-based in nature, at least towards their centre flowline where ice was thickest (Clapperton, 1993; Glasser and Jansson, 2008). Warm-based glaciers are highly effective agents of erosion (Benn and Evans, 2014). Because the spallogenic production rate of ^{10}Be becomes negligible 3 m below a flat rock surface (Dunai, 2010; Balco, 2011), high rates of subglacial erosion cause both fresh rock surfaces and clasts detached from an eroding glacier bed to be free of inherited cosmogenic ^{10}Be.

Thus, due to the temperate and warm-based nature of Patagonian outlet glaciers, and due to the availability of quartz-bearing lithologies, TCN exposure dating of ice-contact glaciogenic deposits and bedrock surfaces often produce relatively clustered exposure-age datasets in many Patagonian study sites (*e.g.* Hein *et al*., 2010; Peltier *et al*., 2021). This technique is thus appropriate to establishing a detailed palaeo-glacier chronology at the study site.

1.2.5. The conundrums on latitudinal and longitudinal asynchronies in the timing of the local LGM across Patagonia

The timing of the maximum PIS extent during the LGC has been a subject of debate within the palaeo-glaciological community. In northwestern Patagonia, robust glacial chronologies utilise numerous bracketing radiocarbon ages to date individual outlet glacier advances in the Chilean Lake District (41° S; Fig. 1.4) that span the entirety of the global LGM period (26-18 ka) of MIS 2 (Denton *et al*., 1999; Moreno *et al*., 2015). In southern Patagonia (51-52° S), however, robust palaeo-glacial chronologies established from TCN exposure dating of moraine boulders (Sagredo *et al*., 2011; García *et al*., 2018) clearly indicate that the local LGM occurred much earlier and during MIS 3, at ~45-48 ka, and was significantly more extensive (50-100 km) than subsequent advances associated with the global LGM. Further north, the major central Patagonian ice lobes of Lago Buenos Aires and Lago Pueyrredón (46.5-47.5° S) reached their maximum LGC extent 15 - 20 ka later, during MIS 2, and more in line with the Northern Hemisphere ice sheets (Kaplan *et al*., 2004; Douglass *et al*., 2006; Hein *et al*., 2010). At the onset of this Ph.D. investigation, some MIS 3 glacial expansions had been identified in northwestern Patagonia within the Chilean Lake District region, but were of similar magnitude to subsequent advances that occurred during MIS 2 (Moreno *et al*., 2015).

Consequently, establishing an informative cosmogenic nuclide-derived glacier chronology of local LGM expansion events in under-studied northeastern Patagonia has implications for resolving long standing-conundrums regarding latitudinal and longitudinal asynchronies in the timing of maximum PIS extent during the LGC. Such investigation presents the potential to answer the following set of research questions:

Research question set 3:

Was the extensive MIS 3 glacial maximum an anomaly geographically restricted to eastern outlet glaciers of southern Patagonia? During the LGC and other middle Pleistocene glacial cycles, when did the former northeastern PIS outlet glaciers reach maximum ice volume and extent? Were these local glacial maxima coeval with previously studied outlet glacier resurgences that occurred in other regions of Patagonia? Are previously posed hypotheses regarding the possible asynchronies of millennial-scale glacier events in Patagonia valid?

1.3. Aims

1. To reconstruct the late-Quaternary evolution of PIS outlet glaciers in the previously understudied northeastern sector of the former ice sheet, with an emphasis on glacier geomorphology, chronology and numerical modelling. This aim will focus on providing answers to questions expressed in research question set 2 (section 1.2.2).

2. To utilise this glacier reconstruction to unravel Patagonian, inter-regional and inter-hemispheric asynchronies and/or synchronies in Quaternary glacial mass balance evolution. This aim relates to questions raised in research question set 3 (section 1.2.5)

3. To utilise this ice-sheet and glacier reconstruction as a proxy for past climate evolution and to shed light on the possible environmental mechanisms driving glacial fluctuations at the study site but also throughout Patagonia and the southern mid-latitudes. This aim will focus on contributing to the scientific body of evidence trying to answer long-lasting research questions such as those phrased in research question set 1 (section 1.2.1).

1.4. Research objectives

In order for this Ph.D. investigation to address the aforementioned aims, the research is structured around four main research objectives described in this section.

1.4.1. Objective 1: Establishing a geomorphological and morphostratigraphic reconstruction of glacial dynamics at the study site

The first objective of this Ph.D. investigation is to construct, for the first time, a detailed map of the glacial geomorphology across the field site: *i.e.* the Río Corcovado, Río Huemul and Lago Palena/General Vintter valleys (43°S; 71°W), by combining remotely-sensed data (from digital elevation models and high-resolution imagery) and field observations. Such an exercise aims at obtaining the necessary understanding of the extent of former glacier advances and of the stratigraphic order of glacial and proglacial events preserved locally. Comprehending the morphostratigrahy is considered an essential pre-requisite for a robust geochronological reconstruction, as it helps identifying the most well-preserved and undisturbed landforms suitable for TCN exposure dating, and fundamentally underpins the research aims.

1.4.2. Objective 2: Establishing a detailed geochronological reconstruction of local glacial and proglacial events during the LGM and last deglaciation

The second main objective of this thesis is to establish a robust geochronological reconstruction of glacial and proglacial dynamics associated with the local LGM, which features the best–preserved glaciogenic, glaciofluvial and glaciolacustrine sediment-landform assemblages of the study site. This involves mostly using TCN surface exposure dating to reconstruct:

1) The extent and timing of distinct local LGM advances of the studied outlet glaciers
2) The timing of the onset of local deglaciation and ice-sheet disintegration.

3) The timing of formation and drainage events of former proglacial lakes during outlet glacier advance-and-retreat phases associated with the local LGM and deglacial periods.

1.4.3. Objective 3: Establishing a reconstruction of paleoclimate dynamics by combining geochronology and glacier numerical modelling

The third main objective of this Ph.D. thesis is to evaluate a range of possible palaeo-climatic conditions at the time of local glacier advances by using glacier surface mass balance as a proxy for past atmospheric temperatures and precipitation. This reconstruction involves combining geomorphological mapping, TCN exposure dating and glacier numerical modelling using a spatially distributed ice flow model coupled with a positive degree-day surface mass balance parameterisation. The aim is to assess whether local glacier advances can provide insights into past climate conditions in northeastern Patagonia during the latter stages of the local LGM.

1.4.4. Objective 4: Establishing a reconstruction of major pre-LGM and pre-Last Glacial Cycle glaciations at the study site and assess the palaeo-climatic context

The fourth main objective of this thesis is to reconstruct the pre-LGM history of ice-sheet evolution evidenced by the local preservation of stratigraphically-older glaciogenic and glaciofluvial deposits. Such investigation involves implementing different approaches to TCN exposure dating of glacial margins than for the younger local LGM deposits. Indeed, different methodologies are required to account for the impact of post-depositional disturbance and rock surface erosion on relatively old surfaces. The aim of this reconstruction is also to complete the multi-glacial-cycle record of PIS advances preserved at the study site and compare our chronology with other regional and global paleoclimate records to better estimate the drivers of major glaciations at the southern mid-latitudes.

1.5. Thesis structure

Chapters 2-5 of this Ph.D. thesis comprises a series of four original research articles published in (n=3), or submitted to (n=1), peer-reviewed journals. These four publications constitute the majority of the scientific results produced within the context of this Ph.D. investigation. For each chapter, a brief introduction of the research conducted and a description of my personal contribution to the final article is included below. The papers are rendered in their pre-print format, and supplementary materials associated with each publication has been integrated to the thesis appendix. Paper abstracts have been removed to avoid repetitions between chapters. The scientific methods employed are specific to each publication, and are thus embedded within each chapter as for the original published/submitted articles, as opposed to constituting a separate thesis chapter. For each of our publications, which can be qualified as long-format papers, a research objective-specific literature review was conducted and is incorporated within the papers. The supplementary materials associated with each publication were collated in the thesis Appendix. Each of these companion publications/chapters address a distinct research objective and are thus ordered according to the list of objectives outlined in section 1.3. These result chapters are followed by chapter 6, which summarises the main findings and conclusions of the Ph.D. investigation and specifies how these results address the main research aims described in section 1.2. Finally, chapter 6 outlines the main avenues and priorities for future investigation aiming to address similar aims and objectives as this Ph.D. research.

1.5.1. Chapter 2

Leger, T.P.M., Hein, A.S., Bingham, R.G., Martini, M.A., Rodrigo, L.S., Sagredo, E.A., and Martínez, O.A., (2020). The glacial geomorphology of the Río Corcovado, Río Huemul and Lago Palena/General Vintter valleys, northeastern Patagonia (43°S, 71°W). *Journal of Maps*, v. 16(2), p. 651-668, doi: https://doi.org/10.1080/17445647.2020.1794990.

This publication describes the methods, results and implications of glacial geomorphological mapping of sediment-landform assemblages associated with three major outlet glaciers of the study site: the Río Corcovado, Río Huemul and Lago Palena/General

Vintter palaeo-glaciers. This paper thus accompanies a detailed geomorphological map that covers 5300 km^2 and differentiates 25 landform types associated with ice-contact glaciogenic, glaciofluvial and glaciolacustrine processes. It is the first map to describe these sediment-landform assemblages to such high spatial resolution at the study site. The map and paper represent a crucial framework on which to build an understanding of the former glacial and proglacial processes at the study site. This work delivers a geomorphological foundation that justifies the investigation strategies followed to address research objectives 2-4 (chapters 3-5) and accounts for the choice of specific sampling locations for TCN exposure dating.

For this study, I undertook geomorphological mapping from remote sensing analysis and in the field, digitised the shapefiles and produced the final map, wrote the manuscript (original draft and review and editing), and produced the figures and tables. Co-authors all conducted fieldwork and/or shared ideas regarding landform interpretations, and all authors reviewed and edited the original manuscript. The paper and map have been published open-access in the *Journal of Maps*, and the georeferenced shapefiles were made accessible through an open-access Mendeley Data online repository.

1.5.2. Chapter 3

Leger, T.P.M., Hein, A.S., Bingham, R.G., Rodés, Á., Fabel, D., and Smedley, R., (2021a). Geomorphology and ^{10}Be chronology of the Last Glacial Maximum and deglaciation in northeastern Patagonia, 43°S-71°W. *Quaternary Science Reviews*, v. 272, doi: https://doi.org/10.1016/j.quascirev.2021.107194.

This study focuses on establishing a detailed and robust chronology of the local LGM expansions of the Río Corcovado glacier, the principal former outlet glacier of this Ph.D.'s study area. Using TCN exposure dating of moraine boulders and Bayesian age modelling, this investigation reconstructs the approximate timing of five distinct local LGM advances of the former PIS outlet glacier, and enables to estimate the timing for the onset of local deglaciation. Moreover, by studying and dating the surface exposure period of palaeo-shoreline sediments and ice-moulded bedrock surfaces, this study also reconstructs the timing of former proglacial lake formation and drainage events associated with the retreat of the local ice fronts during

deglaciation and prior to final ice-sheet disintegration. This TCN chronology is the first reconstruction of the extent and timing of PIS outlet glacier advances in the Río Corcovado and neighbouring valleys during the LGM. It provides a benchmarking framework for understanding the timing of maximum ice volume during the LGC in the understudied northeastern region of Patagonia.

For this investigation, I co-conceived the study with A.S.H., organised and conducted fieldwork with help from A.S.H. and R.G.B., wrote NERC CIAF grant application together with A.S.H., conducted cosmogenic nuclide laboratory analyses on all samples with help from A.R., conducted result analyses and interpretations with advices from A.S.H. and A.R., wrote the manuscript (original draft and review and editing) as well as the supplementary materials (located in the thesis Appendix) with feedback from all co-authors, and generated maps, figures and tables.

1.5.3. Chapter 4

Leger, T.P.M., Hein, A.S., Goldberg, D., Schimmelpfennig, I., Van Wyk de Vries, M.S., Bingham, R.G., and ASTER Team, (2021b). Northeastern Patagonian Glacier Advances (43°S) Reflect Northward Migration of the Southern Westerlies Towards the End of the Last Glaciation. *Frontiers in Earth Science*, v. 9, 751987, doi: https://doi.org/10.3389/feart.2021.751987.

This study focuses on the former late-LGM expansion of isolated mountain glaciers located within the highest valleys of the study site. It combines glacial geomorphological mapping, TCN exposure dating of moraine boulders and numerical glacier modelling to establish the timing of these advances and reconstruct the three dimensional geometry and surface mass balance of these glaciers when reaching the studied margins. The spatially-distributed ice-flow model is thus coupled with a positive degree-day surface mass balance parameterisation, which, after correcting for cumulative local surface uplift associated with glacial isostatic adjustment since the advances, enables to estimate a range of possible mean annual temperature and total annual precipitation values at the time of the advance. Therefore, as well as establishing a TCN chronology for specific advances of local mountain glaciers, this

investigation enables to draw conclusions on the palaeo-climate dynamics associated with regional expansion events of mountain glaciers towards the end of the LGM in northeastern Patagonia.

For this paper, I conceived the study, raised the finances for fieldwork via a crowdfunding platform, conducted fieldwork with help from Pablo Tapia Gonzalez, wrote applications for the British Society for Geomorphology Postgraduate Research Grant and Scottish Alliance for Geoscience, Environment and Society (SAGES) small grant scheme with help from A.S.H, conducted cosmogenic nuclide laboratory analyses on all samples with help from I.S., conducted glacier numerical modelling analysis with help from D.G., wrote the manuscript (original draft and review and editing) as well as the supplementary materials (located in the thesis Appendix) with feedback from all co-authors, and generated maps, figures and tables.

1.5.4. Chapter 5

Leger, T.P.M., Hein, A.S., Rodés, Á., Bingham, R.G., Schimmelpfennig, I., Fabel, D., Gonzalez, P.T., ASTER Team., (2022). A cosmogenic nuclide-derived chronology of pre-Last Glacial Cycle glaciations during MIS 8 and MIS 6 in northern Patagonia. *Climate of the Past, in (open) review,* doi: https://doi.org/10.5194/cp-2022-32.

This paper focuses on the pre-LGC geomorphological record preserved at the study site, and more specifically in the RC and RH valleys. By doing so, the investigation aims to complete previous chapters/papers and provide a full picture of the extent and timing of all palaeo-glacial events preserved at the study site. This work builds on previous work by Hein *et al*. (2009; 2011, 2017), who pioneered TCN exposure dating of proglacial outwash surface sediment in eastern Patagonia, to numerically date pre-LGM and pre-LGC glacial expansion events. This previous work had shown that, in the semi-arid eastern Patagonian steppe environment, proglacial outwash sediments, and more specifically quartz-bearing surface cobbles, often proved to be more reliable target samples than moraine boulders by yielding less exposure-age scatter (*ibid*). The aim of this work was to employ that approach and adapt it to the study area in order to provide a robust, direct chronology of three morphologically-distinct moraine-outwash complexes preserved in the RC and RH valleys and located outboard (thus older) of

the outermost LGM moraine dated, namely the RC 0, RC I and RC II glacial margins. By combining these results with the remaining ages, this chapter/paper draws conclusions on the timing of the most prominent middle-to-late Pleistocene glaciations in northern Patagonia, and compares these findings with other Patagonian regions and other glacial records worldwide. Finally, obtaining a broad picture through a multi-glacial-cycle chronology enables this investigation to assess the various climatic and orbital drivers of major late-Quaternary glaciations in the southern mid-latitudes.

For this investigation, as for the study associated with Chapter 4, I conceived the study, raised the finances for fieldwork via a crowdfunding platform, and conducted fieldwork with help from P.T.G., wrote applications for the British Society for Geomorphology Postgraduate Research Grant and Scottish Alliance for Geoscience, Environment and Society (SAGES) small grant scheme with help from A.S.H. Cosmogenic nuclide laboratory analyses on most samples was conducted by Á. R. at SUERC, while I processed a subset of 6 samples with help from I.S. at the LN_2C laboratory of CEREGE. I conducted the analysis/interpretation of TCN exposure-age data, wrote the manuscript (original draft and review and editing) as well as the supplementary materials (here located in the thesis Appendix), with feedback from all co-authors. I created the associated maps, figures, and tables.

Chapter 2

|

The glacial geomorphology of the Río Corcovado, Río Huemul and Lago Palena/General Vintter valleys, northeastern Patagonia (43°S, 71°W)



Publication details

Authors

Tancrède P. M. Leger[1], Andrew S. Hein[1], Robert G. Bingham[1], Mateo A. Martini[2,3,4], Rodrigo L. Soteres[2,3], Esteban A. Sagredo[2,3,5], Oscar A. Martínez[6]

[1]*School of GeoSciences, the University of Edinburgh, Edinburgh, United Kingdom*
[2]*Millenium Nucleus Paleoclimate, ANID Millenium Science Initiative, Santiago, Chile*
[3]*Instituto de Geografía, Facultad de Historia, Geografía y Ciencia Política, Pontificia Universidad Católica de Chile, Santiago, Chile*
[4]*Centro de Investigaciones en Ciencias de la Tierra (CICTERRA, CONICET-Facultad De Ciencias Exactas, Físicas y Naturales, UNC), Córdoba, Argentina*
[5]*Estación Patagonia de Investigaciones Interdisciplinarias UC, Pontificia, Universidad Católica de Chile, Santiago, Chile*
[6]*Facultad de Ciencias Naturales y Ciencias de la Salud, Universidad Nacional de la Patagonia San Juan Bosco, Ruta 259, km 16.5, Esquel, Chubut, Argentina*

Author contributions

Tancrède P. M. Leger: Conceptualization, Data curation, Formal analysis, Map production, Investigation, Methodology, Project administration, Software, Visualization, Writing (original draft and review & editing)

Andrew S. Hein: Conceptualization, Data curation, Funding acquisition, Methodology, Project administration, Supervision, Validation, Writing (original draft and review & editing).

Robert G. Bingham: Data curation, Supervision, Writing (original draft).

Mateo A. Martini: Data curation, Writing (original draft)

Rodrigo L. Soteres: Data curation, Writing (original draft)

Esteban A. Sagredo: Writing (original draft)

Oscar A. Martínez: Writing (original draft)

Lead Author contact details

Tancrède P.M. Leger, PhD student, University of Edinburgh, School of GeoSciences,
Address: Institute of Geography, Drummond Street, Edinburgh EH8 9XP, United Kingdom
Email: Tancrede.leger@ed.ac.uk

Publication details

Journal: Journal of Maps; open access

2020, Vol. 16, No. 2, p. 651–668

Doi: https://doi.org/10.1080/17445647.2020.1794990

Received: 22 May 2020

Revised: 9 July 2020

Accepted: 9 July 2020

Final published map

Link to download:

https://www.tandfonline.com/doi/suppl/10.1080/17445647.2020.1794990?scroll=top

Link to shapefiles:

https://doi.org/10.17632/c2hy8rkbyd.1

2.1 Introduction

The Patagonian region of southern South America was host to the most extensive Quaternary ice sheet of the southern hemisphere outside of Antarctica, the Patagonian Ice Sheet (PIS). The PIS covered a latitudinal extent of ~2000 km (38°S - 56°S; Fig. 2.1) along the spine of the Patagonian and Fuegian Andes (Caldenius, 1932; Glasser *et al*., 2008; Martínez *et al*., 2011; Davies *et al*., 2018; 2020). Patagonia is part of the only continental landmass that fully intersects the precipitation-bearing southern westerly winds (Garreaud *et al*., 2013) and is one of few regions in the southern mid-latitudes containing a well-developed Quaternary glacial geomorphological record (Clapperton, 1993; Glasser *et al*., 2008). Patagonia therefore offers a unique opportunity to study Quaternary climatic and environmental change in the southern mid-latitudes.

Robust palaeoglaciological reconstructions of PIS outlet glaciers can help us to investigate the landscape evolution and climate-forcing mechanisms responsible for Quaternary ice-sheet fluctuations (*e.g.* Rabassa *et al.*, 2000; Hein *et al*., 2010). They can provide insights into the timing and causes of Quaternary glacial cycles in the southern mid-latitudes, and enable determination of the regional drivers of glaciation as well as inter-hemispheric glacial (a)synchronicity (Denton *et al.*, 1999; Bentley *et al.*, 2005; Glasser *et al.*, 2008). For these reasons, the PIS has been subject to an increasing number of glacial geochronological reconstructions. However, with a few exceptions (*e.g.*, Iglesias *et al*., 2016; Van Daele *et al*., 2016; García *et al*., 2019) there remains a general lack of published detailed mapping and geochronological data across the northeastern sector of the former ice sheet, between ~39°S and ~46.5°S (Darvill *et al.*, 2015; Mendelova *et al*., 2017; Davies *et al*., 2020). Robust reconstructions from this region are needed to understand fully the PIS response to the Last Glacial Maximum (LGM) at these latitudes, and to investigate latitudinal dependencies on the timing of the local LGM throughout Patagonia (Sagredo *et al*., 2011; Darvill *et al*., 2015; García *et al*, 2018; 2019; Davies *et al*., 2020). A vital component of such reconstructions is detailed, glacier-scale geomorphological mapping (Evans & Orton, 2015; Chandler *et al*., 2018; Clark *et al*., 2018). This provides spatial information that facilitates interpretations of palaeoglaciological behaviour and equips glacial geologists with an essential framework upon which to build robust chronologies (Darvill *et al*., 2016; Bendle *et al.,* 2017a;

Chandler *et al*., 2018). We thus present in this paper the first detailed glacial geomorphological map of three valleys in northeastern Patagonia (43.5°S), the Río Corcovado, Río Huemul and Lago Palena/General Vintter valleys (Fig. 2.1b). Our aim is to provide benchmark geomorphological data for future geochronological interpretations of their glacial history.

2.2 Study location and previous work

The geomorphological map is centered on a region located east of the Patagonian Andes, between 43.3°S and 44.0°S, and covers an area of ~5300 km^2 (Fig. 2.1b). At these latitudes, a major westward-dipping over-deepened valley, the Río Palena trough, cuts through the Andes to drain the contemporary Río Corcovado, Río Huemul and Lago Palena/General Vintter catchments westward to the Pacific Ocean. At this location, the PIS was characterised by ice flowing towards the east-northeast from the centre of the former ice sheet, located near Macizo Nevado. Glacier ice thus flowed along the Río Palena trough to the mountain front, where it diverged into two glaciers occupying the Río Huemul valley to the east, and the Río Corcovado valley to the south (Fig. 2.1b). The two outlet glaciers extended up to 60 km to the east and southeast of the Argentinian town of Corcovado (43°54'S; 71°46'W) (Caldenius, 1932; Haller *et al*., 2003; Martínez *et al*., 2011). Here, we refer to these as the Río Huemul glacier and the Río Corcovado glacier; the latter to distinguish it from the Golfo Corcovado outlet glacier that drained the western side of the PIS (Denton *et al*., 1999). The Lago Palena/General Vintter outlet glacier drained a separate, smaller catchment located ~30 km southeast of the Río Palena trough. This glacier flowed eastward, at times extending to converge with the Río Corcovado glacier coming from the north (Fig. 2.2). Subsequent retreat into an over-deepened basin led to the formation of the moraine-dammed Lago Palena/General Vintter lake, still present to this day (43°55'S; 71°31'W) (Fig. 2.2). Our mapping focuses on the former terminal environment of these three outlet glaciers. Subglacial erosion and over-deepening of the Río Palena trough is greater towards the centre of the former PIS where ice thickness and duration of ice cover were largest (Clapperton, 1993; Hubbard *et al*., 2005; Kaplan *et al*., 2009). Thus, at our study site, asymmetrical subglacial erosion generated a progressive eastward migration of the Atlantic-Pacific drainage divide following each Quaternary glaciation, causing the contemporary drainage divide to be located ~70-80 km east of the central spine of the

Andes (Kaplan *et al*., 2009; Davies *et al*., 2020) (Fig. 2.2). The semi-arid eastern sectors of the Río Corcovado, Río Huemul and Lago Palena/General Vintter valleys, which belong to the Patagonian steppe climate zone, are characterized by extensive, well-preserved and easily discernible moraine complexes, along with their associated glaciofluvial and glaciolacustrine sediment-landform assemblages (Haller *et al*., 2003; Martínez *et al.*, 2011).

Geomorphological mapping of major moraine limits in the Río Corcovado, Río Huemul and Lago Palena/General Vintter valleys was conducted by Caldenius (1932), Glasser & Jansson (2008), and Davies *et al.* (2020), in their respective efforts to record the glacial geomorphology of the entire PIS (Table 2.1). Haller *et al.* (2003), meanwhile, produced a regionally-focused geological map of the three valleys including main glaciogenic deposits (area located between 43-44°S and 72-70.3°W). These deposits were also mentioned in studies by Lapido (1990) and Martínez *et al.* (2002; 2011). However, all previous mapping was part of ice-sheet-wide geomorphological investigations or geological surveys and was focused primarily on identifying the most prominent moraines and glaciofluvial deposits for each glaciated valley. All previous studies interpreted the landforms as Pleistocene glaciogenic deposits associated with three distinct glaciation events, with the innermost preserved moraines suggested to relate to the local LGM. However, the ages of Río Corcovado, Río Huemul and Lago Palena/General Vintter deposits were inferred solely from morpho-stratigraphic observations and comparisons with other dated Patagonian records (*e.g.* the Lago Buenos Aires record, 46.5°S), with numerical dating yet to be applied. Here, we thus undertake the first detailed mapping of the complex glacial sediment-landform assemblages preserved in the three valleys. This work will serve as a geomorphological framework for new geochronological reconstructions in progress.

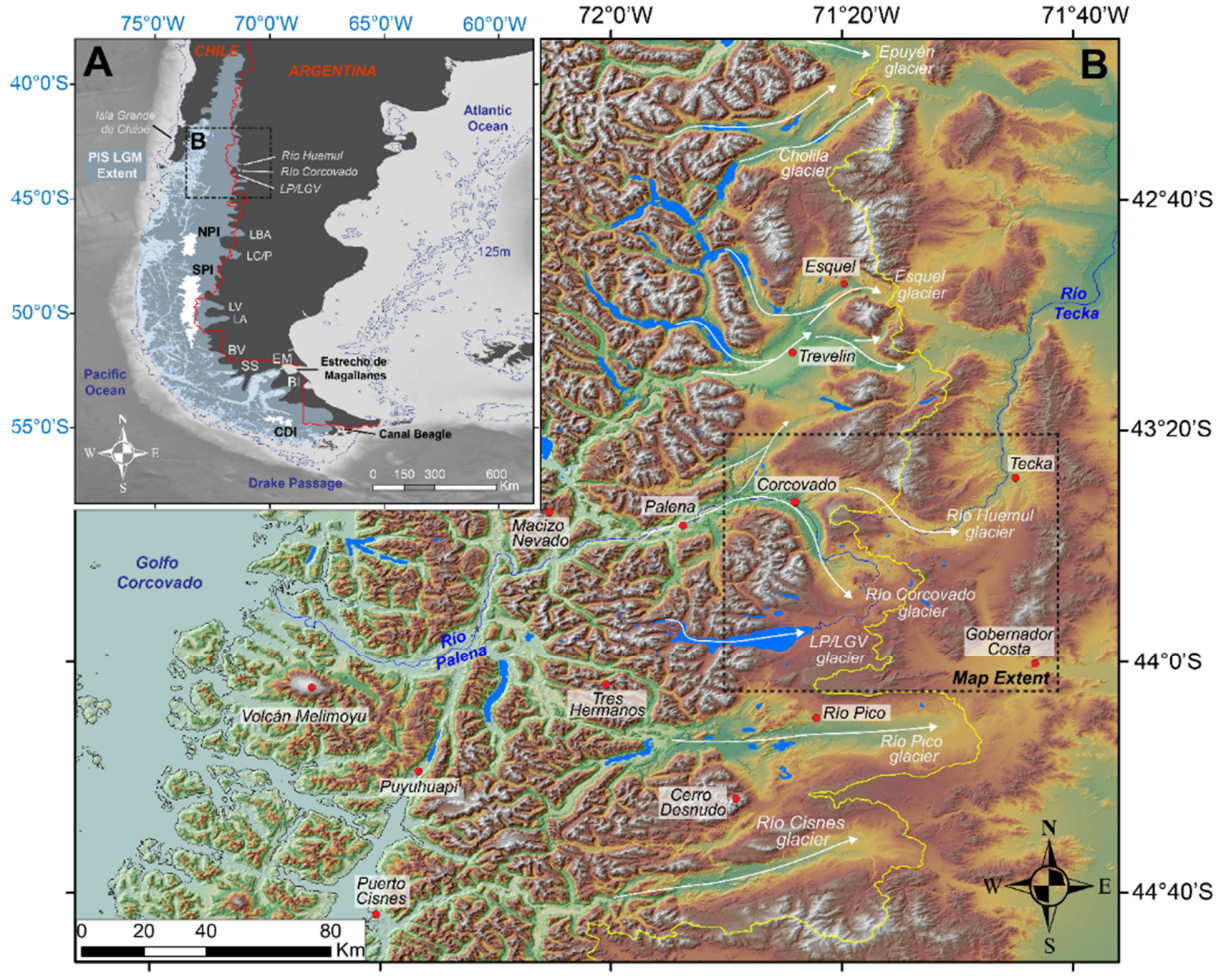

Figure 2.1. Geographical and glaciological context of the study area. (A) Approximate former extent of the Patagonian Ice Sheet (PIS) at the Last Glacial Maximum (LGM), redrawn after Glasser *et al.* (2008) and Glasser and Jansson (2008). Overlain in white are the contemporary North Patagonian (NPI), South Patagonian (SPI), and Cordillera Darwin (CDI) Icefields. Major eastern PIS glaciers are designated; BI: Bahía Inútil, EM: Estrecho de Magallanes, SS: Seno Skyring, BV: Bella Vista, LA: Lago Argentino, LV: Lago Viedma, LC/P: Lago Cochrane/Pueyrredón, LBA: Lago Buenos Aires. Bathymetric data of ocean basins were obtained from the General Bathymetric Chart of the Oceans (GEBCO) and are displayed in greyscale. A -125m contour line is applied to simulate the approximate former position of coastlines at the LGM (Lambeck *et al*., 2014). The Chile/Argentina border is highlighted in red. (B) Digital elevation model (DEM) of northern Patagonian region from the ALOS WORLD 3D missions (version 2.2; JAXA; https://www.Eorc.jaxa.jp/ALOS/en /aw3d30/) with a shaded relief background and a black sea level contour line highlighting modern coastlines. White arrows indicate former ice-flow of major northeastern PIS outlets, including the Río Corcovado, Río Huemul and Lago Palena/General Vintter glaciers. The yellow line designates the contemporary Atlantic/Pacific drainage divide. Lake bodies and key river channels are drawn in blue. The black dotted box delineates the extent of the geomorphological map presented with this paper.

2.3 Methods

2.3.1 Remote sensing

Initial identification of major landforms and topographic features was conducted using the ALOS WORLD 3D - 30 m resolution (AW3D30) Digital Elevation Model (DEM) (version 2.2; https://www.Eorc.jaxa.jp/ALOS/en/aw3d30/) (Fig. 2.2). Hillshade backgrounds of different azimuths were produced using ArcGIS (v10.5), along with topographic contour lines. When displaying significant positive relief (>15 m), cross-section elevation profile graphs were generated to further distinguish major landforms according to their morphometry. All mapped landforms were digitized manually in the WGS84 geographic reference coordinate system using the ESRI™ World Imagery layer, characterized by 1.0 m resolution images from DigitalGlobe (GeoEye, IKONOS, 2000-2011) at the study site. To increase landform identification potential, three-dimensional views of this imagery layer were produced in the 'Windows Maps' application (Microsoft Corporation). In areas with high vegetation cover, different colour-rendering comparisons were made using 10 m resolution Sentinel 2A true colour (TCI) and false colour (bands 8,4,3) products (https://scihub.copernicus.eu/). Similar mapping methodologies were used by Darvill *et al.* (2014), Bendle *et al.* (2017a), Mendelová *et al*. (2020) and Soteres *et al.* (2020) to conduct high spatial resolution glacial geomorphological mapping of other Patagonian regions.

2.3.2 Field mapping

Field mapping was conducted over the austral summers of 2018 (Lago Palena/General Vintter only), 2019 and 2020 (all three valleys). Fieldwork focussed primarily on ground-truthing and/or corrections of preliminary landform interpretations, with additional geomorphological mapping undertaken in key accessible locations (Chandler *et al*., 2018). To aid understanding of landform genesis, landform sedimentology was also analysed where possible.

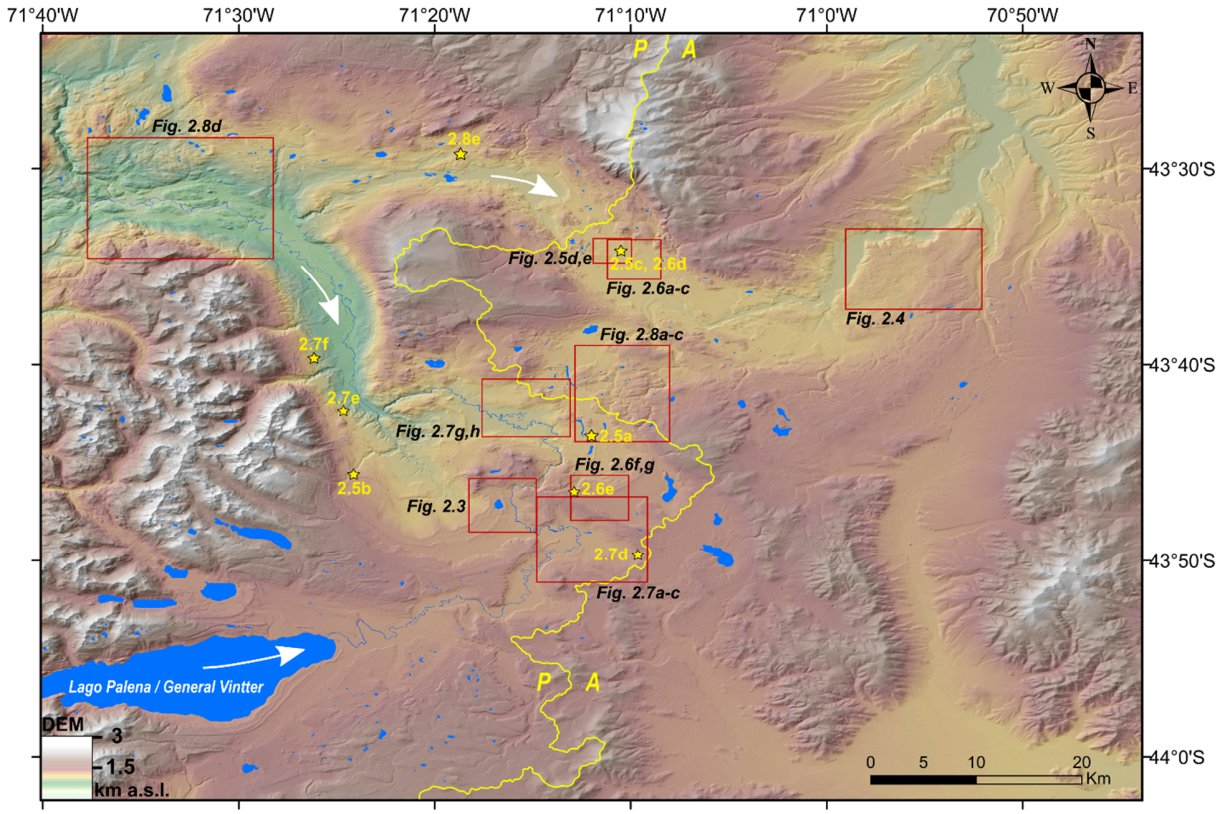

Figure 2.2. Digital elevation model (AW3D30 and hillshade) showing the area covered by the map presented with this chapter. Locations of imagery / geomorphology comparison maps presented in Figs. 2.3-2.8 are shown by red boxes. Locations of photographs presented in Figs. 2.3-2.8 are indicated with yellow star symbols. The Atlantic (A) / Pacific (P) drainage divide is delineated in bright yellow, while ice-flow direction of the Lago Palena/General Vintter, Río Corcovado and Río Huemul glaciers is indicated by the white arrows. The Río Corcovado and lakes / water bodies are mapped in dark blue.

2.4 Results

2.4.1 Glacial geomorphology

The glacial geomorphology in the study area records the terminus positions of the Río Corcovado, Río Huemul and Lago Palena/General Vintter outlet glaciers over multiple glacial cycles. Glacial depositional and erosional features thus heavily dominate the three valleys' geomorphological records. Our mapping reveals twenty-five landform types, classified and manually digitized as polyline and polygon shapefiles (Table 2.1). These comprise seventeen glacial geomorphological landform types, including a variety of ice-contact glaciogenic landforms (*e.g.*, moraines, hummocks), glaciofluvial (*e.g.*, outwash plains, meltwater channels), glaciolacustrine landforms (*e.g.*, palaeo-shorelines, raised deltas) and subglacial landforms (*e.g.*, ice-moulded bedrock, lineations). Identification criteria for these seventeen landforms are described below, and uncertainty assessments related to landform identification are summarised in Table 2.1. The map also features six geomorphological features providing wider geographical context, including empty cirques, alluvial fans, rotational slumps or landslides, and modern hydrological features (*e.g.* rivers, lakes etc.). Furthermore, a polyline delineates the contemporary Atlantic-Pacific drainage divide, extrapolated from the DEM (Fig. 2.2).

2.4.2 Ice-contact glaciogenic landforms

2.4.2.1 Moraine complexes and kettle-kame topography

We differentiate here between two types of ice-contact glaciogenic sediment composites. Relatively confined, narrow (<3 km wide) and easily discernible sediment complexes of arcuate shape comprising prominent and continuous moraine ridges (Section 4.2.2), as well as concentrated, hummocky ridges in parallel to each other (Section 4.2.3), are here termed moraine complexes (Fig. 2.3). In contrast, large (>3 km) deposits composed of chaotic hummocks (or kames) irregularly interspersed with hollows and kettle holes, presenting few moraine ridges and low concentrations of hummocky ridges, are here defined as kettle-kame topography (Darvill *et al.*, 2014; Fig. 2.4). Although both composites essentially highlight former glacier margins, we

feel that it is important to distinguish between their dissimilar morphologies to highlight possible variability in former ice-marginal environments (*e.g.*, Raedecke, 1978; Benn & Clapperton, 2000; Darvill *et al.,* 2014). In contrast to well-defined moraine complexes diagnostic of the less extensive, younger deposits (Fig. 2.3), the most distal deposits discernible from imagery and in the field in the Río Huemul valley consist of a large belt of kettle-kame topography, previously termed the "Tecka drift" (Lapido *et al.*,1990; Haller *et al.*, 2003; Martínez *et al.,* 2011) (Fig. 2.4). Consequently, differentiating between distinct glaciogenic sediment compounds morphologies in our mapping can prove useful when producing subsequent geomorphological interpretations of local palaeoglaciological behaviour (Darvill *et al.*, 2014).

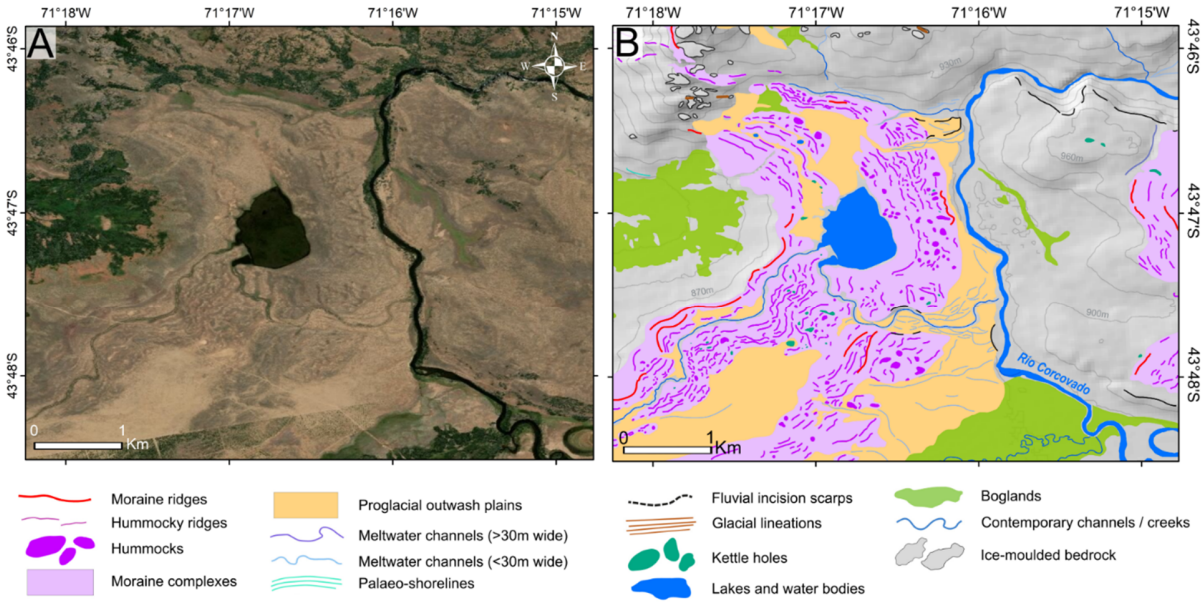

Figure 2.3. (A) Satellite imagery (ESRI™, DigitalGlobe) and (B) glacial geomorphological mapping comparison (contour lines interval: 30m) of two-closely-spaced, well-defined terminal moraine complexes located in the Río Corcovado valley, to the east and southeast of the Arroyo El Fango headwaters. Despite being closely-spaced, the two moraine complexes are separated in most parts by a distinct proglacial outwash plain deposit which suggests that the innermost moraine complex represents a younger re-advance or still-stand of the Río Corcovado outlet glacier. See Fig. 2.2 for location.

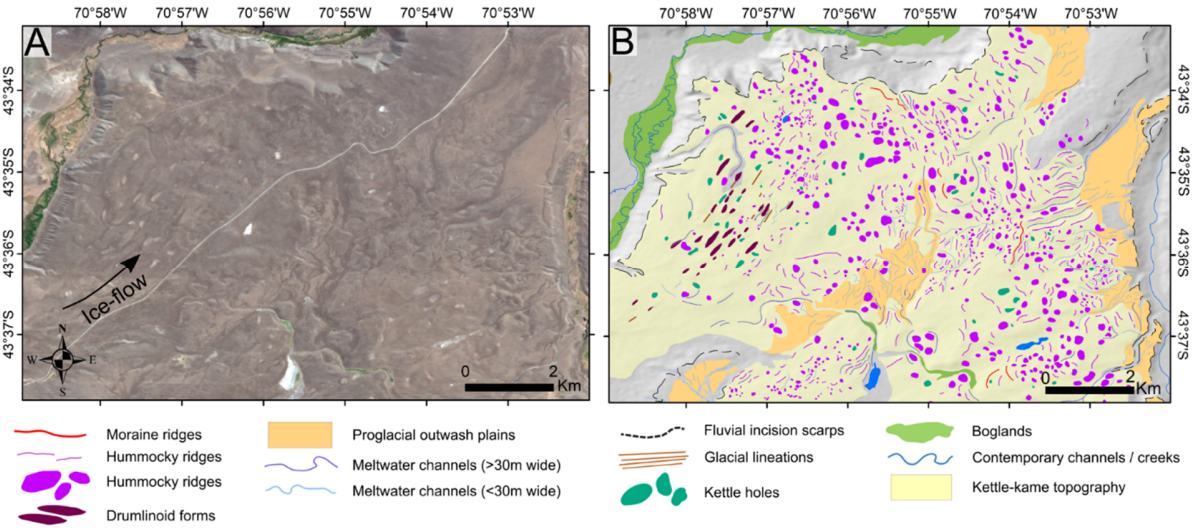

Figure 2.4. (A) Satellite imagery (Sentinel 2A TCI image 02/03 2018) and (B) glacial geomorphological mapping comparison of the Tecka Drift (as termed by Lapido *et al.*, 1990; Haller *et al.*, 2003; and Martínez *et al.*, 2011) located to the east of the Río Huemul valley. This deposit is characterised, unlike moraine complexes, by a chaotic and extensive array of ice-contact glaciogenic mounds such as hummocks and hummocky ridges with low parallelism, interspersed with numerous kettle-holes and large (>30 m wide) former meltwater channels. Such a low-gradient deposit is diagnostic of a stagnant, progressively thinning ice front (dead-ice scenario), and was here mapped as kettle-kame topography. See Fig. 2.2 for location.

2.4.2.2 Moraine ridges

The eastern sector of the mapped area exhibits numerous well-preserved landforms identified as linear- to arcuate-shaped, steep-sided (20-40°) ridges displaying positive relief (5-45 m), a clear break-of-slope, and sharp undulating crests. Such features were interpreted as moraine ridges (Benn & Evans, 2014) delineating former lateral and terminal ice-front margins; the moraine crests were mapped as polylines. Moraine ridges in the field can occur as well-preserved, cross-valley continuous ridges outlining former latero-terminal ice margins over several kilometres (Fig. 2.5). However, they can also occur as fragmented, discontinuous and shorter ridges (a few hundred metres in length), clustered alongside multiple, smaller hummocky features. Well-preserved, prominent and continuous moraine ridges can be discerned from the DEM due to their significant

positive relief and arcuate shape (Fig. 2.2). Such moraine ridges are characteristic of the innermost moraine sequences of the Río Corcovado, Río Huemul and Lago Palena/General Vintter valleys, which are likely associated with the local LGM (Lapido *et al*., 1990; Martínez *et al*., 2011; Fig. 2.5a,c). The older, more distal moraine complexes are morphologically distinct and characterised by wider, more subdued and broad-crested ridges. They also display lower slope gradients, making them more challenging to distinguish and map from imagery. In such older environments, identifying ice limits can be problematic, and often requires the adjacent detection of other proglacial deposits such as kettle holes, meltwater channels and proglacial outwash plains, which on the Argentine forelands tend to remain better preserved than moraine ridges due to lower erosion and mass-wasting potential (Hein *et al*., 2009, 2011; Dunai, 2010). Thus, fewer prominent, continuous moraine ridges could be mapped for the older, most extensive moraine complexes of the study site.

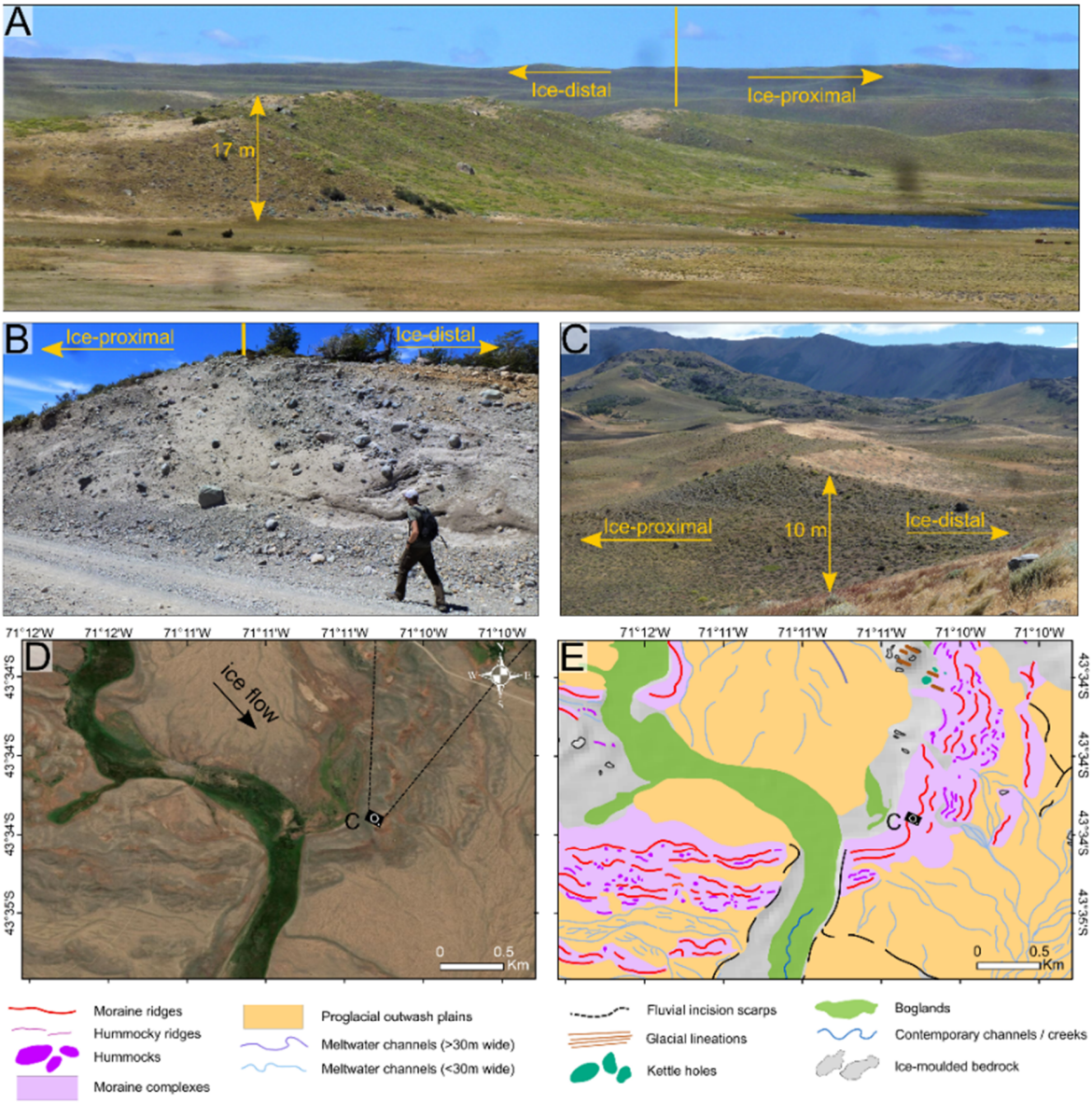

Figure 2.5. (A) View towards the south/southeast of a well-preserved, prominent terminal moraine in the eastern Río Corcovado basin (camera location: 43°43'40.64"S, 71°12'2.48"W). (B) Photograph of a road-cut section through a well-preserved latero-terminal moraine ridge of the Río Corcovado palaeoglacier western margin displaying glacio-tectonic till structures (location: 43°45'37.99"S, 71°24'9.06"W). (C) View towards the northeast as indicated on panel D (camera symbol) of a well-preserved terminal moraine ridge in the Río Huemul valley. (D) Satellite imagery (ESRI^{TM}, DigitalGlobe) and (E) glacial geomorphological mapping comparison of the well-preserved terminal moraine ridges located in the Río Huemul valley forming a well-defined arcuate moraine complex. Panels (D) and (E) also display two extensive proglacial outwash plains to the southeast (time-synchronous with photographed moraine – panel (D)) and the northwest (younger than photographed moraine) and exhibiting braided former meltwater channels. See Fig. 2.2 for location.

2.4.2.3 Hummocks and hummocky ridges

Throughout the three valleys mapped in this study, we find an abundance of rounded to sub-rounded mounds of glaciogenic sediments, often termed hummocks in glacial geomorphology (Benn & Evans, 2014). When hummocks are arranged in short (<300 m wide) ridges of limited relief (<30 m), they are often described as hummocky ridges/moraines (Eyles *et al*., 1999; Darvill *et al.,* 2014). Hummocky ridges were mapped as polylines along identified crestlines while distinct hummocks were mapped as polygons. These features are widespread throughout our study site and occur as; 1) isolated features in kettle-kame topography, where their linearity often originates from supraglacial or ice-contact glaciofluvial deposition (Darvill *et al*., 2014), or 2) ridges observed in latero-terminal moraine complexes, clustered in parallel successions orientated perpendicular to ice flow, sometimes alongside prominent moraine ridges (Fig. 2.5e). In this latter case, hummocky ridges are likely to represent discontinuous recessional moraines, eroded and diminished by meltwater runoff (Clapperton *et al*., 1995; Eyles *et al*., 1999). On the other hand; abundant, highly concentrated, parallel- and perpendicular-to-ice-flow hummocky ridges can indicate a relatively stable ice margin, such as observed within the well-defined younger terminal moraine complexes located in the Río Corcovado valley, to the southeast of the Arroyo El Fango headwaters (Fig. 2.3a,b).

2.4.2.4 Kettle holes

In both moraine complexes and kettle-kame topography of the Río Corcovado, Río Huemul and Lago Palena/General Vintter valleys, numerous examples of circular to semi-circular hollows and dry pits of shallow depth (<20 m) can be observed chaotically dispersed within hummocky terrain. We interpreted these features as kettle holes, which are landforms commonly associated with slowly retreating or stagnant glacier fronts (Price, 1969; Russel *et al.,* 2006; Evans & Orton, 2015). Kettle holes are typically formed through burial of ice blocks by till and glaciofluvial sediments, leading to the formation of enclosed rounded depressions near the ice-margin as the ice block subsequently melts (Benn *et al*., 2007; Knight, 2011). Figure 2.4 depicts a complex of kettle

holes distributed across kettle-kame topography within the southeastern latero-terminal margin of the former Río Huemul glacier (43°40’S; 70°55’W).

Table 2.1. Summary of mapped glacial landform morphologies, identification criteria from remote sensing, mapping uncertainties and previous mapping conducted in the Río Corcovado, Río Huemul and Lago Palena/General Vintter valleys.

Feature/ landform	Morphology	Identification criteria from remote sensing	Mapping uncertainties	Palaeoglaciological significance	Previous mapping
Moraine ridges	Distinct linear to arcuate shaped, steep-sided (20-40°) and continuous (>200 m) ridges displaying positive relief (5-45m), a clear break-of-slope, and sharp undulating crests.	Easily identified on DEM hillshade if prominent enough as light-shadowing highlights positive relief with arcuate, narrow shape. Dark grey in colour on DG imagery. Different in texture to surrounding terrain (Fig. 5d).	May be difficult to identify heavily subdued ridges from imagery for oldest ice marginal deposits. Lower relief moraine ridges can in some cases be confused with palaeo-shorelines.	Indicate former ice-front position. Prominence, crest undulation, continuity and slope gradients combined can be indicators of erosion and relative age of moraine deposit / glacial advance.	Glasser & Jansson (2008); Davies *et al*. (2020) (main features only)
Hummocks	Rounded to sub-rounded mounds of glacigenic sediments arranged chaotically.	Best identified on high-resolution imagery although sometimes possible from DEM. Dark grey or brown in colour on Digital Globe (DG) imagery, although lighter than meltwater channels. Sub-rounded light shadowing demonstrates positive relief (Fig. 4a).	May be challenging to identify limits of feature from remote sensing for relatively old, subdued deposits, or in vegetated areas.	Indicate marginal ice contact.	Unmapped
Hummocky ridges	Mounds of glacigenic sediments arranged in a linear fashion and generating a distinct ridge crest of limited length (<300 m).	Best identified on high-resolution imagery although sometimes possible from DEM. Dark grey or brown in colour on DG imagery, although lighter than meltwater channels. Narrow, linear light shadowing demonstrates positive relief and ridge structure (Fig. 3a)	May be challenging to map accurately for older deposits due to erosion and lack of prominence, thus creating potential for under-discovery. In such cases, differentiation between moraine and hummocky ridges can be less conspicuous. Although no eskers were explicitely identified in the area, some may have been mis-interpreted as hummocky ridges.	Indicate marginal ice contact. Abundant, prominent, and parallel ridges are likely to suggest substantial till deposition and thus a relatively stable, long-lasting glacier margin.	Unmapped
Moraine complexes	Relatively confined, narrow (<3 km) and easily discernible drift belts of arcuate shape comprising prominent and continuous moraines ridges as well as concentrated, parallel hummocky ridges.	Best identified on high-resolution imagery. Dark grey or brown in colour deposit belts composed of hummocks, hummocky and moraine ridges, and different in colour to surrounding terrain e.g. proglacial outwash plains (Fig. 3a).	May be challenging to identify limits of feature for relatively old deposits, or vegetated areas.	Indicate former glacier front positions following glacial advance or still-stand.	Caldenius et al. (1932); Haller et al. (2003); Glasser & Jansson (2008); Davies *et al.* (2020) (main features only)
Kettle holes	Circular to semi-circular / elongate hollows and pits of shallow depth (<20 m).	Best identified from high-resolution imagery. Light grey/white circular to elongate pockmarks, may be water-filled. No percievable light-shadowing as no positive relief (Fig. 4a).	Potential for under-discovery in areas exploited by subsequent and/or modern drainage. Depressions can also be exploited by modern lacustrine bodies and thus be confused with features characteristic of modern hydrology.	Indicates former presence of ice front. High feature concentration can mark presence of progressively thinning and stagnant ice.	Unmapped
Kettle-kame topography	Extensive (>3 km in width) drift deposits composed of chaotic and disorganised hummocks (or kames) irregularly interspersed with hollows and kettle holes.	Best identified from high-resolution imagery. Areas comprising high concentration of chaotically arranged kettle holes, small lakes, hummocks and hummocky ridges. Such glacigenic deposits gives the ensemble a dark grey or brown colour on DG imagery (Fig. 4a).	May in some cases be difficult to identify the boundary with moraine complexes as difference between an organised, arcuate group of glacigenic sediment and a more scattered form of hummocky terrain can be open to doubt.	Indicates former ice-marginal zone, possibly under a stagnant, dead-ice front scenario.	Unmapped
Proglacial outwash plains	Broad, low-gradient surfaces composed of fluvially-rounded sand- and gravel-sized sediment, in some cases prograding from former ice-margins. Can demonstrate former braided meltwater channel networks on their surfaces.	Feature limits identified from imagery, although broad terrace characteristics make it distinguishable from DEM. Little to no positive relief, light brown to orange in colour, and imagery can reveal surface channels. Feature limits often associated with fluvial incision scarps (Fig. 6a,f).	Surface grading can be difficult to distinguish from remote sensing (DEM only) and it can be challenging to identify the limits of outwash features from imagery.	Indicates former pathways of meltwater during glacier advance or still-stand.	Caldenius (1932); Glasser & Jansson (2008); Davies *et al.* (2020) (main features only)
Meltwater channels	Incised sinuous conduits formed by larger discharge regimes than contemporary runoff, commonly occurring as highly concentrated multi-channel systems with in many cases no association with modern drainage.	Dark brown sinuous conduits, discernible from high-resolution imagery on proglacial outwash plains due to darker colour. Large (>30m) isolated channels can display light-shadowing due to negative relief (e.g. Fig. 6a,f).	Potential for under-discovery when former drainage pathways are re-exploited by modern runoff. Braided channel systems can be challenging to distinguish from imagery on older outwash plain deposits.	Indicates former detailed pathways and flow-direction of glacial metlwater. Their abundance and ease of discovery can be a good proxy for age of glaciofluvial deposit.	Unmapped
Fluvial incision scarps	Continuous break-in-slope with relatively steep surface gradients (20-40°), curving basal convexities and sharp concave crests.	Discernible from DEM in cases of significant incision (>20m) due to break in slope, but also from imagery in vegetation-free areas, due to sudden colour and/or texture change between features and light shadowing due to steep incision slope (e.g. Fig. 5e,d)	Can be mis-interpreted and/or difficult to identify from remote sensing when fluvial incision is not sufficient to appear on DEM (<20-30 m). Possible confusion (although unlikely) with landslide/rockslide or tectonic scarps.	Marks location and patterns of fluvial incision into deposits. If located across outwash plains, they mark different regimes of meltwater flux and sediment loading, which can sometimes serve as a proxy for glacial advances / still-stands.	Unmapped
Possible GLOF deposits	Fan-shaped, sub-aerial deposit prograding from the mouth of a tributary valley and demonstrating fluvial sorting, but displaying large (b axis >1m) imbricated boulders and braided surface channels wider than modern runnoff allows. Such features can also be associated with large breaches in terminal moraines damming nested lakes.	Characteristics and sedimentology of unique feature identified as such were discussed on the field. (see paragraph 4.3.4.). Smooth terrace characteristics and post-deposition incision of feature are discernible from DEM. Fan shape and wide surface channels can be distinguished from imagery.	Although mapped seperately, the one deposit mapped as such requires a more specific and detailed geomorphological and sedimentological investigation to produce a more confident interpretation. There is potential for mis-interpretation here.	Indicate former high-magnitude, sudden flood event mobilizing substantial quantities of till material.	Unmapped

Palaeo-shorelines	Very linear, continuous, undulating and smooth outline of sediment, characterised by a mono elevation-interaction with topography. Sometimes easy to discern from imagery when numerous, parallel ridges can be observed following contour lines over tens of kilometres.	Only visible from high-resolution imagery due to lack of positive relief. Appear as gently curving lines spread across slopes at single elevations and alternating in colour between light and dark brown (in vegetation-free areas), particularly discernible when numerous shorelines run parallell to each other (Fig. 7 a).	If one isolated, discontinuous feature is identified, there is potential for confusion with a low-relief moraine ridge or other linear features such as an esker (although not so likely).	Mark former lake surface level. In the case of an ice-dammed lacustrine system, it can also indicate the lowest elevation of a usable drainage spillway.	Unmapped
Raised deltas	Fan-shaped feature of fluvially deposited sands and gravel, deposited near tributary valley mouths, with similar properties to alluvial fans. However a raised delta is nested on modern valley slopes and unused by modern hydrology (often incised post-depositionally). It's prograding slope does not reach the valley floor: but instead an elevation matching observed palaeoshorelines, in some cases.	Can be identified from DEM due to homogeneous and smooth surface prograding towards valley floors and further incised by modern river channel. Fan-shaped and often lighter and different in texture than surrounding terrain. For vegetation-free cases, braided surface palaeochannels typical of alluvial fans can be distinguished.	Although features mapped as such were checked to match elevation of mapped and field-verified palaeo-shorelines, there is possibility of confusion (although unlikely) with ice-dammed proglacial outwash deposits from tributary glacier meltwater. If sedimentology wasn't verified on the field: such alluvial deposits could also be related to former GLOF deposits occuring during proglacial lake residence.	Can further designate former lake level.	Unmapped
Glaciolacustrine deposits	Deposit accumulations are characterised by distinctive white and light grey colouration on imagery. Easily eroded due to unconsolidated fine nature of sediments leading to distinct incision patterns and sharp crests.	Best visible in flat basins from imagery due to lack of positive relief. However DEM can reveal deeply incised exposures forming steep gorges through dark/light shadowing. Light grey to white in colour on DG imagery, their texture is distinct from surrounding terrain. (Fig. 7g).	True extent of the sediment accumculations is easily underestimated from imagery. Field investigation is required to reduce such uncertainty.	Demonstrates existence and extent of former proglacial lake system.	Unmapped
Glacial lineations	Highly linear, parallel and relatively narrow landforms with length-to-width ratios of approximately 10:1 and aligned to former interpreted ice flow.	Visible either on DEM and hillshade for prominent features (>20 m) as positive relief generates dark/light shadowing, or on high-resolution imagery. Such linear, narrow and elongated landforms often occur in groups of parallel features (Fig. 8a,b).	Potential bias in former ice-flow interpretation can lead to mis-interpretations of a particular bedrock outcrop orientation as subglacially streamlined when outcrop orientation is instead related to tectonics, geological structural properties, slope failures or other geomorphic processes.	Marks former areas of relatively thick, fast-flowing and warm-based ice and indicates directionality of former ice-flow. Streamlining can be depositional (in the case of sediment flutes for instance) or erosional (in the case of streamlined bedrock.	Glasser & Jansson (2008); Davies *et al*. (2020) (main features only)
Drumlinoid forms	Depositional linear hills characterised by oval to ellipsoidal shapes, significant positive relief (>10 m), and which are aligned to former interpreted ice flow.	Visible either on DEM (if prominent enough) or imagery. Features appear dark grey to brown in colour and display dark/light shadowing due to significant positive relief. They are non-undulating (linear) and oval/ellipsoidal in shape (Fig. 8).	May be challenging to identify limits of feature for relatively old deposits (pre-LGM) and can be confused with sediment flutes (lineations). Identification bias due to former ice-flow knowledge is possible.	Marks former areas of relatively thick, fast flowing ice on low-gradient glacigenic sediment surfaces.	Unmapped
Ice-moulded bedrock	Prominent bedrock outcrops ranging from 20 m to 1 km in width, displaying significant positief relief (>30m) and located in areas of warm-based ice-flow (with high concentrations of lineations).	Large outcrops visible from DEM due to significant positive relief. Steep side-walls generate light shadowing on imagery. The light-to-dark grey and sometimes brown colour of exposed surfaces is often different than adjacent terrain, especially in more vegetated areas. Exposed surfaces display an irregular, rough texture (Fig. 8d).	Possible confusion of small features with human infrastructure, although very unlikely given remoteness of field site.	Marks former areas of relatively thick, fast-flowing and warm-based ice causing efficient subglacial erosion. Large scale striations and plucking patterns can indicate former ice-flow directionality.	Unmapped
Contemporary channels / creeks	Any river channel used by modern runoff and detectable from remote sensing.	Large channels causing substantial incision can be discerned from DEM, however in vegetation-free areas high-resolution imagery enables clear identification of active or seasonally active channels and creeks.	Small creeks (<10m width) sometimes surrounded or covered by vegetated terrain can be challenging to accurately locate from imagery. Mapping in such cases relies on computed watershed analysis using DEM data.	In recently (Quaternary) glaciated landscapes, the geometry of modern channels can demonstrate anomalies such as diversions from quickest downvalley path highlighting damming effect of glacial deposits on topography, thus aiding identification of ice margins.	Haller *et al.* (2003); Glasser & Jansson (2008 - Río Corcovado only)
Atlantic-Pacific drainage divide	Line separating Atlantic versus Pacific- directed drainage of surface runoff. This line was generated by extrapolating drainage catchments from the AW3D30 DEM using a standard watershed analysis in ArcGIS.	Computed using DEM (AW3D30).	Geolocation uncertainties associated with DEM accuracy. Tarolli & Mudd (2019) report 90% linear errors to vary between 5 and 10 metres with a positive correlation to slope gradients for this dataset.	Current position of drainage divide indicates the effect and magnitude of subglacial erosion and valley over-deepening during cycles of Quaternary glaciations. It can also inform on the potential location of Atlantic-ward spillways of former ice-dammed lake systems following ice retreat into overdeepened basins.	Unmapped
Boglands	Accumulation of surface water and thus vegetation in areas of low surface gradients.	Appear as light to dark green areas composed of numerous small creeks / channels and/or small lakes, they are characterised by little to no positive relief (e.g. Fig. 3).	When relying on imagery, natural bogland formation can be sometimes confused with anthropogenic irrigation of fields and agricultural practice.	Extensive bogland surfaces in arid steppe landscape can sometimes indicate former lacustrine and/or fluvial sediment deposition: as vegetation favours fine sediments. Can also indicate patterns of former meltwater pathways exploited by modern hydrology.	Unmapped
Rotational slump and landslides	Bowl-shaped area of a slope demonstrating a depression with steep upper break in slope (crown scarp), highlighting the exposed part of the failure surface, and numerous parallel (transverse) scarps or fissures accumulated below.	Large features can be distinguished from DEM due to steep upper break in slope displaying dark/light shadowing. Transverse failure fissures and ridges located below the crown scarp are best identified on high-resolution imagery.	Possible confusion with large rock-slope failures in heavily vegetated zones. Transverse ridges or fissures enabling identification of slump can be confused with moraine or hummocky ridges, thus requiring field verification.	Demonstrates slope instability and large-scale mass wasting event; common in former paraglacial environments due to combination of glacial debuttressing and atmospheric exposure of unconsolidated, unsorted and non-vegetated sediments.	Unmapped
Empty cirques	Bowl-shaped depression near mountain ridge tops with a concave floor open on its downhill side, and a steeper: cupped headwall on its uphill side	Can be distinguished from DEM due to steep headwall on many portions of bowl-shaped valley generating significant dark/light shading as well as sharp mountain ridges on cirque's boundaries.	Glacial cirques can, in some cases, be mistaken for bowl-shaped structural bedrock formations, thus not formed by glacier build-up and subglacial erosion.	Records local cirque glaciation during phases of ice-sheet advance/retreat.	Glasser and Jansson (2008) (features were re-mapped at higher spatial resolution)

2.4.3 Glaciofluvial landforms

2.4.3.1 Proglacial outwash plains

Glaciofluvial outwash plains are characterised by broad, low-gradient surfaces composed of fluvially-rounded sands and gravels (Denton *et al.,* 1999; Hein et al., 2009; Evans & Orton, 2015; Darvill *et al.,* 2015; Alloway *et al.,* 2018). They often occur adjacent and down-valley to latero-frontal moraine systems and are sometimes associated with the presence of palaeo-meltwater channels (Coronato *et al*., 2013; Darvill *et al*., 2014). In the Río Corcovado, Río Huemul and Lago Palena/General Vintter valleys, numerous well-preserved outwash plains prograde on the ice-distal sides of moraine complexes and kettle-kame belts, with average slopes of ~0.5-1° (Fig. 2.6). The younger outwash plains are often characterised by well-preserved former meltwater channels with clear braiding patterns (Fig. 2.6c,g), while these features are less common for older deposits. At the older margins, the flat nature of outwash plains combined with the arid, windy conditions of the Argentine foreland often enables better preservation levels than their associated moraines (Bentley *et al.*, 2005; Hein *et al*., 2009; 2011; 2017; Darvill *et al.*, 2015). Such long-term preservation properties make identifying outwash surfaces a vital component of mapping older ice-marginal environments.

2.4.3.2 Meltwater channels

Abandoned sinuous channels associated with former ice margins, and formed by larger discharge regimes than contemporary runoff would enable, are common across the glaciofluvial and glaciogenic depositional environments of the Río Corcovado, Río Huemul and Lago Palena/General Vintter valleys (Fig. 2.6a,c,f,g). They were interpreted as former glacial meltwater channels, and commonly occur as concentrated multi-channel systems, braided and etched into the surface of glaciofluvial outwash plains, with up to 5-10 m relief. Individual traceable channels vary in length between 100 m and 5 km and between 5 m and 250 m in width. In low-gradient, lateral ice-marginal environments, wider palaeo channels (>30 m) can be found isolated within moraine complexes and oriented parallel to lateral moraine ridges and former ice flow. Such channels are abundant within the Río Huemul glacier's latero-terminal kettle-kame topography (Lapido *et al*., 1990; Haller *et al*., 2003; Martínez *et al*., 2011) (Fig. 2.5). In many instances across

the field site, such large meltwater channels now act as natural pathways for contemporary, lower discharge drainage systems.

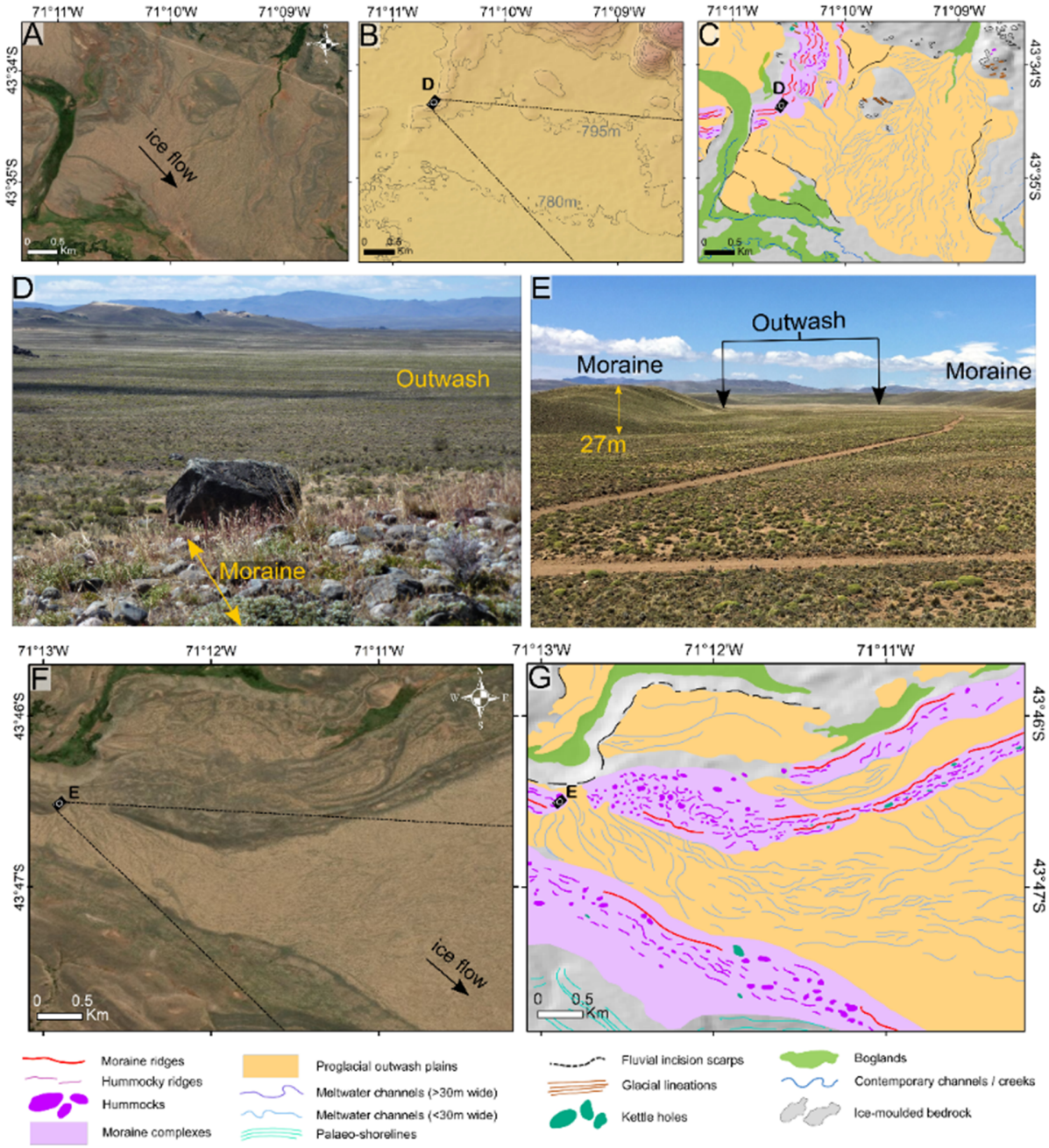

Figure 2.6. (A) Satellite imagery (ESRI™, DigitalGlobe), (B) DEM with topographic contour lines (15 m interval) and (C) glacial geomorphological mapping comparisons of an extensive, proglacial outwash plain of the Río Huemul valley, which exhibits remarkable preservation of now inactive braided meltwater channels. (D) View towards the Southeast (as shown on panel B) of the proglacial outwash plain formed when the Río Huemul glacier deposited the moraine ridge from which the photograph is taken (location: 43°34'21.00"S, 71°10'32.82"W). (E) View towards the Southeast (as shown on panel F) of a well-preserved proglacial outwash plain confined between two prominent terminal moraine complexes of the Río Corcovado valley (location: 43°46'30.94"S, 71°12'52.03"W). (F) Satellite imagery (ESRI™, DigitalGlobe) and (G) glacial geomorphological mapping comparisons of the proglacial outwash plain photographed (panel E), which demonstrate clear patterns of former braided meltwater channel systems. See Fig. 2.2 for location.

2.4.3.3 Fluvial incision scarps

Incision scarps are characterised by relatively steep surface gradients (20-40°), curving basal concavities and sharp convex crests and are locally formed by former or active river incision into till or glaciofluvial terrace deposits. These landforms were mapped as polylines highlighting their upper breaks in slope. The location, concentration and preservation of incision scarps can prove useful when assessing changes in glacial and postglacial fluvial discharge and sediment-load regimes. Identifying such features and their distribution can help to understand the incision and erosion patterns of former glaciogenic deposits and thus help to elucidate the lack of preserved glacial sediment-landform assemblages at a given location (Hein *et al.*, 2017). Mapping such features can also facilitate the interpretation of former shifts in proglacial meltwater drainage pathways associated with different glacier front positions (Bentley *et al.*, 2005). Furthermore, mapped scarps constitute useful data for fluvial geomorphologists wishing to investigate former terrace aggradations as indicators of former runoff regimes, sediment loads and local postglacial isostatic response (Olszak, 2011; Moreiras *et al.*, 2017).

2.4.3.4 Glacial lake outburst flood deposits

At 43°33'S; 71°29'W, 2 km to the southwest of Corcovado, a unique deposit covering an area of ~2 km^2 was investigated. The landform is a fan-shaped, subaerial deposit prograding from the mouth of a tributary valley to the valley floor of the Río Corcovado valley. Its valley-floor elevation suggests it was deposited after the drainage of the proglacial lake occupying the valley. It is associated with a 500 m-wide breach through lineated subglacial deposits of the Río Corcovado glacier and has been incised into by the narrow (<10 m width) modern tributary river. A road-cut section of the 5 m thick deposit exhibits some evidence of fluvial sediment sorting. However, the deposit comprises a high concentration of large (b axis >1 m) rounded to sub-rounded imbricated boulders of varied lithologies, and exhibits wide (up to 25 m) braided surface channels discernible from imagery. Such characteristics are diagnostic of a sudden, high-magnitude mass-wasting event causing mobilization of substantial till volumes (Blair, 2002; Russel *et al.*, 2006). The landform was thus interpreted and mapped as a potential glacial lake

outburst flood deposit. One possible source of floodwaters could have been waters dammed by ice or glacial deposits at the tributary head, now an empty cirque occupied by a 1200 m^2 lake (43°36'2"S; 71°33'2"W). Although this deposit requires further geomorphological and sedimentological investigation to produce a confident interpretation, we believe it is pertinent here to distinguish it from other alluvial deposits.

2.4.4 Glaciolacustrine landforms

2.4.4.1 Glaciolacustrine deposits

Numerous examples of extensive laminated glaciolacustrine sediment outcrops were found in the Río Corcovado and Río Huemul valleys along road and river cuttings, particularly in areas located on the ice-proximal side of the innermost moraine complexes, at elevations below 790 m (Fig. 2.7). The glaciolacustrine sediments are characterised by fine, occasionally laminated deposits of clay and silts (cf. Rabassa *et al*., 2000; Evans, 2014; Henriquez *et al.,* 2017; Thorndycraft *et al.,* 2019) (Fig. 2.7e). On imagery, large sediment accumulations can appear as white and grey-coloured assemblages of heavily incised, fragmentary landforms (Fig. 2.7g). Indeed, soft and unconsolidated glaciolacustrine deposits are more susceptible to post-depositional erosion than coarser till deposits and other proglacial sediment assemblages (*e.g.* glaciofluvial sands and gravels), especially in the semi-arid Argentine foreland (Bendle *et al*., 2017b; Thorndycraft *et al*., 2019). Such deposits indicate the former presence of substantial proglacial lake bodies following glacier recession. To decrease the potential for misinterpretation, we exclusively mapped glaciolacustrine deposits within flat basins enclosed by conspicuous palaeo-shorelines (Fig. 2.7c,h).

2.4.4.2 Palaeo-shorelines

Platforms demonstrating a gently curving and convex frontal break of slope nested at single elevations and stretching over extensive distances (sometimes tens of kilometres) were interpreted as former notched proglacial lake shorelines (Sissons, 1978; Glasser & Jansson, 2008; Hein *et al*., 2010) (Fig. 2.7d,f). Such erosional features can be discriminated from continuous moraine ridges

through a lack of positive relief, a lower degree of sinuosity, and their occurrence at continuous elevations over great distances. Moreover, lake level fluctuations often lead to several palaeo-shorelines running parallel to each other and to topographic contour lines, which were used additionally to aid feature identification (Fig. 2.7a,c). Well-preserved examples of palaeo-shorelines can be observed on the windier eastern slopes of the Río Corcovado valley, at elevations of 680 m and 790 m (Fig. 2.7f), as well as towards the terminal environment of the former Río Corcovado glacier, nested between 910 m and 990 m in elevation (Fig. 2.7a,c).

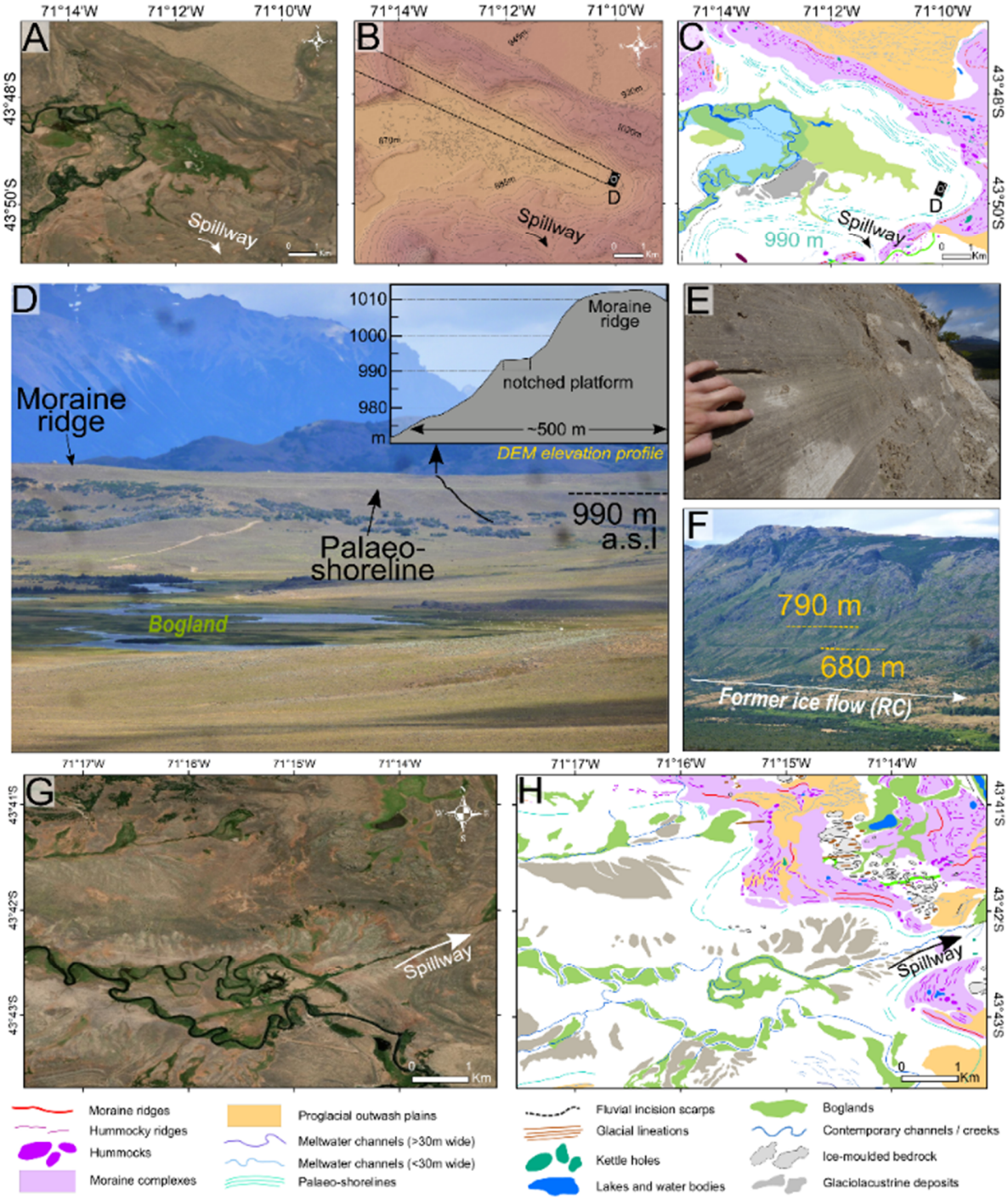
A
B
C
D
E
F
G
H
71°14'W
71°12'W
71°10'W
43°48'S
43°50'S
Spillway
990 m
Moraine ridge
notched platform
~500 m
DEM elevation profile
1010
1000
990
980
m
990 m a.s.l
Palaeo-shoreline
Bogland
790 m
680 m
Former ice flow (RC)
71°17'W
71°16'W
71°15'W
71°14'W
43°41'S
43°42'S
43°43'S
0
1
Km
Moraine ridges
Hummocky ridges
Hummocks
Moraine complexes
Proglacial outwash plains
Meltwater channels (>30m wide)
Meltwater channels (<30m wide)
Palaeo-shorelines
Fluvial incision scarps
Glacial lineations
Kettle holes
Lakes and water bodies
Boglands
Contemporary channels / creeks
Ice-moulded bedrock
Glaciolacustrine deposits

Figure 2.7. (**A**) Satellite imagery (ESRI^{TM}, DigitalGlobe), (**B**) DEM with topographic contour lines (15 m interval) and (**C**) glacial geomorphological mapping comparisons of a former glaciolacustrine basin in the Río Corcovado valley encircled by well-preserved, highly continuous and parallel palaeo-shorelines (nested between 910 and 990 m) running over tens of kilometres at singular elevations. The former lake basin floor displays a low gradient surface now host to the Río Corcovado as well as an extensive bogland. (**D**) View towards the northwest (as shown on panel B) of a palaeo-shoreline nested on the ice-distal slope of a terminal moraine ridge in the Río Corcovado valley. This shoreline is associated with the former proglacial lake, which resided in the basin mapped on panel C (camera location: 43°49'43.46"S, 71° 9'54.92"W). An elevation profile graph extrapolated from DEM highlights the geomorphology of the palaeo-shoreline and adjacent moraine ridge. (**E**) Road cut section through well-preserved laminated varve sediments (location: 43°42'08,0"S, 71°24'41,6"W). (**F**) View towards the northeast of two continuous palaeo-shorelines cut into the eastern slopes of the Río Corcovado valley (camera location: 43°40'00,5"S, 71°26'26,0"W). (**G**) Satellite imagery (ESRI^{TM}, DigitalGlobe) and (**H**) glacial geomorphological mapping comparison of another, lower-elevation drained glaciolacustrine basin located in the Río Corcovado valley. This basin displays a high concentration of glaciolacustrine sediment accumulations on its low-gradient basal surface. The hillshade was replaced with a white background on maps C and H to improve visualisation. See Fig. 2.2 for location.

2.4.4.3 Raised deltas

The mapped region features several fan-shaped, smooth terrace surfaces gently sloping towards valley floors, yet nested distinctively above the valley floors. These deposits are composed of well-sorted, rounded sands and gravels indicating fluvial deposition near the mouths of tributary valleys. After matching the elevations of such features with abandoned palaeo-shorelines, we interpreted these terraces as raised lacustrine deltas formed by tributary rivers flowing into former proglacial lake systems (Glasser *et al.*, 2016; Bendle *et al.*, 2017a; 2017b). Raised deltas can serve as additional geomorphological evidence of former glaciolacustrine systems and help to identify their former surface elevations. For instance, a well-preserved raised delta can be discerned on the western flank of the Río Corcovado trough, perched on the southern edge of the Río Poncho Moro valley mouth (43°40'5"S; 71°25'4"W). This landform sits at a similar elevation than the prominent 680 m palaeo-shoreline discerned within the valley. Large raised deltas like this specific example can be strong indicators of relatively stable proglacial lake systems (Turner *et al.*, 2005; Hein *et al.*, 2010; Bendle *et al.*, 2017a).

2.4.5 Subglacial landforms

2.4.5.1 Glacial lineations, flutings, drumlinoid forms and ice-moulded bedrock

We identified linear, parallel and relatively narrow landforms displaying positive relief with length-to-width ratios of ~10:1 (Fig. 2.8). Such features are common in areas of assumed greater former ice-thicknesses, where warm-based, fast-flowing ice could generate either substantial subglacial bedrock erosion, or deposition and/or re-arrangement of glaciogenic sediment along flow lines (Smith *et al.*, 2008; Darvill *et al.,* 2014; 2017; Bingham *et al*., 2017; Clark *et al.,* 2018). The latter case can lead to the formation of sediment flutes (<10 m in height, Fig. 2.8a-c). Depositional lineations characterised by oval to ellipsoidal shapes and significant positive relief (>10 m) were interpreted and mapped as drumlinoid forms (Knight, 1997; Spagnolo *et al*., 2012). In the mapped regions, prominent bedrock outcrops ranging from 20 m to 1 km in width often demonstrate large-scale streamlining (Davies *et al*., 2020; Fig. 2.8d,e). Individual outcrops displaying such properties were interpreted and mapped as ice-moulded bedrock. The regional distribution and orientation of subglacial lineations including sediment flutes, drumlinoid features

and ice-moulded bedrock outcrops are useful indicators of former ice-flow direction (Boulton & Clark, 1990: Bentley *et al*., 2005). For instance, at our field site, they enable asserting the former convergence of the Río Corcovado and Río Huemul outlets (Fig. 2.8a-c).

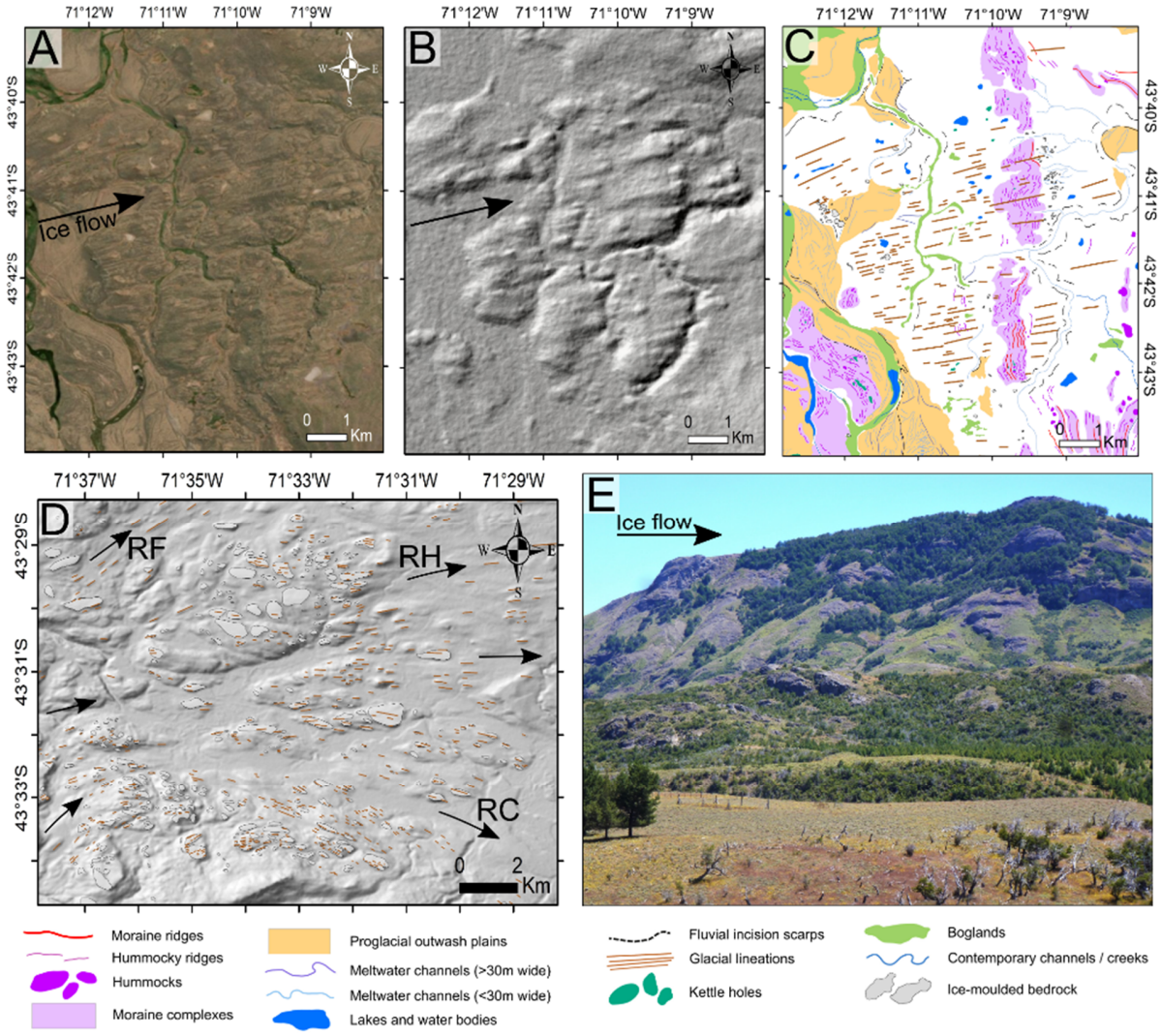

Figure 2.8. (**A**) Satellite imagery (ESRI™, DigitalGlobe), (**B**) DEM hillshade (light azimuth: 315°, incline: 45°) and (**C**) glacial geomorphological mapping comparisons of the heavily streamlined sediments draped between the eastern Río Corcovado terminal moraine complexes and the Río Huemul valley. These features indicate convergence of the Río Corcovado and Río Huemul outlet glaciers at this location during extensive glaciations. (**D**) DEM hillshade with glacial lineations and ice-moulded bedrock landforms mapped (with other mapped features removed for visualisation purposes). This bedrock-dominated area presents substantial evidence of subglacial erosion and thus warm-based, fast-flowing ice, and was characterised by the divergence of the PIS into three outlet glaciers: the Río Corcovado glacier to the southeast, the Río Huemul to the east, and the Río Frío (RF) glacier to the northeast. (**E**) View towards the northwest of ice-moulded bedrock outcrops in the Río Huemul valley (camera location: 43°29'14.16"S, 71°18'23.51"W). See Fig. 2.2 for location.

2.5 Summary and conclusions

Our map illustrates the sediment-landform assemblages formed by the Quaternary fluctuations of three outlet glaciers in the northeastern sector of the former Patagonian Ice Sheet, the Río Corcovado, Río Huemul and Lago Palena/General Vintter outlet glaciers. This map builds on previous local geological (Haller *et al*., 2003) and broad-scale glacial geomorphological mapping (Caldenius, 1932; Glasser & Jansson, 2008; Davies *et al*., 2020) to deliver the first detailed glacial geomorphological map of these valley systems. The mapped landforms incorporate well-established glacial geomorphological features of four major depositional and erosional domains: 1) ice-contact glaciogenic landforms (moraine ridges, hummocks, hummocky ridges, kettle holes, moraine complexes and kettle-kame topography) highlighting the former expansion of outlet glaciers into the Argentine foreland; 2) glaciofluvial landforms (proglacial outwash plains, meltwater channels, fluvial incision scarps, potential glacial lake outburst flood deposits) providing detailed geolocation of former meltwater drainage pathways; 3) glaciolacustrine landforms (palaeo-shorelines, raised deltas and glaciolacustrine deposits) indicating the past formation of ice-dammed proglacial lakes following glacier retreat; and 4) subglacial landforms (ice moulded bedrock, glacial lineations and drumlinoid forms) diagnostic of ice-flow direction and glacier basal conditions.

This map will underpin geomorphological and geochronological investigations aimed at reconstructing the former behaviour of the Río Corcovado, Río Huemul and Lago Palena/General Vintter outlet glaciers during Quaternary glacial cycles. It will also represent an essential geographical dataset for investigations aiming to reconstruct former glaciolacustrine systems as well as major shifts in fluvial drainage pathways during and following local glaciations. Finally, this map provides local empirical boundaries that could be used for high-resolution glacial or ice sheet-scale numerical modelling investigations.

2.6 Additional methods (not included in publication)

The identification of the multiple sediment-landform associations linked to past glaciogenic, glaciofluvial or glaciolacustrine activity in the Río Corcovado, Río Huemul and Lago Palena/General Vintter valleys was conducted primarily from remotely-sensed data. Field surveys were then conducted to either verify or correct initial landform interpretations and to provide an additional understanding of former glacier-landscape interactions at the study site. In this section, additional descriptions of the methods used and of the decisions made during this mapping exercise are detailed. The following paragraphs thus act as complementary information to the brief Methods section (*section 2.3*) presented in chapter 2 and the short-format Journal of Maps paper.

2.6.1 Digital mapping

Glacial geomorphological mapping was first conducted digitally from remotely-sensed data, such as Digital Elevation Models (DEM), DEM hillshades, and satellite imagery. Details concerning the remote-sensing products used are provided in section *2.3*. As described in section *2.2*, previous mapping (*e.g.* Caldenius, 1932; Haller *et al.*, 2003) of the most prominent landforms, such as moraine complexes, associated with the terminus positions of former outlet glaciers at the study site have been conducted prior to this investigation. While these maps were originally consulted to help choose a study site for this investigation, geomorphological mapping was conducted in significantly more detail and at finer spatial scale than any previous work. Geomorphological mapping was thus initialized from a "blank" visualisation of the topography and imagery products, without the addition of layers or shapefiles from previous mapping. This strategy was chosen in order to avoid introducing bias from other individuals' own landform interpretations. Mapping was not conducted at a fixed spatial scale, but instead by zooming in or out depending on the feature mapped and depending on the spatially variable landform details available and quality of the ~1.0 m spatial resolution DigitalGlobe imagery, which at the study site is a mosaic of the GeoEye and IKONOS 2000-2011 satellite imagery products. The mapping methodology was originally set out to be conducted one landform type at a time, starting by the landform types associated with the highest interpretation confidence levels. However, it is important to state that subjective choices made when interpreting the genesis of a specific landform

are sometimes influenced by the previous identification of another proximal landform type. For instance, the occurrence of a well-preserved, low-gradient proglacial outwash plain located outboard and adjacent to a different, arcuate feature displaying positive relief, can substantially increase the confidence in mapping the latter feature as a moraine complex. Therefore, as more information was progressively revealed by the exercise itself, mapping would in some cases alternate between landform types, and any previous mapping produced by this investigation was made visually accessible at all times throughout the mapping exercise. Furthermore, in challenging cases where confidence in landform identification is lower, the decision to interpret and map a certain feature as such was only taken if additional knowledge from the mapping of other landforms was consistent. This was the case for glaciolacustrine deposits for instance (*section 2.4.4.1*), which were mapped only when located in valley floors and basins enclosed by high-confidence palaeo-shorelines. Further geomorphological mapping criteria and uncertainties related to each of the twenty-five landform types identified are provided in Table 2.1.

2.6.2 Field surveys

Two distinct, eight weeks-long field surveys were carried out in January/February of 2019 and 2020. These surveys were essential in either confirming or rejecting initial landform interpretations from remote sensing. Although a good proportion of the vast 5300 km^2 study site was covered during fieldwork, it is important to stress that the ground trothing exercise was exclusively conducted at key locations along axes of communication, where access was made feasible. This is due to the study site being primarily characterised by mountainous terrain (western side of study site) featuring dense vegetation cover and little hiking infrastructure, or by private land (eastern side of study site). In the latter case, obtaining authorized access did not necessarily enable good spatial coverage of the vast private lands, as they did not necessarily feature enough roads and trails. Therefore, implementing the recommended method of systematic traverses of the study area (Chandler *et al*., 2018) was impractical in this case. On two occasions, additional analyses of valley-constrained landforms were conducted from high vantage points around the Río Corcovado valley. While we did not employ such technology, using an uncrewed aerial vehicle to produce a higher resolution DEM and obtain high quality imagery over large sectors of the study area would have certainly been beneficial and well adapted to solving some of the above issues.

However, the usage of such tools over private land undoubtedly poses ethical issues and requires additional and specific authorizations from landowners. Field-based interpretation of glacial landforms was here dominated by the analysis of surface geomorphology. However, in order to provide additional strands of field evidence, the assessment of a landform's sedimentological characteristics was conducted when sections were found and accessible. This exercise involved the identification of well-established lithofacies based on assessments of several sedimentological characteristics including mineralogy, grainsizes and section-wide grainsize heterogeneity, clast-roundness, sediment sorting, clast-to-matrix ratios, the occurrence of clast imbrication etc. Because our research objective is focused on reconstructing the glacial sediment-landform assemblages across a large study area, and does not aim to produce detailed process-form models (*e.g.* Evans & Orton, 2015), such sedimentological analyses are not reported in detail in this chapter/paper. However, they proved essential in testing our hypotheses of landform interpretation. Finally, instead of systematically choosing a landform interpretation that would fit a larger-scale scenario of glacial processes, we attempted to propose several working hypotheses prior to progressively eliminating the ones deemed less likely as more evidence was collected. The resulting glacial geomorphological map produced following these methods and the ones described in section *2.3.* represents the foundation for the glacial geochronological and modelling components of this Ph.D. investigation, which are here presented in the following chapters/publications.

Chapter 3

Geomorphology and ^{10}Be chronology of the Last Glacial Maximum and deglaciation in northeastern Patagonia, 43°S - 71°W



Publication details

Authors

Tancrède P. M. Leger[1], Andrew S. Hein[1], Robert G. Bingham[1], Ángel Rodés[2], Derek Fabel[2], Rachel K. Smedley[3]

[1] *School of GeoSciences, University of Edinburgh, Drummond Street, Edinburgh, EH8 9XP, Scotland, UK*
[2] *Scottish Universities Environmental Research Centre, Scottish Enterprise Technology Park, East Kilbride, G75 OQF, Glasgow, Scotland, UK*
[3] *University of Liverpool, Department of Geography and Planning, Chatham Street, Liverpool, L69 7ZT, UK*

Author contributions

Tancrède P. M. Leger: Conceptualization, Data curation, Formal analysis, Funding acquisition, Investigation, Methodology, Project administration, Software, Visualization, Writing (original draft and review & editing).

Andrew S. Hein: Conceptualization, Data curation, Funding acquisition, Methodology, Project administration, Supervision, Validation, Writing (original draft and review & editing).

Robert M. Bingham: Data curation, Supervision, Writing (original draft and review & editing).

Ángel Rodés: Data curation, Methodology, Writing (original draft).

Derek Fabel: Data curation, Writing (original draft)

Rachel K. Smedley: Data curation, Writing (original draft)

Lead Author contact details

Tancrède P.M. Leger, PhD student, University of Edinburgh, School of GeoSciences,
Address: Institute of Geography, Drummond Street, Edinburgh EH8 9XP, United Kingdom
Email: Tancrede.leger@ed.ac.uk

Publication

Journal: Quaternary Science Reviews
2021, Vol. 272, Issue 107194
Doi: https://doi.org/10.1016/j.quascirev.2021.107194
Received: 21 June 2021
Revised: 30 August 2021
Accepted: 14 September 2021

3.1 Introduction

Patagonia, the southernmost region of South America, is ideally located to further our understanding of Quaternary cryospheric and climatic change in the southern mid-latitudes (Mercer, 1976). The formerly heavily-glaciated Patagonian Andes are part of the only continental landmass that fully intersects the circum-hemispheric Southern Westerly Winds (SWW) and its coupled Antarctic Circumpolar Current (ACC) (Clapperton, 1993; Fig. 3.1). The mountains span a large latitudinal range and thereby provide the unique opportunity to better understand former migration patterns of key atmospheric- and oceanic-energy re-distributing mechanisms during palaeoclimate transitional phases (Davies *et al*., 2020).

The once ~2000 km-long (N-S) Patagonian Ice Sheet (PIS) largely terminated off-shore on its western margin, but was land-terminating north of ~43° S (Glasser *et al*., 2008; Fig. 3.1), enabling geomorphological records to be preserved and accessible (Fig. 3.1b). Detailed geochronological reconstructions utilising radiocarbon dating have been produced for this land-terminating northwestern sector of the former ice sheet (*e.g.* Denton *et al*., 1999; Moreno *et al*., 2015). Over the past decades, several investigations have moreover produced palaeo-glacier chronologies focusing on the central eastern and southeastern regions of Patagonia (Davies *et al*., 2020), using mainly terrestrial cosmogenic nuclide (TCN) exposure dating of glacial deposits. However, to date, the ~800 km-extensive (N-S) northeastern sector of the former ice sheet remains less studied (García *et al*., 2019), although it offers a unique opportunity to compare palaeo-glacier behaviour on both sides of the former ice sheet. This region is currently diagnosed by a lack of knowledge on the characteristics of local PIS development during the last glacial cycle, such as the timing, number and extent of outlet glacier expansion events and their associated meltwater drainage patterns. In this sector, thereby, the precise timing of the local Last Glacial Maximum (LGM) and the last glacial termination are not well constrained.

Numerous investigations from central eastern, southeastern and northwestern Patagonia have reported pre-global LGM maximum outlet glacier expansions occurring for instance during Marine Isotope Stage (MIS) 3 (*e.g.* Darvill *et al*., 2015), MIS 4 (*e.g.* Peltier *et al*., 2021) and even MIS 5 (Mendelová *et al*., 2020), but with variable relative magnitude compared to their global LGM (MIS 2) extent. Hence, a latitudinal asynchrony in the magnitude of pre-global LGM advances, with more extensive ice in southeastern Patagonia, has been proposed. Such asynchrony is also thought to characterise the timing of the onset of local deglaciation (García *et al*., 2019). Therefore, as well as addressing a geographical knowledge gap, establishing robust glacial chronologies from the understudied northeastern region of the former PIS is required to resolve uncertainties concerning

latitudinal asynchronies in the precise timing of the local LGM and onset of deglaciation across Patagonia (Darvill *et al*., 2016). Such information can help to determine the drivers of Quaternary glaciations in the southern mid-latitudes (Kaplan *et al*., 2008; Kelley *et al*., 2014; Darvill *et al*., 2016). Additionally, detailed reconstructions of glaciolacustrine histories during local deglaciation have implications for understanding PIS retreat rates (Bendle *et al*., 2017a) and events of continental-scale drainage reversal, which can abruptly introduce significant freshwater volumes to coastal environments and force local changes in marine ecosystems and circulation (Glasser *et al*., 2016; Thorndycraft *et al*., 2019).

The primary objective of this investigation is to produce a robust chronology of local LGM and deglacial events in a valley system of northeastern Patagonia formerly host to a major PIS outlet glacier; the Río Corcovado (RC) valley system, 43°S, Argentina (Fig. 3.1). To establish such geochronological reconstruction, we here focus on the remarkably well-preserved record of terminal moraine complexes and associated glaciogenic deposits left by this land-terminating eastern outlet glacier of the PIS, which spans several Quaternary glacial cycles (Caldenius, 1932). While local semi-arid conditions make radiocarbon dating challenging, these moraine records are highly suitable for TCN dating, a method successfully employed in several Patagonian valleys to produce LGM glacial chronologies hitherto (*e.g.*, Kaplan *et al*., 2004; 2007; 2008; Douglass *et al*., 2006; Hein *et al*., 2010; Murray *et al*., 2012; García *et al*., 2018; Mendelová *et al*., 2020). Here, by combining interpretations of detailed glacial geomorphological mapping (Leger *et al*., 2020) and a novel ^{10}Be TCN chronology further constrained with Bayesian age modelling, we provide the first reconstruction of the extent and timing of PIS outlet glacier advances in the RC and neighbouring valleys during the LGM (Fig. 3.1). In so doing, we also provide insights into the location, elevation and timing of former proglacial lake formation and drainage events associated with retreat patterns of the studied outlet glaciers following the last glacial termination. In addition, our geomorphological and geochronological reconstruction provides an empirical benchmarking framework for tracking the former regional ice-flow direction, palaeolake dynamics, subglacial thermal conditions, and the timing of ice-free environments, all of which are important for improved calibration of numerical ice-sheet models (*e.g.*, Hulton *et al*., 2002; Hubbard *et al*., 2005).

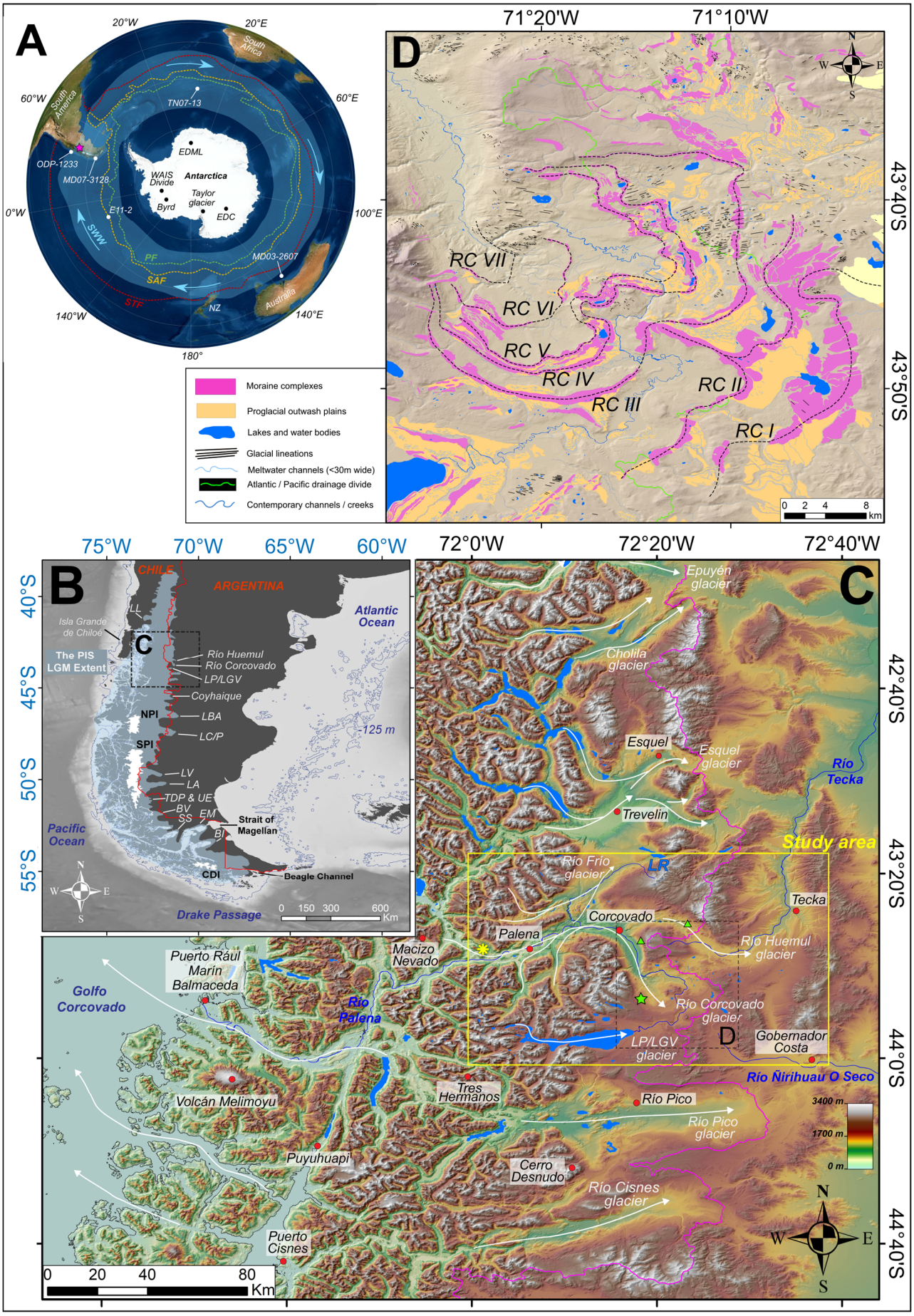
A
20°W
20°E
South Africa
60°W
60°E
South America
TN07-13
EDML
ODP-1233
MD07-3128
WAIS Divide
Antarctica
Taylor glacier
Byrd
EDC
E11-2
0°W
100°E
SWW
PF
MD03-2607
SAF
STF
NZ
Australia
140°W
140°E
180°
Moraine complexes
Proglacial outwash plains
Lakes and water bodies
Glacial lineations
Meltwater channels (<30m wide)
Atlantic / Pacific drainage divide
Contemporary channels / creeks
D
71°20'W
71°10'W
43°40'S
43°50'S
RC VII
RC VI
RC V
RC IV
RC III
RC II
RC I
0 2 4 8 km
B
75°W
70°W
65°W
60°W
40°S
45°S
50°S
55°S
CHILE
ARGENTINA
Isla Grande de Chiloé
LL
C
The PIS LGM Extent
Río Huemul
Río Corcovado
LP/LGV
Coyhaique
NPI
LBA
LC/P
SPI
LV
LA
TDP & UE
BV
SS
EM
BI
Strait of Magellan
CDI
Beagle Channel
Atlantic Ocean
125 m
Pacific Ocean
Drake Passage
0 150 300 600 Km
C
72°0'W
72°20'W
72°40'W
42°40'S
43°20'S
44°0'S
44°40'S
Epuyén glacier
Cholila glacier
Esquel
Esquel glacier
Río Tecka
Trevelin
Study area
Río Frío glacier
LR
Tecka
Corcovado
Palena
Río Huemul glacier
Macizo Nevado
Río Corcovado glacier
LP/LGV glacier
D
Gobernador Costa
Río Ñirihuau O Seco
Puerto Rául Marín Balmaceda
Golfo Corcovado
Río Palena
Tres Hermanos
Río Pico
Río Pico glacier
3400 m
1700 m
0 m
Volcán Melimoyu
Puyuhuapi
Cerro Desnudo
Río Cisnes glacier
Puerto Cisnes
0 20 40 80 Km
N
W
E
S

Figure 3.1. Location maps of study area. (**A**) Map of Southern Hemisphere highlighting the approximate contemporary positions of the Southern Westerly Winds (SWW: after Sime *et al*., 2013) belt (light blue), the Polar Front (PF: green), the Sub-Antarctic Front (SAF: orange), and the Sub-Tropical-Front (STF: red), adapted from Darvill *et al*. (2016) and based on Orsi *et al*. (1995) and Carter *et al*. (2008). The map also highlights the location of our northern Patagonia study site (purple star). The locations of key marine and ice core palaeoclimate records mentioned in the text are illustrated with white dots. Background imagery is from DigitalGlobe (GeoEye, IKONOS, 2000-2011). (**B**) Adapted from Leger *et al*. (2020). Approximate former extent of the Patagonian Ice Sheet (PIS) during the Last Glacial Maximum (LGM), modified from Glasser *et al*. (2008) and Glasser & Jansson (2008). Modern extents of the North Patagonian (NPI), South Patagonian (SPI), and Cordillera Darwin (CDI) Icefields are displayed in white. Major former outlet glaciers of the PIS are designated: BI: Bahía Inútil, EM: Estrecho de Magallanes, SS: Seno Skyring, BV: Bella Vista, TDP & UE: Torres del Paine & Última Esperanza, LA: Lago Argentino, LV: Lago Videma, LC/P: Lago Cochrane/Pueyrredón, LBA: Lago Buenos Aires, LL: Lago Llanquihue. Bathymetric data were acquired from the General Bathymetric Chart of the Oceans (GEBCO) and are here shown in greyscale. A -125 m contour roughly simulating former coastline locations at the LGM is displayed (Lambeck *et al*., 2014). The Chile/Argentina border is shown in red. (**C**) Adapted from Leger *et al*. (2020). Digital Elevation Model (DEM) of northern Patagonian Andes extrapolated from the ALOS WORLD 3D missions (version 2.2; JAXA; https://www.Eorc.jaxa.jp/ALOS/en/ aw3d30/) with a shaded relief background (light azimuth: 315°, incline: 45°) and a sea-level contour (black line) indicating modern coastlines. White arrows designate ice-flow direction of major former PIS outlet glaciers. The pink line delineates the contemporary Atlantic (East) / Pacific (West) drainage divide. Main lake bodies and river channels were manually digitised and are displayed in blue, and labelled when mentioned in the text. Locations of sampling for TCN dating are symbolised by the green star (moraine boulders), the green triangle (shoreline cobbles) and the yellow asterisk (bedrock samples). (**D**) Glacial geomorphological map adapted from Leger *et al*. (2020) focused on the RC valley moraine and outwash record. Black dashed lines represent our interpretation of the different moraine limits preserved (RCI – RCVII) and their connectivity throughout the field site.

3.2 Study location and physical setting

3.2.1 Geographical setting

Our study focuses on a major palaeo-outlet glacier of the northern PIS (Fig. 3.1), the Palena outlet glacier, which flowed east-northeast from the centre of the former ice sheet, near Macizo Nevado, along the Río Palena (RP) valley. Upon reaching the eastern mountain front, the Palena outlet glacier diverged (43.3°S, 71.3°W) into three branches occupying the Río Frío (RF) valley to the north, the Río Huemul (RH) valley to the east, and the RC valley to the south, where we focus our moraine chronology. The RH and RC outlet glaciers extended up to 60 kilometres to the east/southeast of the Argentinian town of Corcovado (43°54'S; 71°46'W) (Caldenius, 1932; Haller *et al*., 2003; Martínez *et al*., 2011). The semi-arid southeastern sectors of the RH and RC valleys (570 mm a^{-1} of precipitation: Fick & Hijmans, 2017), which belong to the Patagonian steppe climate zone, host a series of well-preserved lateral and frontal moraine complexes, along with associated glaciofluvial and glaciolacustrine sediment-landform assemblages (Haller *et al*., 2003; Martínez *et al.*, 2011; Leger *et al*., 2020). The RC valley exhibits preservation of at least seven distinct moraine complexes, here termed RC I-VII moraines, from oldest to youngest (Fig. 3.1d).

The Palena outlet glacier and its RC, RH and RF branches advanced up reverse-graded slopes from a valley floor elevation of ~150 m a.s.l. near the former ice divide, to the elevation of the major terminal moraine ridges nested between 800 and 1100 m a.s.l. east of the mountain front. Therefore, the modern hydrographic drainage of the Río Palena catchment is reversed relative to the flow direction of the former glaciers, with the modern drainage divide located ~70-80 km east of the central spine of the Andes (Davies *et al*., 2020). Geomorphological mapping of glacial lineations and ice-moulded bedrock outcrops (Leger *et al*., 2020) indicates that the westward dipping RP, RC and RH valleys were subglacially eroded by warm-based ice. This suggests in turn that the valleys were former conduits for fast-flowing, topographically-controlled outlet glaciers capable of generating significant valley over-deepening during Quaternary glaciations. Such valley over-deepening, greater toward the western margins of the former PIS relative to its eastern margins, is characteristic of the topography for much of Patagonia (*e.g.* Clapperton, 1993; Singer *et al*., 2004; Kaplan *et al*., 2009). The topographic setting helps to explain the preservation of multiple moraine sequences over the Argentinian foreland (Clapperton, 1993; Kaplan *et al*., 2009), as well as the formation of proglacial lakes during episodes of deglaciation.

3.2.2 Geologic setting

The field site is located 300 km to the northeast of the Chile triple junction (Hervé *et al*., 2017), where the Nazca and Antarctic plates subduct in a north-easterly direction beneath the South American plate (~66 mm a^{-1}; Rosenau *et al*., 2006). The site lies directly east of the Liquiñe-Ofqui Fault Zone (LOFZ), a dextral intra-arc transform fault formed during the late Miocene (10-5 Ma) which extends ~1200 km in a NNE-SSW orientation (from 43°S to 38°S) and has experienced periods of substantial pluton emplacement (Thomson & Hervé, 2002; Lange *et al*., 2008). The geology of the Palena outlet glacier catchment is dominated by the North Patagonian batholith, formed during the Mesozoic due to local subduction beneath the continental margin and exposed more recently during late-Miocene uplift (Hervé *et al*., 2017). The batholith in this region is characterised by quartz-bearing pink leuco-monzonite, giving way to darker diorite/tonalite and white granodiorite toward the west (Pankhurst *et al*., 1992). East of Palena and along the RC and RH valleys, the batholith gives way to four main formations of volcanic and sedimentary assemblages (Pankhurst *et al*., 1992; Haller *et al*., 2003). These are characterised by: 1) The prevailing Jurassic *Lago La Plata* formation, composed of Andesites, andesitic tuffs, dacites and rhyolites, 2) the lower-cretaceous *Divisadero* formation of lavas, basic to andesitic breccia and andesitic to rhyolitic pyroclastic deposits, interspersed with sedimentary units, 3) the upper cretaceous *Morro Serrano* formation of basic-stock intrusives, veins and dykes, and 4) the rarer mid-cretaceous Río Hielo formation of granites with vein and dyke intrusions (Haller *et al*., 2003). Consequently, glaciogenic deposits in the field site are characterised by a wide variety of lithologies.

3.2.3 Climatic setting

The climate of Patagonia is strongly influenced by the Southern Westerly Winds (SWW). The SWW deliver precipitation to the Patagonian Andes, which act as a potent orographic barrier, resulting in a strong west-east rain-shadow effect (Garreaud *et al*., 2013). At the core of the modern wind-belt, located around central Patagonia (between ~45°S and ~50°S), precipitation on the Pacific coast ranges between 5,000 and 10,000 mm a^{-1}, while it diminishes to less than 300 mm a^{-1} east of the mountain front (Garreaud *et al*., 2013; Lenaerts *et al*., 2014). In north Patagonia, the SWW are thought to migrate northward and weaken during austral winters, thus causing lower precipitation levels relative to austral summers (Aravena & Luckman, 2009). Annual precipitation near Macizo Nevado, the approximate former ice divide, averages ~1850 mm a^{-1} according to *WorldClim* 2 data (Fick & Hijmans, 2017). Near the terminal margins of the former RC and RH glaciers, which are in

the Patagonian steppe climate zone, annual precipitation decreases by 70% to ~570 mm a^{-1}, while modelled mean annual temperature at 1000 m a.s.l is around 7 °C (*ibid*). The SWW are also an important driver of the Antarctic Circumpolar current (ACC), which after separating into two branches near the Chilean Pacific coast at 45°S, generates the northward-directed Peru-Chile current, bringing cold Subantarctic waters to the Pacific coast of northern Patagonia (Kaiser *et al*., 2007).

3.2.4 Previous work in study area

The glacial geomorphology in the study site was first examined and mapped by Caldenius (1932), and later by Lapido (1990), Martínez (2002) and Martínez *et al*. (2011). Three main glacial sequences were also included in ice-sheet-wide geomorphological investigations by Glasser & Jansson (2008) and Davies *et al*. (2020) as well as a regional geological map by Haller *et al*. (2003). While no direct chronology exists, the innermost and youngest preserved moraine sequences were assumed to relate to the local LGM based on morpho-stratigraphic observations and comparisons with other dated moraine records in Patagonia. The first detailed, large-scale geomorphological mapping of ice-contact glaciogenic, glaciofluvial and glaciolacustrine deposits was published recently by Leger *et al*. (2020).

3.3 Methods

3.3.1 Geomorphological mapping

Initial identification of major landforms and topographic features was carried out using the freely available ALOS WORLD 3D - 30 m resolution (AW3D30: Japan Aerospace Exploration Agency) Digital Elevation Model (DEM). All mapped landforms were digitized manually in the WGS84 geographic reference coordinate system using the ESRI^{TM} World Imagery layer, characterized by 1.0 m resolution images from DigitalGlobe (GeoEye, IKONOS, 2000-2011) at the study site. In areas with high vegetation and/or cloud cover, different colour-rendering comparisons were made using 10 m resolution Sentinel 2A true colour (TCI) and false colour (bands 8,4,3) products (available from https://scihub.copernicus.eu/).

Ground-truthing and/or corrections of preliminary landform interpretations were conducted during two separate field seasons (8 weeks in total) during the 2019 and 2020 austral summers. Geomorphological mapping criteria along with the complete geomorphological map of the area are presented by Leger *et al*. (2020).

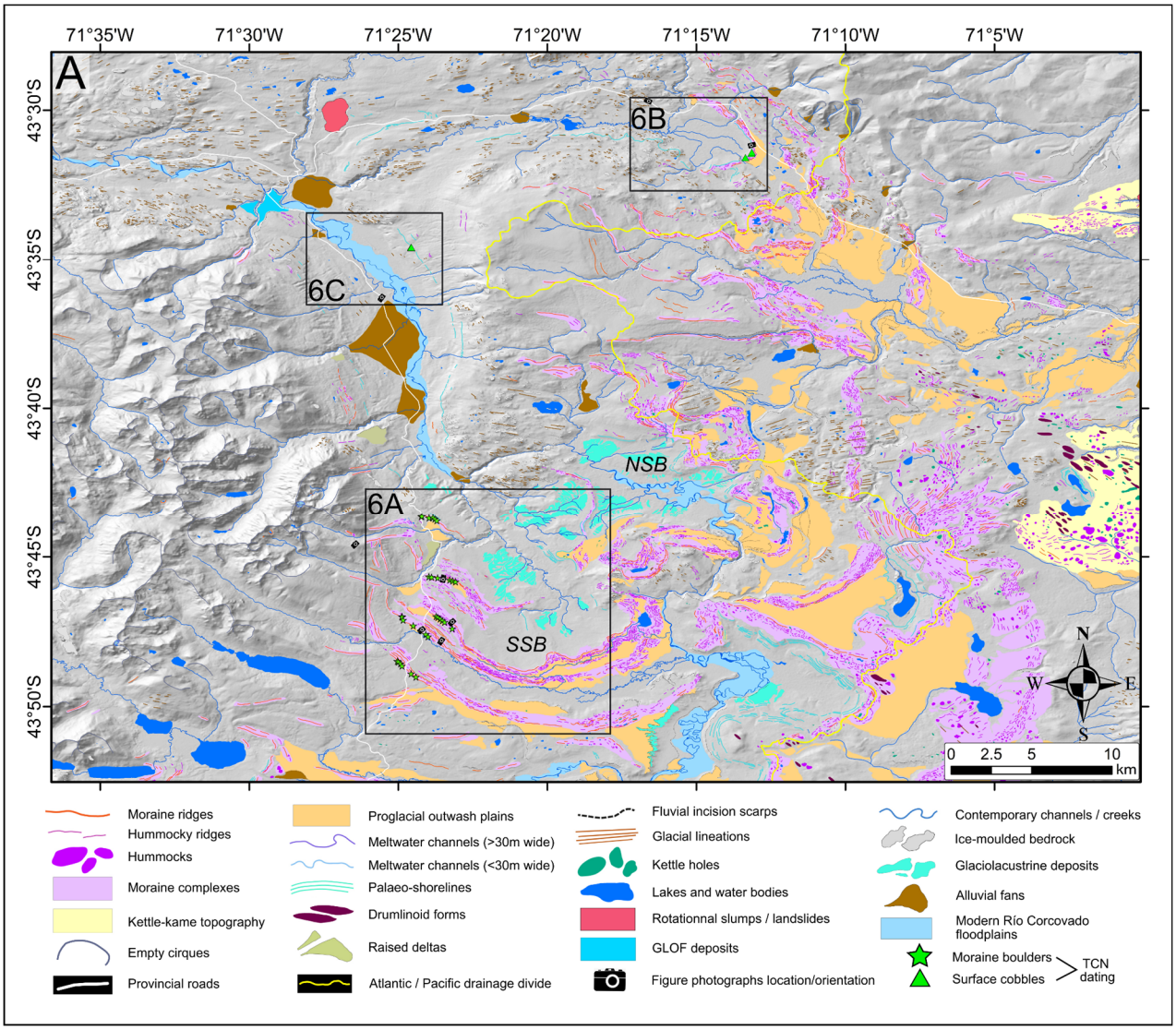

Figure 3.2. Geomorphological map (**A**) DEM hillshade (AW3D30 DEM, light azimuth: 315°, incline: 45°) and glacial geomorphological map (adapted from Leger *et al*., 2020) of the RC and RH valleys and their glaciogenic, glaciofluvial and glaciolacustrine landform-sediment assemblages. The location of moraine boulders and former proglacial lake shoreline surface cobbles sampled for TCN dating are indicated by green star and green triangle symbols, respectively. Camera symbols highlight the location of photographs taken on the field and shown in Figures 3.3-3.5. *SSB*: RC southern sub-basin, *NSB*: RC northern sub-basin.

3.3.2 Moraine morphology/sedimentology analyses

In order to obtain empirical information on glaciogenic sediment deposition history, moraine ridge preservation and its variability across the studied sequence, characteristics of moraine morphology and surface sediments were analysed in the field. We produced topographic profiles for each of the moraine ridges that were sampled for TCN dating using handheld GPS (spatial accuracy: 3-5 m). Where possible, between two and four transects were measured per moraine at >200 m intervals to assess variability along individual ridges. For each transect, we calculated the mean ice-proximal and ice-distal slopes and width-to-height ratios. RC IV-VII moraine clast sediments were investigated on ridge-crest surfaces using a 16 m^2 quadrangle over an area deemed undisturbed and representative of surface sediments. For each quadrangle, surface clast-shape and roundness data were collected (n = 30 clasts), and clast lithology was recorded. Clast-shape data were plotted on a ternary diagram scaled using *b:a* and *c:a* ratios (Sneed & Folk, 1958; Benn & Ballantyne, 1993) and displaying C_{40} indices (% of *c:a* ratios ≤ 0.4). Clast-roundness data were plotted as histograms and statistically assessed using *RWR* and *RA* indices (Evans & Benn, 2004; Martin *et al*., 2019).

3.3.3 Dating approach and sampling

The wider, highly subdued and less sharp-crested geomorphology of the RC I-II moraines along with a set of twenty-five preliminary (yet unpublished) exposure ages is suggestive of a pre-last glacial cycle age for these outer margins (Leger *et al*., 2020). The chronology presented here thus focuses exclusively on the younger RC III-VII moraines. To establish a detailed TCN chronology of glacial advances/stillstands and deglacial events in the field area, we measured ^{10}Be concentrations in thirty moraine boulders, six palaeo-shoreline cobbles, and two ice-moulded bedrock surfaces across the study site (Figs. 3.1c, 3.2). All sample sites were assessed for topographic shielding using a compass and clinometer.

To establish the timing of the RC III-VII advances/stillstands, we sampled moraine boulders for surface exposure dating (*e.g.* Gosse & Phillips, 2001; Hein *et al*., 2010; Heyman *et al*., 2011). Due to road-access conditions and moraine preservation, we chose the western lateral-frontal environment of the RC basin for sampling of the five most prominent ridges, each belonging to a separate moraine complex (Fig. 3.2). We targeted large granodiorite boulders (50-190 cm tall) resting directly on the moraine crest that exhibited glacial polish and, in some cases, preserved striations, indicating minimal surface erosion. We collected 1-2 kg samples by hammer, chisel and angle grinder from the top 2-5 cm of the centre of the boulders (Fig. 3.3). For each target moraine, we sampled six boulders along a

single continuous ridge (Fig. 3.2). This sampling strategy aims to reduce potential uncertainties resulting from geological scatter due to post-depositional processes (Putkonen & Swanson, 2003; Applegate *et al*., 2010; Heyman *et al*., 2011). We interpret the exposure ages as dating moraine stabilisation following ice-front retreat, hence providing a minimum age for the glacier advance/stillstand.

Two preserved palaeo-shorelines in the RC and RH valleys represent proglacial lake phases during deglaciation. To date the palaeo-shorelines, we sampled three rounded to subrounded, smooth (*i.e*., unweathered) surface cobbles from wave-cut platforms etched into sediments draping the valley sides. The cobbles were collected from the flattest sections of the palaeo-shoreline platform, and care was taken to sample away from the backing slope to reduce the risk of post-depositional surface disturbance and contamination from debris-fall. The formation of lake shorelines in sediment deposits is an erosive process mostly conducted by wave action and sediment liquefaction (Sissons, 1978). Our sampling approach thus considers a shoreline wave-cut platform as continuously disturbed by wave action throughout the time of lake residence at its elevation. Such an interpretation is supported by the general presence of more prominent and discernible palaeo-shorelines on the downwind, more wave-exposed eastern valley slopes of the field area (Leger *et al*., 2020; Figs. 3.2, 3.4). We targeted surface cobbles rather than boulders because they are more easily disturbed by wave action, and are thus less likely to start accumulating cosmogenic radionuclides during lake residence. We therefore suggest the granitic palaeo-shoreline surface cobbles sampled started accumulating ^{10}Be only following shoreline abandonment/stabilisation, and thus interpret their exposure ages as minimum ages for the timing of lake lowering (Fabel *et al*., 2010; Lifton *et al*., 2001; 2015; Mendelová *et al*., 2020b).

To date the final drainage of the proglacial lake, and reconstruct the approximate timing of PIS disintegration in the region, we sampled two ice-moulded (striated/polished) granite bedrock surfaces within the mountain interior and near to the RP valley floor (Figs. 3.1, 3.5). The sample sites are separated by 4.8 km along the valley and differ in elevation by 90 m. We do not expect the bedrock surfaces to have been shielded following the palaeolake drainage and suggest the two bedrock samples date the final lake-level drop below their respective elevations of 254 and 343 m a.s.l.

To provide further chronological constraints on the palaeolake history of the RC valley, we attempted to date the deposition of laminated glaciolacustrine sediments in three different locations using single-grain optically-stimulated luminescence (OSL) dating. The samples were collected using

opaque tubes following the methodology described by Smedley *et al*. (2016) (detailed methodology in supplementary materials).

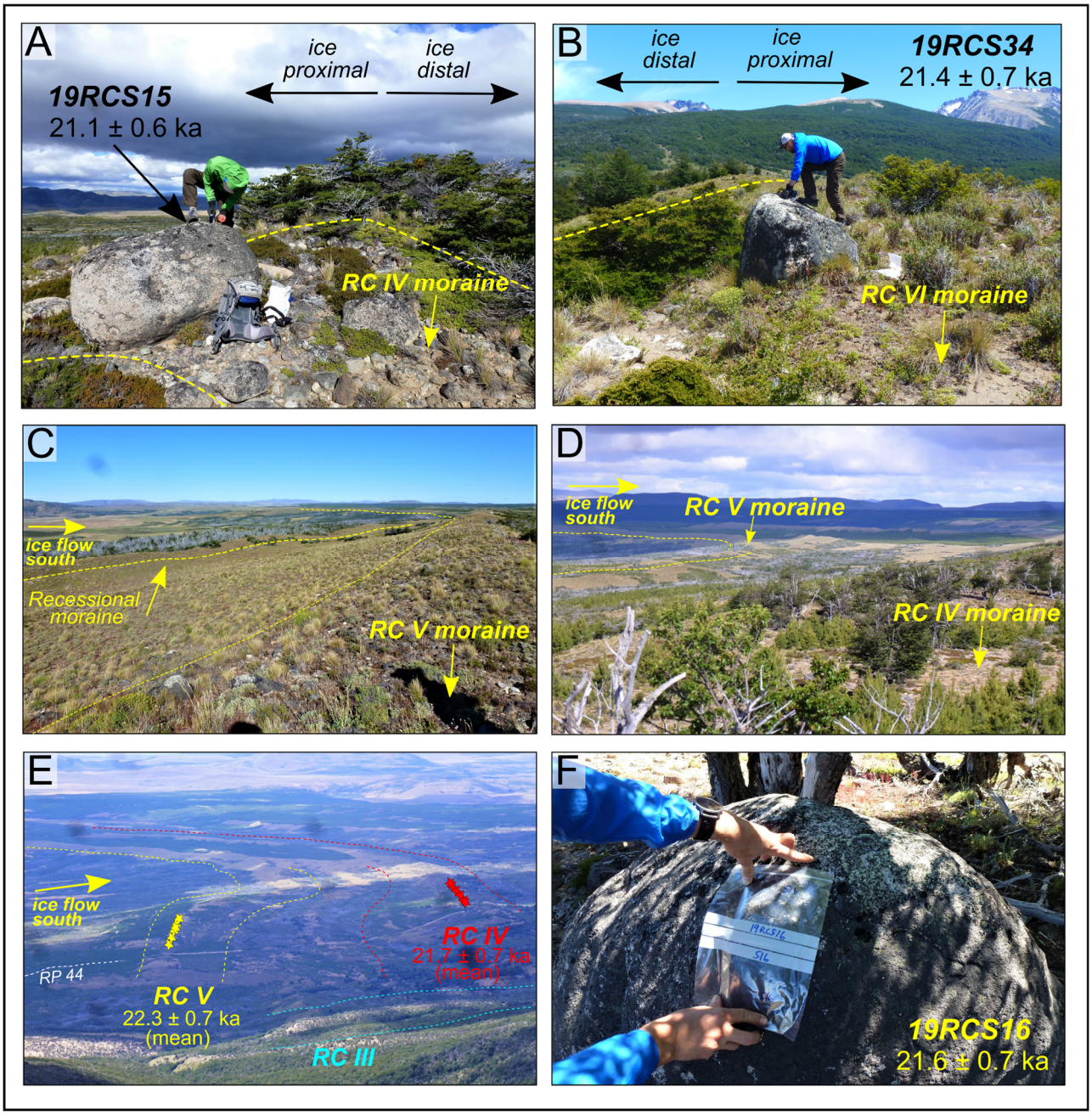

Figure 3.3. Field photographs of moraines and sampled boulders. (**A**) Southeast-facing photograph of an erratic granite boulder (sample 19RCS15) deposited on the crest of a RC IV moraine ridge and sampled for TCN dating with hammer and chisel. (**B**) Northwest-facing photograph of a RC VI moraine ridge crest and a granite boulder (19RCS34) sampled for TCN dating. (**C**) Eastward view of the RC V moraine complex, with the most prominent moraine ridge (targeted for sampling) in the foreground, and preserved, smaller recessional ridges in the background (camera location: 43°47'3.67"S). (**D**) Southeastward view from the RC IV moraine complex depicting the terminal environment of the RC V moraine complex, which demonstrate a curved lobate shape (camera location: 43°48'0.14"S, 71°23'28.52"W). (**E**) Photograph captured from the southern mountain ridge of the El Loro valley (camera location: 43°44'38.01"S, 71°27'21.58"W) and looking southeastwards towards the RC V and RC IV moraine complexes in the RC southern sub-basin, which are crossed by the visible RP 44 road. (**F**) Close-up photograph of a granite moraine boulder (19RCS16) sampled for TCN dating from a RC IV moraine ridge, indicating the rounded and preserved nature of its surface.

3.3.4 Sample preparation and wet chemistry

Samples were prepared at two cosmogenic nuclide laboratories: the University of Edinburgh's Cosmogenic Nuclide Laboratory for sample crushing/sieving and the Natural Environment Research Council's Cosmogenic Isotope Analysis Facility (NERC-CIAF) for the wet chemistry. The samples were crushed and sieved to isolate the 250-500 μm and 125-250 μm grain fractions. To avoid the impact of ^{10}Be concentration decrease with depth on resulting cobble exposure ages, the exposed top 3-5 cm of cobbles with thicknesses greater than 10 cm (n=2) were cut, crushed and selected for cosmogenic isotope analysis. Smaller (<10 cm) cobbles (n=4) were crushed whole, however. All $^{10}Be/^{9}Be$ ratios were measured at the Scottish Universities Environmental Research Centre (SUERC) Accelerator Mass Spectrometry (AMS) facility. Further details of the wet chemistry methodology are described in the supplementary materials.

3.3.5 Age calculations

To ease the comparison of our data with existing regional data (*e.g.* Davies *et al.*, 2020), ^{10}Be ages were calculated using the online exposure age calculator formerly known as the CRONUS-Earth online calculator (version 3, Balco *et al.*, 2008), and calibrated using the Patagonia (50°S) production rate (Kaplan *et al.*, 2011) obtained from the ICE-D online database (http://calibration.ice-d.org/). In this study, we report ages (including recalculated ages from other studies) using the LSDn-time-dependent scaling scheme of Lifton et al. (2014). Our exposure ages are up to 5.8% and 1.5% older relative to calculations made using the global ^{10}Be production rate (Borchers *et al.*, 2016) and the New Zealand production rate (Putnam *et al.*, 2010), respectively. The contribution of geological scatter on the spread of exposure ages from individual moraines is assessed based on the mean square weighted deviation (MSWD), also referred to as reduced chi-squared (Wendt & Carl, 1991), and whether it is inferior (low scatter) or superior (increasing scatter) to one (Jones *et al.*, 2019). Moreover, we display the MSWD's inferior/superior relationship to the criterion *k* indicating whether the MSWD value falls within a 2σ envelope, thus testing how well the data represent a single landform (Spencer *et al.*, 2017; Jones *et al.*, 2019). Topographic shielding is negligible, ranging between 0.99 and 1 (Table 3.1). Exposure ages presented here are interpreted as minimum ages, as we do not include a correction for rock surface erosion, nor for shielding by snow, vegetation or soil. However, applying the erosion rate of 0.2 mm ka^{-1} estimated for semi-arid central Patagonia (46°S; Douglass *et al.*, 2007; Hein *et al.*, 2017) increases our ages by less than 1%, which is within 1σ analytical uncertainties. The semi-arid steppe vegetation of the Argentinian foreland, diagnostic of our field site, allows for sparse vegetation and/or soil cover. According to proxy and modelled palaeoclimate data,

seasonal precipitation was 40-50% lower than present at the LGM east of the Patagonian Andes (Berman *et al*., 2016). Moreover, strong and persistent westerly winds (annual mean speed of ~5.3 m. s^{-1} at RC moraines location; *WorldClim* 2 data; Fick & Hijmans., 2017) are locally responsible for minimal annual snow cover on protruding landforms, such as moraine crests (Hein *et al*., 2010; Mendelová *et al*., 2020a; 2020b).

We employ a Bayesian age model to facilitate interpretation of the moraine chronology because our chronology presents instances of age reversals relative to the stratigraphic order of events. The Bayesian age model independently integrates sample ages and the relative order of events based on landform stratigraphy to refine probability distributions and produce a stratigraphically consistent chronology. Bayesian models have been widely applied to establish chronologies of lake/marine sediment cores (*e.g.*, Bronk Ramsey, 2008; Bendle *et al*., 2017a), and is increasingly used for TCN chronologies exhibiting closely spaced landform ages (*e.g.* Chiverrell *et al*., 2013, Small *et al*., 2019). Our Bayesian age model uses the same statistical framework as *OxCal* v4.3 (Bronk Ramsey, 2017) to produce a probability distribution (also termed a posterior density estimate) for each landform, by employing a Markov Chain Monte Carlo sampling approach (model code provided in supplementary materials). The age model was tested with and without prior stratigraphic outlier removal. Such tests only modified modelled mean moraine ages by ≤ 0.8%, thus remaining lower than 1σ analytical uncertainties. Best Gaussian fit statistics were also calculated for each landform and were found to vary by less than 0.1% relative to arithmetic means.

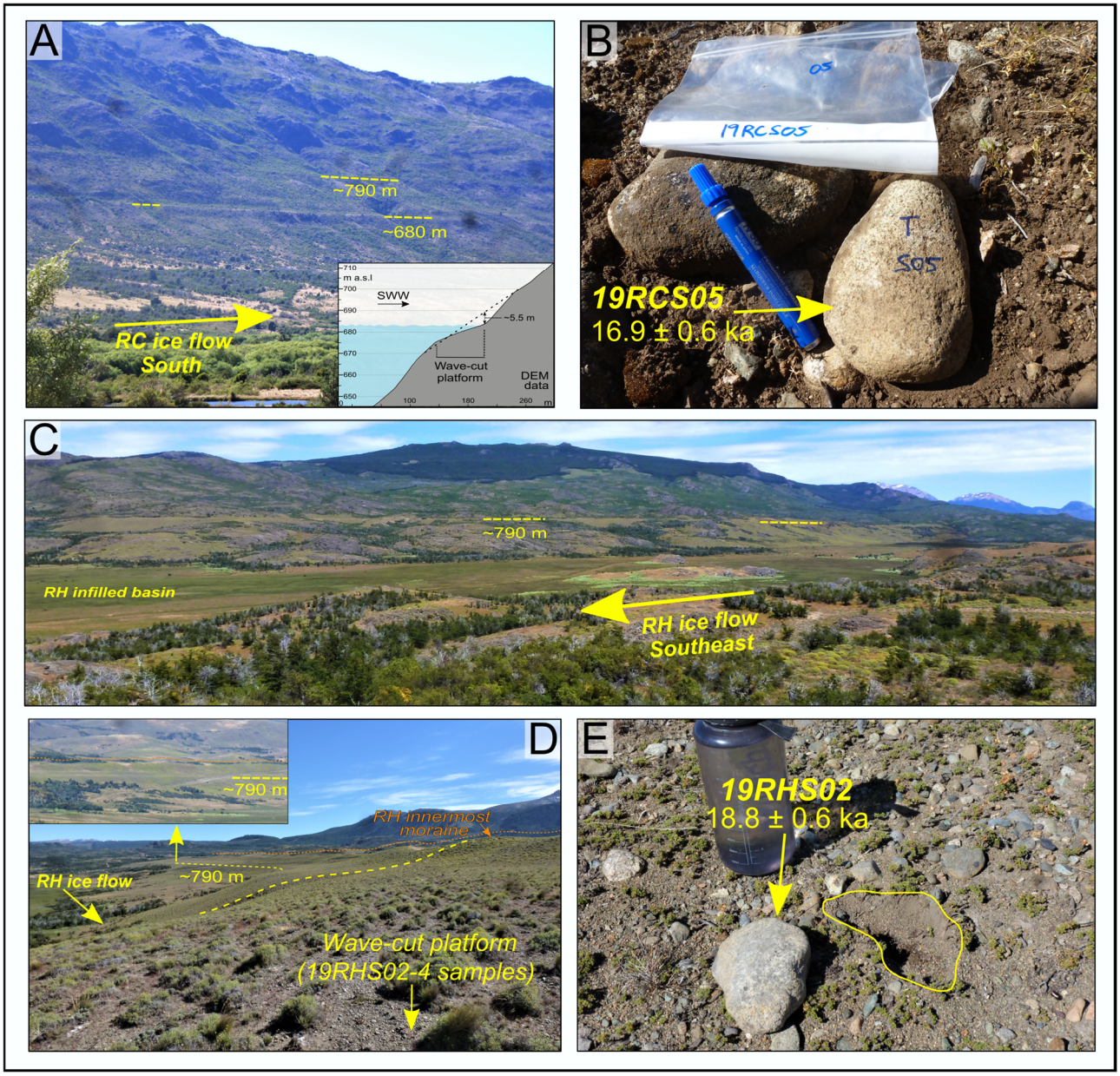

Figure 3.4. Field photographs of palaeo-shorelines and surface cobbles sampled (**A**) Southeast-facing photograph of the RC valley trough's eastern mountain slopes showing two well-preserved former proglacial lake shorelines, nested at elevations of ~680 and ~790 m (camera location: 43°36'15.23"S, 71°25'33.20"W). Inset diagram displays a topographic elevation profile from DEM of the lower 680 m palaeo-shoreline photographed, at location of sampling for TCN dating. (**B**) Example of a ~1 kg, well-rounded cobble sampled whole from the RC_{680} former proglacial lake shoreline for TCN dating (19RCS05). This granite cobble was selected for its stable, well-grounded position and because it displayed surface polishing and little evidence of erosion. (**C**) Southeast-facing view of the RH valley's southern/western mountain slope, characterised by numerous outcrops of ice-moulded bedrock and, in some locations, by the preservation of a clear former proglacial lake shoreline (RH_{790}), notched at the elevation of ~790 m (camera location: 43°29'43.45"S, 71°16'31.65"W). (**D**) Northwest-facing photograph captured from the wave-cut platform associated with the RH_{790} former proglacial lake shoreline (highlighted in yellow), and which is notched on the ice-proximal slope of the RH valley's innermost preserved moraine complex (highlighted in orange). The 19RHS02-04 samples were taken from near this location (camera location: 43°31'6.09"S, 71°13'8.59"W). The panel inset is a zoomed-in photograph of this same notched platform, along with the moraine ridge, as seen from the RP 17 road, 3.5 km to the north. (**E**) Photograph of a surface cobble, along with its imprint location, sampled from the RH_{790} former proglacial lake shoreline, which one can observe is mostly composed of sands and well-rounded pebbles and cobbles.

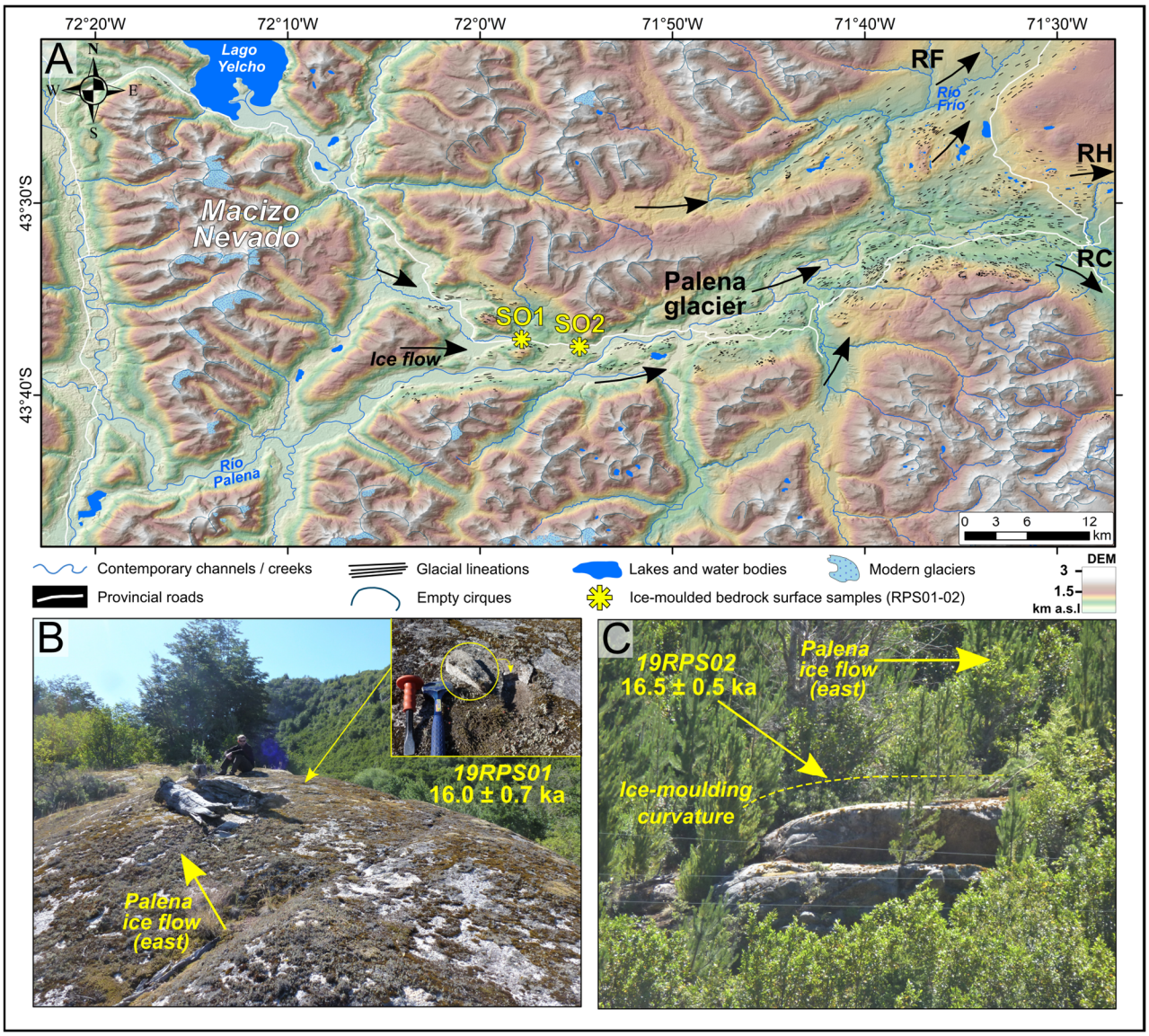

Figure 3.5. Ice-moulded bedrock surfaces sampled and geomorphological context. (**A**) DEM and hillshade (AW3D30 DEM, light azimuth: 315°, incline: 45°) of the RP valley, host to the former RP outlet glacier, which fed the former RC, RF and RH outlet glaciers. The map also features the Macizo Nevado mountain massif, which marks the approximate location of the former PIS ice divide during the LGM. The two yellow asterisks demarcate the locations of the two ice-moulded bedrock surfaces sampled for TCN dating (19RPS01-02). Black arrows indicate the approximate former ice-flow direction as suggested by the orientation of mapped lineations. (**B**) Eastward-facing, hence along-former-ice-flow, view of the lower (254 m a.s.l), rounded and smooth, ice-moulded bedrock surface sampled (19RPS01). (**C**) Photograph captured from the road of the higher (343 m) ice-moulded bedrock surface sampled (19RPS02: camera location: 43°37'30.8"S, 71°54'51.8"W).

3.4 Results

3.4.1 Geomorphology/Sedimentology

3.4.1.1 The RC III-VII moraines geomorphology

The RC III-VII moraines are located at the southern margin of the former RC outlet glacier (Fig. 3.6a; 43°46'S, 71°23'W). Geomorphological mapping highlighted five distinct moraine complexes composed of over 40 individual ridges reflecting numerous stillstands of the RC glacier front. The moraines range from m-scale, hardly perceptible ridges, to prominent, high relief (10-40 m), arcuate and sharp-crested ridges with steep slopes (9-19°), thus indicating a more prolonged period of ice-front stability. The most pronounced ridges appear unbroken and can be traced as continuous ridges over tens of km. They exhibit a double-lobate outline indicative of two former piedmont lobes across the width of the RC valley; caused by a valley-central 300 m-high bedrock step acting as an obstacle to ice flow (Fig. 3.2). In certain ice-front configurations (RC III – RC V), geomorphological mapping therefore suggests a RC glacier terminus branching off into two piedmont outlets occupying two respective sub-basins of the RC valley (Fig. 3.2). The northern sub-basin exhibits a low slope gradient, and the moraine complexes are more widely separated than in the steeper southern sub-basin.

The innermost (RC VII) and outermost (RC III) moraines lie 10.2 km from each other and range in elevation (at the location of sampling) from ~820 m a.s.l to ~1100 m a.s.l, respectively (Figure 6a). The five sampled moraines exhibit mean height-to-width ratios of between 6.6 and 11.4, and range in ice-proximal and ice-distal slope gradients from 9° to 19° (Figure 7). Clast-shape analyses from the RC IV-VII moraine surfaces (n = 30 per moraine) indicate a clear dominance of blocky clasts, with a uniform C_{40} percentage of 13.3%. All RC IV-VII moraines have a greater percentage of rounded to sub-rounded surface clasts (Figure 7). However, the RC VII moraine surface presents a comparatively higher percentage of angular clasts (30%) relative to the RC IV-VI average (12%). Although analogous to other RC moraines in orientation, size, slope gradients and surface clast-shape-and-size, the RC VII moraine is not as sharp-crested, and has a flatter, wider and more subdued crest surface with little variation in crest-line elevation. Contrary to the RC III-VI moraines, the RC VII moraine is not part of a complex including numerous superimposed recessional ridges, instead comprising a single, prominent ridge.

Along with other igneous extrusive lithologies (andesites, andesitic tuffs, dacites and rhyolites), the RC III-VII moraines contain an abundance of quartz-bearing granodiorite boulders (Figure 3). Moraine boulder erosion is variable and not correlated with the relative age of the moraine. For

example, on each sampled moraine we found some boulders with polished, striated, and well-rounded surfaces, while others displayed minor erosion by granular disintegration (depth < 2cm), and still others displayed significant (depth 2-4 cm) surface weathering pits. All surfaces sampled for TCN dating, however, demonstrated evidence of smooth polish, in some cases emerging from more weathered adjacent surfaces, and indicative of limited surface erosion where sampled.

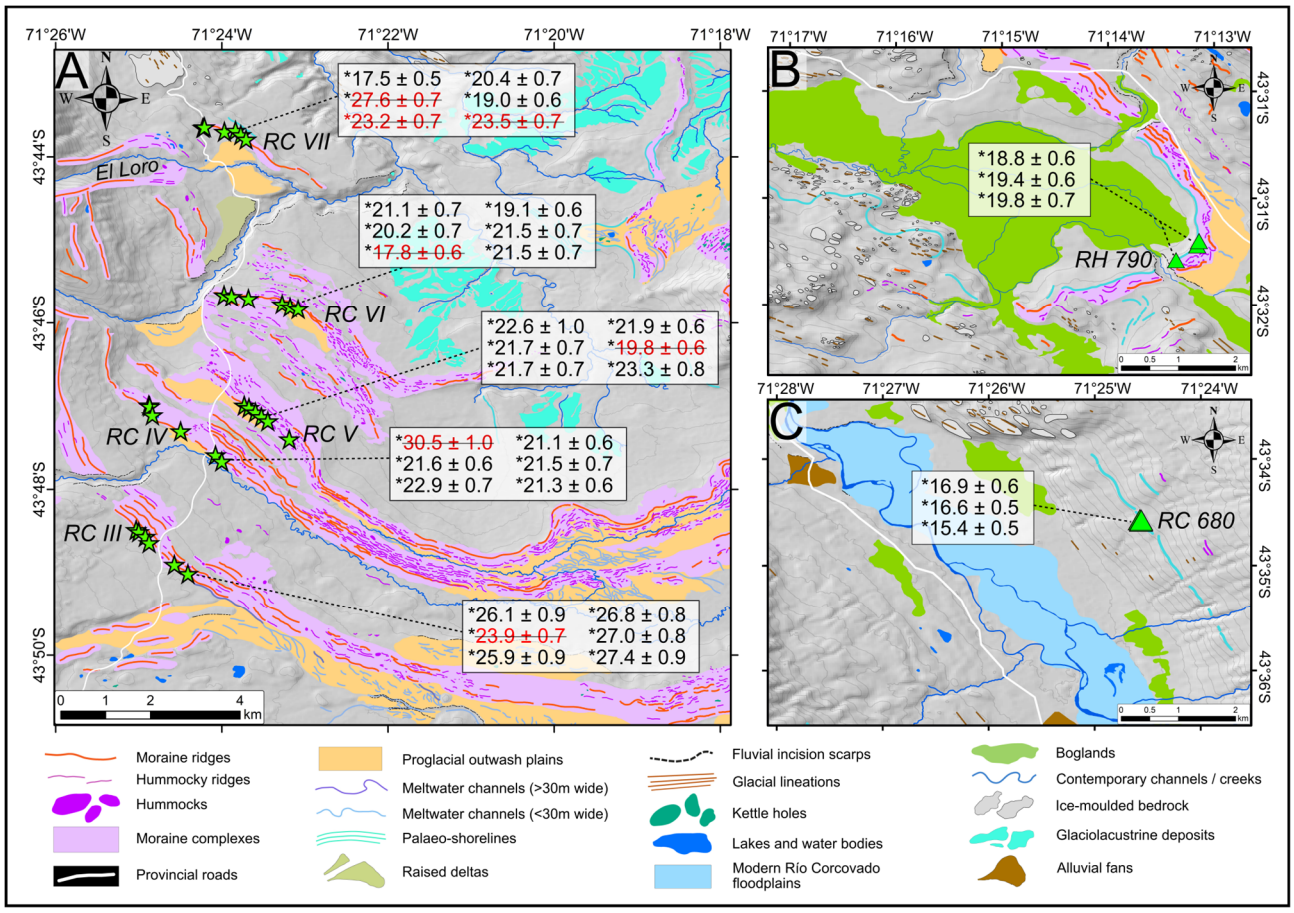

Figure 3.6. TCN dating chronology and geomorphological context of moraine boulder and palaeo-shoreline surface cobble samples (**A**) DEM hillshade (AW3D30 DEM, light azimuth: 315°, incline: 45°) and glacial geomorphological map (adapted from Leger *et al.*, 2020) enhanced on the RC LGM moraine sequence sampled. Individual ^{10}Be exposure ages (prior to Bayesian age model correction) and analytical internal uncertainties (n=6 per moraine) are indicated, along with identified outliers (in red). (**C**) and (**D**) maps focusing on the location and exposure ages of surface cobbles sampled from the RH_{790} and RC_{680} former proglacial lake shorelines, respectively.

3.4.1.2 The RH and RC former glaciolacustrine phases

Our geomorphological mapping revealed an abundance of glaciolacustrine sediment-landform assemblages in the RC and RH valleys, such as palaeo-shorelines, laminated clay-to-sand-sized sediment accumulations, raised deltas and spillway openings (Leger *et al*., 2020; Fig. 3.4). We interpret these assemblages as associated with proglacial lakes and as indicative of ice damming the westward, Pacific-directed drainage of the Corcovado, Huemul and Frío rivers following initial ice retreat from local LGM margins. We reconstructed former palaeolake elevations by matching the elevations of palaeo-shorelines, raised deltas, glaciolacustrine sediment deposits and major spillways indicative of the lowest drainage route through terminal glaciogenic deposits (Clapperton *et al*., 1993; Turner *et al*., 2005). Indeed, such geomorphological markers can procure evidence for lake-level falls following ice-front retreat and spillway shifts (Turner *et al*., 2005; Bell, 2008; Hein *et al*., 2010; Glasser *et al*., 2016; Thorndycraft *et al*., 2019). All geomorphological observations interpreted as markers of former proglacial lake levels are compiled in Chapter 3 Supplementary table 1, while our interpretation of the strongest sources of lake-level evidence are described in the discussion section of this manuscript. Our mapping and field interpretations suggest at least three main glaciolacustrine phases in the study region during and following local LGM glacial expansions. Phase one describes a proglacial lake formed at the elevation of 990 ± 5 m when the RC glacier ice-front was positioned at the RC III moraine while phase two is associated with a proglacial lake initially formed in the RC northern sub-basin, at the elevation of ~790 m, and following RC ice-front retreat from its RC V margin. OSL samples from exposures of rippled sands and varves elevated at 709 m and 686 m, thought to be deposits associated with proglacial lake phase two, yielded burial ages of 34.9 ± 2.9 ka and 52.1 ± 4.4 ka, respectively (Supplementary materials). The third phase is characterised by the formation of a larger lake system elevated at ~680 m and connecting all valleys of the field site during local deglaciation of outlet glaciers. Our geomorphological interpretations based on field investigations of former proglacial lake geographic extent, timing, drainage directions, spillway locations and residence time for each reconstructed phase is described further in the discussion section of this paper as well as in the supplementary materials.

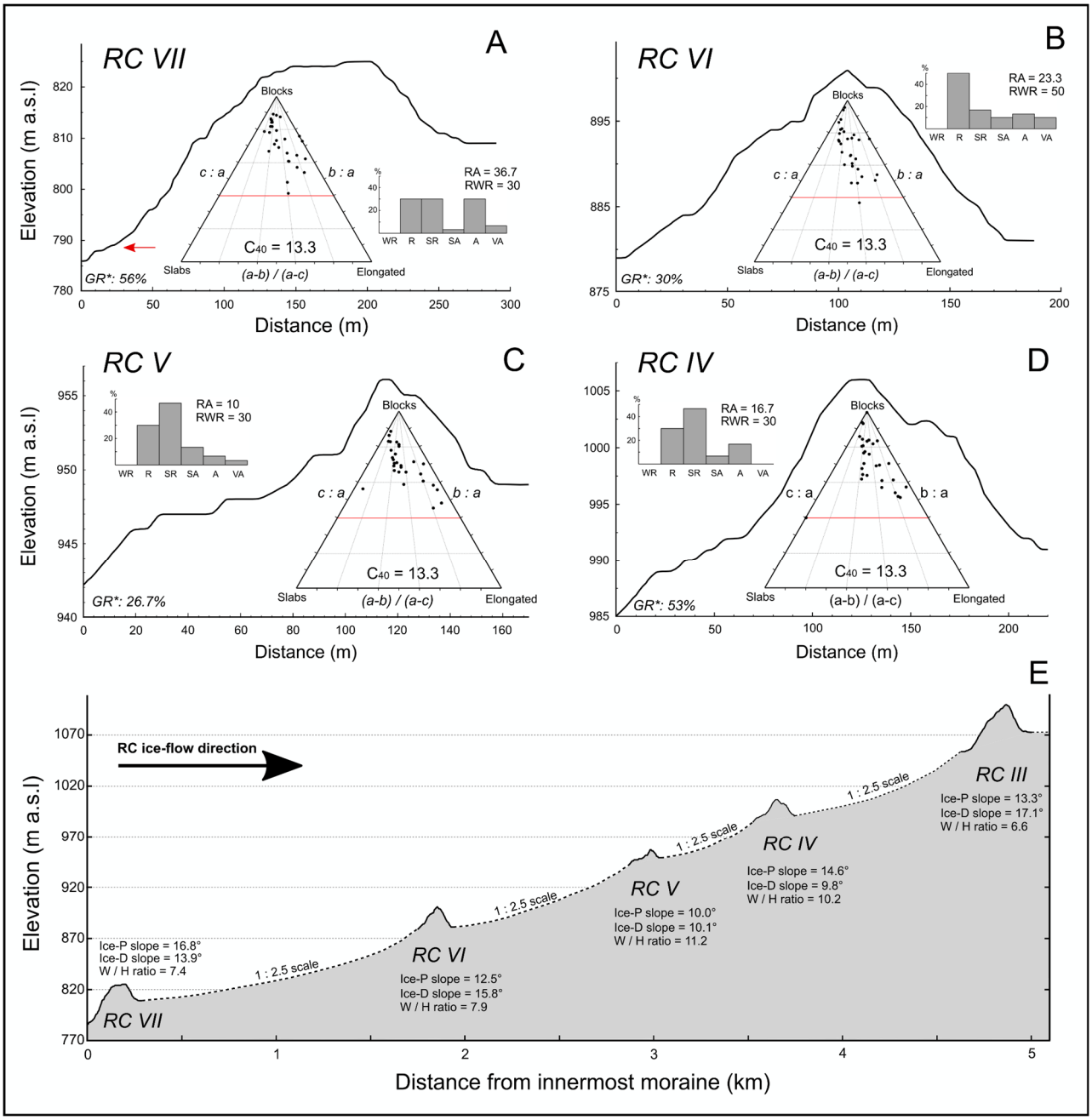

Figure 3.7. Geomorphological and sedimentological data for the RC III – RC VII moraines near the TCN dating locations. (**A-D**) Two-dimensional cross elevation profiles of the RC IV – RC VII moraines, measured from hand-held GPS transects (3-5 m vertical/spatial accuracy), along with ternary diagrams (scaled using *b:a* and *c:a* ratios) depicting moraine clast shape data from surface 16 m^2 quadrangles (n = 30 clasts per quadrangle). Clast-roundness histograms are also displayed for each of these moraines (WR = Well-rounded ; VA = Very angular). *RWR* and *RA* indices indicate, respectively, the percentages of rounded and well-rounded clasts and the percentages of angular and very angular clasts for each sampled population (Evans & Benn, 2004; Martin *et al*., 2019). (GR*) in each panel notes the percentage of granitic clasts sampled per population. (**E**) Elevation profile of the entire RC LGM moraine sequence, with GPS transects displayed for each moraine. The GPS transects, along with moraine absolute and relative elevations, are displayed to scale. The horizontal distance separating moraines, however, is displayed at a 1: 2.5 scale (dotted black lines). Also annotated against each moraine are ice-proximal (Ice-P) and ice-distal (Ice-D) slope gradients, and width-to-height (W/H) ratios.

3.4.2 Dating results

3.4.2.1 Cosmogenic ^{10}Be exposure ages

The ^{10}Be data (n = 38) are summarised in Tables 3.1 and 3.2 while kernel density estimates (1σ ranges) per individual sample and landform along with Bayesian age modelling probability distributions are presented in Figure 3.8.

The outermost RC III moraine yielded ages ranging from 23.9 ± 0.7 ka to 27.4 ± 0.9 ka (n = 6). The youngest age was interpreted as an outlier as it lies outside the remaining population's 95% confidence (2σ) envelope and was statistically rejected on the basis of a χ^2 test at 95% confidence (Ward & Wilson, 1978). The remaining exposure ages range from 25.9 ± 0.8 ka to 27.4 ± 0.9 ka, display a well-clustered age distribution, with a low MSWD value of 0.53, and yield an arithmetic mean of 26.6 ± 0.6 ka.

The six boulders from the RC IV moraine range in age from 21.1 ± 0.6 ka to 30.4 ± 1.0 ka. The oldest age, being significantly older than the older RC III moraine, is discarded as a stratigraphic outlier. The remaining dataset (n = 5) ranges from 21.1 ± 0.6 ka to 22.9 ± 0.7 ka, yielding a mean exposure age of 21.7 ± 0.7 ka, and representing a clustered dataset (MSWD = 1.08).

The six boulders from the RC V moraine range in age from 19.8 ± 0.6 ka to 23.3 ± 0.8 ka. We consider the youngest age an outlier because it lies outside the remaining population's 95% confidence (2σ) envelope, is younger than the mean age of the adjacent younger RC VI moraine (see below), and was taken from a comparatively short boulder (45 cm in height). Moreover, this younger age was statistically rejected on the basis of a χ^2 test at 95% confidence. We therefore consider it likely that this boulder was exhumed post-deposition and underestimates the age of the moraine. The remaining population (n=5) ranges from 21.7 ± 0.7 ka to 23.3 ± 0.8 ka, yields a mean exposure age of 22.3 ± 0.7 ka, and demonstrates a well-clustered dataset (MSWD = 0.76) (Table 3.2, Fig. 3.8).

Table 3.1. Sample details and nuclide concentrations.

Sample ID	Latitude (DD)	Longitude (DD)	Elevation (m a.s.l)	Boulder height (m)	Thickness (cm)	Shielding correction	Qtz mass dissolved (g)	^{10}Be atoms g^{-1} (SiO_2)	±1σ atoms g^{-1} (SiO_2)	^{10}Be / ^{9}Be ratio	±1σ	AMS ID - Laboratory facility
RC III - VII moraine boulders												
19RCS21	-43.80806	-71.41719	1105	0.65	2.0	0.999885	19.9171	2.597E+05	8.684E+03	3.253E-13	9.661E-15	b11801 CIAF
19RCS23	-43.80942	-71.41534	1101	1.20	4.0	0.999866	15.8740	2.626E+05	8.216E+03	2.760E-13	7.523E-15	b11775 CIAF
19RCS24	-43.81067	-71.41458	1101	1.40	3.0	0.999866	13.8700	2.340E+05	6.900E+03	2.124E-13	5.254E-15	b11908 CIAF
19RCS25	-43.81500	-71.40953	1102	1.20	3.5	0.999913	16.2847	2.653E+05	7.907E+03	2.733E-13	6.953E-15	b11803 CIAF
19RCS27	-43.81553	-71.40936	1101	1.20	3.5	0.999913	20.0920	2.538E+05	8.328E+03	3.202E-13	9.290E-15	b11804 CIAF
19RCS28	-43.81683	-71.40681	1101	0.55	2.0	0.999902	18.0367	2.723E+05	8.623E+03	3.098E-13	8.569E-15	b11805 CIAF
19RCS13	-43.79436	-71.40003	1003	1.00	2.5	0.999848	17.6247	2.789E+05	9.360E+03	3.087E-13	9.189E-15	b11797 CIAF
19RCS15	-43.79294	-71.40147	1014	0.60	2.5	0.999823	20.1200	1.902E+05	5.476E+03	2.504E-13	6.102E-15	b11774 CIAF
19RCS16	-43.78314	-71.41467	1040	1.00	1.5	0.999628	20.0033	2.011E+05	5.826E+03	2.541E-13	6.216E-15	b11798 CIAF
19RCS17	-43.78328	-71.41444	1037	0.95	1.0	0.999628	19.9809	2.009E+05	6.749E+03	2.531E-13	7.497E-15	b11799 CIAF
19RCS51	-43.79319	-71.40125	1017	0.70	2.0	0.999823	18.3354	2.097E+05	6.529E+03	2.444E-13	6.551E-15	b11800 CIAF
19RCS52	-43.78831	-71.40828	1038	0.80	1.5	0.999708	19.4590	1.975E+05	5.785E+03	2.531E-13	6.314E-15	b11786 CIAF
19RCS38	-43.78992	-71.38647	944	0.80	1.0	0.999810	18.9125	1.964E+05	8.458E+03	2.355E-13	9.337E-15	b11811 CIAF
19RCS40	-43.78544	-71.39206	950	0.40	1.5	0.999744	19.6800	1.898E+05	5.516E+03	2.455E-13	6.053E-15	b11780 CIAF
19RCS41	-43.78453	-71.39325	955	0.65	4.0	0.999744	20.0916	1.850E+05	6.295E+03	2.360E-13	7.084E-15	b11812 CIAF
19RCS42	-43.78364	-71.39456	953	0.45	1.5	0.999708	19.0720	1.700E+05	4.799E+03	2.146E-13	5.055E-15	b11781 CIAF
19RCS43	-43.78317	-71.39550	959	1.30	1.0	0.999708	13.1830	1.902E+05	5.916E+03	1.669E-13	4.413E-15	b11784 CIAF
19RCS44	-43.78278	-71.39633	954	1.00	1.5	0.999708	10.0460	2.030E+05	6.900E+03	1.364E-13	3.985E-15	b11785 CIAF
19RCS30	-43.76381	-71.38469	884	0.60	2.0	0.999657	14.3670	1.706E+05	5.672E+03	1.621E-13	4.664E-15	b11777 CIAF
19RCS31	-43.76414	-71.38417	892	0.65	0.8	0.999662	20.7070	1.561E+05	5.040E+03	2.118E-13	5.951E-15	b11778 CIAF
19RCS33	-43.76167	-71.39467	902	0.65	2.0	0.999720	20.4102	1.651E+05	5.434E+03	2.129E-13	6.105E-15	b11806 CIAF
19RCS34	-43.76119	-71.39819	903	1.35	1.5	0.999330	20.0644	1.776E+05	5.945E+03	2.260E-13	6.633E-15	b11807 CIAF
19RCS32	-43.76281	-71.38789	896	0.50	2.0	0.999678	19.9450	1.438E+05	4.744E+03	1.907E-13	5.477E-15	b11779 CIAF
19RCS36	-43.76125	-71.39806	902	0.35	2.0	0.999330	20.0644	1.768E+05	5.965E+03	2.251E-13	6.668E-15	b11810 CIAF
19RCS07	-43.72744	-71.40378	832	1.90	1.5	0.987187	19.1640	1.325E+05	4.112E+03	1.689E-13	4.458E-15	b11772 CIAF
19RCS08	-43.72981	-71.39514	824	1.15	0.4	0.998614	19.5762	1.585E+05	5.614E+03	1.979E-13	6.186E-15	b11792 CIAF
19RCS09	-43.72889	-71.39619	824	0.70	0.8	0.998605	20.2413	2.185E+05	5.834E+03	2.771E-13	6.073E-15	b11793 CIAF
19RCS11	-43.72803	-71.39725	829	0.70	3.5	0.998826	20.0857	1.435E+05	4.678E+03	1.821E-13	5.106E-15	b11794 CIAF
19RCS12	-43.72733	-71.40350	835	1.12	3.5	0.987187	20.5940	1.771E+05	5.074E+03	2.397E-13	5.790E-15	b11773 CIAF
RC20-29	-43.72755	-71.40289	832	0.86	1.0	0.997521	11.7200	1.850E+05	5.500E+03	1.443E-13	3.493E-15	b11909 CIAF

RC and RH palaeo-shoreline surface cobbles												
19RHS02	-43.52400	-71.21931	792	n/a	3.5	0.999062	14.9340	1.365E+05	4.729E+03	1.362E-13	4.078E-15	b11787 CIAF
19RHS03	-43.52631	-71.22264	788	n/a	4.0*	0.999010	20.3670	1.399E+05	4.480E+03	1.881E-13	5.202E-15	b11788 CIAF
19RHS04	-43.52631	-71.22264	788	n/a	4.8*	0.999010	20.0991	1.427E+05	4.815E+03	1.836E-13	5.377E-15	b11814 CIAF
19RCS05	-43.57639	-71.40939	673	n/a	3.0	0.996840	20.7050	1.102E+05	4.215E+03	1.493E-13	5.079E-15	b11771 CIAF
19RCS04	-43.57617	-71.40958	671	n/a	2.9	0.996840	14.2900	1.082E+05	3.300E+03	1.033E-13	2.445E-15	b11907 CIAF
19RCS03	-43.57617	-71.40958	671	n/a	2.8	0.996840	14.7000	9.980E+04	3.200E+03	9.636E-14	2.385E-15	b11905 CIAF
Río Palena valley surface bedrock samples												
19RPS01	-43.61828	-71.96400	343	n/a	3.5	0.985559	19.9158	7.616E+04	3.554E+03	9.789E-14	4.026E-15	b11813 CIAF
19RPS02	-43.62458	-71.91403	254	n/a	1.5	0.979415	23.5850	7.310E+04	2.400E+03	1.160E-13	3.262E-15	b11790 CIAF

Table footnotes.

Rock density is assumed to be 2.65 g cm^{-3}.

*Samples that were cut prior to crushing, reported thickness relates to top, exposed surfaces selected for analysis after cutting.

Concentrations were corrected for process blanks; blank corrections ranged between ~ 1.4 and 4.6% of the sample $^{10}Be/^{9}Be$ ratios. The uncertainty of the blank correction is included in the stated one-sigma uncertainties. Measurements were normalised to NIST SRM4325 with nominal $^{10}Be/^{9}Be$ ratios of 2.79 x 10^{-11}, corresponding to a ^{10}Be half-life of 1.36 Ma (Nishiizumi *et al*., 2007). CIAF: Cosmogenic Isotope Analysis Facility, all measurements were made at the AMS facility at the Scottish Universities Environmental Research Centre (SUERC), East Kilbride, Scotland.

The six boulders from the RC VI moraine range in age from 17.8 ± 0.6 ka to 21.5 ± 0.7 ka. We consider the youngest age an outlier because it is 1 ka younger than the mean age of the younger adjacent RC VII moraine (see below). Moreover, it was statistically rejected on the basis of a χ^2 test at 95% confidence and was also sampled from a comparatively short (50 cm in height) boulder that may have been exhumed post moraine deposition. The remaining sample ages (n = 5) range from 19.1 ± 0.6 ka to 21.5 ± 0.7 ka, yield a mean exposure age of 20.6 ± 1.0 ka, and demonstrate a high and >1 MSWD value of 2.33, thus suggestive of greater age scatter than predicted solely by analytical uncertainties.

The six boulders from the RC VII moraine range in age from 17.5 ± 0.5 ka to 27.6 ± 0.7 ka. Based on stratigraphy, we interpret the three oldest exposure ages of 23.2 ± 0.7 ka, 23.5 ± 0.7 ka and 27.6 ± 0.7 ka as outliers yielding inheritance as their ages are greater than the older, adjacent RC VI-IV moraines and lie outside of the 2σ envelope. The remaining population (n = 3) ranges from 17.5 ± 0.5 ka to 20.4 ± 0.7 ka, yields a mean exposure age of 19.00 ± 1.5 ka, and exhibits a high and >1 MSWD value of 5.34, indicating greater age scatter than can be predicted by analytical uncertainties only.

The three cobbles sampled from the RH_{790} palaeo-shoreline range in age from 18.7 ± 0.6 ka to 19.8 ± 0.7 ka. The distribution of ages is well-clustered, with a MSWD value of 0.62. The population's mean exposure age is 19.3 ± 0.5 ka.

The three cobbles sampled from the RC_{680} palaeo-shoreline range in age from 15.4 ± 0.5 ka to 16.9 ± 0.6 ka, and exhibit a reasonably clustered dataset, with a MSWD value of 2.24, which is inferior to *k* (3.0). The MSWD value is greater than 1, however, and is diagnostic of some geologic scatter in the age distribution. The three samples yield a mean exposure age of 16.3 ± 0.8 ka.

The two RP ice-moulded bedrock surfaces provide ages of 16.0 ± 0.7 ka and 16.5 ± 0.5 ka. The ages are well-clustered, with a MSWD value of 0.24 The mean exposure age for the two samples is 16.3 ± 0.3 ka.

Table 3.2. Exposure ages and summary statistics.

	Kaplan *et al.* (2011) production rate									
Sample ID	LSDn: *Lifton et al. (2014)*			St: *Lal (1991) and Stone (2000)*			Lm: *Lal (1991) and Stone (2000)*			
	Age	Internal	External	Age	Internal	External	Age	Internal	External	Outlier?
	Cal Yr BP			Cal Yr BP			Cal Yr BP			
RC III moraine boulders										
19RCS21	26075	877	2310	27149	914	2419	26157	880	2329	
19RCS23	26845	846	2357	27992	882	2473	26943	849	2378	
19RCS24	23907	709	2082	24721	733	2166	23932	710	2096	Yes
19RCS25	26981	810	2355	28138	845	2471	27081	813	2376	
19RCS27	25887	855	2287	26933	890	2393	25961	857	2305	
19RCS28	27365	873	2407	28553	911	2526	27468	876	2429	
Mean (n = 6): 26.18 ka; 1σ std: 1.24 ka										
Mean (n = 5): 26.63 ka; 1σ std: 0.63 ka; 1σ internal: 1.91 ka; 1σ internal + PR%: 2.90 ka										
Bayesian age model (n = 5): **26.43** ka; 1σ std: **1.39** ka; model correction: -0.7 %										
Uncertainty weighted mean (n = 5): 26.63 ka; 1σ std: 0.56 ka										
MSWD: 0.53 < *k* : 2.41 (n=5); Peak age (n=5): 26.70 ka										
RC IV moraine boulders										
19RCS13	30447	1029	2701	31800	1076	2838	30485	1031	2719	Yes
19RCS15	21074	610	1829	21434	621	1872	20942	606	1828	
19RCS16	21575	629	1874	22031	642	1925	21480	626	1876	
19RCS17	21525	727	1906	21970	742	1957	21426	724	1907	
19RCS51	22895	717	2007	23497	736	2072	22809	714	2010	
19RCS52	21254	626	1849	21662	638	1895	21148	623	1849	
Mean (n = 6): 23.13 ka; 1σ std: 3.64 ka										
Mean (n = 5): 21.66 ka; 1σ std: 0.72 ka; 1σ internal: 1.48 ka; 1σ internal + PR%: 2.31 ka										
Bayesian age model (n = 5): **22.41** ka; 1σ std: **1.15** ka; model correction: +3.5 %										
Uncertainty weighted mean (n = 5): 21.63 ka; 1σ std: 0.63 ka										
MSWD: 1.08 < *k* : 2.41 (n=5); Peak age (n=5): 21.37 ka										
RC V moraine boulders										
19RCS38	22650	981	2098	23142	1002	2155	22486	974	2092	
19RCS40	21936	641	1907	22349	653	1954	21767	636	1902	
19RCS41	21745	744	1929	22136	758	1975	21576	738	1924	
19RCS42	19803	562	1715	19956	566	1738	19586	556	1705	Yes
19RCS43	21747	680	1906	22143	693	1952	21582	675	1901	
19RCS44	23272	796	2065	23835	815	2127	23126	791	2063	
Mean (n = 6): 21.86 ka; 1σ std: 1.17 ka										
Mean (n = 5): 22.27 ka; 1σ std: 0.67 ka; 1σ internal: 1.74 ka; 1σ internal + PR%: 2.52 ka										
Bayesian age model (n = 5): **21.67** ka; 1σ std: **0.91** ka; model correction: -2.7 %										
Uncertainty weighted mean (n = 5): 22.22 ka; 1σ std: 0.59 ka										
MSWD: 0.76 < *k* : 2.41 (n=5); Peak age (n=5): 21.97 ka										

RC VI moraine boulders										
19RCS30	21060	704	1862	21280	711	1892	20804	695	1849	
19RCS31	19124	620	1683	19152	621	1695	18839	611	1666	
19RCS33	20151	667	1778	20287	671	1801	19891	658	1765	
19RCS34	21451	722	1898	21740	732	1935	21221	714	1888	
19RCS32	17825	591	1573	17753	588	1575	17526	581	1554	Yes
19RCS36	21462	728	1901	21750	738	1938	21231	720	1891	

Mean (n = 6): 20.18 ka; 1σ std: 1.46 ka
Mean (n = 5): 20.65 ka; 1σ std: 1.01 ka; 1σ internal: 1.54 ka; 1σ internal + PR%: 2.29 ka
Bayesian age model (n = 5): **20.75** ka; 1σ std: **1.05** ka; model correction: +0.5 %
Uncertainty weighted mean (n = 5): 20.59 ka; 1σ std: 0.92 ka
MSWD: 2.33 < *k* : 2.41 (n=5); Peak age (n=5): 21.18 ka

RC VII moraine boulders										
19RCS07	17532	547	1534	17382	542	1530	17177	535	1511	
19RCS08	20443	728	1824	20526	731	1842	20111	716	1804	
19RCS09	27654	743	2386	28454	765	2470	27412	737	2378	Yes
19RCS11	19015	623	1675	18971	621	1681	18668	611	1653	
19RCS12	23192	668	2013	23600	680	2061	22914	660	2000	Yes
RC20-29	23535	704	2052	23968	717	2102	23257	695	2038	Yes

Mean (n = 6): 21.90 ka; 1σ std: 3.66 ka
Mean (n = 3): 19.00 ka; 1σ std: 1.46 ka; 1σ internal: 1.10 ka; 1σ internal + PR%: 1.91 ka
Bayesian age model (n = 3): **19.88** ka; 1σ std: **1.07** ka; model correction: +4.6 %
Uncertainty weighted mean (n = 3): 18.86 ka; 1σ std: 1.18 ka
MSWD: 5.34 > *k* : 3.0 (n=3); Peak age (n=3): 19.19 ka

Río Huemul 795 m palaeo-shoreline surface cobbles										
19RHS02	18790	654	1670	18660	649	1668	18381	640	1642	
19RHS03	19355	623	1701	19268	620	1703	18949	610	1674	
19RHS04	19834	672	1757	19791	671	1762	19435	659	1730	

Mean (n = 3): 19.33 ka; 1σ std: 0.52 ka; 1σ internal: 1.13 ka; 1σ internal + PR%: 1.94 ka
Bayesian age model (n = 3): **18.99** ka; 1σ std: **0.95** ka; model correction: -1.8 %
Uncertainty weighted mean (n = 3): 19.32 ka; 1σ std: 0.42 ka
MSWD: 0.62 < *k* : 3.0 (n=3); Peak age (n=3): 19.34 ka

Río Corcovado 680 m palaeo-shoreline surface cobbles									
19RCS05	16917	650	1528	16576	637	1505	16407	630	1489
19RCS04	16640	510	1453	16291	499	1430	16142	494	1416
19RCS03	15416	496	1354	15009	483	1326	14930	481	1318
Mean (n = 3): **16.32** ka; 1σ std: **0.80** ka; 1σ internal: 0.96 ka; 1σ internal + PR%: 1.65 ka									
Uncertainty weighted mean (n = 3): 16.27 ka; 1σ std: 0.66 ka									
MSWD: 2.24 < *k* : 3.0 (n=3); Peak age: 16.69 ka									
Río Palena valley surface bedrock samples (Atlantic/Pacific drainage reversal)									
19RPS01	16023	751	1510	15473	725	1465	15328	718	1450
19RPS02	16474	543	1452	15925	525	1411	15749	519	1395
Mean (n = 2): **16.25** ka; 1σ std: **0.32** ka; 1σ internal: 0.93 ka; 1σ internal + PR%: 1.62 ka									
Uncertainty weighted mean (n = 2): 16.28 ka; 1σ std: 0.22 ka									
MSWD: 0.24 < *k* : 3.83 (n=2); Peak age (n=2): 16.36 ka									

Table footnotes:

Ages were calculated using the online calculator formerly known as the CRONUS-Earth online calculator version 3 (Balco *et al*., 2008) with the Patagonian production rate (Kaplan *et al*., 2011) obtained from the ICE-D online database (http://calibration.ice-d.org/). Scaling schemes: St-time-independent version of Lal (1991) and Stone (2000), Lm is the time dependent version of Lal (1991) and Stone (2000), and LSDn-time-dependent scheme of Lifton *et al*. (2014). In the text, we report ages calculated using the LSDn scaling scheme within internal uncertainties. Ages are reported with 1σ internal and external uncertainties, the latter including production rate and scaling uncertainties. These ages assume zero erosion and no correction for shielding by snow, soil and/or vegetation. Elevation flag is std. Summary statistics were calculated for each dated landform. This includes arithmetic means with 1σ standard deviations (std), 1σ propagated (from individual ages) internal uncertainties, and propagated 1σ internal plus production rate uncertainty (PR%). It also includes uncertainty weighted mean and 1σ standard deviation, MSWD and Peak age statistics; calculated using equations described in the iceTEA tools for exposure ages online calculator (Jones *et al*., 2019). For the RC III – RC VII moraines and the RH_{790} palaeo-shoreline, summary statistics also display Bayesian age model outputs, which include arithmetic means, 1σ standard deviations, and model correction percentages relative to original landforms arithmetic means. Ages in bold represent the ones used throughout the paper for discussion.

3.4.2.2 Bayesian age modelling results

Bayesian age model probability distributions were produced for the RCIII-RCVII moraine and the RH_{790} palaeo-shoreline age populations to resolve age-inconsistencies when compared to the relative order of events based on our geomorphological interpretations. For instance, the RC IV moraine is ~1.1 km further from the ice source than the RC V moraine and thus is morphostratigraphically older (Figs. 3.2, 3.6a), yet the exposure ages from both moraines exhibit overlapping age distributions and reversed mean ages (*i.e.*, RC V is older than RC IV). This suggests the two moraine ages are indistinguishable within analytical dating uncertainties. Moreover, our morphostratigraphic interpretation suggests the RC VII advance/stillstand should be older than the proglacial lake abandonment of the RH_{790} palaeo-shoreline (proglacial lake phase 2/3 transition). Mean exposure ages indicate the opposite (RH_{790} ~0.3 ka older than RC VII); a mismatch that we attribute to analytical surface exposure dating uncertainties and the significant scatter in RC VII moraine boulder ages. Consequently, Bayesian age modelling was employed to produce more realistic age probability distributions that follow the relative order of events based on our geomorphological reconstruction. Discussions regarding the age of the RC_{680} palaeo-shoreline and the ice-moulded bedrock samples (19RPS01-02), however, are based on the arithmetic mean and 1σ analytical uncertainty associated with the original exposure ages, as they did not display any age-inconsistencies in the relative order of events, and because including them in the Bayesian age model would add a mathematical bias resulting in slightly older, less-realistic mean ages relative to original exposure ages. Therefore, exposure ages from these two landforms were not included in the Bayesian age model.

The Bayesian age model probability distributions resulted in mean output ages of 26.4 ± 1.4 ka (-0.7% correction), 22.4 ± 1.15 ka (+3.5% correction), 21.7 ± 0.9 ka. (-2.7% correction), 20.7 ± 1.0 ka (+0.5% correction), 19.9 ± 1.1 ka (+4.6% correction) and 19.0 ± 0.9 ka (-1.8% correction) for the RC III, IV, V, VI, VII and RH_{790} landforms, respectively (Table 3.2, Fig. 3.8).

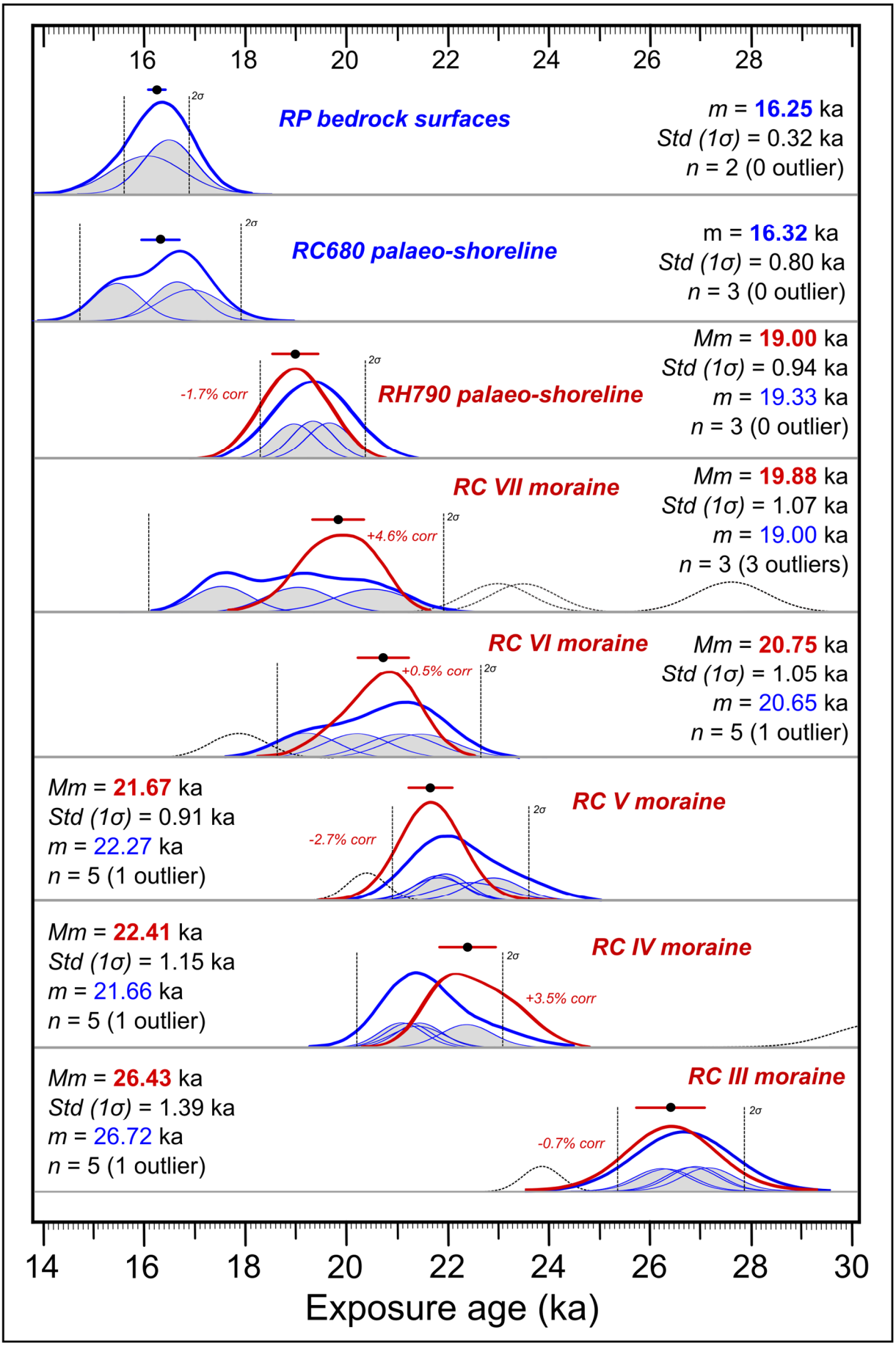
16
18
20
22
24
26
28
RP bedrock surfaces
2σ
m = 16.25 ka
Std (1σ) = 0.32 ka
n = 2 (0 outlier)
RC680 palaeo-shoreline
m = 16.32 ka
Std (1σ) = 0.80 ka
n = 3 (0 outlier)
-1.7% corr
RH790 palaeo-shoreline
Mm = 19.00 ka
Std (1σ) = 0.94 ka
m = 19.33 ka
n = 3 (0 outlier)
RC VII moraine
+4.6% corr
Mm = 19.88 ka
Std (1σ) = 1.07 ka
m = 19.00 ka
n = 3 (3 outliers)
RC VI moraine
+0.5% corr
Mm = 20.75 ka
Std (1σ) = 1.05 ka
m = 20.65 ka
n = 5 (1 outlier)
Mm = 21.67 ka
Std (1σ) = 0.91 ka
m = 22.27 ka
n = 5 (1 outlier)
-2.7% corr
RC V moraine
Mm = 22.41 ka
Std (1σ) = 1.15 ka
m = 21.66 ka
n = 5 (1 outlier)
+3.5% corr
RC IV moraine
Mm = 26.43 ka
Std (1σ) = 1.39 ka
m = 26.72 ka
n = 5 (1 outlier)
-0.7% corr
RC III moraine
14
16
18
20
22
24
26
28
30
Exposure age (ka)

Figure 3.8. Probability density diagrams for each of the landforms dated with TCN dating. Thick blue curves represent the summed probability distribution for each sampled landform, excluding outliers. Thin blue curves depict the 1 σ Gaussian curves for individual exposure ages. Black dotted curves represent outliers. Thick red curves illustrate the summed probability distribution after Bayesian age model correction (RC III – RH_{790} only). Black dots describe the arithmetic means (excluding outliers) while red/blue horizontal error bars indicate the standard deviation of the exposure ages. Vertical, black dotted lines denote the 2 σ confidence interval associated with exposure-age populations prior to Bayesian age model corrections. *Mm* stands for "Modelled mean" and indicates the Bayesian age model arithmetic mean, while *m* stands for "mean" and displays the arithmetic mean prior to Bayesian age model correction. *Std* stands for "standard deviation".

3.5 Discussion

3.5.1 Style of glaciation

Our geomorphological and sedimentological analyses of the sampled LGM RC moraines highlight relatively steep moraine slopes, sharp ridges, and exceptional ridge continuity throughout the field site (Figs. 3.2, 3.7). The continuity of moraine ridges suggests progressive ice recession without re-advances that could partially dismantle or over-print older moraines, in part due to the westward-dipping nature of bed topography, which might play a role in preventing moraine over-printing and glaciofluvial erosion of older moraines. The sampled ridges (~10-15 m in mean height) are part of relatively wide moraine complexes composed of numerous smaller ridges, interspersed by narrow, confined glaciofluvial deposits (Leger *et al*., 2020; Figs. 3.2, 3.7). Such characteristics are indicative of significant sediment volume delivery to the ablation zone during LGM advances/stillstands of the RC glacier. Along with widespread geomorphological evidence of efficient subglacial erosion through mapping of lineations and ice-moulded bedrock surfaces (*ibid*), the evidence indicates the RC outlet glacier was highly erosive and warm-based in nature.

3.5.2 Chronological and geomorphological results interpretation

Our results indicate at least five (RC III-VII) distinct advances/stillstands of the RC glacier during the LGM. Bayesian age modelling of boulder exposure ages suggests that the RC III-VII moraines were deposited over a 6-7 ka period, with major advances/stillstands occurring at 26.4 ± 1.4 ka, 22.4 ± 1.15 ka, 21.7 ± 0.9 ka, 20.7 ± 1.0 ka and 19.9 ± 1.1 ka (Fig. 3.8). Our ^{10}Be chronology therefore suggests that all dated RC moraines were formed during the global LGM (*ca*. 26.5-19 ka; Clark *et al*., 2009), and that maximum local LGM ice-extent was reached at ~26.5 ka. We argue that the RC glacier remained close (within 15 km) to its outermost LGM extent until 19.5-20 ka. The

timing of these advances/stillstands is in good agreement with LGM records from other Patagonian regions (*e.g.* Denton *et al*., 1999; Kaplan *et al*., 2004; Hein *et al*., 2010; Boex *et al*., 2013; Moreno *et al*., 2015; Stern *et al*., 2015; Smedley *et al*., 2016; Garcia *et al*., 2019). Our analysis also revealed three phases of proglacial lake formation. Exposure ages from the RH_{790} palaeo-shoreline surface cobbles, interpreted as representing the timing of shoreline abandonment and phase two proglacial lake-level drop (19.0 ± 0.9 ka; Table 3.2, Fig. 3.8), enable us to constrain the onset of local deglaciation and understand former glaciolacustrine drainage shifts. Finally, exposure ages from the RP valley ice-moulded bedrock surfaces (16.3 ± 0.3 ka) provide geochronological insights into the timing of local PIS disintegration and Atlantic/Pacific drainage reversal, coeval with the age of glaciolacustrine phase three shoreline-abandonment (16.3 ± 0.8 ka). In this section, and with reference to the schematic Figure 3.9, we present our interpretation of local LGM and deglacial events supported by the geomorphological and geochronological evidence.

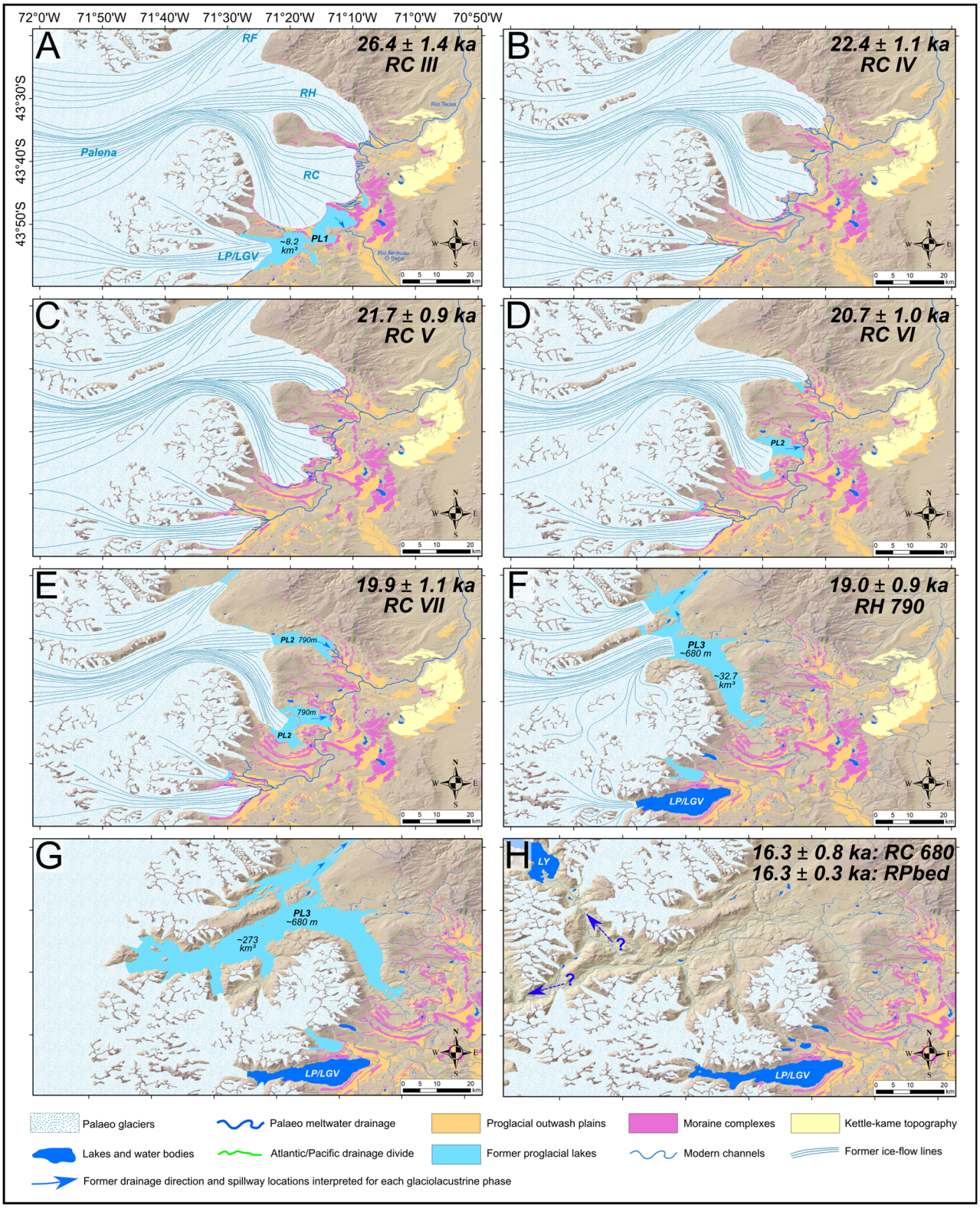

Figure 3.9. Palaeoglacial and palaeolake reconstructions for the RC, RH, RF and Lago Palena/General Vintter valleys, for each LGM advances/stillstands and deglacial events interpreted in this investigation. Ice-sheet and mountain glacier models were digitised manually in ArcGIS. Apart from when delineated by confidently mapped moraine limits (*e.g.* the RC, RH and LP/LGV LGM moraine sequences), the position of ice margins are inferred. (**A-E**) Ice extents associated with the RC III to RC VII moraine complexes. This includes the formation of glaciolacustrine phase one and two (here termed PL1 and PL2, respectively). There are no previously published chronologies in the RH, RF and LP/LGV valleys. The relative ice extent in those

neighbouring valleys is thus inferred based on our RC chronology and cross-valley comparisons of moraine numbers, preservation and morphostratigraphy. Hence, these inferences yield some uncertainties. (**F**) Reconstruction of the opening of the RF valley scenario and the subsequent RC proglacial lake lowering to 680 m (dated with surface cobbles from the RH_{790} shoreline), marking the onset of glaciolacsutrine phase 3 (here denoted: PL3), according to our geomorphic interpretation. (**G**) Reconstruction of the westward retreat of the RP outlet glacier towards the core of the Andes and the associated expansion of the 680 m proglacial lake. (**H**) Reconstruction of the onset of PIS disintegration, enabling ice-dam collapse and the Pacific-directed, final drainage of the 680 m proglacial lake (PL3). Proglacial lake volume estimates were computed from DEM data (AW3D30). Panel H question marks relate to the uncertainty regarding the former drainage pathway(s) employed during the local Atlantic/Pacific drainage reversal event. Location of ice fronts for panels F-H are hypothetical as not correlated to specific geomorphic limits, but are aimed at representing specific events/scenarios.

3.5.2.1 The local LGM (RC III) and proglacial lake phase one (Figure 3.9a)

We interpret the RC III moraine, dated to 26.4 ± 1.4 ka, as representing the maximum extent of the local LGM for the RC outlet glacier. Our geomorphological reconstruction suggests this advance coincided with the formation of the first proglacial lake, located in the RC southern sub-basin (Fig. 3.9a). The geomorphology suggests the lake was dammed in the northwest by the RC glacier ice-front when positioned at the RC III moraine, in the south and east by the older RC II moraine complex, and in the southwest by the Lago Palena/General Vintter ice-front. This relatively small proglacial lake (Figure 9a), was fed by meltwater from both the RC and Lago Palena/General Vintter outlet glaciers into a 100 m deep basin, now host to the modern Río Corcovado and its floodplain (Fig. 3.2). Preserved palaeo-shorelines indicate a maximum former lake elevation of 990 ± 5 m and a main spillway (43°50'59"S, 71°11'13"W) suggestive of southeast-directed drainage towards the contemporary Ñirihuau O Seco river. Using a DEM we estimate a maximum lake area of 139 km^2 and volume of 8.2 km^3 (Fig. 3.9a).

The RC III advance is coeval with a glacial expansion event documented on the western side of the Patagonian Andes at similar latitudes to this study (Isla de Chiloé; 42-43°S; García *et al*., 2012), and more recently dated to 26.0 ± 2.9 ka through OSL dating (García *et al*., 2021). Moreover, several advances at about 26 ka have been reported across the entire latitudinal extent of the former PIS (Chapter 3 Supplementary Figure 2). For instance, moraine and glaciofluvial outwash deposits dating to 28-26 ka were discovered for the Bahía Inútil-San Sebastían glacier (53-54°S: Río Cullen drift: Kaplan *et al*., 2007; 2008; Darvill et al., 2015), the Magellan glacier (52°S: Primera Angostura and B limits: Kaplan *et al*., 2007; 2008), the Lago Cochrane/Pueyrredón glacier (47.5°S: Río Blanco I moraine: Hein *et al*., 2010), the Lago General Carrera/Buenos Aires glacier (46.5°S: Fenix IV, V moraines: Kaplan *et al*., 2004; Douglass *et al*., 2006), and for several outlet glaciers of the Chilean

Lake District (Denton *et al*., 1999; Moreno *et al*., 2015). Moreover, numerous synchronous glacial advances were also recorded in the New Zealand Southern Alps at around 26.5 ka (the *Otira 5* advance: Shulmeister *et al*., 2019). Such synchronous glacial response implies that potent cooling and/or increased precipitation occurred at 28-26 ka throughout Patagonia and across the southern mid-latitudes.

Several other Patagonian and southern hemisphere investigations reconstructing detailed glacier geochronologies have reported maximum ice extents of the last glacial cycle occurring before the global LGM, during MIS 3 (*e.g.* Denton *et al*., 1999; Darvill *et al*., 2015; Moreno *et al*., 2015; García *et al*., 2018; 2021), MIS 4 (Schaefer *et al*., 2015; De Deckker *et al*., 2019; Hall *et al*., 2020; Peltier *et al*., 2021; García *et al*., 2021), and even MIS 5 (Mendelová *et al*., 2020). Evidence of MIS 3 glacial activity was detected as far north as the Chilean Lake District (40°S; Denton *et al*., 1999), where outlet glaciers reached a similar extent at ~33 ka to that during the global LGM (MIS 2). Furthermore, a new study from Isla de Chiloé (42-43°S; García *et al*., 2021), located on the western side of the Andes at an equivalent latitude to our study site, suggest that local maximum glaciation occurred earlier in the last glacial cycle, at 57.8 ± 4.7 ka, and this advance was approximately 4 km more extensive than the local MIS 2 advance. In southern Patagonia, these early advances were far more extensive than during the global LGM, in some cases (Torres del Paine glacier: 51°S, Última Esperanza glacier: 51.4°S, and the Bahía Inútil–San Sebastián glacier: 53.5°S) extending twice as far as during MIS 2 (García *et al*., 2018; Darvill *et al*., 2015). The MIS 3 local maximum appears to fade out toward central Patagonia where there is evidence for MIS 3 glacial activity of similar magnitude to the global LGM at Lago Pueyrredón (47.5°S; Hein *et al*., 2010) and Lago Buenos Aires (46.5°S; Smedley *et al*., 2016). In northeastern Patagonia, however, our new TCN reconstruction reveals the first assessment of the local maximum glaciation on both sides of the former ice sheet. In contrast to the west, we find the local maximum glaciation on the eastern side occurred during the global LGM. This suggests that any MIS 3 glacial activity in the RC valley was comparatively restricted and subsequently overridden by the RC III advance (MIS 2: 26.0 ± 2.9 ka). Hence, in addition to supporting a latitudinal disparity across Patagonia, our results also suggest a West/East disparity in the relative magnitude and extent of PIS expansions during MIS 3. The precise mechanisms causing such zonal disparity remain unknown and represent an area of future research. However, one could hypothesise that the PIS was potentially less sensitive to relatively short-lived, millennial-scale stadials characteristic of MIS 3 in its central eastern and northeastern sector, due to locally-specific conditions of upward-sloping valley floors, a strong rain-shadow effect causing lower moisture availability and the widespread occurrence of large proglacial lakes amongst other environmental factors (García *et al*., 2021). Combined, these factors may delay ice build-up in northeastern and

central eastern Patagonia, a region where PIS outlet glaciers may require more stable and long-lived stadials to advance up reversed slopes.

3.5.2.2 The RC IV-RC VII advances and proglacial lake phase two (Figure 3.9b-e)

Bayesian age modelling of RC moraine boulder exposure ages indicates that the second oldest LGM advance occurred at 22.4 ± 1.15 ka (RC IV moraine, Fig. 3.9b). Our chronology displays a ~4 ka period between age model outputs from the RC III and RC IV sampled ridges during which time the stability and location of the RC glacier front is unknown. Indeed, the RC III moraine boulders were sampled on the outermost of five distinct, more subtle moraine ridges within this complex (Leger *et al*., 2020; Fig. 3.2). These smaller ridges are indicative of periods of ice-front stability following the deposition of the RC III moraine. Further dating on these ridges could resolve whether the ice margin terminated within this intermediate zone at this time, or whether it is more likely the glacier retreated within the basin and then readvanced to deposit the RC IV moraine. Within either scenario, topographic analyses and detailed mapping of meltwater channels and glaciofluvial deposits suggest that subsequent retreat of the RC glacier from its RC III margin caused a complex re-arrangement of local meltwater drainage pathways. By opening a lower, northeast-directed drainage pathway, meltwater from the Lago Palena/General Vintter glacier and the RC southern sub-basin shifted from draining southward towards Río Ñirihuau O Seco (and Río Senguer) to a network of channels flowing northeastwards towards Río Tecka (and Río Chubut). We suggest this event also led to the end of proglacial lake phase one (Fig. 3.9a,b). In both cases, meltwater drained eastward into the Atlantic but via different routes (Martínez *et al*., 2011).

The RC V moraine (modelled age: 21.7 ± 0.9 ka, Fig. 3.9c) was deposited close to the RC IV moraine, just 0.9 km inboard at the location of sampling, compared with a separation of 2.25 km between RC III and IV. Despite this proximity, we consider the RC IV and V moraine complexes to represent distinct deposits because they are interspersed by a narrow yet distinct glaciofluvial outwash plain near their terminal environment (Leger *et al*., 2020; Fig. 3.2). However, exposure ages from the two moraines overlap and display means that are reversed with their relative stratigraphic age. In other words, the mean age of the two moraines are indistinguishable within analytical uncertainties. The geographical and chronological proximity of these two moraines and the significant sediment volume they represent suggests a relatively long period of ice-front stability for the RC glacier at around 22 ka (Fig. 3.9b, c).

The RC VI moraine (modelled age: 20.7 ± 1.0 ka) was deposited ~2 km further inboard, ~50 m lower in elevation (at location of sampling) and approximately 1 ka after the RC V moraine (Figs 3.7, 3.8, 9d). Our RC VI samples come from the most prominent ridge of a 1.5 km-wide moraine complex featuring a minimum of four older and five younger distinct moraine ridges (Leger *et al*., 2020; Fig. 3.2), thus suggestive of another prolonged period of ice-front stability at around 21 ka.

Geomorphological mapping of palaeo-shorelines indicates that the western retreat of the RC ice-front from the RC V moraine complex initiated the formation of a second proglacial lake phase (surface elevation: 790 m) in the RC northern sub-basin (Fig. 3.9d). Indeed, remote sensing and field observations revealed the relatively widespread occurrence of palaeo-shorelines nested at the elevation of ~790-800 m in both the RC and RH valleys (Leger *et al*., 2020, main map). In the RC valley, the palaeo-shorelines can be discerned across the northern sub-basin, notched on the ice-proximal slopes of the RC V moraine complex (Supplementary materials). We propose a lake formation age, bracketed by the modelled RC V and RC VI formation ages, of between 20.7 ± 1.0 ka and 21.7 ± 0.9 ka. Ages from the RH_{790} shoreline were interpreted as indicating shoreline abandonment and thus lake-level drop from ~790 m to ~680 m associated with the transition from glaciolacustrine phase two to phase three. Based on a mean modelled age of 19.0 ± 0.9 ka for the RH_{790} palaeo-shoreline (Fig. 3.8), we suggest a total residence time for the proglacial lake at ~790 m of 1.5 to 2.5 ka. During this time, we argue that this proglacial lake enabled meltwater runoff from the LP/LGV, RC and RH glaciers to drain towards the Atlantic via Río Tecka. We suggest the 790 m proglacial lake's main spillway occurred at 43°42'S, 71°13'W, where the prominent shoreline bends eastwards into a 200 m-wide gorge breaching the RC V and RC IV moraine complexes.

Approximately 10 km to the northwest, in the more topographically constrained RC trough, isolated remnants of the 790 m palaeo-shoreline can be discerned on the eastern hillslope (Fig. 3.4a), while evidence of this shoreline disappears north of 43°37'S. This indicates that the 790 m proglacial lake expanded and persisted during the early stages of local deglaciation, when the RC calving front progressively retreated northward. This is supported by the finding of fine, sand to clay-sized sediment deposits exposed through sections of the valley's main road (RP44), at elevations of 686 m (43°42'7.2"S), 709 m (43°42'15.2"S) and 720 m (43°42'11.7"S). These exposures exhibit laminations and varves, represent the topmost unit below soil, and were interpreted as glaciolacustrine deposits. OSL samples from the exposures of rippled sands and varves at 709 m and 686 m yielded burial ages of 34.9 ± 2.9 ka and 52.1 ± 4.4 ka, respectively (Supplementary materials). We consider these ages to be older than the deposition of these sediments, despite the use of single grains to overcome the effects of incomplete bleaching. OSL dating determines the time elapsed since mineral

grains were last exposed to sunlight. For these sediment-laden, turbulent glaciolacustrine sediments deposited near ice fronts where the opportunity for exposure to sunlight is minimal, the last sunlight exposure may relate to a former depositional cycle, and so caused OSL age-overestimation in this context (Wallinga, 2002; Alexanderson & Murray, 2012; Johnsen *et al*., 2012).

In the RH valley, field mapping revealed a prominent flat bench running over several km on the southern valley slopes, perched at an elevation of ~790 m, and notched on the ice-proximal side of the innermost preserved RH terminal moraine (Figs. 3.6b, 3.4 c,d). This landform was interpreted as a palaeo-shoreline and was sampled for TCN dating using three polished granite surface cobbles. It indicates the formation of a separate, isolated proglacial lake in the RH valley, formed as the RH glacier retreated westward. The comparable elevation of shorelines in both RC and RH valleys suggests that the two proglacial lakes could have been connected following northward/westward retreat of both ice fronts beyond Corcovado (43°32'S, 71°27'W), and thus arguably experienced final lowering and shoreline abandonment synchronously. The main spillway draining the RH palaeolake towards the Atlantic occurs at 43°31'42"S, 71°13'26"W, where a central, 130 m-wide breach through the innermost RH moraine complex displays a basal elevation of 780 m (Fig. 3.6b).

After depositing the RC VI moraine, the RC glacier experienced another period of retreat prior to stabilising or re-advancing around 19.9 ± 1.1 ka, thus causing the formation of the innermost preserved LGM moraine (RC VII, Fig. 3.9e), which is located 3.5 km inboard and ~70 m lower than the RC VI moraine at the location of sampling (Figs. 3.2, 3.7). The sampled RC VII moraine crest is only 20-30 m above the 790 m shoreline level, and geomorphological mapping indicates no preserved matching ridges further east towards the former RC frontal-terminal environment, suggesting that while the RC glacier front was grounded above water level at its western lateral margin, it may have been calving at its frontal margin toward the centre of the RC basin.

Our ages from the RC VI and RC VII moraines coincide with a fairly widespread glacial expansion event that occurred in numerous other Patagonian valleys at around 20-21 ka. Indeed, this expansion event was for instance recorded in the Strait of Magellan (52°S; outermost C limit, Kaplan *et al*., 2007; 2008), the Torres del Paine valley (51°S: TDP I moraine; García *et al*., 2018), the Lago General Carrera/Buenos Aires valley (46.5°S: Fenix I moraine, Kaplan *et al*., 2004; Douglass *et al*., 2006), and the Río Cisnes valley (44°S: CIS IV: García *et al*., 2019). A coeval event, locally named the *Otira 6* advance, was also found to occur in several New Zealand Southern-Alps valleys, with a reported mean age of ~20.5 ka (*e.g.* Shulmeister *et al*., 2019).

3.5.2.3 The onset of local deglaciation and proglacial lake phase three (Figure 3.9f)

Bayesian age modelling suggests a mean age of 19.9 ± 1.1 ka for the RC VII advance/stillstand. As we did not find evidence for younger moraine deposits related to the RC glacier, we interpret this result as a maximum-limiting age for the onset of local deglaciation. However, our confidence in moraine-age interpretation is lower for RC VII than for other RC moraines due to its significantly higher degree of boulder exposure-age scatter (MSWD: 5.34, n = 3) and high number of proposed outliers (n=3) (Table 3.2, Fig. 3.8), suggestive of substantial inheritance and/or post-depositional disturbance signals. The ridge is similar to the RC III-VI moraines in orientation (at the location of sampling: northwest-southeast), vertical relief, width-to-height ratio (7.4), slope gradients (Ice-P: 17° and Ice-D: 14°), and surface clast lithologies and shape (GR% = 56; C_{40}: 13.3, block-dominated) (Fig. 3.7). These geomorphological and sedimentological similarities support our interpretation of the ridge as a moraine formed by the RC glacier. However, the RC VII moraine is distinctively less sharp-crested, and exhibits a flatter, wider and more subdued crest surface with little variation in crest-line elevation (Fig. 3.7). Contrary to the RC III-VI moraines, the RC VII moraine is not part of a complex displaying numerous superimposed recessional ridges, and only exhibits one, prominent but relatively subdued ridge. Surface clast analysis (Fig. 3.7) also reveals a higher proportion of angular-to-very-angular clasts than for other moraines (RA: 36.7). Given these geomorphological differences, one might argue that the RC VII moraine was either former under different conditions, or experienced more post-depositional disturbance.

One possible disturbance mechanism is the presence of a proglacial lake at ~790 m in the RC valley between ~21 and ~19 ka. Indeed, glacier-front recession from the grounded RC VII margin would likely have resulted in waves pounding the RC VII moraine. This is supported by DEM cross-moraine elevation profiles (n = 7) drawn along the preserved moraine ridge, which display a notched platform, here interpreted as a palaeo-shoreline, on the ice-proximal moraine slope at the approximate elevation of 785-795 m (Fig. 3.7, red arrow). Wave pounding of the ice-proximal moraine slope may have destabilised the 20-30 m protruding moraine crest, causing lateral creep, and generating crest-surface lowering and flattening. Such disturbance may have caused subsequent moraine-boulder rotation and/or exhumation and enhance the potential for under-estimating exposure ages.

However, our chronological and stratigraphical interpretation suggests that outliers (n = 3) from the RC VII exposure-age population seem to be over-estimating ages suggestive of inheritance signals (Fig. 3.8). A more realistic potential source of age-scatter could be the contamination of the RC VII moraine by older, more ice-distal LGM deposits. Indeed, unsorted and unconsolidated lateral till

deposits mantling steep valley slopes could fall as supraglacial debris onto glacier surfaces following ice-thinning from outermost LGM margins. This hypothesis would support the observed negative correlation between LGM moraine age and boulder age-scatter, but also the slightly higher angularity of RC VII surface clasts (Fig. 3.7).

The RC valley displays a second, easily discernible bench cutting through the entire north-to-south extent (over 15 km) of the eastern hillside (slope16-19°) at an elevation of ~680 m (Figs. 3.4a, 3.6c). We interpreted this as a wave-cut proglacial lake shoreline, and it was sampled for TCN dating using polished granite surface cobbles (Table 3.2; Fig. 3.6c). Twenty-seven cross-section elevation profiles were drawn across the platform from DEM in locations exhibiting a preserved terrace. They revealed a mean maximum shoreline excavation of ~6 m. This shoreline roughly matches (within ~10 m) the elevations of numerous other shorelines, raised deltas and raised outwash deposits located in the RC, RH, RF and RP valleys (Supplementary materials). Such geomorphic evidence indicates the formation of a third proglacial lake phase, diagnosed by a geographically widespread proglacial lake eventually connecting all valleys of the studied region. This is further evidenced by field observations of uppermost (below soil) units of fine, sand to clay-sized and occasionally laminated, varved sediments exposed at numerous road-cut sections across the RC, RP and RF valley floors (Supplementary materials). We sampled one of these road-cut exposures located near the RC valley floor, at an elevation of 544 m (43°41'50,3"S, 71°24'22,4"W), and composed of laminated and varved clay-to-silt sized sediments, for OSL dating. The sample yielded a burial age of 65.4 ± 7.1 ka. Following the same reasoning described above (5.2.2), we consider this age to be significantly older than the deposition of these sediments.

The third glaciolacustrine phase is inferred to have started with the abandonment of the RH_{790} shoreline at 19.0 ± 0.9 ka (Table 3.2, Fig. 3.8), when the lake-level dropped from ~790 m to ~680 m (Fig. 3.9f). We suggest that this ~100 m lake lowering reflects the continued retreat of the RC, RH and RF ice-fronts into the RP valley. We hypothesise that once the ice front retreated westward beyond Corcovado (Fig. 3.9f), such retreat enabled northward drainage of the palaeolake through the RF valley, which also contains preserved palaeo-shorelines and raised deltas at ~680 m (Chapter 3 Supplementary materials). However, the lowest potential spillway towards the northeast today lies at approximately 750 m, about 70 m higher than the palaeolake elevation. We hypothesise that this drainage elevation mismatch can be attributed to the post-glacial accretion of a large (~5 km^2) arcuate alluvial fan into a narrow col located between the RF and Lago Rosario basins (43°17'S; 71°24'W; see supplementary materials). The RF spillway would enable waters to drain towards contemporary Lago Rosario. We thus propose, during glaciolacustrine phase three, a complex network of connected

palaeolakes enabling meltwater drainage from the former RC, RH and RF-connected lake (~680 m) into the current Lago Rosario (665 m), and into a former proglacial lake occupying the Trevelin basin to the north (~650 m; Andrada de Palomera, 2002; Martínez *et al*., 2011), which eventually spilled eastward towards Río Tecka and the Atlantic Ocean (proposed spillway: 43°05'57"S, 71°02'48"W).

Overall, if assuming the former ice-sheet divide was located near Macizo Nevado (Fig. 3.1c), our reconstruction thus suggests that by ~19 ka, the RC glacier had experienced ~30 km of retreat from its innermost RC VII margin, representing a ~40 km retreat and ~40% glacier-length loss relative to its full local LGM extent (RC III). We thereby interpret the age of 19.0 ± 0.9 ka as a minimum-limiting age for the onset of significant local deglaciation.

For several other glaciated regions of Patagonia, a predominant late-LGM event of PIS expansion and/or stabilisation was reported at around 17-18 ka, towards the onset of Heinrich Stadial 1 (Hemming, 2004). Glacier advance/stillstands around this time were reported, for instance, for the Magellan outlet glacier (innermost C limit, Kaplan *et al*., 2007; 2008), the Río Guanaco glacier (49°S: La Sofia and San Jorge moraines: Murray *et al*., 2012), the Lago Belgrano glacier (47°S: Menelik innermost moraine: Mendelová *et al*., 2020a) and several glaciers of the Chilean lake district (Moreno *et al*., 2015) (Supplementary materials). Such event coincides furthermore with the widespread *Otira 7* signal of glacial advance in New Zealand (Shulmeister *et al*., 2019). However, our chronological reconstruction shows no evidence of advances/stillstands of the RC glacier younger than 19.9 ± 1.1 ka. A similar lack of late-LGM PIS expansion signal was reported for the Río Cisnes outlet glacier 90 km to the south of our field site (García *et al*., 2019). The available evidence thus argues deglaciation of main PIS outlets initiated somewhat earlier in northeastern Patagonia, as any possible readvance of the RC glacier during the late-LGM was not recorded in the geomorpholgocial record. This is further supported by new glacial geochronological TCN dating results suggesting that subsequent glacier advances/still-stands in the region were restricted to local mountain glaciers (Leger *et al*., *2021b*).

3.5.2.4 The timing of ice-sheet disintegration and Atlantic/Pacific drainage reversal (Figure 3.9G,H)

Our TCN dating of ice-moulded bedrock surfaces from the RP valley (Fig. 3.5) suggests that by 16.3 ± 0.3 ka, the Palena ice-stream had retreated at least towards the foothills of Macizo Nevado (Figs 3.1, 3.9g,h), west of 72°W, facilitating final drainage of the ice-dammed ~680 m proglacial lake beneath or between shrinking mountain ice caps. The opening of a westward drainage route represents an Atlantic to Pacific drainage reversal (Fig. 3.9h) and a 70 km shift in the drainage divide, which is common to other over-deepened eastern Patagonian valleys (Glasser *et al.*, 2016; Thorndycraft *et al.*, 2019). Since the bedrock surfaces sampled are elevated at 343 m and 254 m a.s.l, the >340 m deep-water overburden during proglacial lake phase three would have been sufficient to reduce ^{10}Be muonogenic and spallation production by >99.9%. We thus argue that the mean exposure age of 16.3 ± 0.3 ka is representative of the approximate timing of local Atlantic/Pacific drainage reversal, and marks the end of glaciolacustrine phase three. We thereby propose that the extensive ~680 m proglacial lake existed for 2.5 to 3 ka, between ~19 ka and ~16 ka. The former maximum lake area and volume may have been as much as ~950 km^2 and ~273 km^3 for this third phase, although these estimates yield significant uncertainties as they were computed (from DEM) using a hypothetical ice-dam location near the foothills of Macizo Nevado (Fig. 3.9g). The timing of lake drainage is further evidenced by the age proximity of the three surface cobbles sampled from the RC_{680} palaeo-shoreline, which suggest a mean exposure age of 16.3 ± 0.8 ka, here interpreted as the onset of the ~680 m proglacial lake drainage and lowering. Our present reconstruction does not allow us to distinguish whether the final Pacific-directed drainage was a progressive or relatively sudden event, nor whether drainage was directed towards Lago Yelcho (Northwest), or Río Palena (Southwest). To resolve this will require further geomorphological investigations.

The PIS recession associated with ice-sheet disintegration and Atlantic/Pacific drainage reversal represents ~70 km of total ice-front retreat from innermost LGM position associated with the RC VII moraine (Fig. 3.9). These results suggest an approximate mean retreat rate of 14 m yr^{-1} between 19.9 ± 1.1 ka and 16.3 ± 0.3 ka (1σ range: 9-36 m yr^{-1}). Such rates are comparable to deglacial retreat rates proposed for other eastern PIS outlet glaciers (*e.g.*, Bendle *et al.*, 2017a: 15.4-18.0 m yr^{-1}). We thus argue that by ~16-16.5 ka, the northeastern PIS (43°S) started disintegrating into separate ice caps and mountain glaciers constrained to higher topography (Fig. 3.9h).

3.5.3 Palaeoclimate

3.5.3.1 The timing of local LGM expansions

Our geomorphological and geochronological reconstruction suggests that the timing of PIS LGM expansion in northeastern Patagonia is broadly coeval with the expansion of northern hemispheric ice sheets, a minimum in northern hemispheric atmospheric temperatures (*e.g.*, NGRIP members, 2004) and a minimum in summer insolation intensity at 60° N (Berger & Loutre, 1991). On the other hand, southern hemispheric summer insolation intensity at 44° S was increasing during the global LGM, reaching a maximum at ~21.5 ka, and was thus out of phase with local glacier expansion (Berger & Loutre, 1991; Doughty *et al*., 2015; Fig. 3.10). The timing of the RC LGM advances/stillstands is however synchronous with a decrease in southern winter insolation intensity at 40° S, which reached a minimum at ~19.5 ka, causing increased seasonality and local winter duration during PIS LGM expansions (Darvill *et al*., 2016; Denton *et al*., 2021; Fig. 3.10).

Furthermore, we observe a good agreement between the timing of RC glacier LGM advances/stillstands and atmospheric cooling over west Antarctica, according to $\delta^{18}O$ data from the West Antarctic Ice Sheet (WAIS) Divide Ice Core (WDC; 79°S; WAIS Divide Project Members, 2013; 2015; Fig. 3.10). Indeed, major $\delta^{18}O$ minima diagnostic of atmospheric cooling over West Antarctica during MIS 2 occurred at ~28.5, ~27.4, ~25.7, ~22, ~21.2 and ~20.0 ka. Ages from the RC moraines broadly match those minima. The most potent of these West Antarctic cooling events seems to have occurred at ~25.7 ka, which coincides approximately with the timing of the outermost RC III advance (26.4 ± 1.4 ka) (Fig. 3.10). Moreover, the 3-4 ka gap separating the ages of the RC III (~26.4 ka) and RC IV (~22.4 ka) moraines coincides with a 2 ka, slight atmospheric warming signal in the WDC record evidenced by a ~2 ‰ increase in $\delta^{18}O$ (between 25.9 and 23.8 ka; *ibid*). Individual RC advances also match maxima in WDC sea-salt sodium concentration record, a local sea-ice expansion/contraction proxy for West Antarctica (Fig. 3.10).

Oceanic conditions in the southeast Pacific and near Patagonia (south of the Subtropical Front) have been inferred from the MD07-3128 (53°S; Caniupán *et al*., 2011) and ODP-1233 (41°S; Kaiser *et al*., 2007) ocean sediment core records (Fig. 3.10g-j). Local sea surface temperature (SST) proxy data from both records indicate sea-surface cooling of between 5 and 6 °C relative to today during the global LGM (Kaiser *et al*., 2005; 2007) and consistent with a minimum in northern hemispheric summer insolation intensity (Fig. 3.10). Furthermore, they demonstrate millennial-scale SST fluctuations broadly consistent with atmospheric temperature variations over west Antarctica and with PIS expansions during the global LGM, although the resolution of those SST LGM records is

often too poor to correlate confidently millennial-scale fluctuations between records. Other investigations (*e.g.*, Doughty *et al.*, 2015; Shulmeister *et al.*, 2019) reconstructing New Zealand LGM glacier advances and local millennial-scale climate variability further support synchronicity between local SST lowering, Antarctic atmospheric cooling, and glacier expansion at the southern middle latitudes during the global LGM, despite out-of-phase local summer insolation intensity.

Consequently, our data support the hypothesis of a synchronous southern hemispheric glacial response to major fluctuations in northern hemispheric insolation intensity, and bolster the hypothesis that a MIS 2 oceanic and atmospheric cooling signal propagated from the northern to the southern hemisphere (Broecker, 1998; Doughty *et al.*, 2015; Buizert *et al.*, 2018). However, we note that our data could also support the new *Zealandia Switch* hypothesis proposed by Denton *et al.* (2021). This hypothesis instead argues that insolation-induced variations in the position and strength of the SWW and their impact on the tropical/subtropical ocean could be the main driver for millennial-scale climate variations in the Southern Hemisphere during the last glacial cycle.

Atmospheric conditions over West Antarctica are thought to be strongly influenced by the strength and position of the ACC, which is mostly controlled by the position of the SWW (Rignot *et al.*, 2019). It has moreover been argued that colder intervals in the southern mid-latitudes are linked to a northward migration and strength reduction of the SWW, which would increase precipitation delivery over northern Patagonia, promote local glacier expansion, and lead to a weakening of the ACC through the Drake Passage (Lamy *et al.*, 2015). In turn, this would cause the Subtropical Frontal zone to migrate northward and promote Antarctic sea-ice build-up, generating colder conditions over West Antarctica (Pedro *et al.*, 2018). The near-synchronicity of West Antarctic sea ice build-up with minima in WDC atmospheric palaeo-temperatures, and thus with northeastern Patagonian glacier advances, as revealed by the WDC sea-salt sodium record (WAIS Divide Project Members, 2013; 2015; Fig. 3.10), supports this mechanism.

$\delta^{13}C$ data from Hollywood Cave (42.5°S), South Island, New Zealand, are used as a local proxy record of palaeo-precipitation and SWW intensity (Whittaker *et al.*, 2011; Fig. 3.10). During the global LGM, this dataset demonstrates significant levels of precipitation variability, with wetter episodes between 30.3 and 27.1 ka, but also around ~24.6 ka and ~22.3 ka (Fig. 3.10). This data does not demonstrate a systematic positive correlation between precipitation over New Zealand at 42.5°S and LGM advances of the RC glacier, although some precipitation maxima overlap with RC moraine ages (*e.g.* RC IV, V, and VII). Palaeo-ecological reconstructions from the Chilean Lake District (41°S; Moreno *et al.*, 2015; 2018) also suggest an increased SWW influence and wetter conditions in northwestern Patagonia between 25 ka and 17.8 ka BP, with a slight warming and

drying during the Varas interstade (22-19.2 ka BP). These data also suggest a precipitation decline along with rapid warming between 17.8 and 14.8 ka BP, likely associated with a poleward shift in the SWW belt (Moreno *et al*., 2018). These data thus support the proposed equatorward migration of the SWW belt during the LGM. Since northeastern PIS outlet glaciers were located toward the northern edge of the wind belt, one could argue that they would have been sensitive to fluctuations in precipitation delivery forced by latitudinal migrations of the SWW (Davies *et al*., 2020). Therefore, along with decreasing atmospheric temperatures, periodic northward migrations of the SWW may have also played a role in controlling the timing of individual LGM advances of northeastern PIS outlet glaciers.

However, there is a dearth of MIS 2 palaeo-precipitation records from northeastern Patagonia and records from the Chilean Lake District (Moreno *et al*., 2015; 2018) may not necessarily be representative of LGM precipitation east of the Patagonian Andes. Recent climate modelling studies (Fogwill *et al*., 2015; Berman *et al*., 2016) and empirical data (Van Daele *et al*., 2016) have instead been used to argue that despite a northward migration of the SWW belt, the enhanced orographic effect of the PIS-covered Andes may have caused up to 50% drier-than-present conditions to the east of the former ice divide throughout the global LGM. Therefore, assessing the former role of precipitation in promoting PIS outlet glacier expansion during the global LGM in northeastern Patagonia remains a challenge.

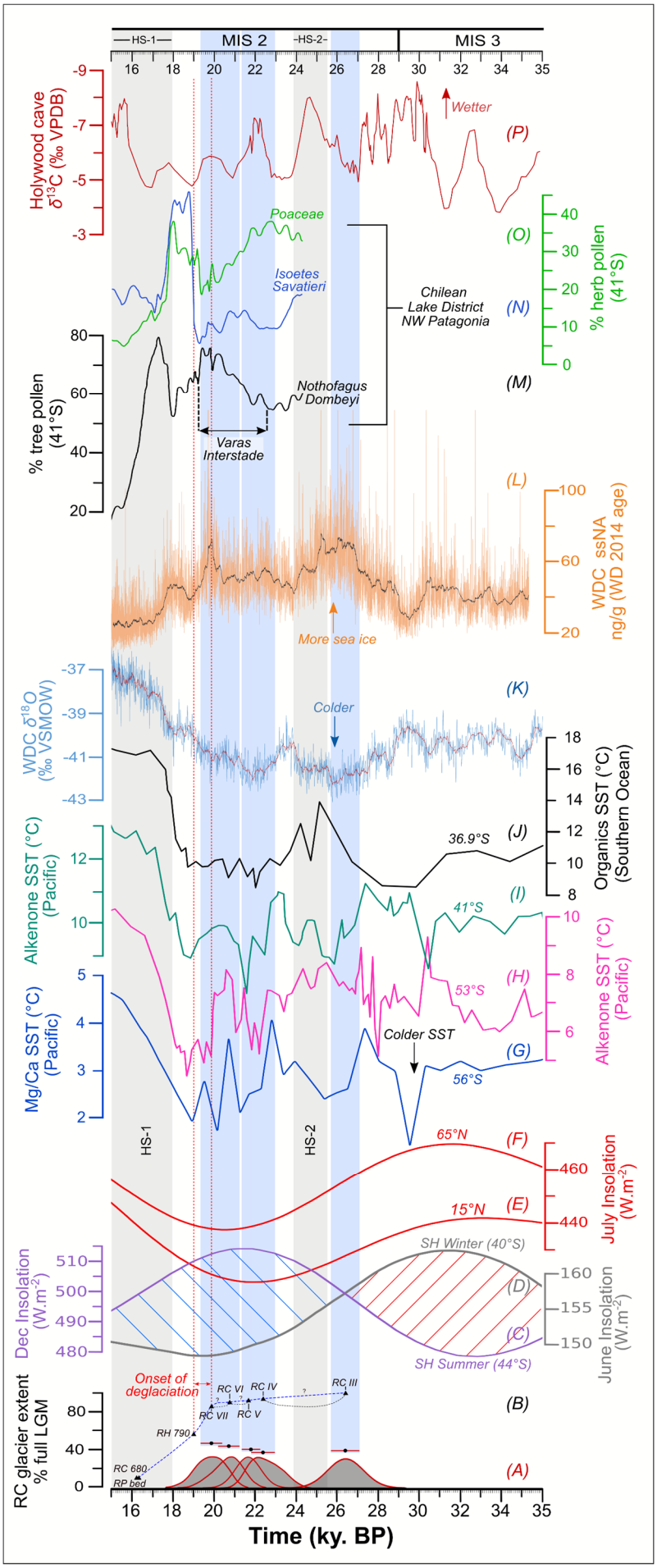
HS-1
MIS 2
-HS-2-
MIS 3
Holywood cave δ13C (‰ VPDB)
Wetter
(P)
Poaceae
Isoetes Savatieri
(O)
(N)
% herb pollen (41°S)
Chilean Lake District NW Patagonia
% tree pollen (41°S)
Nothofagus Dombeyi
(M)
Varas Interstade
(L)
WDC ssNA ng/g (WD 2014 age)
More sea ice
WDC δ18O (‰ VSMOW)
Colder
(K)
Organics SST (°C) (Southern Ocean)
36.9°S
(J)
Alkenone SST (°C) (Pacific)
41°S
(I)
53°S
(H)
Mg/Ca SST (°C) (Pacific)
Colder SST
(G)
56°S
HS-1
HS-2
65°N
(F)
July Insolation (W.m-2)
15°N
(E)
SH Winter (40°S)
Dec Insolation (W.m-2)
(D)
(C)
June Insolation (W.m-2)
SH Summer (44°S)
Onset of deglaciation
RC VI
RC IV
RC III
RC VII
RC V
RH 790
RC 680
RP bed
RC glacier extent % full LGM
(B)
(A)
Time (ky. BP)

Figure 3.10. Vertical plot comparing our RC III - RC VII ^{10}Be chronology with other palaeoclimate proxy records. (**A**): 1σ probability density distributions, arithmetic means (black dots) and standard deviation (error bars) from Bayesian age model outputs for the RC III – RC VII moraines. (**B**): Reconstructed, approximate percentage extent of the RC glacier relative to full LGM extent (RC III) for each glacial and deglacial event dated in this study. Blue dashed lines represent a scenario of linear ice-front retreat and stillstands while black dashed lines represent potential scenarios of RC ice-front retreat and re-advance (**C-F**): Insolation intensity for (**C**) 44°S, December; (**D**) 40°S, June; (**E**) 15°N, July; and (**F**) 65°N, July (Berger & Loutre, 1991). Hatching in between the southern summer and winter insolation curves highlights periods of high (blue) and low (red) seasonality (**G**): Sub-antarctic SST (Mg/CA) record from the southern Pacific Ocean, 56°S (core E11-2; Mashiotta *et al*., 1999). (**H**): Alkenone SST record from the Southeast Pacific (Chilean coast), 53°S (core MD07-3128; Canupian *et al*., 2011). (**I**) Alkenone SST record from the Southeast Pacific (Chilean coast), 41°S (core ODP-1233; Kaiser *et al*., 2007). (**J**) Organics SST (TEXH 86) from the Southern Ocean (southern Australian coast), 36.9°S (core MD03-2607; Lopes Dos Santos *et al*., 2013). (**K**): $\delta^{18}O$ record (‰ Vienna Standard Mean Ocean Water scale) from the WDC Antarctic ice core (WAIS Divide Project Members, 2013; 2015) displayed with a 12-point moving average. (**L**) Sea-salt sodium data (ssNa; ng/g) from the WDC Antarctic ice core, interpreted as a proxy for regional sea-ice production (*ibid*). (**M-O**): Weighted moving average of (**M**) *Nothofagus dombeyi*, (**N**) *Isoetes savatieri*, and (**O**) *Poaceae* pollen-type concentration (%) from the Lago Pichilaguna record (41°S; Moreno *et al*., 2018). (**P**) $\delta^{13}C$ data from a speleothem record located at Hollywood Cave (42.5°S; Whittaker *et al*., 2011), South Island, New Zealand interpreted as a local palaeo-precipitation and SWW intensity record.

3.5.3.2 The onset of local deglaciation

Patagonian palaeoglacial records seem to indicate an asynchronous deglacial response of major PIS outlet glaciers during the Last Glacial Termination (*e.g.*, Kaplan *et al*., 2008; Hein *et al*., 2010; Moreno *et al*., 2015; Bendle *et al*., 2017a; García *et al*., 2019). With the onset of ice recession from LGM margins appearing to be glacier-specific, and to vary between 19-20 ka in northeastern Patagonia and 17-18 ka in northwestern, central and southern Patagonia (Chapter 3 Supplementary Figure 2). However, most records seem to agree on a rapid, extensive retreat of outlet glaciers towards the mountain front occurring prior to ~16 ka, leading to the establishment of warm, near-Holocene conditions by ~15 ka (*e.g.*, Hein *et al*., 2010; Boex *et al*., 2013; García *et al*., 2019; Davies *et al*., 2020).

The Patagonian asynchronous deglacial response has been addressed by several studies (*e.g.* Bendle *et al*., 2017a; García *et al*., 2019). García *et al.* (2019) highlight an early atmospheric and oceanic warming signal arguably widespread throughout the southern mid-to-high latitudes and beginning at around 20-22 ka. The occurrence of this warming is supported by numerous local palaeoclimate records including pollen records from the Chilean Lake District; which indicate a sharp increase in *Nothofagus dombeyi* arboreal pollen percentage values from ~21.8 ka and peaking at ~19.5 ka (Denton *et al*., 1999; Moreno *et al*., 2015, 2018; Fig. 3.10m). This increase in glacial arboreal

populations was interpreted as a shift in the regional treeline resulting from increasing air temperatures (Moreno *et al*., 2018). This relatively warm and drier late-LGM interval, termed the Varas interstade in northwestern Patagonia (Denton *et al*., 1999; Mercer, 1972), is argued to have started at around 22.6 kcal. yrs BP and peaked at 19.3 kcal yrs BP. This event preceded a return to colder, wetter conditions between 19.3 and 17.8 kcal. yrs BP, as demonstrated by sharp positive anomalies in *Poaceae* and *Isoetes savatieri* pollen concentrations at Lago Pichilaguna (41°15'S; 73°3'W; Moreno *et al*., 2018; Fig. 3.10o,p). Southeast Pacific Sea Surface Temperature (SST) records from 56°S (Mashiotta *et al*., 1999), 53°S (Caniupán *et al*., 2011) and 41°S (Kaiser *et al*., 2007) all indicate a 2-3°C SST warming signal starting between 21.5 and 22 ka and reaching a maximum at ~20.5 ka prior to renewed cooling, thus indicating a local SST increase approximately coeval with the Varas interstade. A similar pattern of SST increase was recorded in the southern Atlantic (41.1°S; Barker *et al*., 2009). In West-Antarctica, $\delta^{18}O$ data from the WDC ice core (79°S) suggest local air temperatures reached a minimum at ~21.8 ka, and demonstrate a ~2.5°C warming until ~18.6 ka, marking the onset of a slight renewed cooling until 17.9 ka, a time of local deglacial warming (WAIS Divide Project Members, 2015; Fig. 3.10). Antarctic sea-ice extent proxy data from the southeast Pacific (WAIS Divide Project Members, 2015) and the Scotia Sea (Collins *et al*., 2012) both suggest a coinciding sea-ice decline starting at 20 ka and 22 ka, respectively, prior to a brief period of build-up between 18.7 and 17.9 ka. Allen *et al*. (2011) provide further evidence that while winter sea-ice extent did not recede until ~19 ka in the Scotia Sea, summer sea ice retreated to south of 61°S by ~22 ka, which suggests a local pattern of seasonally ice-free waters during the Varas interstade. Therefore, as previously argued by García *et al*. (2019), we propose that local coupled atmospheric and oceanic warming between ~22.5 and ~19.5 ka might have caused some sensitive Patagonian glaciers to experience early destabilisation and recession (19-20 ka; *e.g.* RC glacier, Río Cisnes glacier, Lago Cochrane/Pueyrredón glacier). The RC moraine record presented here thus provides further evidence that PIS outlet glaciers in northeastern Patagonia experienced relatively early recession from their LGM margins. However, subsequent cooling and northward migration of the SWW leading to wetter conditions between ~19.5 and ~18 ka (Moreno *et al*., 2018) caused certain PIS outlets to stabilise and/or re-advance towards LGM margins, such as observed in the Chilean Lake District (*e.g.* Llanquihue glacier; Denton *et al*., 1999; Moreno *et al*., 2015). Similarly to the Río Cisnes glacier (García *et al*., 2019), our investigation provides no evidence of a pronounced re-advance of the RC glacier between ~19.5 and ~18 ka. Our chronology suggests instead that the RC glacier had experienced significant retreat (at least ~40% glacier-length loss relative to its full LGM extent) by ~19 ka. This could indicate a local east/west asymmetry whereby northeastern PIS outlets glaciers were more sensitive to warming during the Varas interstade than glaciers of the wetter, western side of the Andes, and thus experienced a more negative mass balance. Conversely, western PIS outlets

in northern Patagonia were perhaps more sensitive and responsive to a late-LGM cooling and wetting between ~19.5 and ~18 ka. The proposed increase in west-to-east precipitation starvation over the Patagonian Andes during the LGM (Berman *et al*., 2016; Van Daele *et al*., 2016) could help to explain the higher sensitivity of drier, northeastern Patagonian glaciers to such atmospheric warming, as well as a lack of outlet glacier response to increased moisture delivery between ~19.5 and ~18 ka. Moreover, the formation of large ice-dammed proglacial lakes during PIS recession is much more common to the east than to the west of the Patagonian Andes, due to the westward–sloping glacially over-deepened nature of the region's main valley troughs. Recent glaciological observations (Jackson *et al*., 2020) and modelling work conducted on temperate mid-latitude mountain glaciers has shown that under identical climate forcing, glaciers calving into proglacial lakes were likely to experience up to four times more extensive and up to eight times faster ice-front retreat than a land-terminating glacier (Sutherland *et al*., 2020). In the RC valley, the formation of glaciolacustrine phase two (between ~20.7 and ~21.7), added to slightly warmer and drier conditions during the Varas interstade (22.6-19.3), may have caused enhanced ablation and extensive, rapid retreat of the ice-front and a lower sensitivity to subsequent cooling and wetting between ~19.5 and ~18 ka. Such glaciolacustrine climate-decoupling mechanism of major eastern PIS outlets has been proposed for several valleys of central Patagonia (*e.g.* Mendelová *et al*., 2017; Davies *et al*., 2018; Thorndycraft *et al*., 2019).

On the other hand, ocean sediment cores from the southern coasts of New Zealand and Australia exhibit little evidence of SST increases prior to 18-19 ka (Pahnke *et al*., 2003; Barrows *et al*., 2007; Lopes dos Santos *et al*., 2013). Similarly, $\delta^{18}O$ data from the EPICA Dome C and Dronning Maud Land (EPICA Community Members, 2006), Dome Fuji (Kawamura *et al*., 2007) and Talos Dome (Stenni *et al*., 2011) ice cores do not display clear evidence of sustained atmospheric warming over East-Antarctica between 22 and 18 ka. In the New Zealand Alps, the onset of glacial termination causing rapid ice-front retreat is agued to have occurred around the early stages of Heinrich Stadial 1, shortly after ~18 ka (Shulmeister *et al*., 2010; Putnam *et al*., 2013; Kelley *et al*., 2014; Doughty *et al*., 2015), while little to no evidence of prior late-LGM warming and significant glacier retreat was found. These data suggest that the early oceanic and atmospheric warming signal beginning at 20-22 ka was perhaps not widespread throughout the southern mid-to-high latitudes, but was possibly more confined to West Antarctica, Patagonia, and local ocean basins.

3.6 Conclusions

- The Río Corcovado Last Glacial Maximum (LGM) moraine record displays at least five (RC III-VII) distinct advances/stillstands of the Río Corcovado glacier. Our results from ^{10}Be terrestrial cosmogenic nuclide dating of moraine boulders suggest that these major advances/stillstands occurred over a 6-7 ka period, at 26.4 ± 1.4 ka, 22.4 ± 1.15 ka, 21.7 ± 0.9 ka, 20.7 ± 1.0 ka and 19.9 ± 1.1 ka, thereby during the global LGM. These glacial expansion events are coeval with a decline and minimum in northern hemispheric insolation intensity, atmospheric cooling over Antarctica, and lowering of sea-surface temperatures in mid-latitude southern ocean basins, thus supporting the hypothesis of a Marine Isotope Stage 2 oceanic and atmospheric cooling signal propagated from the northern to the southern hemisphere.

- Our geochronological reconstruction of the Río Corcovado glacier advances/stillstands provides no evidence for Marine Isotope Stage 3 advances more extensive than those that occurred during the global LGM in this area. Therefore, our results support the idea of large latitudinal and longitudinal disparities across Patagonia in the timing and magnitude of maximum glaciation during the last glacial cycle.

- The oldest LGM advance recorded in the Río Corcovado valley is associated with the formation of the first of three glaciolacustrine phases, dated to 26.4 ± 1.4 ka, and characterised by a surface lake level of ~990 m a.s.l. Gradual glacier retreat from late-LGM margins led to the formation of a second glaciolacustrine phase, formed between ~20.5 and ~22 ka, with the proglacial-lake surface at an elevation of ~790 m a.s.l. for 1.5 to 2.5 ka.

- The onset of local deglaciation and Río Corcovado glacier retreat from LGM margins occurred between 19 and 20 ka. Our chronology thus supports an early deglaciation scenario for outlet glaciers of northeastern Patagonia relative to northwestern and southern Patagonia, which may indicate a high local glacier sensitivity to atmospheric warming and drying during the Varas interstade (~19.5-22.5 ka), and/or to the enhanced ablation effect of large proglacial lake formation.

- At around 19.0 ± 0.9 ka, further ice-front retreat into the Río Palena valley precipitated a third and last glaciolacustrine phase associated with a new proglacial-lake spillway opened into the north Río Frio valley, causing a lake-level drop from ~790 a.s.l. m to ~680 m a.s.l. We propose that this extensive ~680 m a.s.l. proglacial lake existed for 2.5 to 3 ka, between ~16 and ~19 ka.

- By ~16 ka, the Palena ice front had retreated westwards by at least ~70 km, towards the mountain front interior, leading to local PIS disintegration and the final westward, Pacific-directed drainage of glaciolacustrine phase three, dated to 16.3 ± 0.3 ka. We interpret this age as the approximate timing of local Atlantic/Pacific drainage reversal, which caused an estimated ~270 km^3 of freshwater to drain, either progressively or suddenly, into the Pacific Ocean and the Golfo Corcovado.

Chapter IV

Northeastern Patagonian glacier advances (43°S) reflect northward migration of the Southern Westerlies towards the end of the last glaciation



Publication details

Authors

Tancrède P. M. Leger[1*], Andrew S. Hein[1], Daniel Goldberg[1], Irene Schimmelpfennig[2], Maximillian S. Van Wyk de Vries[3], Robert G. Bingham[1] and, ASTER Team[2Ψ]

[1] *School of GeoSciences, University of Edinburgh, Edinburgh, Scotland, United Kingdom of Great Britain and Northern Ireland*

[2] *Aix-Marseille Université, CNRS, IRD, INRAE, CEREGE, 13545, Aix-en-Provence, France*

[3] *Department of Earth & Environmental Sciences and Saint Anthony Falls Laboratory, University of Minnesota, Minneapolis, MN, United States*

[Ψ] *Consortium: Aumaitre Georges- Keddadouche Karim - Zaidi Fawzi*

Author contributions

Tancrède P. M. Leger: Conceptualization, Data curation, Formal analysis, Funding acquisition, Investigation, Methodology, Project administration, Software, Visualization, Writing (original draft and review & editing)

Andrew S. Hein: Conceptualization, Methodology, Project administration, Supervision, Validation, Writing (original draft)

Daniel Goldberg: Data curation, Investigation, Methodology, Software, Writing (original draft)

Irene Schimmelpfennig: Data curation, Supervision, Writing (original draft)

Maximilian S. Van Wyk de Vries: Data curation, Methodology, Writing (original draft)

Robert G. Bingham: Supervision, Writing (original draft)

[*]Corresponding Author contact details

Tancrède P.M. Leger, PhD student, University of Edinburgh, School of GeoSciences,

Address: Institute of Geography, Drummond Street, Edinburgh EH8 9XP, United Kingdom

Email: Tancrede.leger@ed.ac.uk

Publication

Journal: Frontiers in Earth Science; open access

2021, Vol. 9, No. 751987

Doi: https://doi.org/10.3389/feart.2021.751987

Received: 02 August 2021; Accepted: 20 September 2021

Published: 09 November 2021

4.1 Introduction

The mechanisms contributing to the globally synchronous termination of the last glacial cycle remain a subject of great discussion and interest (Putnam *et al*., 2013). The main source of debate revolves around "Mercer's paradox", the phenomenon that ice sheets reached maxima and then demised synchronously in both hemispheres despite summer insolation intensity being anti-phased (Mercer, 1984). Indeed, in recent decades, an increasing number of detailed glacier chronologies from Patagonia and New Zealand have demonstrated that southern mid-latitude glacier volume fluctuations were not influenced directly by orbitally-controlled local summer insolation intensity during the last glacial cycle, in contrast to northern hemispheric glaciers (Denton *et al*., 1999; 2021; Hein *et al*., 2010; Doughty *et al*., 2015; Darvill *et al*., 2016; Shulmeister *et al*., 2019). Denton *et al*. (2021) proposed that the widespread deglaciation towards the end of the Last Glacial Maximum (LGM), at ~18 ka (ka: thousand years before present), was instead triggered by an insolation-induced poleward shift of the Southern Westerly Winds (SWW) and the coupled Subtropical Front (STF). Tracking the movement of the SWW during the last glacial termination (LGT; ~18 ka) is therefore important for improving our understanding of sudden global climate change during the Quaternary.

Located close to the northern edge of the precipitation-bearing SWW belt and STF, the northern Patagonian Andes are ideally suited for assessing interhemispheric phasing of climate change and for investigating the precise timing of millennial-scale latitudinal shifts in the SWW during the LGT (Mercer, 1972; 1976; 1984; Clapperton, 1990; 1993; Denton *et al*., 1999). However, the northeastern region of the Patagonian cordillera currently lacks empirical palaeo-climate data covering this key period of rapid environmental change (García *et al*., 2019). Palaeo-climate proxy data from northwestern Patagonia suggest a return to colder, wetter conditions in the late LGM, between ~19.5 and ~18 ka, during which it is hypothesised that the SWW locally reached their maximum LGM influence (Denton *et al*., 1999; Moreno *et al*., 2018). Moreover, numerous late-LGM expansion and/or stabilisation events have been reported for several Patagonian and New Zealand glaciers at ~17-18 ka (*e.g.* Denton *et al*., 1999; Kaplan *et al*., 2007; 2008; Murray *et al*., 2012; Putnam *et al*., 2013; Moreno *et al*., 2015; Shulmeister *et al*., 2010; 2019; Davies *et al*., 2020; Mendelová *et al*., 2020a, Peltier *et al*., 2021), which suggest a somewhat synchronous late-LGM glacial response across the southern

mid-latitudes. However, recent geochronological evidence from the northeastern sector of the former Patagonian Ice Sheet (PIS) does not fit this pattern. Instead, major outlet glaciers experienced relatively early (~19-20 ka) deglaciation from LGM margins, approximately 1.5 kyr prior to outlet glaciers of the northwestern, central eastern and southeastern Patagonian regions (García *et al*., 2019; Leger *et al*., 2021), where rapid glacial demise was instead found to occur shortly after ~18 ka (Darvill *et al*., 2016; Davies *et al*., 2020). It remains unclear whether the cooler, wetter late-LGM conditions experienced in northwestern Patagonia extended to northeastern Patagonia, and whether early deglaciation of the northeastern PIS outlet glaciers was driven primarily by a difference in climate, or by other negative mass-balance inducing factors.

Here, we reconstruct the behaviour of two independent, climate-sensitive mountain glaciers in northeastern Patagonia to shed light on regional climatic conditions around the last glacial termination and to help unravel the causes of asynchronous PIS deglaciation. We focus our investigation on the El Loro and Río Comisario valleys, two adjacent glaciated mountain valleys of the Poncho Moro massif (Fig. 4.1). Both valleys display geomorphological evidence of glacier expansion following the retreat of the Río Corcovado glacier, a major former outlet of the PIS (Leger *et al*., 2020; 2021). We combine geomorphological mapping and ^{10}Be terrestrial cosmogenic nuclide (TCN) dating of moraine boulders to reconstruct the extent and timing of these glacier advances/still-stands, and employ a spatially-distributed ice-flow model coupled with a positive degree-day surface mass balance parameterisation to evaluate possible climatic conditions at the time of glacier resurgence. Our analysis takes into account a correction of local topographic elevation change caused by glacial isostatic adjustment (GIA) since the time of glacier advance. We find the mountain glaciers re-advanced during the late LGM, at around ~18 ka, partly in response to increased precipitation that we propose reflects an increased influence of the SWW. Our results support the hypothesis of an equatorward migration of the SWW belt over Patagonia towards the end of the last glaciation, between ~19.5 and ~18 ka, a few centuries prior to widespread glacial demise and the onset of the LGT after 18 ka.

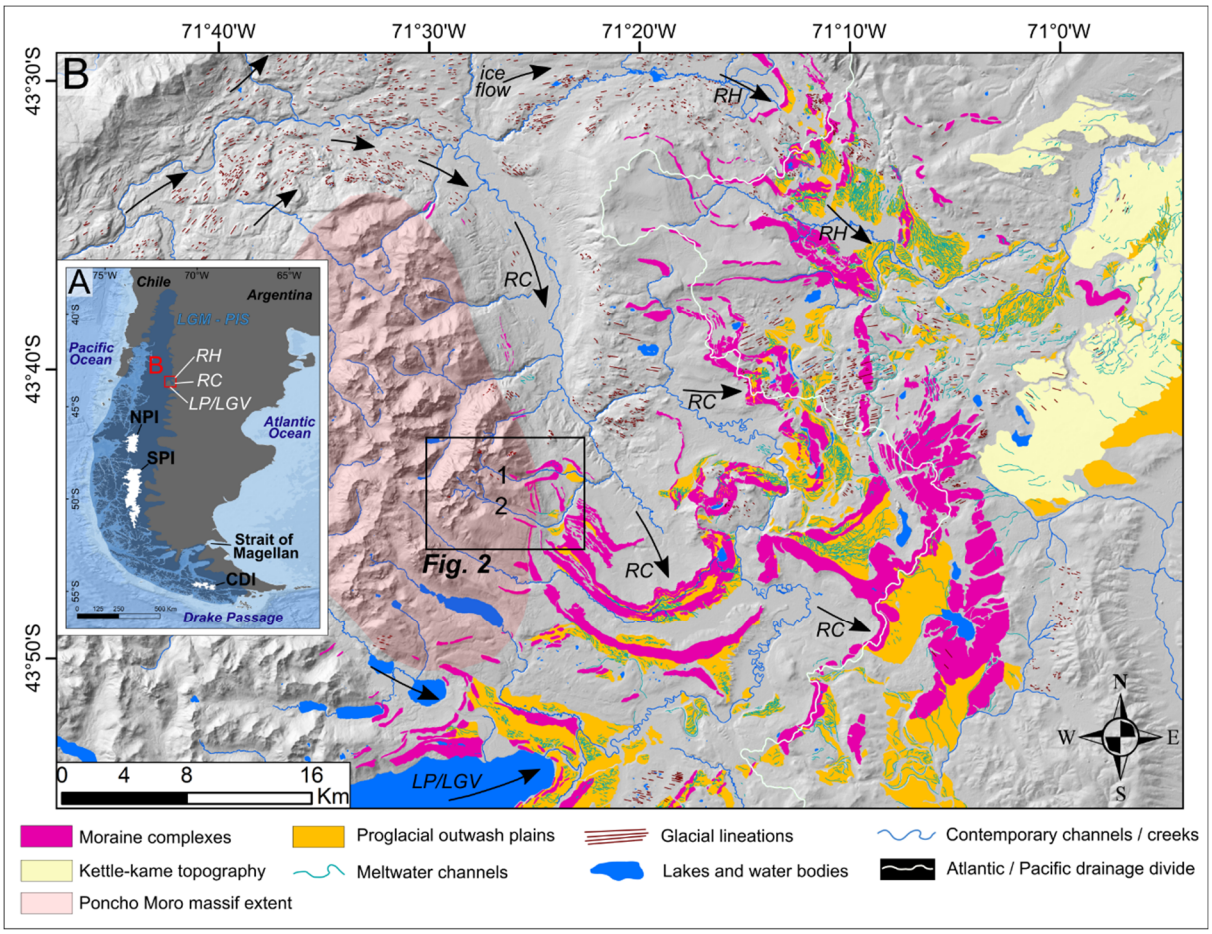

Figure 4.1. Location of study area. (**A**) Approximate former extent of the Patagonian Ice Sheet (PIS) during the Last Glacial Maximum (LGM), modified from Glasser *et al*. (2008) (dark blue polygon). Modern extents of the North Patagonian (NPI), South Patagonian (SPI), and Cordillera Darwin (CDI) Icefields are displayed in white. Bathymetric data from General Bathymetric Chart of the Oceans (GEBCO). Outlet glaciers that formerly occupied the study region are designated: RC: Río Corcovado, RH: Río Huemul, LP/LGV: Lago Palena/General Vintter glaciers. Spatial data are displayed in WGS84. (**B**) Shaded relief map (light azimuth: 315°, incline: 45°) based on the AW3D30 Digital Elevation Model (DEM) with overlaid glacial geomorphological data, adapted from Leger *et al*. (2020). Geomorphological data focus on the RC, RH and LP/LGV lateral and terminal glaciogenic deposits. The black box highlights the location of the El Loro (EL; 1) and Río Comisario (RCO; 2) valleys (Fig. 4.2). Black arrows denote former ice-flow direction. The light red, transparent polygon highlights the geographical extent of the Poncho Moro massif. Spatial data are displayed in WGS84 and projected to UTM zone 19S.

4.2 Study location

This study focuses on the mountain valleys and land-terminating palaeo-glaciers of the Poncho Moro massif, which is located on the eastern edge of the northern Patagonian Andes (Fig. 4.1). The Poncho Moro massif today is characterised by maximum summit elevations of ~2100 m a.s.l., and is mostly ice-free, with the exception of one small glacier (~0.1 km^2) perched in the El Loro upper catchment (Figs 4.2, 4.3a). The current climate is classified as cool-temperate, due to the combined effects of the Peru-Chile current offshore from the Chilean Pacific coast and the SWW (Denton *et al*., 1999; Kaiser *et al*., 2007). However, due to the strong zonal orographic effect of the Patagonian Andes, total annual precipitation at the study site is reduced by ~60% relative to the centre of the cordillera at ~43°S. Consequently, the eastern valleys of the Poncho Moro massif are located at the western edge of the semi-arid Patagonian steppe climate zone (Garreaud *et al*., 2013; Fick & Hijmans, 2017). The massif is delineated to the north and east by the Río Corcovado valley, formerly host to a major topographically-controlled outlet glacier (Río Corcovado glacier) of the Patagonian Ice Sheet (PIS), which flowed eastwards from the ice-sheet divide during major Quaternary glaciations (Caldenius, 1932; Haller *et al*.,2003; Martínez *et al*., 2011; Leger *et al*., 2020). To the southeast of the Poncho Moro massif, the former Río Corcovado outlet glacier deposited a series of at least eight distinct moraine complexes (RC 0 – VII) preserved across large expanses of the Argentinian foreland, five of which (RC III – VII) mark the local LGM and have been dated to marine isotope stage 2 (Leger *et al*., 2021). The Poncho Moro massif is therefore located towards the former eastern extremity of the PIS during the global LGM. Many valleys of the Poncho Moro massif display well-preserved sequences of lateral and terminal moraine complexes which enable the reconstruction of former mountain glacier extents (Leger *et al*., 2020, Figs 4.1, 4.2). We targeted two adjacent valleys for our investigation; the El Loro (EL) and Río Comisario (RCO) valleys (Fig. 4.2), which are both oriented broadly northwest-southeast and were formerly host to western tributary glaciers of the Río Corcovado glacier. We chose these valleys because they both exhibit geomorphological evidence of glacier advances that locally cross-cut the RC III-VI margins, indicating younger moraine deposition occurred after the retreat of the Río Corcovado glacier from its LGM margins. These distinct lateral and terminal moraine complexes located near the EL and RCO valley mouths share similar distance-to-headwall properties (EL: 6.1 km; RCO: 7.1 km) (Fig. 4.2). When reaching

their respective outermost moraines, the former EL and RCO glaciers covered elevation ranges of between 2100-890 m a.s.l. and 2050-1100 m a.s.l., respectively.

The Poncho Moro massif surface geology is characterised by numerous lithologies including volcanic extrusives and sedimentary assemblages, and the EL and RCO catchments are dominated by the mid-cretaceous Río Hielo formation of granites with vein and dyke intrusions (Haller *et al*., 2003). Moraine boulders located on the outermost EL moraines are almost exclusively granitic and quartz-abundant, making these moraine deposits suitable for ^{10}Be terrestrial cosmogenic nuclide (TCN) dating (Fig. 4.3 c,e,f).

4.3 Materials and methods

4.3.1 Geomorphological mapping

Major landforms and topographic features were initially identified using the freely available ALOS WORLD 3D - 30 m resolution (AW3D30: Japan Aerospace Exploration Agency) Digital Elevation Model (DEM). All mapped landforms were manually digitised in the WGS84 reference coordinate system projected to UTM zone 19S using the ESRI^{TM} World Imagery layer, characterized by ~1.0 m resolution images from DigitalGlobe (GeoEye, IKONOS, 2000-2011) at the study site. In areas with dense vegetation and/or cloud cover, we undertook different colour-rendering comparisons using 10 m resolution Sentinel 2A true colour (TCI) and false colour (bands 8,4,3) products (available from https://scihub.copernicus.eu/). Detailed geomorphological mapping criteria along with the complete geomorphological map of the area are presented by Leger *et al*. (2020). Field-based mapping, ground-truthing and corrections of preliminary landform interpretations in the EL valley were conducted during the austral summer of 2020.

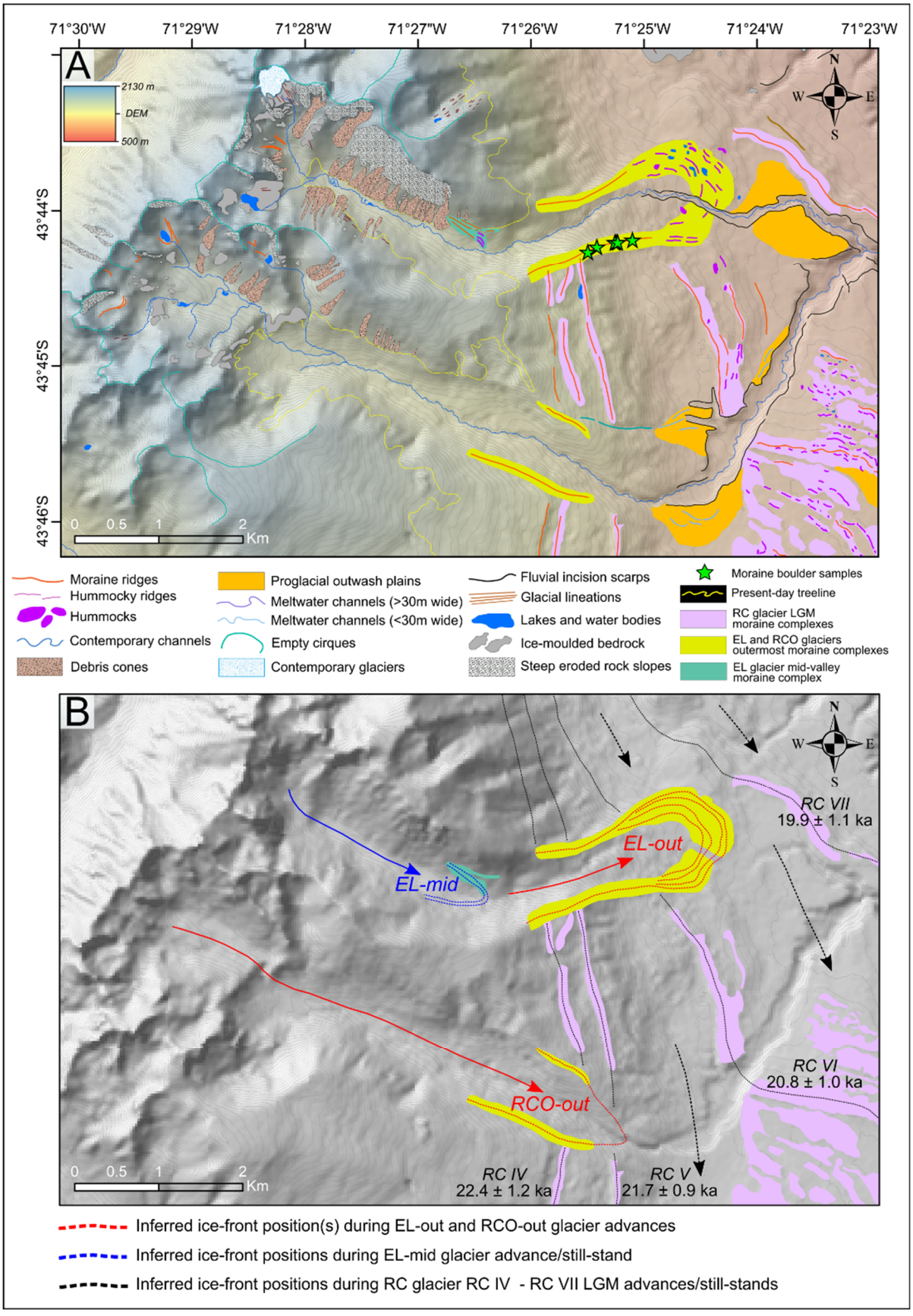
71°30'W
71°29'W
71°28'W
71°27"W
71°26'W
71°25'W
71°24'W
71°23'W
43°44'S
43°45'S
43°46'S
A
2130 m
DEM
500 m
N
W
E
S
0 0.5 1 2 Km
Moraine ridges
Hummocky ridges
Hummocks
Contemporary channels
Debris cones
Proglacial outwash plains
Meltwater channels (>30m wide)
Meltwater channels (<30m wide)
Empty cirques
Contemporary glaciers
Fluvial incision scarps
Glacial lineations
Lakes and water bodies
Ice-moulded bedrock
Steep eroded rock slopes
Moraine boulder samples
Present-day treeline
RC glacier LGM moraine complexes
EL and RCO glaciers outermost moraine complexes
EL glacier mid-valley moraine complex
B
EL-mid
EL-out
RCO-out
RC VII
19.9 ± 1.1 ka
RC VI
20.8 ± 1.0 ka
RC IV
22.4 ± 1.2 ka
RC V
21.7 ± 0.9 ka
Inferred ice-front position(s) during EL-out and RCO-out glacier advances
Inferred ice-front positions during EL-mid glacier advance/still-stand
Inferred ice-front positions during RC glacier RC IV - RC VII LGM advances/still-stands

Figure 4.2. Geomorphological map of the EL and RCO valleys, northeastern Patagonia (see location in wider context, Fig. 4.1). (**A**) DEM hillshade (AW3D30 DEM, light azimuth: 315°, incline: 45°) and geomorphological map of the EL and RCO valleys. Locations of moraine boulders sampled for TCN dating are indicated by green star symbols. The variable colouring of moraine complexes (pink/yellow/green) highlights the stratigraphic order of distinct palaeo-glacier advances/stillstands according to our geomorphological interpretations. (**B**) DEM hillshade, inferred moraine-complex stratigraphic relationships and former ice-flow directions of the Río Corcovado outlet glacier LGM advances/still-stands (black arrows), EL-mid advance/still-stand (blue arrow), EL-out and RCO-out advances (red arrows). The ages of the Río Corcovado LGM advances/still-stands are arithmetic mean ± 1σ standard deviations of moraine boulder exposure age populations reported by Leger *et al*. (2021) following Bayesian age model correction. Spatial data are displayed in WGS84 and projected to UTM zone 19S.

4.3.2 ^{10}Be Terrestrial Cosmogenic Nuclide dating

4.3.2.1 Dating approach and sampling

To establish the timing of local mountain glacier re-advances following initial PIS retreat, we targeted the outermost EL lateral moraines (Figs 4.2, 4.3), and sampled moraine boulders for ^{10}Be surface exposure dating (*e.g.* Gosse & Phillips, 2001; Hein *et al*., 2010; Heyman *et al*., 2011). The selected granodiorite boulders (60-90 cm in height) resting directly on the moraine crest exhibited glacial polish and, in some cases, preserved striations, indicating minimal post-depositional surface erosion (*e.g.* Fig. 4.3 e,f). 1-2 kg samples were collected by hammer, chisel and angle grinder from the central section of the upper-most boulder surface, to a depth of 2-5 cm. Six boulders were sampled along a single continuous lateral moraine ridge (Table 2, Figs. 4.2, 4.3). Collecting this number of samples from one landform aims to reduce potential uncertainties resulting from geological scatter and post-depositional processes (Putkonen & Swanson, 2003; Applegate *et al*., 2010; Heyman *et al*., 2011). Exposure ages were interpreted as dating moraine stabilisation following ice-front retreat and/or glacier tongue thinning, hence providing a minimum age for the glacier advance.

4.3.2.2 Sample preparation, wet chemistry and exposure-age calculations

Samples were prepared at two cosmogenic nuclide laboratories: 1) the University of Edinburgh's Cosmogenic Nuclide Laboratory for sample crushing/sieving and quartz purification/isolation; and 2) the National laboratory for Cosmogenic Nuclides (LN_2C) of CEREGE, Aix-en-Provence, France for post-purification wet chemistry. All $^{10}Be/^{9}Be$ ratios were measured by accelerator mass spectrometry at ASTER-CEREGE.

The samples were crushed in their entirety and sieved to isolate the 250-500 μm grain-size fractions. One to three treatments in HCl and H_2SiF_6 on a shaker table, which lasted up to seven days per treatment, was performed to remove as much non-quartz minerals as possible (Bourlès, 1988). Pure quartz was obtained by repeated etching in a 2% HF and 1% HNO_3 solution for 24 hours in a heated ultrasonic bath, with a sample to acid ratio of about 12 g L^{-1}. At least three etches were subsequently performed to remove atmospheric ^{10}Be. The purified quartz samples were dissolved in concentrated HF and each sample, as well as one process blank, were spiked with between 0.42 and 0.46 mg of ^{9}Be, in the form of an in-house carrier

solution made from phenakite. After dissolution, the *HF* was evaporated off, and the solid residue was dissolved in *HCl* (10.2 mol L^{-1}), followed by $Be(OH)_2$ precipitation at pH ~9 through the addition of NH_3 and re-dissolution in *HCl*. The solutions were first passed through anion exchange chromatography columns to remove *Fe, Ti* and *Mn*. After another evaporation and $Be(OH)_2$ precipitation step, *HCl* of lower concentration (1 mol L^{-1}) was added to dissolve the *Be* prior to passing the solution through cation exchange chromatography columns to isolate *Be* from *B* and *Al*. The *Be* fractions were then precipitated again as hydroxides and oxidised at ~700 °C. The resulting *BeO* samples were mixed with *Nb* powder and pressed into nickel cathodes for AMS measurements. Measurements are based on the in-house standard STD-11 with a $^{10}Be/^{9}Be$ ratio of (1.191 ± 0.013) 10^{-11} (Braucher *et al.*, 2015) and a ^{10}Be half-life of (1.387 ± 0.0012) 10^{6} years (Chmeleff *et al.*, 2010; Korschinek *et al.*, 2010). Analytical uncertainties include ASTER counting statistics and stability (~5%; Arnold *et al.*, 2010) and machine blank correction. Process blank corrections ranged between 0.83% and 1.01% of calculated sample ^{10}Be atoms.

Exposure ages were calculated using the online calculator formerly known as the CRONUS-Earth online calculator version 3 (Balco *et al.*, 2008) with the ^{10}Be Patagonian production rate of 3.71 ± 0.11 atoms g^{-1} (SiO_2) yr^{-1} (original value: Kaplan *et al.*, 2011) obtained and re-calculated from the ICE-D online database (http://calibration.ice-d.org/). In this study, exposure ages were calculated using the time-dependent LSDn scaling scheme of Lifton *et al.* (2014) with 1σ analytical uncertainties. These ages assume no boulder surface erosion post-deposition and present no correction for shielding by snow, soil, or vegetation, following the rationale described in detail by Leger *et al.* (2021).

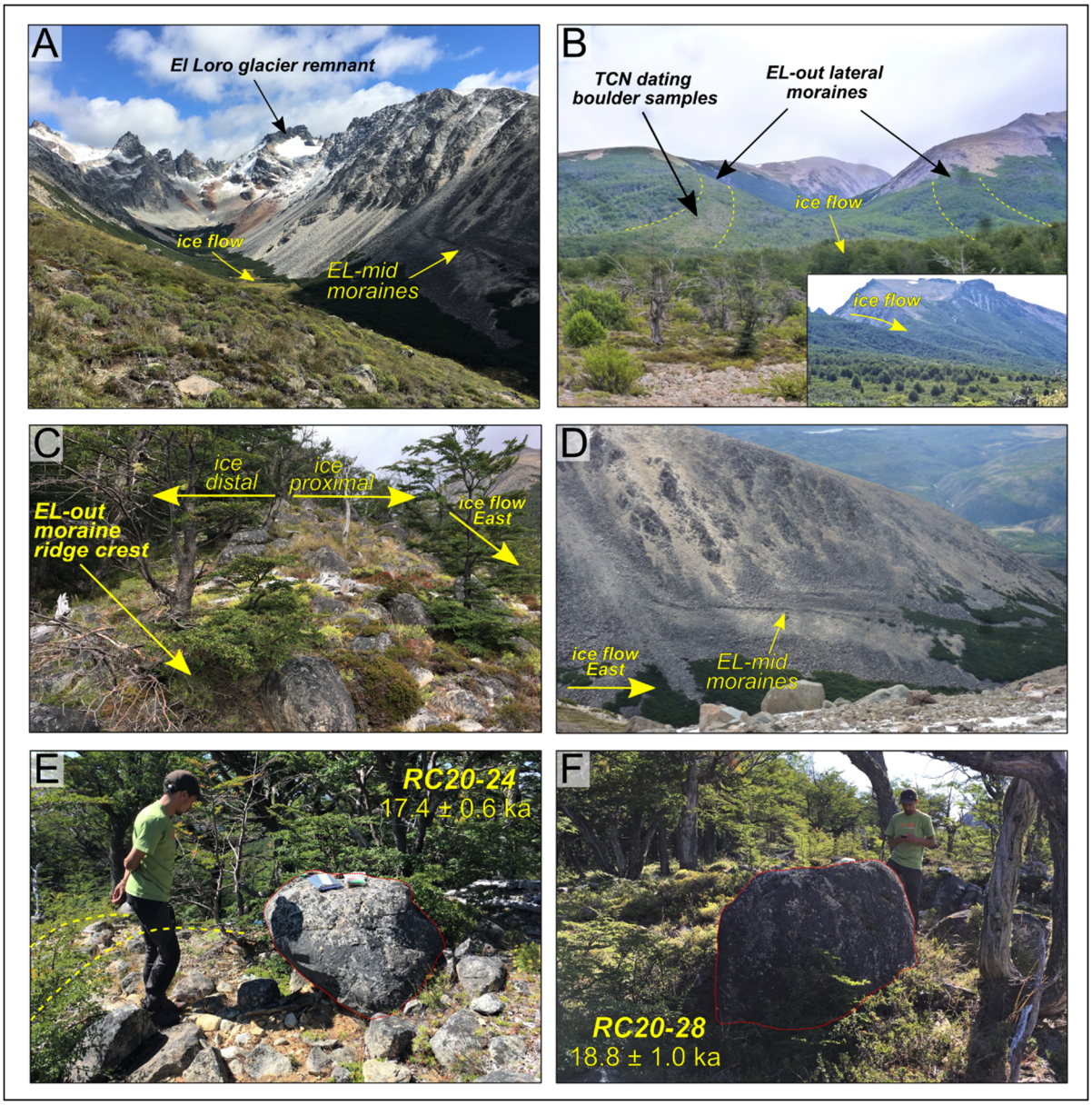

Figure 4.3. Field photographs of the EL valley, moraines and sampled boulders. (**A**) Northwest-facing photograph of the EL valley and its upper catchment displaying the EL-mid moraine ridges nested on the northern valley side. (**B**) Westward view of the EL valley mouth from the provincial road 44 (RP44). The EL-out lateral northern and southern (targeted for sampling) moraine ridges are highlighted by yellow dashed lines. The inset panel provides another, northward view of the same features from further afield. (**C**) Westward-facing photograph captured from the EL-out southern lateral moraine crest (targeted for sampling), ilustrating moraine crest sharpness, ice-proximal and ice-distal moraine-slope angles, moraine-surface boulder sizes, rough lithologies and concentration. (**D**) Northward view of the portion of the northern EL valley side displaying the preserved EL-mid moraine ridges. (**E**) South-facing photograph of an erratic granite boulder (sample RC20-24, highlighted by red line) deposited on the crest of the EL-out southern lateral moraine ridge and sampled for TCN dating. The curvature of the moraine crest is highlighted by yellow dashed lines (**F**) West-facing photograph of an erratic granite boulder (sample RC20-28, highlighted by red line) sampled for TCN dating.

4.3.3 GIA-related uplift estimates

The former PIS covered much of the study area during several Quaternary glaciations, resulting in glacial isostatic adjustment (GIA) of the land surface (Davies *et al*., 2020). Modern GPS station data from the region (Nevada Geodetic Laboratory data[1]) report uplift rates of less than 1 mm yr^{-1}. If assumed to be constant through the period of exposure, such uplift rates would have an insignificant impact on ^{10}Be production rates and numerical modelling outputs. However, the study area is located at the eastern limit of the Patagonian Andes and a significant amount of GIA-related surface uplift is expected to have occurred there during the Last Glacial – Holocene transition. Ice-sheet-wide glacial geomorphological mapping and palaeo-glacial reconstructions (Glasser & Jansson, 2008; Davies *et al*., 2020) suggest that the PIS was ~240 km wide at around 43°S during the local LGM, while data from the PaleoMIST global ice-sheet reconstruction dataset (Gowan *et al*., 2021) estimate that maximum PIS thickness during the global LGM reached approximately 1650 m at these latitudes. In this region of Patagonia, the majority of the ice mass is thought to have melted between 19 and 15-16 ka (Moreno *et al*., 2015; Leger *et al*., 2021), with crustal unloading leading to GIA and to significant surface uplift. To estimate the effect of local GIA on ^{10}Be production and palaeo-climate outputs from glacial numerical modelling, we evaluated former time-varying isostatic uplift and subsidence rates using the ~5 km resolution PaleoMIST global ice-sheet reconstruction dataset (ice-thickness data: Gowan *et al*., 2021) and the gFlex lithospheric flexure model (Wickert, 2015). We calculated the GIA signal for three spatially-invariant lithospheric elastic thickness values (30, 35 and 40 km; after Lange *et al*., 2014). As estimates of local mantle viscosity (Ivins & James, 2004; Lange *et al*., 2014) indicate isostatic response timescales shorter than PaleoMIST's 2.5-kyr temporal resolution, we consider isostatic adjustment to be fully completed within each time step. With this analysis, we produced a paleo-elevation change time series and corrected palaeo-topography at the study site from 25 ka to present.

[1] http://geodesy.unr.edu/NGLStationPages/gpsnetmap/GPSNetMap_MAG.html

4.3.4 Numerical modelling of the EL and RCO palaeo-glaciers

In order to investigate the interaction between climate and the dynamics of the former EL and RCO glaciers, we employed a spatially-distributed ice-flow model, coupled with a positive degree-day (PDD) surface mass balance (SMB) parameterisation. Model parameters were tuned to fit best the simulated ice extent with the observed geomorphological moraine record. Similar models have been used elsewhere to investigate glacier response to climate change (*e.g.* Adhikari & Marshall, 2012; Jouvet & Funk, 2014; Wijngaard *et al*., 2019). The ice-flow model used here follows standard equations of the Shallow Ice Approximation (SIA; Hutter, 1983). While this approximation does not resolve all of the terms of the nonlinear glacial stress balance (*i.e.* longitudinal and transverse stresses), it is much faster to run than higher-order or Stokes models, allowing for ensembles of multi-century simulations exploring a comprehensive range of SMB and ice-dynamical parameters (see below). Other studies have shown this to be an appropriate approximation for modelling small mountain glaciers with small aspect ratios (Wijngaard *et al*., 2019). We implemented the model over a ~30-m resolution topographic grid derived from the AW3D30 DEM.

4.3.4.1 Ice flux

In our model, ice flux was calculated recurrently at a given time-step interval, set to 0.1 years, for each ~900 m^2 grid cell, and accounted for both internal deformation and basal sliding. Internal deformation is controlled by the interaction of the glacier's surface slope and combined weight. In this study we used a uniform ice density value of 916.7 kg m^{-3}. Ice flow occurs when basal shear stress (τ), defined by Glen's flow law (Eq. 1), exceeds a given yield stress value (Cuffey & Paterson, 2010):

$$\varepsilon = A\tau^n \quad (1)$$

where ε is the horizontal shear strain, τ is basal shear stress (Pa) and n and A are constants representing the combined rheological impacts of ice temperature and ice crystal orientation. n and A were here set to values of 3.0 and 1.0 $x10^{-16}$ Pa^{-3} yr^{-1} (Hubbard *et al*., 2005), respectively. Such values are commonly used to account for irregularities in glacier-ice structure such as crevasse fields, meltwater pockets and other impurities (Cuffey & Paterson, 2010).

As geomorphological evidence of subglacial lineations and ice-moulded bedrock outcrops suggests the EL and RCO glaciers were at least partly warm-based, modelled ice flux therefore also needed to incorporate basal sliding, which is defined by equation (2) based on Weertman's law (Weertman, 1957):

$$u_s = A_s \tau_d{}^{\rho} \quad (2)$$

where u_s is basal sliding velocity (m yr^{-1}), A_s and ρ are constants, and τ_d (Pa) is a given value for driving stress. In this study, ρ = 3, which is within the range observed in laboratory and field-based investigations (Budd *et al*., 1979; Bindschadler, 1983). Based on empirical measurements of sliding velocity obtained for similarly-sized, mid-latitude temperate mountain glaciers (*e.g.* Engelhardt *et al*., 1978; Blake *et al*., 1994; Cohen *et al*., 2000), we use a uniform value of 5.0 $x10^{-15}$ Pa$^{-1/3}$ m yr^{-1} for A_s, which yields a sliding rate of 5.0 m yr^{-1} where driving stress (τ_d) is 1 bar. For the EL-outermost advance reconstruction, this parameterisation of basal sliding increased the mean glacier surface velocity by ~6.2 m yr^{-1} relative to simulations implementing no basal sliding. Such a contribution represents ~18% of mean steady-state glacier surface velocity; a ratio that is close to those reported by empirical measurements of sliding speed versus surface speed of glaciers sharing similar properties (*e.g.* Cohen *et al*., 2000; 16%). However, it is important to note that estimating a meaningful value for basal sliding velocity is amongst the most challenging and uncertain components of modelling warm-based glaciers (Cohen *et al*., 2005). Moreover, asuming that the modelled glaciers were warm-based across their entire area and not polythermal is subject to debate and yields uncertainties further addressed in the discussion section of this paper.

4.3.4.2 Surface mass balance

Modelled ice thickness for a given grid cell controls the modelled glacier profile and is defined by the sum of ice flux and SMB. Here we parameterised SMB (*b:* m w.e.) using a PDD model, defined, at a given elevation (*z*), by equations 3-5:

$$b = Pr - (PDD)T,\ T > 0 \quad (3)$$

$$b = Pr,\ T < 0 \quad (4)$$

$$T = zELA\frac{\gamma}{1000} + TSL \quad (5)$$

where *Pr* is precipitation (m ice yr^{-1}), *PDD* is the positive degree-day melt factor (m ice $°C^{-1}$ yr^{-1}), and γ is an adiabatic lapse rate (ALR; °C km^{-1}), which enables interpolating atmospheric temperature *T* (°C) at an elevation *z* (m a.s.l.) using a given value for temperature at sea level (*TSL*: °C). We use an ALR of 6.5 °C km^{-1} (*e.g.* Wallace & Hobbs, 2006; Roe & O'Neal., 2009). As shown by the above equations, *PDD* only causes surface melt when atmospheric temperature exceeds 0 °C (Fig. 4.4). A constant precipitation rate is applied and normally distributed across the domain (*e.g.* Roe & O'Neal, 2009; Roe, 2011), thus assuming little geographical and altitudinal variation across the relatively small EL and RCO valley catchments (~7.5 km^2 and ~10.3 km^2, respectively). This simple SMB model does not independently consider ablation caused by sublimation or ice-front breakoff, nor does it take into account other sources of accumulation such as avalanches. It also neglects the percolation and refreezing of meltwater and assumes that all melting ends up as runoff (after Roe & O'Neal, 2009).

4.3.4.3 Modern climate

Investigating former climate change from palaeo-glacier SMB requires the determination of base values for precipitation and temperature that are representative of average modern local climate. Mean annual temperature data were acquired from five different weather stations located in the towns of Corcovado (n = 1, 43°54'S; 71°46'W), Trevelin (n = 3, 43°5'S; 71°27'W) and Río Pico (n = 1, 44°10'S; 71°22'W). These data were obtained from the Argentinian National Agricultural Technology Institute (www.argentina.gob.ar/inta). *TSL* values were extrapolated from mean annual temperatures using an ALR of 6.5 °C km^{-1}, for the years between 1982 and 2015 (depending on the weather station). The values ranged between 12.06 and 12.65 °C. Given these data, a mean *TSL* value of 12.35 °C was here considered representative of modern regional atmospheric mean annual temperature. Using a 6.5 °C km^{-1} ALR, this is equivalent to a mean annual 0 °C isotherm elevation of 1900 m a.s.l. As measured precipitation data was unavailable, local modern precipitation was obtained from the 1-km spatial resolution global-land WorldClim 2 dataset (WC2; Fick & Hijmans., 2017), which

spatially interpolates available weather station data and provides monthly climate data averaged over 1970-2000. From this dataset, modern-time total annual precipitation was averaged over the simulated steady-state surface area of the EL (16 data points) and RCO (19 data points) palaeo-glaciers to derive estimates of 740 mm *w.e.* and 722 mm *w.e.*, respectively. Using an ice density of 916.7 kg m^{-3}, and assuming that all precipitation is accumulated as ice, these values are equivalent to 0.8072 and 0.7876 m^3 ice m^{-2} yr^{-1} of accumulation, respectively. Consequently, for each simulation, we calculated precipitation and temperature variations relative to modern-day base values of Pr_{EL} = 0.8072 m ice yr^{-1} , Pr_{RCO} = 0.7876 m ice yr^{-1}, TSL = 12.35 °C.

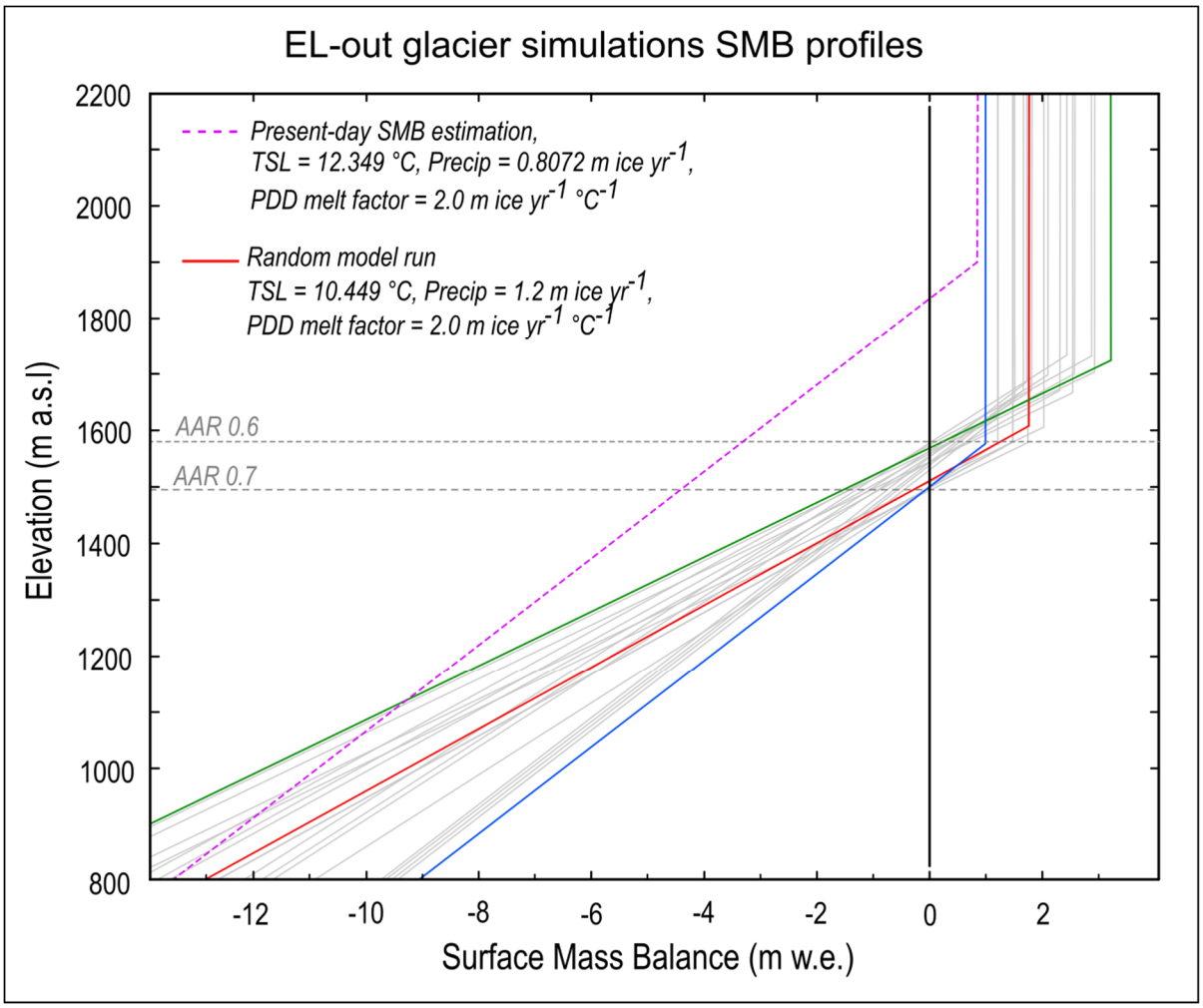

Figure 4.4. A sample (n=20) of Surface Mass Balance (SMB) profiles (grey and coloured lines) of the EL-out ice-flow model simulations using a positive degree-day SMB parameterisation. The pink dashed line is a surface mass balance profile representative of our modern-day climate estimation, according to our assessment of modern local atmospheric temperature and precipitation (section 3.3.3), when using a *PDD* value of 5 mm *w.e.* d^{-1} $°C^{-1}$. Note that the SMB profiles for EL-out model runs intersect the 0 SMB value (*i.e.* the glacier equilibrium line) at elevations associated with AAR values of between 0.6 (green line) and 0.7 (blue line), which are used as threshold values to constrain our model simulations.

4.3.4.4 Model simulations

The model was used to simulate two distinct former advances/still-stands of the EL palaeo-glacier (EL-out and EL-mid) and one advance of the RCO palaeo-glacier (RCO-out), each relating to well-defined moraine complexes observed in the field (Figs 4.2, 4.3). Model simulations were constrained by PDD melt factor thresholds of 5.0 and 9.0 mm *w.e.* d^{-1} $°C^{-1}$, consistent with values reported from stack measurements on mid-latitude mountain glaciers from different regions of the world (Braithwaite *et al*., 2000; Hock, 2003). This is also consistent with PDD melt factors measured on Patagonian glaciers, which typically range from 5.0 to 7.5 mm *w.e.* d^{-1} $°C^{-1}$ (De Angelis *et al*., 2014). Accumulation area ratios (AAR) of 0.6 and 0.7 were also implemented as additional constraints for our simulations. Such values are based on worldwide observations that AARs > 0.7 or < 0.6 have produced less realistic SMB profiles for debris-free, mid-latitude temperate mountain glaciers in a state of mass-balance equilibrium, and > 4 km^2 in surface area (Benn *et al*., 2005; Kern & László, 2010; Pellitero *et al*., 2015). However, this assumption yields significant uncertainties as it is challenging to estimate former glacier debris cover evolution, which, if sufficiently thick, could substantially lower the AAR through glacial surface insulation (Osmaston *et al*., 2005). Moreover, surface debris cover is likely to fluctuate through time as glacier retreat and thinning causes valley-side destabilisation. The AAR was calculated for each simulated ice extent deemed to match the sampled moraines using model-output ice-thickness raster data and the SurfaceVolume_3D ArcGIS tool (following Pellitero *et al*., 2015). Ice-front to moraine fit was assessed by producing modelled ice-surface longitudinal cross-section profiles along the glacier centre flowline for each simulation and comparing ice-front location with terminal moraines. ArcGIS 10.8 software was subsequently employed to digitize ELA polylines and total glacier and accumulation zone polygons using ice-surface topographic contour lines, prior to computing AARs using polygon 3D surface areas. Therefore, within such PDD melt factor and AAR constraints, a minimum of thirty to forty simulations were adjusted for each of the EL and RCO glaciers and for each reconstructed glacier-front position (EL = 2 positions, RCO = 1 position) to determine ranges of ideal precipitation and temperature parameter combinations producing moraine-matching glacier extents. In total, near one hundred multi-century model simulations with differing SMB parameters were adjusted to fit the geomorphological record, excluding model sensitivity test runs (see section 3.2.5 below) and multi-century simulations that correlated poorly with observed moraine locations. For each given round-number PDD melt factor (5-9), a second order polynomial regression equation with a R^2 value greater than 0.99

was calculated to provide a relationship between ideal precipitation and temperature parameter combinations.

In contrast to Stokes or high-order numerical glacier models, our model does not require high computational speeds and enables comparing numerous simulations against the geomorphological record using a wide range of SMB parameter values. It also enables palaeo-temperature and palaeo-precipitation estimations even in the absence of a modern active glacier at the study site, although the lack of studied modern glaciers in the Poncho Moro massif makes calibrating the model against present-day glaciological and meteorological conditions challenging, leading to larger uncertainties in SMB parameter range estimates. Unlike palaeo-climate estimations relying on ΔELA comparisons (*e.g.* Sagredo *et al*., 2018; Sun *et al*., 2020), our method does not require a modern ELA value to derive palaeo-temperature estimates. Furthermore, it does not assume that precipitation was identical to the present at the time of the reconstructed glacier advance/still-stand, because accumulation is already taken into account in our SMB parameterisation. We thus consider SMB model outputs as more realistic palaeo-climate indicators and chose not to compare our results with an estimated modern ELA, as in the absence of active glaciers in the study area, this would be highly subjective.

4.3.4.5 Model sensitivity tests

In order to test confidence in using our SMB parameter combinations as potential palaeo-climate indicators, we tested the model by running simulations with different ice softness parameters (constant A in Glen's flow law; Eq.1) to simulate different ice-temperature regimes. While the default value chosen is $1.0\ x10^{-16}$ Pa^{-3} yr^{-1}, which corresponds approximately to a mean glacier-ice temperature of -2 °C, we also conducted model runs with boundary values of $0.5\ x10^{-16}$ and $1.5\ x10^{-16}$ Pa^{-3} yr^{-1}, corresponding to ice temperatures of approximately -5 °C and 0 °C (Cuffey & Paterson, 2010), respectively (Table 1). The results generated a maximum glacier volume increase ($A = 0.5\ x10^{-16}$) of 16% and a maximum decrease ($A = 1.5\ x10^{-16}$) of 7%. Such fluctuations in ice thickness are mostly confined to the accumulation zone of the glacier, and therefore they have minimal impact on the extent and thickness of the glacier tongue. The greatest change observed in glacier-front location as a result of sensitivity to fluctuations in A values was a retreat of 94 m, which represents a 2.5% decrease in glacier extent. For most other simulations, maximum glacier extent remained within a 1% fluctuation to the original ($A = 1.0\ x10^{-16}$). Therefore, modifying the glacier-ice temperature regime within

a -5 °C to 0 °C range has little impact on the model's ability to match the geomorphological moraine record.

Note that our adjustment of the ice-softness parameter is equivalent to the consideration of a correction factor in Wijngaard *et al.* (2019) -- *i.e.*, a factor meant to represent the inaccuracies inherent in the SIA. In this sense, the low sensitivity to Glen's flow constant suggests a wide range of correction factors, or equivalently that the assumptions of the SIA have a relatively small impact on steady glacier geometry and length.

We also conducted test model runs by removing the effect of basal sliding (Table 4.1). The results showed that although the glacier took up to 30 years longer to build up, steady-state glacier extent and thickness were identical to runs conducted with basal sliding, indicating that changing the basal sliding velocity within a realistic range had little impact on steady-state ice thickness, ice-front location and glacier surface profile. However, we do note that doubling of the baseline sliding parameter described in section 3.4.1 caused a noticeable reduction in simulated ice-thickness and augmentation in ice-front extent.

We also tested the model's sensitivity to DEM spatial resolution by running a series of simulations using the ALOS PALSAR DEM product (Dataset[2]) which, in the studied region, uses radiometric terrain correction to re-sample the AW3D30 DEM product to 12.5 m spatial resolution. Despite a 2.4 times greater spatial resolution, the simulated ice thickness, glacier extent, surface velocity and years required to reach steady-volume were all identical to simulations conducted using a ~30 m spatial resolution DEM.

To compare our model outputs to the more commonly-used method of land-terminating glacier surface reconstruction using a simple flowline model (*e.g.* Huss *et al.*, 2007; Banerjee & Shankar, 2009), we conducted simulations using GlaRe (Pellitero *et al.*, 2016) and included the associated methodology and results in the Supplementary materials.

To assess variability in PDD melt factor values from different palaeo-glaciers of the region, and to obtain further local climatic constraints during the late-glacial period, we

[2] Dataset: ASF DAAC 2015, ALOS PALSAR_Radiometric_Terrain_Corrected_low_res; Includes Material © JAXA/METI 2007. Accessed through https://asf.alaska.edu on 20th September 2018.

compared SMB parameters required for moraine-matching simulation of both the EL and RCO glaciers. We considered it reasonable to assume that climatic conditions are and were likely very similar between the two adjacent valleys. This is supported by WC2 total annual precipitation data, indicating a 1970-2000 mean of 722 mm *w.e.* over the simulated RCO glacier surface area (Fick & Hijmans., 2017), representing a 2.4% decrease relative to the adjacent EL valley (740 mm *w.e.*). Using identical AAR and PDD melt factor constraints for the SMB model as for the EL glacier simulations, we adjusted thirty model runs with a simulated ice-front extent that matches the RCO valley moraine system in order to analyse input SMB parameter combinations required. Assuming that this advance was contemporaneous with the EL late-glacial advance sampled for TCN dating, analysing the overlap in the resulting climate constraints from the two sets of simulations can provide better confidence in resulting temperature and precipitation ranges required for moraine-matching simulations, and enables assessment of surface melt-rate variability between the two glaciers. Indeed, it is feasible and has been observed in other modern glaciated massifs (*e.g.* Glacier d'Arsine and Glacier Blanc, Ecrins massif, France; Vivian, 1967; Vivian & Volle, 1967), that two proximal mountain glaciers with similar elevation ranges and climatic conditions can display substantially different surface debris covers, mainly as a result of contrasting susceptibility of upper catchment slopes to rockfall and rock-slope failures (Benn *et al*., 2003). Therefore, some variability in former surface melt rates between the two glaciers may be expected, which may hinder the quality of overlaps in SMB parameter ranges required for the moraine-matching simulations of both glacier advances, in the hypothetical case of these advances being triggered by the same climatic event.

Table 4.1. Coupled ice-flow and positive degree-day SMB model input parameters.

Model parameter	Unit	Initial value / range	Test range
Time step	Yr	0.1	0.05 - 0.1
Ice softness (A)	$Pa^{-3}\ yr^{-1}$	$1.0\ x\ 10^{-16}$	$0.5\ x\ 10^{-16}$ - $1.5\ x\ 10^{-16}$
Ice-flow law exponent	constant	3.0	n/a
Ice density	$kg\ m^{-3}$	917	n/a
DEM spatial resolution	m	27.15	12.5 - 30
Atmospheric lapse rate	$°C\ km^{-1}$	6.5	n/a
Weertman 's law constant A_s	$Pa^{-1/3}\ m\ yr^{-1}$	$5.0\ x\ 10^{-15}$	0 - 10.0^{-14}
Weertman's law constant ρ	constant	3.0	n/a
Degree-day melt factor *(PDD)*	$mm\ w.e\ d^{-1}\ °C^{-1}$	5.0 - 9.0	5.0 - 9.0
Glacier AAR	n/a	0.6 - 0.7	0.6 - 0.7

4.4 Results

4.4.1 Geomorphology

4.4.1.1 Valley geomorphology

In the upper EL and RCO catchments, above the treeline (1400-1500 m a.s.l.), the valley floors are characterised by thick glacial debris cover and patterned ground displaying polygonal structures that are characteristic of periglacial environments and indicative of cryoturbation and frost heaving following ice retreat. These debris accumulations are interspersed in the steeper portions of the valley bottom by outcrops of ice-moulded and striated bedrock (Fig. 4.2a). The upper EL and RCO catchments contain numerous empty cirques, while the EL valley still features one glacier remnant (~0.05 km^2) perched below its highest summit (~2095 m a.s.l.; Fig. 4.2a). Debris cones and rock talus mantle the steep valley sides and indicate frost shattering of cliffs and local catchment ridges. Consequently, substantial volumes of rockfall debris partly obscure the palaeo-glacier bed topography.

4.4.1.2 Glacial moraines

Geomorphological mapping from field and remotely-sensed observations reveals the preservation of three distinct moraine complexes deposited by glacier-ice confined within the EL valley, two of which are also present in the RCO valley (Fig. 4.2).

In the EL valley, the outermost set of moraine ridges (*EL-out*) is located towards the eastern edge of the Poncho Moro massif, 1.5-2 km to the east of the valley mouth, and indicates a northeastward advance of the EL glacier. This complex can be linked to well-defined, ~1.5 km long, single-crested and prominent (30-35 m above the valley floor) lateral moraines preserved on both valley flanks (mean crest-surface slope: 13°; Fig. 4.3). Both of these lateral ridges bifurcate downstream into a series of cross-valley arcuate ridges and hummocks spreading at least 1 km across a gently-sloping surface, which is suggestive of numerous episodes of terminus extent fluctuation and/or re-advances of the EL glacier (Fig. 4.2a). The geometry of these terminal ridges and mounds suggest a piedmont-style former EL glacier terminus. The lateral moraine complex cross-cuts at right angles the RC III-VI moraines previously deposited by the Río Corcovado outlet glacier (Fig. 4.2). Consequently, the advance

of the EL glacier must post-date the RC VI moraine, which has been dated using ^{10}Be TCN dating to 20.7 ± 1.0 ka (Leger *et al.*, 2021). Moreover, directly downstream of the terminal moraines, a broad (0.85 km^2 in area) low-gradient (2°) and homogeneous surface composed of fluvial sand and gravel progrades eastwards (43°43'59"S; 71°23'53"W). This terrace deposit, which was incised by the EL river post-deposition (~10-15 m incision), is interpreted as a proglacial outwash plain. It thus provides further evidence of a former glacier margin stabilised directly upstream from its location. The location of this deposit indicates that former proglacial rivers were constrained towards the north by the previously-deposited RC VII moraine. Such stratigraphic relationships further suggest that the EL-out advance is younger or similar-in-age to the deposition of the RC VII moraine, previously dated to 19.9 ± 1.1 ka (Leger *et al.*, 2021). We targeted the prominent, sharp-crested southern lateral moraine ridge for TCN dating based on the assumption that it highlights maximum palaeo-glacier thickness and thus the most extensive, morphostratigraphically-oldest advance of the EL glacier into this moraine complex.

The RCO valley contains an analogous set of single-crested and prominent lateral moraine ridges nested on both valley flanks, which are located towards the mouth of the valley (Fig. 4.2). These moraines exhibit curved geometries towards their distal ends, enabling a rough extrapolation of the former ice-front position during this advance. However, the exact position of the terminal moraine is uncertain as a consequence of local erosion by post-retreat fluvial incision. This moraine complex and associated advance are termed *RCO-out* and we consider it morphostratigraphically-equivalent to the *EL-out* moraine complex.

A second, younger complex of latero-terminal moraine ridges are evident in the EL valley, located approximately 3.8 km from the valley headwall. These moraines demarcate a former glacier front positioned ~2.4 km upstream (~40% glacier-extent decrease) from the EL-out margins. This younger complex is composed of three adjacent ridges that extend for ~500 m, are curved towards their distal ends, and reach an elevation of ~1300 m a.s.l. The ridges are relatively low in relief (2-5 m), with less well defined crests, and are only discernible on the northern valley flank (Fig. 4.3 a,d). Their proximal end seems to have been buried by the post-glacial accretion of rock talus. Their geomorphology is suggestive of a significantly lower sediment volume delivery and/or ice-front residence time than the EL-out moraine sequence. We refer to these deposits as the *EL-mid* moraine complex and associated glacier advance/still-stand. We did not identify geomorphic evidence of a similar mid-valley moraine complex in the RCO valley.

Finally, in both the EL and RCO valleys, smaller moraine ridges can be discerned in the upper catchment limits, near the downstream edge of isolated eastward-facing (down-wind) cirques, nested at elevations of between 1500 and 1800 m a.s.l. (Fig. 4.2). We only observed a single set of these moraines in the EL valley while the RCO catchment displays at least four cirques where such ridges are preserved. They highlight the former stabilisation/re-advance of small glaciers nested on the catchment's highest, wind-sheltered slopes. We hypothesise these deposits to be relatively young, perhaps late-Holocene or Neoglacial in age, given the late-Holocene relative glacier-extent loss observed in other Patagonian mountain valleys (*e.g.* Nimick *et al*., 2016, Reynhout *et al*., 2019).

4.4.2 ^{10}Be surface exposure ages

The six boulders from the southern lateral moraine of the EL valley range in age from 16.4 ± 0.5 ka to 19.5 ± 0.6 ka and yield an arithmetic mean exposure age of 18.0 ± 1.15 ka. The age population demonstrates a relatively high and >1 mean square weighted deviation (MSWD) value of 3.78, thus suggestive of greater age scatter than can be predicted solely by 1σ analytical uncertainties (Table 4.3, Fig. 4.5). Furthermore, the MSWD value exceeds the criterion *k*, which is dependent on the degree of freedom, and is equal to 2.26 given the number of samples (n = 6; Wendt & Carl, 1991; Jones *et al*., 2019a). Statistically, a MSWD > *k* suggests that the probability that the age population is representative of a single landform is <95% and thus the weighted mean cannot be used as an estimate of the average exposure age for the moraine (Jones *et al*., 2019a). Despite significant geological scatter, we do not identify obvious outliers as all ages fall within the population's 2σ envelope (Fig. 4.5).

Table 4.2. Sample details and nuclide concentrations

Sample ID	Latitude (DD)	Longitude (DD)	Elevation (m a.s.l)	Boulder height (m)	Thickness (cm)	Shielding correction	Qtz mass dissolved (g)	$^{10}Be/^{9}Be$ ratio	±1σ	^{10}Be atoms $g^{-1}(SiO_2)$	±1σ atoms $g^{-1}(SiO_2)$	ASTER Cathode code
El Loro southern lateral moraine boulders												
RC20-23	-43.73891	-71.42438	1130	0.75	2.0	0.995836	19.9409	1.229E-13	3.987E-15	1.812E+05	5.943E+03	CHJE
RC20-24	-43.73847	-71.42151	1062	0.57	3.5	0.997264	20.6879	1.167E-13	3.665E-15	1.586E+05	5.042E+03	CHJF
RC20-25	-43.73849	-71.42172	1066	0.90	3.5	0.997264	20.5538	1.068E-13	3.344E-15	1.492E+05	4.732E+03	CHJG
RC20-26	-43.73944	-71.42575	1167	0.70	2.0	0.994171	19.0499	1.325E-13	4.080E-15	1.978E+05	6.154E+03	CHJH
RC20-27	-43.73849	-71.42128	1058	0.75	2.8	0.995988	19.4417	1.085E-13	3.463E-15	1.583E+05	5.114E+03	CHJI
RC20-28	-43.73828	-71.41911	1005	0.89	4.0	0.996217	19.4481	1.112E-13	5.998E-15	1.639E+05	8.934E+03	CHJJ

Table footnotes. Rock density is assumed to be 2.65 g cm^{-3}. Samples were collected in january 2020.

Table 4.3. Exposure ages and summary statistics

	Kaplan *et al.* (2011) production rate									
Sample ID	LSDn: *Lifton et al. (2014)*			St: *Lal (1991) and Stone (2000)*			Lm: *Lal (1991) and Stone (2000)*			Outlier
	Age	Internal	External	Age	Internal	External	Age	Internal	External	
	Cal Yr BP			Cal Yr BP			Cal Yr BP			
El Loro southern lateral moraine boulders										
RC20-23	18462	608	1628	18636	614	1653	18365	605	1628	no
RC20-24	17373	555	1525	17397	555	1536	17201	549	1518	no
RC20-25	16358	521	1435	16307	519	1439	16177	515	1427	no
RC20-26	19483	609	1706	19796	619	1744	19441	608	1712	no
RC20-27	17318	562	1523	17333	563	1533	17142	556	1516	no
RC20-28	18811	1031	1852	18907	1036	1870	18614	1020	1840	no
Mean (n = 6): **17.97** ka; 1σ std: **1.15** ka; 1σ internal: 1.64 ka; 1σ internal + PR%: 2.20 ka										
Uncertainty weighted mean (n = 6): 17.85 ka; 1σ std: 1.07 ka										
MSWD: 3.78 > *k*: 2.26 (n=6); Peak age (n=6): 17.42 ka										

Table footnotes. Scaling schemes: St is the time-independent version of Lal (1991) and Stone (2000), Lm is the time-dependent version of Lal (1991) and Stone (2000), and LSDn is the time-dependent scheme of Lifton *et al.* (2014). External uncertainties include production rate (PR%) and scaling uncertainties. Elevation flag is std. Landform summary age reported in the paper's results and discussion sections is here highlighted in bold.

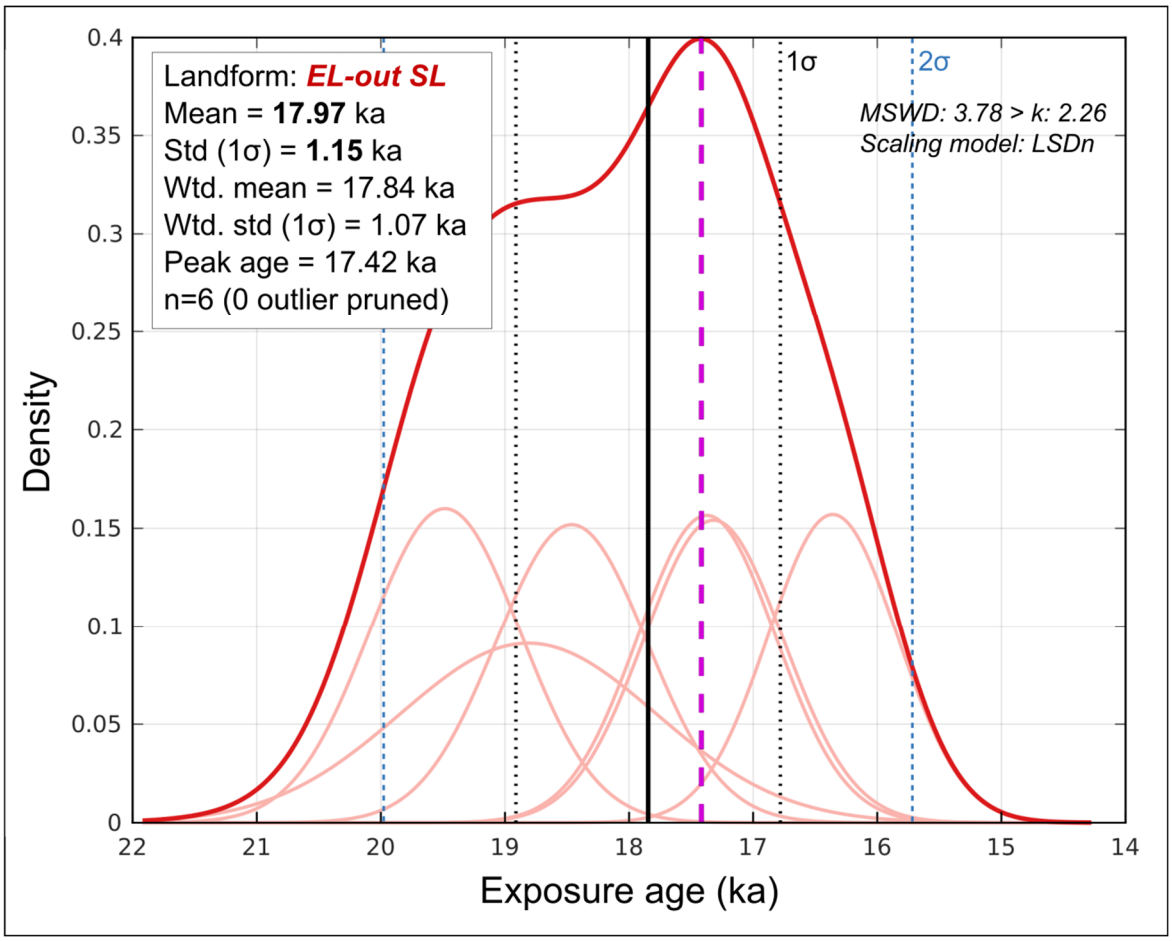

Figure 4.5. Kernel density plot, adapted from plots produced using the iceTEA tools for exposure dating (Jones *et al*., 2019a; http://ice-tea.org/en/) and TCN dating summary statistics for the EL-out southern lateral (EL-out SL) moraine boulder samples (n=6). Thick red curve represents the summed probability distribution for the age population while thin red curves depict Gaussian curves for individual samples. Vertical black lines denote the arithmetic mean, while thin black and blue vertical dashed lines denote the 1 σ and 2 σ confidence intervals of the mean, respectively. Thick purple and dashed vertical line highlights the peak age associated with the summed probability distribution. *Std*: standard deviation, *Wtd. mean*: uncertainty-weighted mean, *Wtd. std*: uncertainty-weighted standard deviation.

4.4.3 GIA-related uplift

Output from the gFlex lithospheric flexure model (Wickert, 2015) suggests that the surface elevation of the study site at 20 ka was between 148 m (40 km elastic thickness) and 151 m (30 km elastic thickness) lower than modern elevations measured in the field (Table 4). These cumulative uplift values are close to the estimate of 113.9 m obtained from the global ICE-6G model (Peltier *et al.*, 2015) and a three-layer approximation of the VM2 Earth model implemented in the IceTEA tools for exposure ages (Jones *et al.*, 2019b). GIA-related uplift modelling using gFlex suggests that over 99% of post-LGT uplift occurred between 20 ka and 12.5 ka in response to local ice-sheet disintegration (Table 4). The 2.5 kyr temporal resolution of the PaleoMIST dataset (Gowan *et al.*, 2021) provides local, time-varying GIA-related uplift rates approximating 9.1, 39.4 and 11.6 mm yr^{-1} between 20-17.5 ka, 17.5-15 ka, and 15-12.5 ka, respectively. Using such uplift rates, a mean elastic thickness of 35 km, and a mean age of 18.0 ka for the EL-out advance based on our exposure age population, we estimate GIA to have caused approximately 131 m of surface uplift since the time of the EL-out glacier advance. The impact of such surface elevation change on former ^{10}Be production rates and exposure ages is inferior or equivalent to 1σ analytical uncertainties (between 0.47 and 0.74 ka; <4% age corrections), and is thus not considered applicable here. However, the inferred mean uplift of 131 m since 18 ka, the approximate time of the EL-out glacier advance, requires taking into account 0.85 °C of local atmospheric temperature adjustment when applying an ALR of 6.5 °C km^{-1}. Consequently, we adjusted our modelling ELA and temperature outputs using 131 m of surface uplift and 0.85 °C of relative temperature lowering for a given model simulation in order to account for GIA-related uplift since the time of the reconstructed advance. These reconstructed uplift rates are inherently subject to uncertainties associated in part with the assessment of parameters such as regional palaeo-ice thicknesses, lithospheric thickness and mantle viscosity (Peltier *et al.*, 2015; Wickert, 2015; Gowan *et al.*, 2021). However, our estimates are similar in magnitude to modern uplift rates observed for regions of Patagonia currently experiencing rapid isostatic uplift due to present-day glacial retreat and ice-sheet thinning. For instance, Lange *et al.* (2014) reported modern uplift rates from geodetic GNSS observations of up to 41 ± 3 mm yr^{-1} near the centre of the Southern Patagonian Icefield (SPI), and of approximately 20 mm yr^{-1} towards the margins of the SPI. Although regional tectonic uplift may also contribute a small part of this uplift (Richter *et al.*, 2016), these modern rates suggest that our post-LGT GIA-uplift estimates are comparable and relatively realistic for Patagonia.

Table 4.4. gFlex GIA-related surface elevation and PaleoMIST ice-thickness data

Age (ka)	Cumulative GIA-related uplift (m)			Uplift per 2.5 ka interval (m)			Ice thickness (m)
	Elastic thickness						PaleoMIST 1.0 data
	30 km	35 km	40 km	30 km	35 km	40 km	Gowan *et al*. (2021)
25	-0.362	-0.362	-0.362	0	0	0	592.541
22.5	-0.146	-0.135	-0.135	0.216	0.227	0.227	601.949
20	-0.350	-0.330	-0.330	-0.204	-0.195	-0.195	573.919
17.5	22.721	23.072	23.072	23.071	23.402	23.402	617.747
15	121.657	121.257	121.257	98.936	98.185	98.185	264.197
12.5	150.980	148.053	148.053	29.323	26.797	26.797	0
10	150.974	148.049	148.049	-0.005	-0.005	-0.005	0
7.5	150.982	148.056	148.056	0.007	0.007	0.007	0
5	150.983	148.057	148.057	0.001	0.001	0.001	0
2.5	150.975	148.049	148.049	-0.008	-0.008	-0.008	0
0	150.974	148.048	148.048	-0.001	-0.001	-0.001	0

Table footnotes. Data reported here are based on ice-thickness data for coordinates of the EL valley study site: 43°43’55”S; 71°27’38”W

4.4.4 Numerical modelling results

4.4.4.1 Glacier geometry

Our spatially-distributed ice-flow model generated simulated glacier surfaces that match lateral and terminal moraine complexes well for a given advance/still-stand. However, while steady-state simulated ice-fronts matched the terminal moraine record for the EL-mid and RCO-out simulations, the simulated EL-out ice front stabilised ~100 m upstream from the moraine complex. Further ELA lowering did not generate significant ice-front advances, instead inducing a wider piedmont-style ice front overrunning the lateral moraine ridges. There are numerous possible reasons for such a misfit, including, for instance, the model's inability to capture spatially-varying basal sliding conditions and ice temperature properties, and the possibility of post-advance debris accumulations near the former glacier terminus, which could have caused a decrease in basal slope gradient. Therefore, for the EL-out simulations, we based our moraine-fit quality assessment on the location of the ice margin relative to the prominent EL-out lateral moraine ridges. Simulated steady-state glacier volume for the EL-out glacier advance ranged between 0.614 km^3 (0.563 Gt) and 0.769 km^3 (0.705 Gt) depending on SMB parameter combinations, while steady-state surface area ranged between 7.154 km^2 and 7.234 km^2 (Table 4.5, Figs. 4.6, 4.7). Simulations took between 100 and 170 years to reach steady volume from a no-ice initial state. Maximum ice thickness ranged between 272 m and 315 m and glacier length along the central flowline approximated 6.1 km from the valley headwall. Mean steady-state glacier-surface velocity, which is positively correlated to accumulation rates and thereby ice flux, ranged between 31.9 m yr^{-1} (run with lowest precipitation) and 61.0 m yr^{-1} (run with highest precipitation) (Table 4.5, Fig. 4.6). These surface velocities are consistent with average surface velocities measured in the field and through remote sensing of land-terminating and similarly-sized glaciers from northern Patagonia (Rivera *et al*., 2012) and other mid-latitude alpine massifs (*e.g.* New Zealand Southern Alps, Mont-Blanc massif; Millan *et al*., 2019). Corresponding glacier geometry statistics for the RCO-out and EL-mid advances/still-stands are compiled in Table 5.

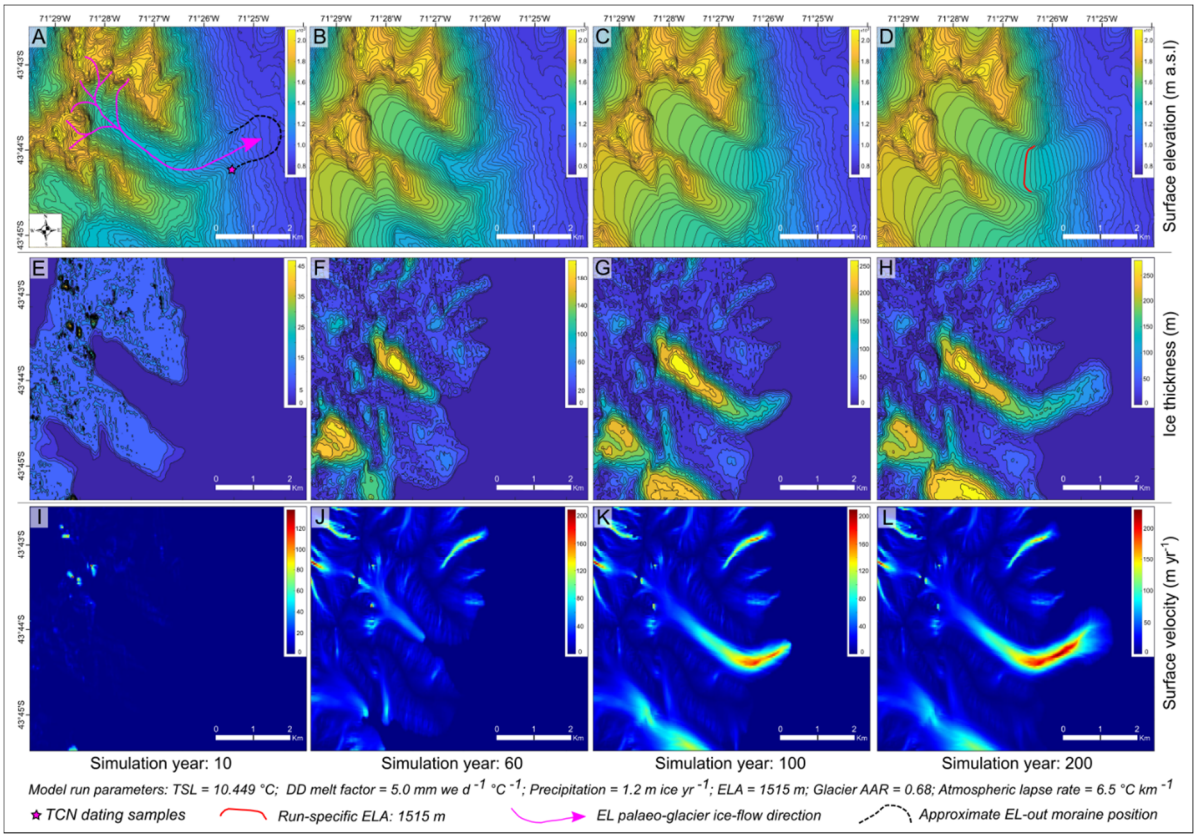

Figure 4.6. Ice-flow model output data (~30 x ~30 m grid-cell spatial resolution) for one selected model simulation of the EL-out advance. (**A-D**) Surface elevation data (m a.s.l.) including AW3D30 DEM data plus simulated ice thickness, (**E-H**) ice thickness data (m), and (**I-L**) ice-surface velocity data (m yr^{-1}); for simulation years 10 (panels A, E, I), 60 (panels B, F, J), 100 (panels C, G, K) and 200 (steady-state volume, panels D, H, L). Note that colorbar values and scaling are panel-specific. Equivalent figures specific to the RCO-out and EL-mid advances/still-stands model simulations can be found in the Supplementary materials (Chapter 4 figures SM 1, 2).

4.4.4.2 Palaeo-temperature

For the EL-out glacier advance, here dated to 18.0 ± 1.15 ka, simulations constrained by PDD melt factor values ranging between 5.0 and 9.0 mm *w.e.* d^{-1} $°C^{-1}$ and by AAR values of between 0.6 and 0.7 required a range of temperature depression values relative to our present-day mean annual atmospheric temperature estimation (section 3.2.3) of between -1.0 °C and -1.9 °C (Table 4.5, Fig. 4.8a). Including correction for cumulative GIA-related surface uplift relative to today (-0.85 °C; Table 4.4) causes temperature depression values to range between -1.85 °C and -2.75 °C. Moraine-matching simulations conducted using a temperature depression that is greater than 2.75 °C caused the ELA to increase and the glacier's

accumulation zone to expand so that the AAR becomes greater than 0.7, a ratio that is rare for a mid-latitude, land-terminating mountain valley glacier in a state of mass-balance equilibrium (Braithwaite & Müller, 1980; Kern & László, 2010), and is here assumed unlikely (Table 5, Fig. 4.8a).

4.4.4.3 Palaeo-precipitation

The model simulations required precipitation values ranging between ~1.2 and ~3.9 m ice yr^{-1}, which, since we are assuming that all precipitation accumulates as glacier ice, translates to total annual precipitation values of 1100 and 3575 mm *w.e.* yr^{-1}, respectively, using an ice density of 916.7 kg m^{-3} (Fig. 4.8a). These precipitation values represent increases of between 49% and 383% relative to modern precipitation (742 mm *w.e.* yr^{-1}; WC2 data; Fick & Hijmans., 2017), respectively. Conducting moraine-matching simulations with similar to, or smaller than, modern-day precipitation caused the simulated glacier AAR to be greater than 0.7. Therefore, our model outputs suggest that local precipitation was greater than present during this late-LGM glacier advance (Table 4.5, Fig. 4.8a). Our results also showed that, when using a minimum PDD melt factor of 5.0 mm *w.e.* d^{-1} $°C^{-1}$, simulations conducted with temperature depressions that are between -1.0 °C and -1.5 °C (-1.85 °C : -2.35 °C with GIA-related uplift correction) required at least twice more and up to four times more precipitation relative to modern values.

Corresponding ice-flow model output statistics for reconstructions of: 1) the RCO-out glacier advance, and 2) the EL-mid glacier advance/still-stand; are compiled in Table 4.5 and Figures 4.7, 4.8.

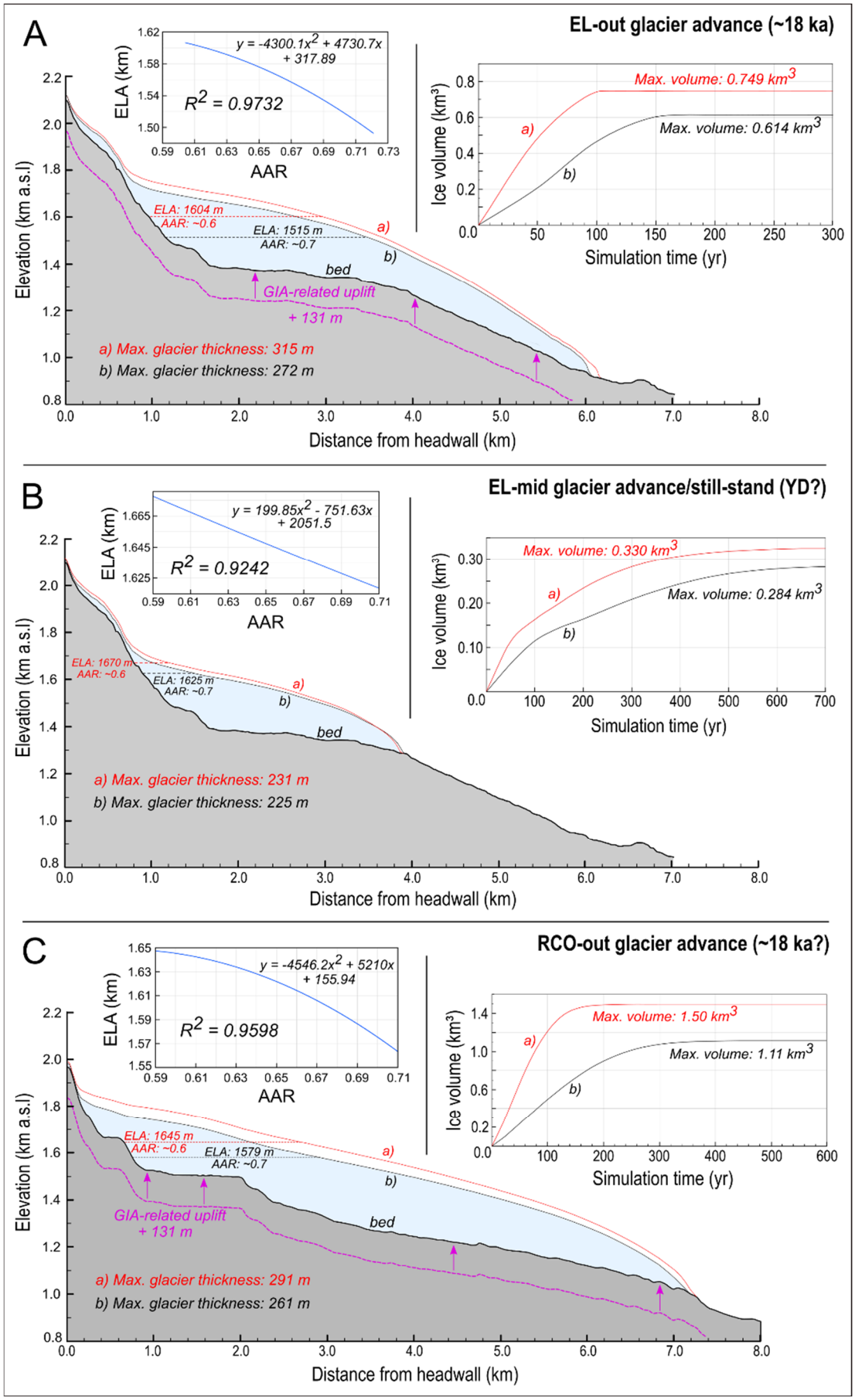
A
EL-out glacier advance (~18 ka)
y = -4300.1x² + 4730.7x + 317.89
R² = 0.9732
ELA (km)
AAR
Max. volume: 0.749 km³
Max. volume: 0.614 km³
Ice volume (km³)
Simulation time (yr)
ELA: 1604 m
AAR: ~0.6
ELA: 1515 m
AAR: ~0.7
bed
GIA-related uplift
+ 131 m
a) Max. glacier thickness: 315 m
b) Max. glacier thickness: 272 m
Elevation (km a.s.l)
Distance from headwall (km)
B
EL-mid glacier advance/still-stand (YD?)
y = 199.85x² - 751.63x + 2051.5
R² = 0.9242
Max. volume: 0.330 km³
Max. volume: 0.284 km³
ELA: 1670 m
AAR: ~0.6
ELA: 1625 m
AAR: ~0.7
a) Max. glacier thickness: 231 m
b) Max. glacier thickness: 225 m
C
RCO-out glacier advance (~18 ka?)
y = -4546.2x² + 5210x + 155.94
R² = 0.9598
Max. volume: 1.50 km³
Max. volume: 1.11 km³
ELA: 1645 m
AAR: ~0.6
ELA: 1579 m
AAR: ~0.7
GIA-related uplift
+ 131 m
a) Max. glacier thickness: 291 m
b) Max. glacier thickness: 261 m

Figure 4.7. Elevation profile graphs (above present-day sea level) of bedrock topography (AW3D30 DEM data) and simulated steady-state ice thickness along the central glacier flowline for the EL-out (**A**), EL-mid (**B**) and RCO-out (**C**) simulations. The purple dashed lines denote the estimated former bed surface elevation at the time of the EL-out advance, prior to GIA-related uplift (131 m). For each profile graph, the two ice-surface profiles highlighting maximum and minimum simulated ice-thicknesses for a given advance/still-stand are represented. These two profiles also represent boundary AAR values (0.6 vs 0.7). Each panel also features an ice-volume time series line graph for minimum and maximum ice-volume simulations, as well as a standard regression analysis establishing the best-fit second-degree polynomial relationship between ELAs (km a.s.l.) and AARs for all simulations of a given glacier reconstruction.

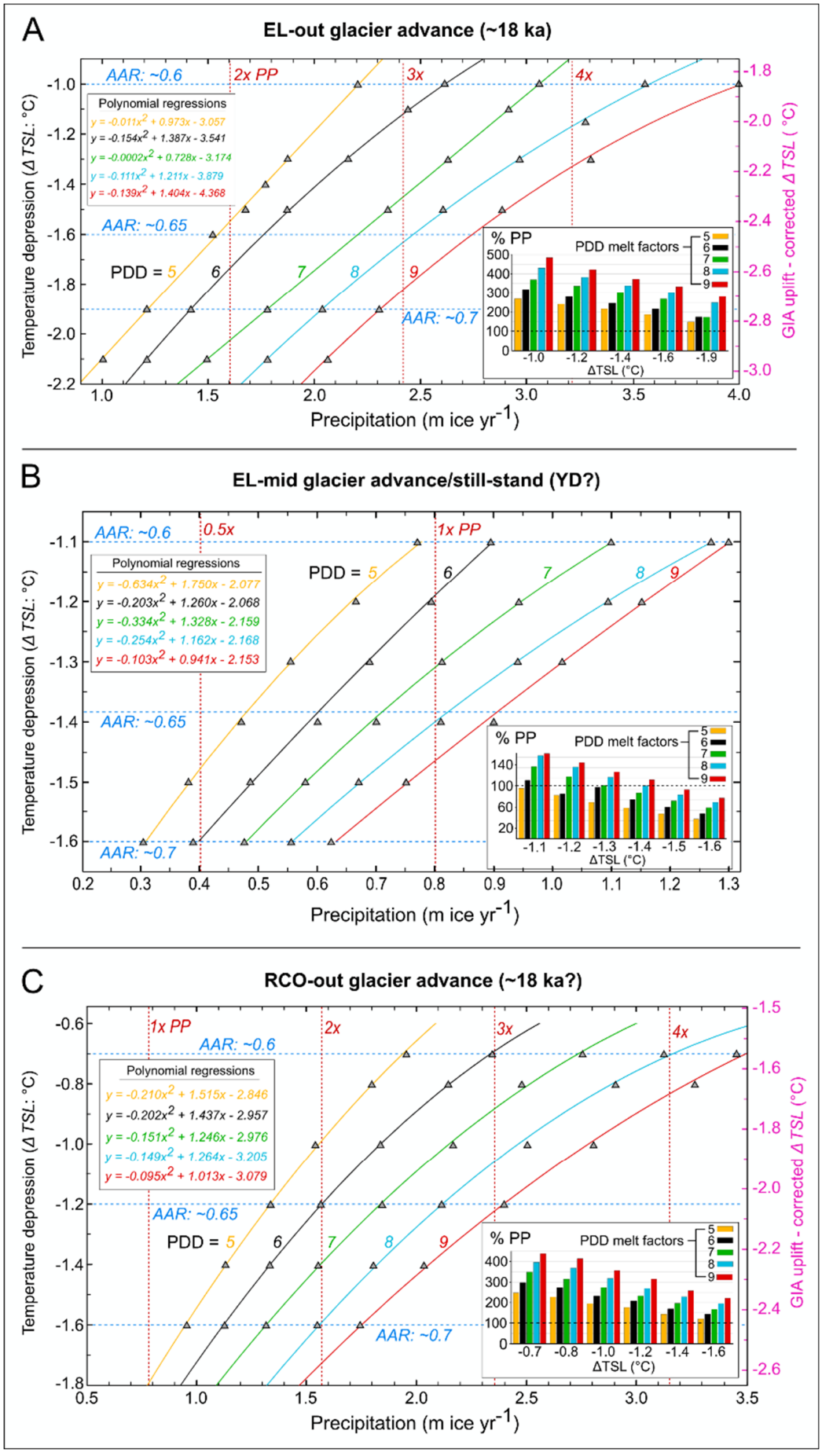
A
EL-out glacier advance (~18 ka)
AAR: ~0.6
2x PP
3x
4x
Polynomial regressions
y = -0.011x2 + 0.973x - 3.057
y = -0.154x2 + 1.387x - 3.541
y = -0.0002x2 + 0.728x - 3.174
y = -0.111x2 + 1.211x - 3.879
y = -0.139x2 + 1.404x - 4.368
AAR: ~0.65
PDD = 5
6
7
8
9
AAR: ~0.7
% PP
PDD melt factors
ΔTSL (°C)
Temperature depression (Δ TSL: °C)
GIA uplift - corrected Δ TSL (°C)
Precipitation (m ice yr-1)
B
EL-mid glacier advance/still-stand (YD?)
AAR: ~0.6
0.5x
1x PP
Polynomial regressions
y = -0.634x2 + 1.750x - 2.077
y = -0.203x2 + 1.260x - 2.068
y = -0.334x2 + 1.328x - 2.159
y = -0.254x2 + 1.162x - 2.168
y = -0.103x2 + 0.941x - 2.153
PDD = 5
6
7
8
9
AAR: ~0.65
AAR: ~0.7
% PP
PDD melt factors
ΔTSL (°C)
Temperature depression (Δ TSL: °C)
Precipitation (m ice yr-1)
C
RCO-out glacier advance (~18 ka?)
1x PP
AAR: ~0.6
2x
3x
4x
Polynomial regressions
y = -0.210x2 + 1.515x - 2.846
y = -0.202x2 + 1.437x - 2.957
y = -0.151x2 + 1.246x - 2.976
y = -0.149x2 + 1.264x - 3.205
y = -0.095x2 + 1.013x - 3.079
AAR: ~0.65
PDD = 5
6
7
8
9
AAR: ~0.7
% PP
PDD melt factors
ΔTSL (°C)
Temperature depression (Δ TSL: °C)
GIA uplift - corrected Δ TSL (°C)
Precipitation (m ice yr-1)

Figure 4.8. Ice-flow model temperature depression and precipitation parameter combinations for each moraine-matching simulation (grey triangles) of the EL-out advance (**A**), the EL-mid advance/still-stand (**B**) and the RCO-out advance (**C**), for a given round-number positive degree-day melt factor value between 5.0 and 9.0 mm *w.e.* d^{-1} $°C^{-1}$. Each graph displays colour-coded second-degree polynomial regression curves and equations for each round-number positive degree-day melt factor (n=5). All regression equations are associated with R^2 values > 0.99. Each diagram also display histograms indicating the % precipitation associated with each simulation relative to present precipitations (% PP) values, for a given temperature depression value and degree-day melt factor (colour-coded bars). The horizontal dashed line represents modern precipitation (100%). Note that GIA-corrected temperature depressions include the hypothetical assumptions that the EL-mid advance/still-stand dates to the YD (~12 ka), and that the RCO-out advance is coeval with the EL-out advance (~18 ka).

4.5 Discussion

4.5.1 Geomorphological considerations and age interpretation

The distribution of exposure ages from the EL southern lateral moraine boulders display greater age scatter than can be predicted by 1σ analytical uncertainties alone (MSWD = 3.78; Table 4.3, Fig. 4.5). This suggests that pre- and/or post-depositional processes likely played an important role in causing exposure age under- and/or over-estimations. Rock surface erosion is not thought to contribute to this age scatter because we observed limited boulder surface erosion pitting (<1 cm), and the erosion rate of 0.2 mm ka^{-1} estimated for semi-arid central Patagonia (46°S; Douglass *et al*., 2007; Hein *et al*., 2017) would increase ages by less than 1%, which is less than the 1σ analytical uncertainties (~3-5%). We here consider two scenarios for such a spread in exposure ages.

The first scenario is based on the assumption that boulders nested on the EL southern lateral moraine were deposited by a single glacier advance, and the exposure-age scatter arose from a combination of ^{10}Be inheritance and post-deposition boulder exhumation. Nuclide inheritance may occur, for example, where sediment is sourced from a rockfall onto the glacier. A 350 m-high and 1.3 km-wide granite cliff on the northern EL valley flank, situated ~2-3.3 km from the location of sampling, is a potential source of rockfall (Figs. 4.2a, 4.3a). Post-depositional boulder exhumation may also have occurred given the steep slopes (>25°) of the single-crested moraine, which make it susceptible to disturbance via gravitational mass wasting (Fig. 4.3c). Our mapping reveals the occurrence of numerous subtle ridges bifurcating towards

their distal ends further downstream, towards the palaeo-glacier's latero-frontal and frontal environments (Fig. 4.2). According to this hypothesis, the lateral moraine crest targeted for TCN dating, deposited by thicker ice, would relate to the outermost and oldest of several advances and/or still-stands of the EL glacier.

Alternatively, the sampled moraine boulders may have been deposited by several glacier advances/still-stands causing the sampled ridge to be a composite moraine. Indeed, the EL glacier may have reached a similar, confined position at its southern lateral margin during several advances/still-stands highlighted by the multiple terminal moraine ridges preserved down-valley (Fig. 4.2a). In this eventuality, several advances/still-stands of the EL glacier could have potentially reworked previously-deposited moraine boulders, eroded moraine-crests, and caused boulder exhumation, as well as possibly incorporating younger material in the lateral moraine crest, thus generating scatter in the exposure ages. Such disturbance would predominantly cause the exposure ages to under-estimate the true age of moraine formation, which would hence be more appropriately estimated by the population's oldest exposure age, *i.e.* 19.5 ± 0.6 ka.

As field investigations of the southern lateral moraine, near to the sample location, revealed a well preserved single, sharp moraine crest, thus presenting a lack of a multi-ridge moraine complex, we consider the first scenario as more likely. We therefore propose that the EL southern lateral moraine crest is representative of the outermost advance, and any lateral moraine ridges deposited inside the EL southern lateral moraine during younger advances/still-stands were likely not preserved. Consequently, we consider the arithmetic mean sample age (18.0 ± 1.15 ka) as the most appropriate minimum age for the EL-out advance. Furthermore, this approximate age fits the wider chronology established for the Río Corcovado outlet glacier, as it is younger than the 20.7 ± 1.0 ka age of the RC VI moraine that it cross-cuts, and it is either younger or similar in age to the 19.9 ± 1.1 ka age of the RC VII moraine that abuts its proglacial outwash deposit (Leger *et al*., 2020; 2021).

4.5.2 Palaeo-climate

4.5.2.1 PIS context and the late-LGM cold/wet episode

The geochronological reconstruction of LGM expansions of the PIS Río Corcovado outlet glacier (Leger *et al*., 2021) suggests that local PIS outlets were sensitive to regional warming and drying during the Varas interstade (22-19.2 ka BP; Denton *et al*., 1999; Mercer, 1972), which caused the retreat of northeastern PIS outlet glaciers from LGM margins to be initiated relatively early, between ~19 and ~20 ka BP (as argued by García *et al*., 2019). However, palaeo-ecological data from the Chilean Lake District (Lago Pichilaguna record; Moreno *et al*., 2018) demonstrate sharp positive anomalies in *Poaceae* and *Isoetes savatieri* pollen concentrations between 19.3 and 17.8 kcal. yrs BP. These data suggest the Varas interstade preceded a return to colder, wetter conditions between ~19.5 and ~18 ka, during which the SWW are proposed to have migrated equatorward and reached their maximum LGM influence in northern Patagonia (Moreno *et al*., 2018). Shortly after 18 ka, a period of rapid drying and atmospheric and oceanic warming drove widespread deglaciation throughout the southern hemisphere (Mashiotta *et al*., 1999; Kaiser *et al*., 2007; Caniupán *et al*., 2011; Lopes dos Santos *et al*., 2013), often interpreted as the timing of the LGT in Patagonia and New Zealand (Lamy *et al*., 2004; 2007; Putnam *et al*., 2013; Hall *et al*., 2013; Davies *et al*., 2020). This proposed ~1.5 kyr-long late-LGM interval of cooling and increased precipitation coincides with the timing of numerous late-LGM PIS expansion and/or stabilisation events reported for several Patagonian and New Zealand outlet glaciers around 18-17 ka (*e.g.* Denton *et al*., 1999; Kaplan *et al*., 2007; 2008; Murray *et al*., 2012; Putnam *et al*., 2013; Moreno *et al*., 2015; Darvill *et al*., 2016; Shulmeister *et al*., 2010; 2019; Davies *et al*., 2020; Mendelová *et al*., 2020a). Moraine boulder exposure ages from the EL southern lateral moraine (Table 4.3, Fig. 4.5), with a mean age of 18.0 ± 1.15 ka, along with the observations of morphostratigraphically similar moraines nested in local mountain valleys (Leger *et al*., 2020), suggest that sensitive mountain glaciers of northeastern Patagonia (*e.g.* the EL and RCO palaeo-glaciers) advanced in response to this late-LGM climatic event. The geomorphological record, by featuring moraines of similar sizes, with comparable preservation levels and distance-to-headwall properties, suggests the EL-out and RCO-out advances are possibly age-equivalent, and thus reflect a response to the same climatic event. The significant overlap between temperature (67%) and precipitation (83%) ranges required for moraine-matching simulations of the EL-out and RCO-out advances (Fig. 4.9, Table 4.5) support this interpretation. Moreover, ice-flow model output suggests time

intervals of 100-170 years and 240-400 years for building steady-state ice volume from ice-free initial states during the EL-out and RCO-out advances (Figs. 4.6, 4.7). Even when considering cold-bedded glacier conditions (no basal sliding: average build-up time increase by 30 years), and moraine formation time (thought to be < 50 years for moraines < 40 m in height; Anderson *et al.*, 2014), estimated maximum glacier build-up times remain < 500 years. We thus argue that a 1.5 kyr cold/wet episode would have been long enough for local mountain glaciers to build up and stabilise, even from an ice-free initial state.

However, our ^{10}Be Río Corcovado moraine chronology suggest the Río Corcovado outlet glacier started to retreat from its LGM margins approximately 1.5-2 ka prior to this late-LGM return to colder/wetter conditions. Furthermore, our reconstruction of deglacial proglacial lake-level evolution and the timing of glaciolacustrine drainage shifts following the initial retreat of the Río Corcovado glacier front implies that the outlet glacier did not experience a significant re-advance towards its LGM margins during the late-LGM climatic event, at around ~18 ka (Leger *et al.*, 2021). The relatively short-lived (~1.5 ka) nature of the late-LGM cooling and high precipitation event could perhaps explain the lack of a major outlet glacier re-advance, as the extensive Río Corcovado outlet glacier may require a longer duration before adjusting its geometry and advancing up a reversed slope. Alternatively, one could argue that, in this region, a negative-mass-balance-inducing feedback mechanism prevented the ice-sheet outlets from being sensitive to a late-LGM colder/wetter episode following earlier initial retreat. Based on recent investigations modelling lake-terminating mountain glaciers (*e.g.* Sutherland *et al.*, 2020), we propose that the enhanced calving rates caused by large and deep proglacial lakes formed in overdeepened eastern Patagonian valleys during deglaciation were likely responsible for this glacier-climate de-coupling effect. Sensitive mountain glaciers (*e.g.* the EL and RCO glaciers) perched on higher massifs of the region, however, were not affected by these proglacial lakes, and were thus able to advance/stabilise in response to this late LGM cold/wet event.

4.5.2.2 Palaeo-precipitation

Our numerical modelling simulations of the EL-out advance suggest a precipitation increase of between ~50% and ~380% greater than present at around 18.0 ± 1.15 ka (Table 5, Figs. 4.8, 4.9). Furthermore, all of the RCO-out simulations also require higher-than-today precipitation (up to 338% higher than today) when constrained by PDD melt factors of between 5.0 and 9.0 mm *w.e.* d^{-1} $°C^{-1}$ and AAR values of between 0.6 and 0.7 (Table 4.5, Figs. 4.8, 4.9). These findings evidence a positive precipitation anomaly at around 18 ka relative to today. By assuming that both glaciers were responding to the same climatic event, we can constrain the estimated precipitation range to 49% - 338% increases relative to the present, which represents the overlap between the EL-out and RCO-out palaeo-glacier simulations when constraining SMB identically (Fig. 4.9). Based on comparisons with results from Patagonian LGM palaeo-precipitation proxy data and palaeo-climate models (*e.g.* Galloway *et al.*, 1988; Cartwright *et al.*, 2011; Berman *et al.*, 2016), we consider the lower-end estimates of our resulting palaeo-precipitation range the most likely (*i.e.* ~50% - ~200% increases). Even with an equatorward-migrated SWW belt, with its core located towards 43°S, the orographic effect associated with the Patagonian Andes would still cause a rain-shadow effect, effectively starving the eastern side of the mountain front of moisture. In comparison, present-day climate displays total annual precipitation increases of more than 50% between 43°S and 49-50°S (the modern core of the SWW belt) only towards the western margin of the cordillera. Towards the centre of the Andes, this latitudinal precipitation increase is reduced to ~20% (Garreaud *et al.*, 2013; Fick & Hijmans., 2017). Given these known orographic effects and the location of our study site towards the eastern margin of the mountain front (71°S; Fig. 4.1), we consider model outputs suggesting precipitation increases > ~200%, to be less likely.

Despite the wide range of possible values that would simulate moraine-matching glacier advances, our results suggest that a local positive precipitation anomaly relative to today was required during the late-LGM. While the breakdown of the PIS and the reduction of its orographic effect may be expected to contribute to local precipitation increases, we do not consider this a primary driver because significant local ice-sheet disintegration did not occur until much later, at 16.3 ± 0.8 ka (Leger *et al.*, 2021). Hence, we suggest that the positive precipitation anomaly identified here is consistent with the proposed hypothesis of high local SWW influence and equatorward migration of the wind belt during the late-LGM (19.5-18 ka). This latitudinal shift potentially induced positive glacier mass balances and reduced summer

temperatures in northern Patagonia at the time (Denton *et al*., 1999; Heusser, 1983; Heusser *et al*., 1999; Moreno *et al*., 2015; 2018).

4.5.2.3 Palaeo-temperatures

Our results from the EL-out simulations suggest that, after accommodating local GIA-related uplift corrections, local temperatures at around 18.0 ± 1.15 ka were between 1.9 °C and 2.8 °C colder than today (Tables 4.4, 4.5, Figs 4.8, 4.9). The RCO-out simulations suggest a similar cooling signal of between -1.6 °C and -2.5 °C. By validating the EL-out and RCO-out moraines to be age-equivalent, one could reduce the envelope of former temperatures to the overlap between the two simulations, resulting in a cooling of between -1.9 °C and -2.5 °C. These figures should be treated with caution, however, as numerous assumptions and sources of uncertainty exist (section 4.5.4). Firstly, we were unable to calibrate ice extents and thicknesses simulated with our modern climate estimation against modern glaciers as these do not exist in the study area. Furthermore, the lack of localised weather station data makes chosing a method for estimating atmospheric temperatures and ALR values representative of modern-day climate challenging, and this uncertainty is enhanced by the assumption that the ALR was constant over the past 18 ka, which is currently implausible to determine for certain. While we here acknowledge such uncertainties, we consider our method for estimating modern-day climate (section 4.3.4.3) to be appropriate, and thus propose that local atmospheric temperatures were between ~1.9 °C and ~2.8 °C lower than present during the late-LGM (19.5-18 ka), as suggested by our model results. This estimation overlaps the LGM mean annual temperature depression range of 2.3 °C – 4.4 °C proposed for eastern Patagonia by palaeo-climate proxy data compilation and modelling using the PMIP3 model (Berman *et al*., 2016).

Table 4.5. Numerical model output statistics and ranges

Glacier advance / still-stand simulated	Temperature depression (ΔTSL, °C)	Palaeo-precipitation (m ice yr^{-1})	% of modern precipitation	ELA range (m a.s.l)	Steady-state glacier volume (km^3)	Steady-state glacier surface area (km^2)	Years required for steady-state	Glacier length (km)	Maximum glacier thickness (m)	Mean steady-state glacier surface velocity (m yr^{-1})	GIA-corrected temperature depression (°C)	GIA-corrected ELA range (m a.s.l)
EL-out	-1.0 - -1.9	1.20 - 3.90	149 - 483	1515 - 1604	0.614 - 0.769	7.154 - 7.234	100 - 170	6.10	272 - 315	31.9 - 61.0	-1.85 - -2.75	1384 - 1473
RCO-out	-0.7 - -1.6	0.95 - 3.45	126 - 438	1579 - 1645	1.110 - 1.500	11.060 - 11.430	240 - 400	7.12	261 - 291	25.4 - 48.0	-1.55 - -2.45 *	1448 - 1514 *
EL-mid (YD?)	-1.1 - -1.6	0.30 - 1.30	37 - 161	1625 - 1670	0.284 - 0.330	4.830 - 4.930	600 - 700	3.86	225 - 231	13.2 - 19.8	-1.10 - -1.60 **	1625 - 1670 **
EL-out (ACR?)	-1.0 - -1.9	1.20 - 3.90	149 - 483	1515 - 1604	0.614 - 0.769	7.154 - 7.234	100 - 170	6.10	272 - 315	31.9 - 61.0	-1.12 - -2.02 ***	1497 - 1586 ***

Table footnotes

All model output ranges result from SMB constrains of PDD melt factors of between 5.0 and 9.0 mm we d^{-1} $°C^{-1}$ and AAR values of betwee 0.6 and 0.7

*Values rely on assumption that the RCO-out glacier advance/still-stand is coeval with the dated EL-out glacier advance advance/still-stand (~18 ka)

**Values rely on hypothetical assumption that EL-mid moraine ridges date to the Younger Dryas stadial (~12 ka)

***Values rely on hypothetical assumption that ACR (~14 ka) advances/still-stands of the EL glacier occurred, with similar extent as EL-out

4.5.2.4 Younger late-glacial advances/still-stands

There is widespread empirical evidence for glacial advances/still-stands occurring after the final disintegration of the PIS, during the Antarctic Cold Reversal (ACR) across Patagonia (Clapperton *et al*., 1995; Ackert *et al*., 2008; Glasser *et al*., 2011; García *et al*., 2012; Nimick *et al*., 2016; Davies *et al*., 2018; Sagredo *et al*., 2018; Reynhout *et al*., 2019; Mendelová *et al*., 2020b), New Zealand (*e.g.* Putnam *et al*., 2010), and other glacierised regions of the southern mid-latitudes such as the Kerguelen Archipelago (*e.g.* Jomelli *et al*., 2017; Charton *et al*., 2020). A new comprehensive ^{10}Be moraine chronology (Soteres *et al*., personal communication) from the Nikita valley (43°57'48"S; 71°38'11"W), located 30 km south of the EL valley, provides robust geochronological evidence for an advance of the Nikita palaeo-glacier during the ACR (14.7-13.0 ka; Pedro *et al*., 2016). This re-advance reached a similar, but slightly less extensive (< 500 m) glacier extent than an older advance/still-stand associated with the outermost ridges of the terminal moraine complex, which is argued to have occurred around ~16 ka (Soteres *et al*., personal communication). Similarly to the EL valley, the Nikita valley also contains a smaller set of mid-valley, more subtle latero-frontal moraines located ~1.7 km further upstream from the outermost moraines. The authors propose that these ridges were likely deposited during the Younger Dryas stadial (YD: 12.9-11.7 ka) based on TCN dating results. Such a pattern of extensive ACR moraines and more subtle but distinct YD moraines located up-valley was also observed in central Patagonia (47 - 48°S; Sagredo *et al*., 2018; Mendelová *et al*., 2020b). According to the geomorphological similarity and proximity of the Nikita and EL moraine records, one could speculate that the innermost terminal ridges of the EL-out moraine complex may also have been deposited during the ACR, while the smaller, mid-valley latero-frontal moraines (EL-mid) observed further up-valley could perhaps date to the YD stadial.

If those hypothetical assumptions, based solely on cross-valley morphostratigraphic comparisons, are valid, our glacier numerical modelling results could be utilised to infer that regional precipitation was likely between 50% and 380% higher than present during the ACR, and between 60% lower and 60% higher (~40% - 160% of modern values) than present during the YD (Table 4.5, Fig. 4.9). Such contrasting results would be in agreement with findings from regional palaeo-ecological proxy data that suggest late-glacial millennial-scale latitudinal shifts of the SWW belt induced increased and then decreased SWW influences in the southern

mid-latitudes during the ACR and YD stadials, respectively (Siani *et al*., 2010; De Porras *et al*., 2012; 2014; Villa-Martínez *et al*., 2012; Montade *et al*., 2013; Moreno *et al*., 2018; 2019; Vilanova *et al*., 2019). Recent work by Skirrow *et al.* (2021) supports a poleward latitudinal shift of the SWW during the YD through Optically Simulated Luminescence dating of a reduction in the water supply of Río Chubut, in northeastern Patagonia. When using the modern climate estimation described in section *3.3.3.* exclusively, and after including GIA-related surface uplift corrections of 17.7 m and 0 m associated with EL glacier advances hypothetically timed at ~14 ka (ACR) and ~12 ka (YD), as suggested by the gFlex model output data (Table 4), our modelling results would suggest that local temperatures were between 1.1 °C - 2.0 °C and 1.1 °C – 1.6 °C lower than today during the ACR and YD stadials, respectively (Table 5, Fig. 4.9). These inferences are close to findings reported by Sagredo *et al*. (2018) using ΔELA depression estimates for the extant Río Tranquilo glacier (47°S), suggesting a minimum cooling for the outermost ACR advance (13.9 ± 0.7 ka) of between 1.6 °C and 1.8 °C. A scenario of northward SWW belt migration and local precipitation increase is also proposed by Sagredo *et al*. (2018) to help explain the widespread trans-Pacific and trans-latitudinal positive mass balance signal of sensitive Patagonian mountain glaciers during the ACR.

According to our model simulations, the EL-mid advance, which we speculate to date to the YD stadial, represents a ~54% ice-volume loss and ~37% ice-extent decrease relative to the EL-out advance dated to 18.0 ± 1.15 ka and perhaps also associated with an ACR re-advance. Given the large overlap in the estimated local palaeo-temperature ranges required during the ACR and YD scenarios, the majority of this significant ice loss would possibly have been caused by a decrease in precipitation during the YD stadial. This suggests that mountain glaciers in northeastern Patagonia were highly sensitive to variations in precipitation, most likely associated with latitudinal shifts of the SWW belt. Model simulations of the EL-mid advance require between 600 and 700 years to reach steady glacier volume (Table 5). Given the YD stadial was ~1.2 kyr long, such inferences presume that the EL-mid moraines were potentially deposited by either a small re-advance, or a still-stand. This hypothesis is also supported by the smaller, more subtle geomorphology of the EL-mid moraines relative to the EL-out moraine complex.

It is however essential to stress that the above discussion (section *5.2.4*) is not based on any chronological evidence, but is instead exclusively based on cross-valley comparisons and

mostly aims at encouraging further work in the study region. The speculative results presented here thus await either confirmation or disproof by future glacier chronological reconstructions.

4.5.3 Positive degree-day melt factor variability

Simulations of the RCO-out glacier advance suggest that, using identical SMB parameters as for simulations of the EL-out glacier advance, PDD melt factor values need to be between 1.4 and 1.7 times greater to produce moraine-matching simulations. Using identical PDD melt factors instead causes the RCO ice-front to overrun the RCO-out lateral moraines. We consider such a former glacier-front position as unlikely, as it would have caused much greater erosion of the RC III-V LGM moraine record than can be observed in the field. Assuming that both advances were most likely coeval and that climatic conditions were similar in both adjacent catchments, this offset in former ice-front extents might therefore suggest a notable difference in former surface melt rates between the two palaeo-glaciers. Geomorphological analyses reveal that, relative to the RCO valley, the EL valley is narrower, its valley slopes are steeper, and it contains a higher concentration of eroded rock slopes with large debris cones and evidence of substantial talus accretion towards their base (Figs. 4.2, 4.3). We therefore suggest that former supraglacial debris cover might have been more substantial for the EL glacier than for the RCO glacier, thus potentially causing ice-surface insulation, lower surface melt-rates, and greater relative ice-extent in the ablation zone. The larger size of the EL-out relative to the RCO-out lateral moraines is potentially indicative of greater debris delivery, despite the EL glacier being smaller in surface area. Heavily debris-covered mountain glaciers are also often characterised by relatively low AARs (Benn *et al.,* 2005). If both advances were synchronous and debris cover on the EL glacier was greater, then the AAR value associated with the RCO-out advance was likely greater than for the EL-out advance. This could explain, if excluding the hypothesis that both advances were not triggered by the same climatic event, why the two palaeo-glacier simulation sets, both constrained with AAR values of 0.6 and 0.7, do not produce identical palaeo-temperature ranges (Fig. 4.9).

4.5.4 Limitations and future work

The outputs of our coupled SMB and ice-flow model simulations are subject to several limiting assumptions, which are as follows: 1) the SIA is appropriate for simulating the former extent of the EL and RCO glaciers. 2) The EL and RCO palaeo-glaciers were climate-sensitive

and in a state of mass-balance equilibrium at the time of the reconstructed advances/still-stands. 3) All precipitation was accumulated as glacier ice, 4) the contribution of avalanching to glacier accumulation was negligible, 5) the ice was at its pressure-melting point uniformly across the glacier domain, and 6) ablation caused by sublimation or ice-front breakoff is not significant enough to be considered by our SMB parameterisation. 7) The EL and RCO glaciers were mostly free of supraglacial debris cover, and 8) the removal of valley-fill debris deposited after glacier retreat would not cause significant impacts on simulated glacier geometries and extent.

In future work, the utilisation of a high-order or Stokes model, along with a more complex SMB model, could enable revisiting and testing the impact of assumptions 1), 3), and 6), although such an approach would require significantly more computational power. Assumption 2) could be re-assessed by dating the RCO-out moraines and by generating glacier-moraine chronologies in other mountain valleys of the region. Uncertainties associated with assumption 7) and 8) could potentially be reduced in future investigations by conducting thorough sedimentological and geomorphological analyses of glaciogenic and debris deposits. Assumptions 4), and 5) however, are likely to be problematic to resolve further. SMB-derived palaeo-climate ranges could potentially be refined by improving future estimations of catchment-specific atmospheric temperatures, ALR, as well as annual and seasonal precipitation representative of modern-day climate. Finally, the dating of the innermost EL-out moraines and the EL-mid moraines is required to assess our assumption that they reflect glacial advances occurring during the ACR and YD cold intervals, respectively.

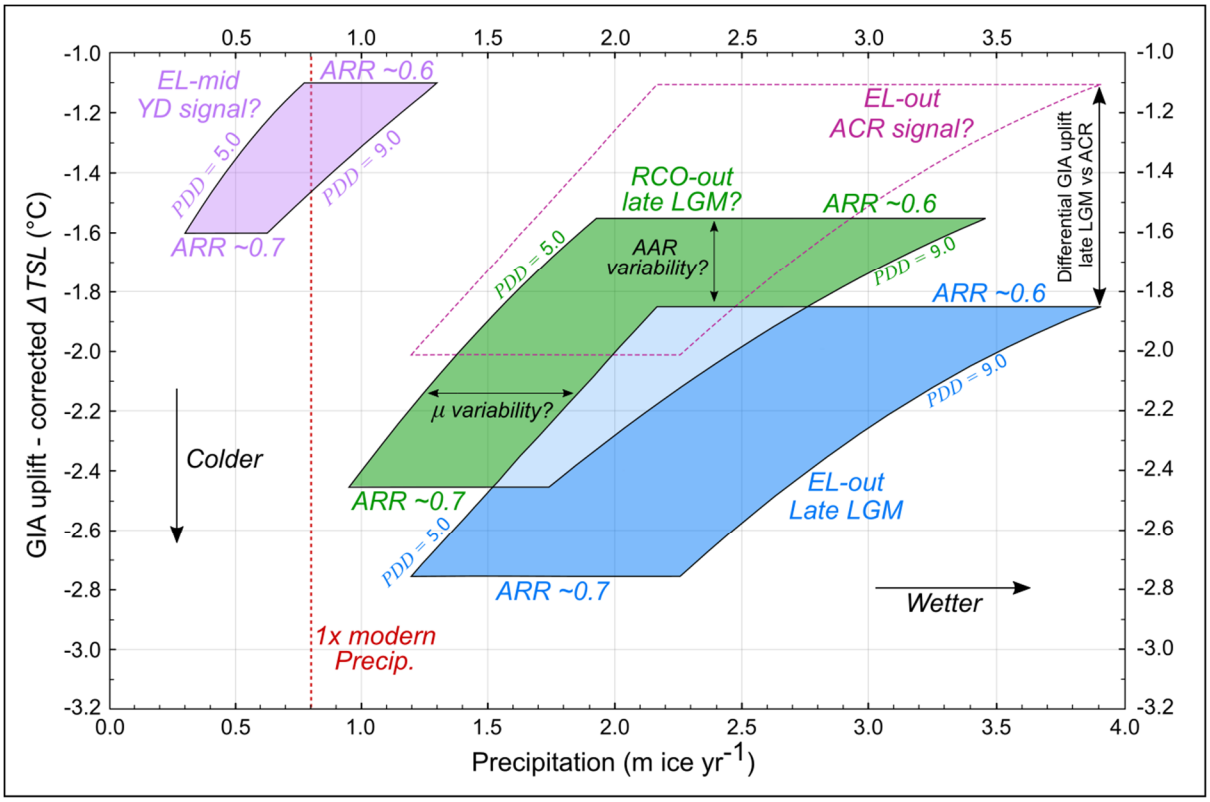

Figure 4.9. Ice-flow model temperature depression and precipitation parameter combinations for moraine-matching simulations of the EL-out (blue), EL-mid (purple) and RCO-out (green) advances/still-stands. Temperature depression values are corrected for modelled GIA-related uplift since time of advance/still-stand. Note that GIA-corrected temperature depressions include the hypothetical assumptions that the EL-mid advance/still-stand dates to the YD (~12 ka), and the RCO-out and EL-out advances are coeval (~18 ka). The dashed purple "SMB parameter box" denotes a hypothetical advance/still-stand of the EL glacier reaching a similar ice-front position to the EL-out advance, but dating to the ACR (~14 ka) and thus associated with less GIA-related uplift (17.7 m).

4.6 Conclusion

- Geomorphological mapping of preserved glacial moraine complexes near the mouths of the El Loro and Río Comisario mountain valleys, northeastern Patagonia (43°S; 71°W), has evidenced former advances/still-stands of local mountain glaciers that are younger than the dated LGM advances/still-stands of the local Patagonian Ice Sheet outlet glacier, the Río Corcovado glacier.

- In the El Loro valley, ^{10}Be surface exposure dating of the inferred outermost advance of the moraine complex suggests a minimum age of 18.0 ± 1.15 ka, while another, undated moraine complex is evident further upstream, indicative of a mid-valley re-advance and/or stabilisation of the EL palaeo-glacier front.

- Our findings suggest that while PIS outlet glaciers in northeastern Patagonia experienced a relatively early initial deglaciation from their LGM margins (~19-20 ka) and no substantial late-LGM re-advances, local sensitive mountain glaciers re-advanced during the late-LGM. We propose that this glacier expansion event was triggered by the late-LGM, 1.5 kyr-long cold and wet interval (~19.5-18 ka) recorded in other regions of Patagonia which followed the Varas Interstade (22-19.2 ka), and which preceded widespread Patagonian deglaciation (17.9-15 ka). We thus hypothesise that climatic conditions during the late-LGM were suitable for glacier expansion in northeastern Patagonia, and that the earlier onset of local PIS outlet glacier retreat at around ~19-20 ka was likely exacerbated by non-climatic factors, such as proglacial lake formation.

- We estimate site-specific cumulative surface uplift caused by Glacial Isostatic Adjustment over the past 18 ka to be approximately 130 m, while time-varying uplift rates are estimated at 9.1, 39.4 and 11.6 mm yr^{-1} between 20-17.5 ka, 17.5-15 ka, and 15-12.5 ka, respectively. The impact of such uplift on ^{10}Be production rates is less than exposure-age 1σ analytical uncertainties. Nevertheless, it requires modification of our surface mass balance-driven temperature and ELA reconstructions by -0.85 °C and -131 m, respectively. Our investigation highlights that GIA-related surface elevation change is an important factor to consider in palaeo-climate investigations using glacier reconstructions. This uplift is particularly relevant in Patagonia, where low mantle viscosities drive rapid uplift following deglaciation.

- Ice-flow model surface mass balance analyses suggest that regional mean annual temperatures were between 1.9 °C and 2.8 °C lower than present at around 18.0 ± 1.15 ka, while precipitation was between ~50% and ~380% higher than today. Our results thus support the hypothesis of increased Southern Westerly Winds influence in northern Patagonia between ~19.5 and ~18 ka, resulting from an equatorward migration of the wind belt, which may have induced positive glacial mass balances across the region.

Chapter 5

|

A cosmogenic nuclide-derived chronology of pre-Last Glacial Cycle glaciations during MIS 8 and MIS 6 in northern Patagonia



Publication details

Authors

Tancrède P. M. Leger[1], Andrew S. Hein[1], Ángel Rodés[2], Robert G. Bingham[1], Irene Schimmelpfennig[3], Derek Fabel[2], Pablo T. Gonzalez[4], ASTER Team[3]

[1]*School of GeoSciences, the University of Edinburgh, Edinburgh, United Kingdom*
[2] *Scottish Universities Environmental Research Centre, Scottish Enterprise Technology Park, East Kilbride, G75 OQF, Glasgow, UK*
[3]*Aix-Marseille Université, CNRS, Coll. France, IRD, INRAE, CEREGE, Aix en Provence, 13545, France*
[4]*Institut Instituto de Geografía, Facultad de Historia, Geografía y Ciencia Política, Pontificia Universidad Católica de Chile, Santiago, Chile*

Author contributions

T.P.M.L co-concieved the study with A.S.H, raised the finances for fieldwork, conducted fieldwork with help from P.T.G, wrote NERC NEIF grant application together with A.S.H, conducted result analyses and interpretations, wrote the manuscript and supplementary materials with feedback from A.S.H. and R.G.B primarily, and A.R., I.S, and D.F. in a second time, and generated maps and figures. TCN exposure-age analyses including wet chemistry and AMS measurements were conducted by A.R and D.F at SUERC and T.P.M.L, I.S and the ASTER Team at CEREGE and the ASTER AMS.

Lead Author contact details

Tancrède P.M. Leger, PhD student, University of Edinburgh, School of GeoSciences,
Address: Institute of Geography, Drummond Street, Edinburgh EH8 9XP, United Kingdom
Email: Tancrede.leger@ed.ac.uk

Publication details

Journal: Climate of the past; Open access
Status: In review

5.1 Introduction

Understanding the environmental mechanisms driving the Quaternary build-up and collapse cycles of Earth's major ice sheets remains a focus of ongoing research. Key to this research is the establishment of detailed chronologies offering direct dating of major ice-sheet expansion and recession events (Darvill *et al*., 2016). Numerical glacier chronologies are most informative when presenting unambiguous dating of ice-sheet margins spanning the entirety of the last glacial cycle (LGC) and ideally earlier Quaternary glacial cycles (Kaplan *et al*., 2010; Schaefer *et al*., 2015). To the east of the Patagonian Andes, the Argentinian foreland contains one of the most complete and well-preserved sequences of Quaternary glacial deposits in the world (Clapperton, 1993). This unique geomorphological record provides the opportunity to reconstruct and date glacier fluctuations of the formerly 2500 km-long (from north to south) Patagonian Ice Sheet (PIS) over several glacial cycles (Mercer, 1976, Hein *et al*., 2011). Furthermore, the PIS occupied a key mid-latitude position in the ocean-dominated Southern Hemisphere (SH) and was the only ice mass to fully intersect the precipitation-bearing southern westerly wind (SWW) belt; a fundamental feature of the southern mid-latitude climate system. Hence, reconstructing the timing of PIS expansion and recession events during several glacial cycles can provide rare insight into southern mid-latitude Quaternary climate evolution (Davies *et al*., 2020).

Palaeo-climate proxy records such as those retrieved from ice- and ocean-sediment cores indicate that some of the most potent Quaternary cooling events occurred during the Middle Pleistocene (Parrenin *et al*., 2013; Shakun *et al*., 2015), a period (~800 - 130 ka; Hughes *et al*., 2020) characterized by 100-ka pacing of glacial-interglacial cycles. Paradoxically, there is a dearth of directly-dated terrestrial glacial records for these glacial events (Hughes *et al*., 2020). In Patagonia, bracketing ages for pre-LGC glaciations have been produced in some places (*e.g.* near Lago Argentino; 50.5°S) with $^{40}Ar/^{39}Ar$ dating, *K-Ar* dating, and palaeo-magnetic measurements on lava flows interbedded between Pliocene/Pleistocene glacial-till units (Mercer, 1976; Sylwan *et al*., 1991; Meglioli, 1992; Singer *et al*., 2004). For instance, Mercer (1976) used such methods to constrain the likely timing of the Greatest Patagonian Glaciation to between 1.2 Ma and 1.0 Ma in the Río Gallegos (52°S) and Lago Buenos Aires (46.5°S) regions. While such studies have been

instrumental in establishing the broad chronological framework for Patagonian glaciations (Rabassa and Coronato, 2009), direct numerical dating of individual outlet-glacier advances is now required to develop detailed knowledge of pre-LGM and pre-LGC ice-sheet activity in Patagonia.

In Patagonia, direct numerical dating of pre-LGC glacial advances, achievable using terrestrial cosmogenic nuclide (TCN) surface exposure dating, has been limited to two outlet glaciers of eastern central Patagonia (Kaplan *et al*., 2005; Hein *et al*., 2009; 2011; 2017; Cogez *et al*., 2018). Throughout the rest of the southern mid-latitudes (23 - 66 °S), terrestrial glacial records yielding TCN exposure ages that pre-date the LGC have been reported using moraine boulders in New Zealand (Putnam *et al*., 2013), the southern central Andes (Terrizzano *et al*., 2017) and Tasmania (Barrows *et al*., 2002; Kiernan *et al*. 2004; 2010; 2014; 2017; Colhoun and Barrows, 2011, Augustinus *et al*., 2017). Because pre-LGC moraines and boulders are often poorly preserved, the majority of these investigations have identified the approximate timing of individual pre-LGC glacial advances with small (< n = 5 per moraine) and scattered sets of ages. Consequently, robust and direct numerical chronologies of pre-LGC glacial expansion events remain particularly scarce in the southern mid-latitudes. Patagonian investigations have shown that TCN exposure dating can yield direct ages for the deposition of pre-LGC moraine-outwash complexes preserved in the Argentinian steppe (*e.g.* Hein *et al*., 2017). While moraine boulders are well-suited to dating glacier advances of the LGC, Hein *et al*. (2009) revealed that targeting outwash terraces in eastern Patagonia can be more appropriate for dating pre-LGC glacial margins, because their low-gradient surfaces are less prone to degradation via gravity-driven diffusion when compared to steep-sided and unconsolidated moraines. On pre-LGC moraines, such degradation more frequently causes moraine surface lowering and boulder exhumation post-deposition, leading to significant exposure-age scatter and underestimations of moraine formation age. In contrast, surface cobbles from well-preserved outwash plains tend to display comparatively less post-depositional scatter and are thought to date the glacial event more closely (Hein *et al*., 2009). This approach has been used successfully to constrain the timing of glacial advances in several locations of central and southern Patagonia (Darvill *et al*., 2015; Hein *et al*., 2009; 2011; 2017; Mendelová *et al*., 2020). However, to date, no pre-LGC glacial events have been dated using this technique in northern Patagonia. Consequently, here we adopt this approach and target both moraine boulders and

outwash surface cobbles to constrain the timing of pre-LGC glacial advances in northeastern Patagonia.

We focus our investigation on the Río Corcovado (RC) valley system (43°S; 71°W), formerly host to a major outlet glacier of the PIS in northeastern Patagonia (Caldenius, 1932). We present a multi-glacial-cycle ^{10}Be and ^{26}Al TCN exposure-age chronology from the three stratigraphically oldest glacial moraine/outwash complexes deposited by the RC outlet glacier. This study builds on our earlier work (Leger *et al*., 2020, 2021a,b) to compile a geochronological reconstruction that spans the entire preserved moraine-outwash record of the RC valley system. We use our cosmogenic nuclide-derived chronology to test whether major middle Pleistocene advances previously dated in central Patagonia (Hein *et al*., 2009; 2017) coincide with moraines found in its northeastern sector (this study), and thus whether such advances depict strong regional climate signals expressed across much of the palaeo-ice front. We then compare the different magnitudes of middle Pleistocene Patagonian glaciations relative to other formerly glaciated regions of the world, and thereby assess the presence of former interhemispheric and inter-regional a/synchronies in ice-sheet behaviour. Finally, we evaluate the synchronicity of PIS expansion events with other global and regional palaeo-climate proxy records, and explore the potential role of various insolation parameters on controlling middle-to-late Pleistocene climate variations in Patagonia and the southern mid-latitudes.

5.2 Setting

Our study site focuses on the ice-marginal environment of the former PIS during Quaternary ice-age maxima, at the latitude of its major eastward-flowing Palena outlet glacier (43°S; Leger *et al*., 2020; 2021a). This up to 100 km-long outlet glacier diverged towards the eastern mountain front into three glaciers occupying the Río Frío valley to the northeast, the Río Huemul (RH) valley to the east, and the RC valley to the south (Fig. 5.1; Leger *et al*., 2021a). The local valleys are characterised by a westward-sloping bed topography such that the former outlet glaciers flowed up along reverse-sloping beds. The surface geology of the study area is characterised by well-preserved and distinct sequences of ice-contact glaciogenic deposits interspersed among their associated glaciolacustrine and glaciofluvial sediment-landform assemblages (Leger *et al*., 2020). Terminal moraine complexes indicate that the RC and RH outlet glaciers re-converged to deposit moraine sequences located approximately 60 km to the east of the Argentinian town of Corcovado (43°54′S; 71°46′W), into an environment presently climatically defined as the semi-arid Patagonian steppe (Fig. 5.1; Garreaud *et al*., 2013). Local aridity (~570 mm a^{-1}; Fick and Hijmans, 2017; Fig. 5.1a) results from the Patagonian Andes acting as a powerful orographic barrier to the dominant SWW (Fig. 5.1a), causing a potent west-east rain-shadow effect (Garreaud *et al*., 2013; Fig. 5.1a). Along the flowlines of the RC outlet glacier, ice flow eroded bedrock mainly sourced from the Mesozoic north Patagonian batholith towards the west (Hervé *et al*., 2017) along with formations of Jurassic/Cretaceous volcanic and sedimentary units located further east (Haller *et al*., 2003). Moraine-outwash complexes studied here thus contain a mixture of rock types including quartz-bearing leuco-monzonite, granite and white granodiorite that are well-suited to TCN exposure dating using *in situ* ^{10}Be and ^{26}Al radionuclides.

Ice sheet-wide geomorphological mapping of glacial sediment-landform assemblages has been conducted by Caldenius (1932), Glasser and Jansson (2008), and Davies *et al*. (2020) while the first detailed glacial geomorphological map specific to the RC and RH valleys was generated by Leger *et al*. (2020). These maps enabled the identification of at least eight stratigraphically-distinct moraine-outwash complexes deposited by the RC outlet glacier (Fig. 5.1c). This study focuses on dating results from the three stratigraphically oldest glacial margins: *i.e*. the RC 0 (outermost), RC I and RC II (Fig. 5.1c) moraine-outwash complexes. Directly inboard of these margins, the RC

outlet glacier deposited another series of at least five younger moraine complexes (RC III-VII moraines), previously dated to between 26.4 ± 1.4 ka and 19.9 ± 1.1 ka using TCN exposure dating and Bayesian age modelling (Leger *et al.*, 2021a). The latter moraine belts reflect the local Last Glacial Maximum (LGM) expansions of the PIS.

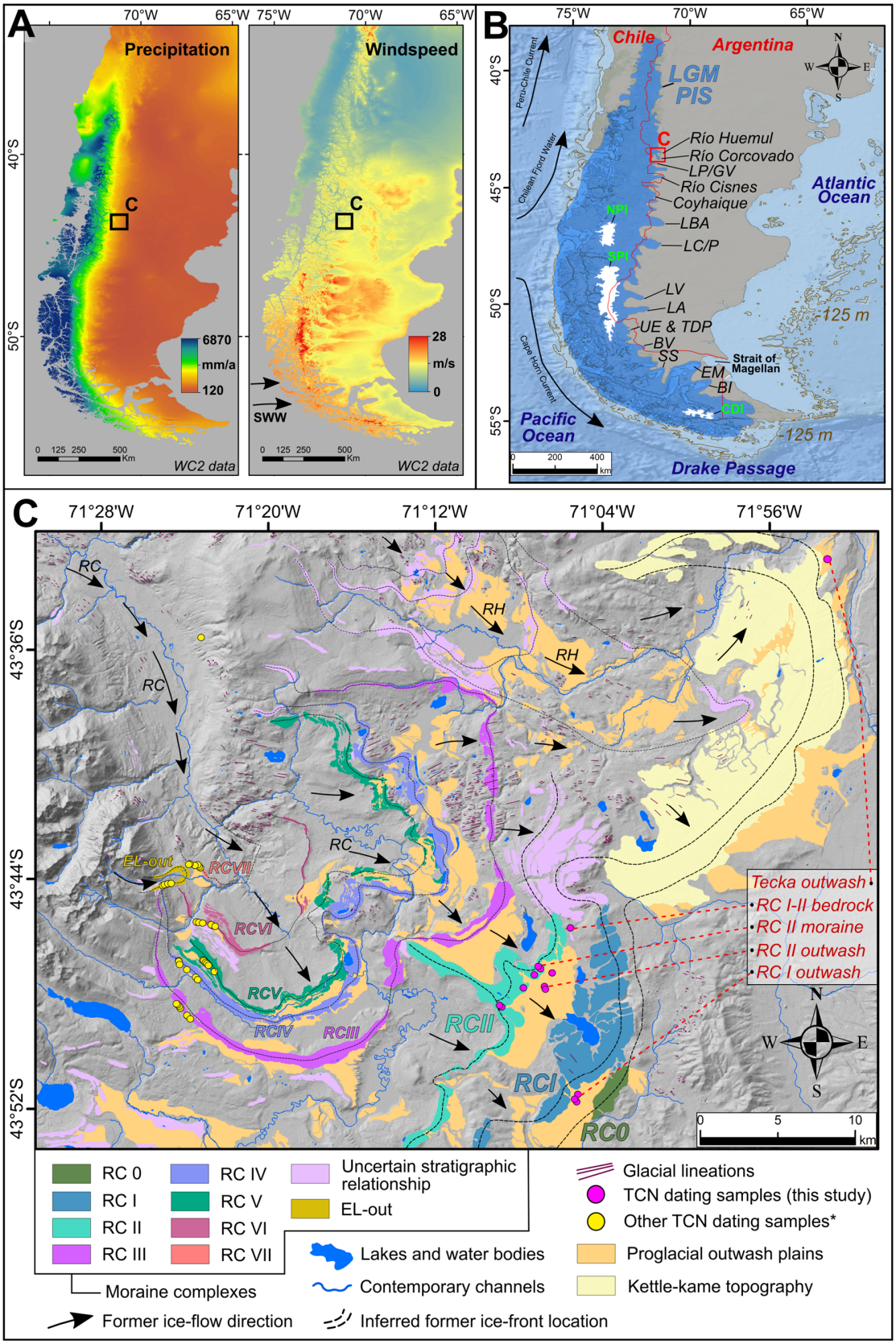
A
Precipitation
Windspeed
70°W
65°W
75°W
40°S
50°S
C
6870
mm/a
120
28
m/s
0
SWW
0 125 250 500 Km
WC2 data
B
Chile
Argentina
LGM
PIS
Peru-Chile Current
Chilean Fjord Water
Cape Horn Current
Río Huemul
Río Corcovado
LP/GV
Río Cisnes
Coyhaique
LBA
LC/P
LV
LA
UE & TDP
BV
SS
EM
BI
NPI
SPI
CDI
Strait of Magellan
Atlantic Ocean
Pacific Ocean
Drake Passage
125 m
45°S
50°S
55°S
0 200 400 km
C
71°28'W
71°20'W
71°12'W
71°04'W
71°56'W
43°36'S
43°44'S
43°52'S
RC
RH
EL-out
RCVII
RCVI
RCV
RCIV
RCIII
RCII
RCI
RC0
Tecka outwash
RC I-II bedrock
RC II moraine
RC II outwash
RC I outwash
0 5 10 km
RC 0
RC I
RC II
RC III
RC IV
RC V
RC VI
RC VII
Moraine complexes
Uncertain stratigraphic relationship
EL-out
Lakes and water bodies
Contemporary channels
Former ice-flow direction
Inferred former ice-front location
Glacial lineations
TCN dating samples (this study)
Other TCN dating samples*
Proglacial outwash plains
Kettle-kame topography

Figure 5.1. (**A**): 1-km^2 spatial resolution total annual precipitation (mm a^{-1}) and mean annual windspeed (m s^{-1}) land data (1970-2000 mean) from the WorldClim version 2.1 dataset (Fick and Hijmans, 2017) overlaying maps of southernmost South America with location of study area highlighted by black box. (**B**): Adapted from Leger *et al*. (2020; 2021 a,b): Approximate former extent of the PIS during the LGM, modified from Glasser and Jansson (2008). Locations of major PIS paleo-outlet glaciers are designated: BI: Bahía Inútil, EM: Estrecho de Magallanes, SS: Seno Skyring, BV: Bella Vista, TDP & UE: Torres del Paine & Última Esperanza, LA: Lago Argentino, LV: Lago Viedma, LC/P: Lago Cochrane/Pueyrredón, LBA: Lago Buenos Aires, LP/LGV: Lago Palena/General Vintter. NPI, SPI and CDI stand for North, South, and Cordillera Darwin Patagonian ice fields, respectively. A -125 m (brown-coloured) topographic contour roughly simulating former coastline locations at the LGM is displayed (after Lambeck *et al*., 2014). Bathymetric data were acquired from the General Bathymetric Chart of the Oceans (GEBCO). (**C**): Glacial geomorphology of the study area indicating stratigraphic relationship of moraine-outwash complexes preserved, sample site location, and former ice-flow direction.

5.3 Methods

Preliminary identification and mapping of major glacial sediment-landform assemblages studied here was carried out using remotely-sensed imagery and topographic data. These geomorphological interpretations were then ground-checked during a 5-week field season during the 2020 austral summer. Details of the geomorphological mapping methodology and criteria, and the complete map of the study area, are given by Leger *et al*. (2020). To date the RC 0 - II glacier advances, we sampled both outwash surface cobbles and moraine boulders. Specifically, we measured ^{10}Be in five cobbles from the outermost proglacial outwash surface sampled; here termed the "Tecka outwash", which we correlate stratigraphically with the RC 0 advance (Fig. 5.1c). We sampled five and six cobbles respectively from the RC I and RC II outwash terraces, six moraine boulders from the RC II moraine complex, and one ice-moulded bedrock surface located between the RC I and II margins (Figs. 5.1-5.3). Additionally, we measured ^{26}Al in five of these 23 samples to determine whether they present simple or complex exposure/burial histories. The chosen moraine boulders are large (90-200 cm high) and rounded to sub-rounded granodiorite and granite erratics embedded in the RC II moraine crest (Fig. 5.3). The top 2-5 cm of boulder surfaces exhibiting glacial polish were sampled using hammer, chisel and angle grinder.

To date the formation of proglacial outwash plains, quartz-bearing and fluvially-rounded cobbles (4-10 cm diameter; crushed whole) were sampled from well-preserved terraces characterised by low surface gradients (~0.5°-1°), following the procedure established by Hein *et al*. (2009; 2011) (Fig. 5.2a-d). Surface ventifacts and desert varnish, indicative of prolonged cobble exposure, were considered a required sampling criterion. Sample preparation and cosmogenic isotope ratio measurements were conducted at three different laboratories: the cosmogenic isotope analysis and AMS facilities of the Scottish Universities Environmental Research Centre (SUERC) (East Kilbride, UK), the French National Cosmogenic Nuclides Laboratory (LN2C) and the ASTER AMS facility of the European Centre for Research and Teaching in Environmental Geosciences (CEREGE, Aix-en-Provence, France), and the University of Edinburgh's Cosmogenic Nuclide Laboratory (Edinburgh, UK). Sample details and nuclide concentrations are displayed in Table 5.1. Details relevant to sample location, photographs, preparation, and wet chemistry are provided in the supplementary materials.

^{10}Be and ^{26}Al exposure ages were calculated using the online calculator formerly known as the CRONUS-Earth online calculator version 3 (Balco *et al*., 2008). Rock density is assumed to be 2.65 g cm^{-3} and elevation flag is STD. For ^{10}Be exposure-age calculations, we used the *NIST_27900* standardisation (equivalent to 07KNSTD within rounding error) and the central Patagonia production rate (Kaplan *et al*., 2011) obtained and re-calculated from the ICE-D online database (http://calibration.ice-d.org/). Details regarding specific AMS standards, nominal $^{10}Be/^{9}Be$ ratios and ^{10}Be half-life employed are included in the supplementary materials. ^{26}Al exposure ages were calculated using the Purdue *Z92-0222* AMS standardisation (equivalent to KNSTD within rounding error) and the default CRONUS-Earth online calculator's global production rate of Borchers *et al*. (2016), as the central Patagonia production rate does not feature $^{26}Al/^{27}Al$ measurements. We however consider it reasonable to use both the central Patagonia and global production rates when comparing ^{10}Be and ^{26}Al ages, as their respective ^{10}Be calibrations agree within error, with reported LSDn scaling- fitting parameter values of 0.823 ± 0.067 and 0.846 ± 0.040, respectively (calibration: ICE-D online database). All exposure ages are displayed in Table 5.2. Below, we discuss exposure ages calculated using the time-dependent LSDn scaling scheme of Lifton *et al*. (2014) with 1σ analytical uncertainties. Exposure ages are between 6-9% and 0.6-1% older when using the *St* and *Lm* scaling schemes of Lal (1991) and Stone (2000),

respectively. The ^{10}Be New Zealand production rate (Putnam *et al.*, 2010), often used for Patagonian TCN exposure-age datasets due to its southern mid-latitude location (44°S), decreases our exposure ages by between 1.7% and 1.5% using LSDn scaling, which is less than 1σ analytical uncertainties (3.5-1.6%).

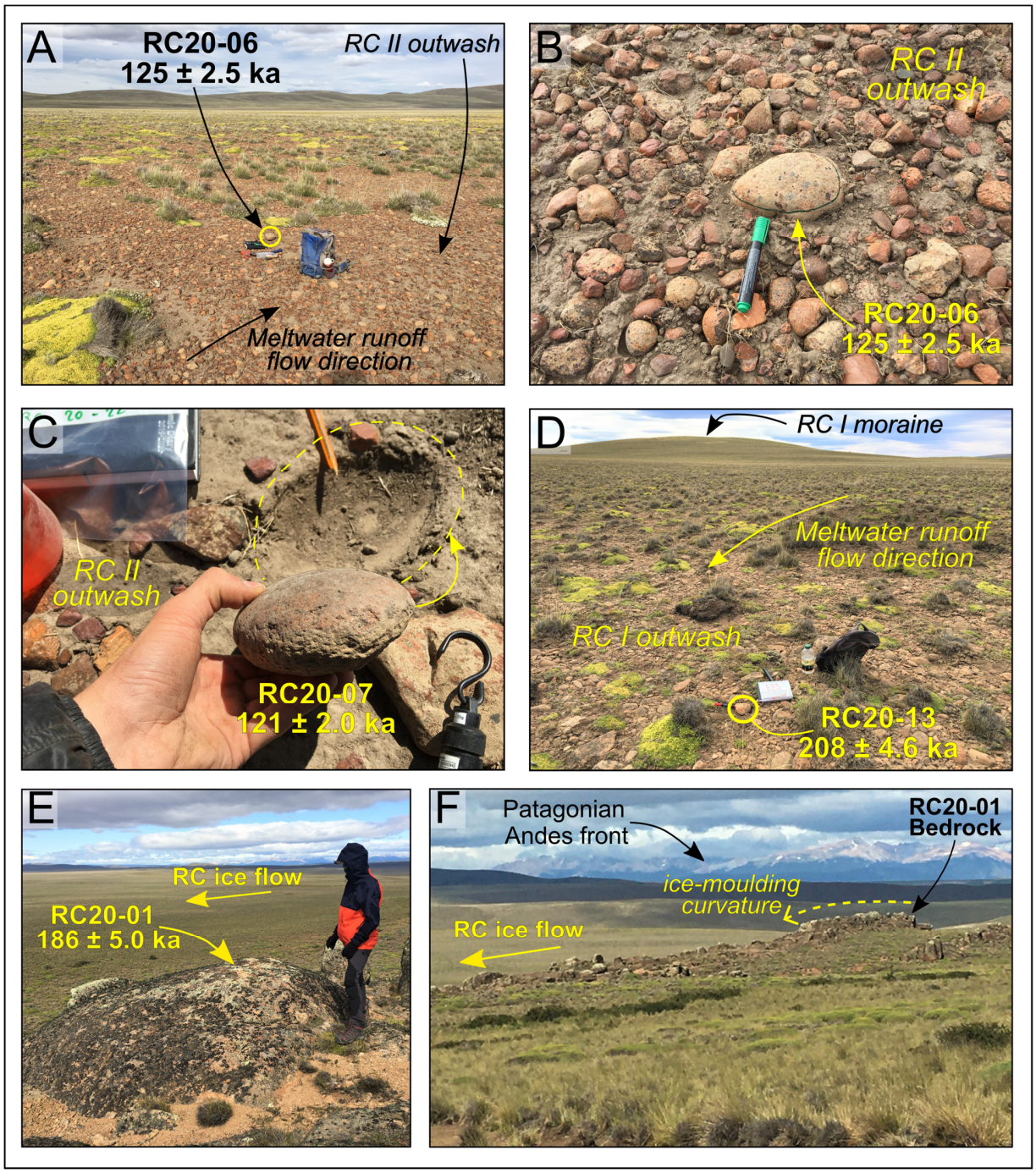

Figure 5.2. Field photographs of: (**A-D**) proglacial outwash plains and outwash surface cobbles sampled for TCN exposure dating and; (**E, F**) the ice-moulded bedrock surface sampled (RC20-01). Ages displayed are ^{10}Be exposure ages ± 1σ analytical uncertainties. Further sample coordinates and characteristics are presented in Table 5.1.

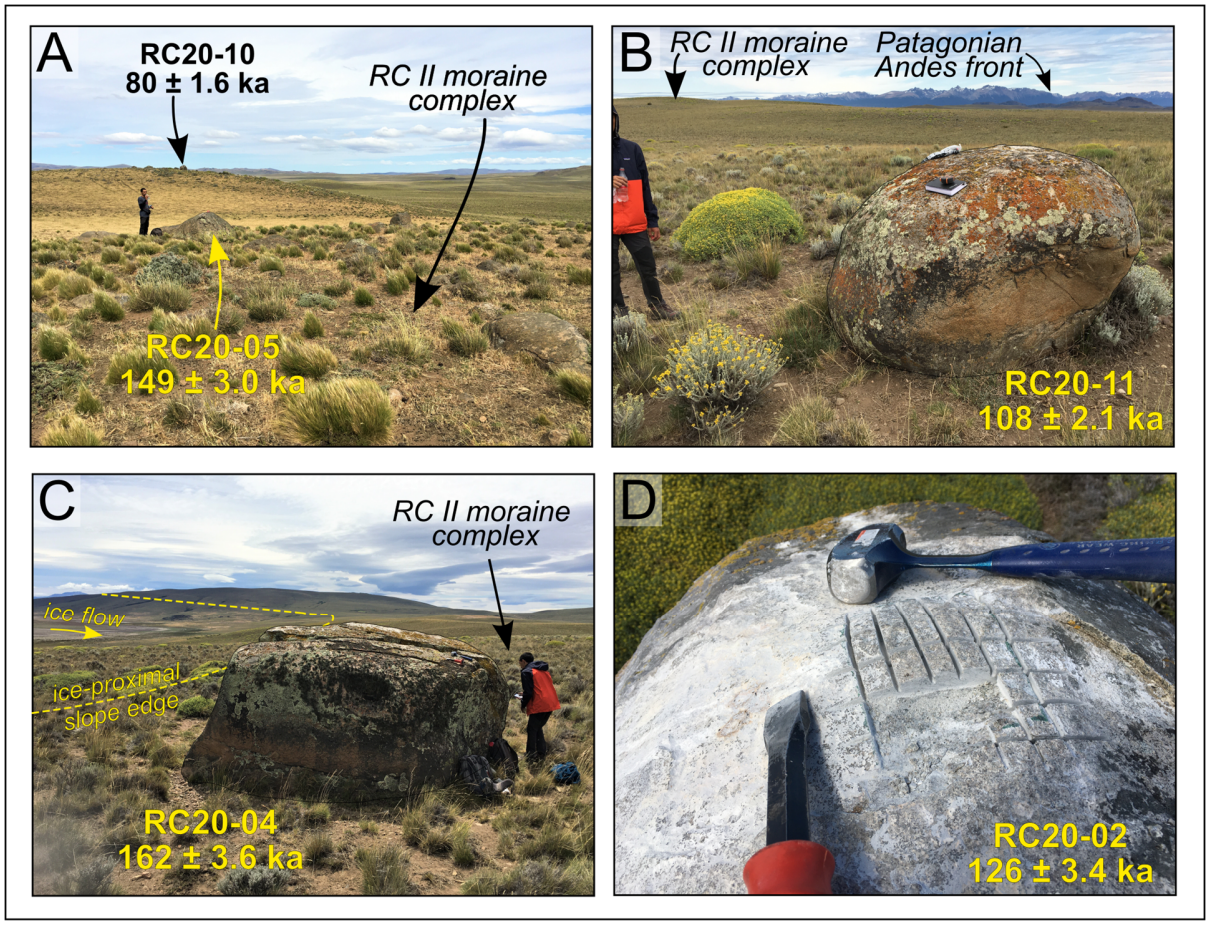

Figure 5.3. Field photographs of moraine granite and granodiorite boulders sampled for TCN exposure dating. Ages displayed are ^{10}Be exposure ages ± 1σ analytical uncertainties.

5.4 Results

5.4.1 Geomorphology

In the RC valley, the three most distal preserved moraine complexes (RC 0-II) are morphologically distinct from the younger LGM moraines (RC III-VII). They display greater relief (70-90 m) than the RC III – VII moraines (10-40 m; Leger *et al*., 2021a), are more subdued, and have broader-crested ridges. The three moraine complexes are 14 km (RC 0), 12 km (RC I) and 5 km (RC II) more distal than the outermost-dated LGM moraine (RC III). The sampled RC II moraine is a ~1 km-wide multi-ridge complex presenting a flat-topped, subdued crest surface elevated up to 45 m above its ice-distal outwash plain. Ice-distal slope gradient is variable but does not exceed 5°, a relatively low grade compared with the slopes of the younger, better preserved LGM moraines which feature slope gradients of 9-19° (Leger *et al*., 2021a). The RC I moraine complex features slope gradients (>5°) and surface geomorphologies for individual moraine ridges comparable to the RC II moraine belt, but is much wider in places (up to 4.6 km) and exhibits a greater concentration of distinct hummocky ridges and moraines. The subdued moraine geomorphologies characteristic of the RC 0-II margins are suggestive of progressive lateral slope downwasting and moraine surface erosion of fine material post-deposition (Clapperton, 1993; Glasser and Jansson, 2008; Hein *et al*., 2017). Geomorphological observations thus suggest the RC II and older moraine complexes were deposited significantly prior to the local LGM. In the adjacent RH valley, the outermost glacial margin consists of a ~2 km-wide belt of kettle-kame topography displaying a chaotic hummocks-and-hollows configuration, and was formerly termed the "Tecka drift" (Haller *et al*., 2003; Leger *et al*., 2020). The sampled Tecka outwash surface marks the distal limit of this kettle-kame glaciogenic deposit (Fig. 5.1c). Based on geomorphological mapping and moraine-complex traceability across the RC and RH valleys, the Tecka limit (RH valley) is assumed here to correspond stratigraphically to the RC 0 advance, for which no well-preserved outwash plain surface could be found in the RC valley (Fig. 5.1c).

The outwash surfaces sampled in this study all present long-term preservation properties (Fig. 5.2). They display low-gradient surfaces (0.5-1°), desert pavements, sparse vegetation cover, and preserved braided palaeo-meltwater channels suggestive of limited surface erosion/deflation (Fig.

5.2a,d; Leger *et al*., 2020). These glaciofluvial terraces are composed of sorted and fluvially-rounded sands and gravel deposits. Near the locations of outwash cobble sampling, the outwash surfaces display no detectable signs of post-deposition activation and/or incision by post-glacial hydrology. Where checked, modern soil thickness varied between 0 and 20 cm. This is comparable to observations made further south in the Lago Pueyrredón (47.3°S) and Lago Belgrano (47.5°S) valleys (Hein *et al*., 2009; Mendelová *et al*., 2020). At the locations of sampling, these terraces occur adjacent to moraine complexes and mark their distal limits (Fig. 5.1c), thus enabling the unambiguous stratigraphic association of an outwash deposit with a specific glacial advance.

Table 5.1. TCN exposure dating sample details and nuclide concentrations

Sample ID	Latitude (DD)	Longitude (DD)	Elevation (m a.s.l.)	Boulder height (m)	Thickness (cm)	Shielding correction	SiO_2 mass dissolved (g)	Nuclide	Total ^{9}Be or ^{27}Al mass (mg)	±1σ (mg)	$^{10}Be/^{9}Be$ or $^{26}Al/^{27}Al$ ratio	±1σ ratio	Blank correction	**^{10}Be (or ^{26}Al) atoms g^{-1} (SiO_2)**	**±1σ atoms g^{-1} (SiO_2)**	AMS Cathode code	$^{26}Al/^{10}Be$
RH Tecka outwash surface cobbles																	
19RHS09$^{\Upsilon}$	-43.55975	-70.88756	828	n/a	9.0	0.99993	21.4250	^{10}Be	0.24843	0.0005	2.6145E-12	6.2270E-14	0.27%	**2.0207E+06**	**6.3160E+04**	b11920	n/a
19RHS10$^{\Upsilon}$	-43.55975	-70.88756	828	n/a	9.0	0.99993	21.4477	^{10}Be	0.24980	0.0005	2.4737E-12	6.2290E-14	0.28%	**1.9201E+06**	**6.2059E+04**	b11921	n/a
19RHS12$^{\Upsilon}$	-43.55975	-70.88756	828	n/a	9.0	0.99993	20.3129	^{10}Be	0.24824	0.0005	2.7806E-12	3.5750E-14	0.25%	**2.2653E+06**	**5.4118E+04**	b11922	n/a
19RHS13$^{\Upsilon}$	-43.55975	-70.88756	828	n/a	10.0	0.99993	20.5896	^{10}Be	0.24882	0.0005	2.5549E-12	2.7690E-14	0.28%	**2.0579E+06**	**4.7039E+04**	b11923	n/a
19RHS15$^{\Upsilon}$	-43.55975	-70.88756	828	n/a	7.5	0.99993	20.6152	^{10}Be	0.24833	0.0005	2.3316E-12	2.7170E-14	0.30%	**1.8715E+06**	**4.3560E+04**	b11924	n/a
RC I outwash surface cobbles																	
RC20-12$^{\Delta}$	-43.86717	-71.09769	989	n/a	5.0	0.99998	1.9101	^{10}Be	0.45617	0.0005	1.3234E-13	4.6198E-15	1.46%	**2.0812E+06**	**7.3876E+04**	IIDL	n/a
RC20-13*	-43.86717	-71.09769	989	n/a	4.0	0.99998	19.9300	^{10}Be	0.22898	0.0005	2.4409E-12	5.0220E-14	0.82%	**1.8577E+06**	**3.8833E+04**	b12115	6.4 ± 0.3
								^{26}Al	2.54269$^{\#}$	0.1086	4.1836E-12	5.8120E-14	0.16%	**1.1893E+07**	**5.3489E+05**	a3380	
RC20-14$^{\Delta}$	-43.87017	-71.10005	993	n/a	9.0	0.99998	3.3260	^{10}Be	0.44301	0.0005	1.9378E-13	5.8904E-15	1.02%	**1.7071E+06**	**5.2498E+04**	IIDM	n/a
RC20-15*	-43.87017	-71.10005	993	n/a	5.0	0.99998	19.6520	^{10}Be	0.22940	0.0005	2.1267E-12	3.1670E-14	0.94%	**1.6425E+06**	**2.5061E+04**	b12118	6.0 ± 0.6
								^{26}Al	2.26658$^{\#}$	0.2380	3.8320E-12	5.8150E-14	0.19%	**9.8440E+06**	**1.0466E+06**	a3381	
RC20-16$^{\Delta}$	-43.87132	-71.09883	991	n/a	4.5	0.99998	4.5739	^{10}Be	0.44368	0.0005	3.5153E-13	8.3475E-15	0.56%	**2.2657E+06**	**5.4143E+04**	IIDK	n/a
RC I/II ice-moulded bedrock surface																	
RC20-01*	-43.77036	-71.10018	1026	n/a	1.5	0.99990	7.3150	^{10}Be	0.24010	0.0005	8.1397E-13	1.9970E-14	2.35%	**1.7405E+06**	**4.4314E+04**	b12105	6.8 ± 0.3
								^{26}Al	2.13039$^{\#}$	0.0748	1.8242E-12	4.4450E-14	0.43%	**1.1803E+07**	**5.0705E+05**	a3375	
RC II outwash surface cobbles																	
RC20-06*	-43.79607	-71.11590	974	n/a	7.0	1.00000	13.9770	^{10}Be	0.24171	0.0005	9.5491E-13	1.8140E-14	1.99%	**1.0800E+06**	**2.1289E+04**	b12111	n/a
RC20-07*	-43.79607	-71.11590	974	n/a	7.5	1.00000	20.5390	^{10}Be	0.24078	0.0005	1.3495E-12	2.1480E-14	1.42%	**1.0412E+06**	**1.7088E+04**	b12112	n/a
RC20-19*	-43.80491	-71.12183	976	n/a	6.0	1.00000	19.8810	^{10}Be	0.23016	0.0005	1.4072E-12	2.6350E-14	1.42%	**1.0724E+06**	**2.0627E+04**	b12119	n/a
RC20-20$^{\Delta}$	-43.80491	-71.12183	976	n/a	4.0	1.00000	4.5249	^{10}Be	0.43875	0.0005	2.0274E-13	5.7110E-15	0.99%	**1.3006E+06**	**3.7057E+04**	IIDN	n/a
RC20-21$^{\Delta}$	-43.80383	-71.12228	977	n/a	5.5	1.00000	6.6173	^{10}Be	0.44192	0.0005	2.8334E-13	7.4642E-15	0.70%	**1.2555E+06**	**3.3338E+04**	IIDO	n/a
RC20-22*	-43.80383	-71.12228	977	n/a	4.0	1.00000	20.7920	^{10}Be	0.23398	0.0005	1.5691E-12	2.4620E-14	1.25%	**1.1643E+06**	**1.8792E+04**	b12120	n/a
RC II moraine boulders																	
RC20-02*	-43.79239	-71.12655	984	1.56	2.0	0.99999	15.0190	^{10}Be	0.24273	0.0005	1.0789E-12	2.7230E-14	1.76%	**1.1433E+06**	**2.9631E+04**	b12106	n/a
RC20-03*	-43.79345	-71.12502	986	0.86	1.4	0.99999	20.0790	^{10}Be	0.24451	0.0005	1.2374E-12	1.7440E-14	1.52%	**9.9050E+05**	**1.4486E+04**	b12107	n/a
RC20-04*	-43.79690	-71.13014	983	2.00	2.3	0.99999	19.7420	^{10}Be	0.23424	0.0005	1.8605E-12	3.8900E-14	1.05%	**1.4586E+06**	**3.1076E+04**	b12108	6.3 ± 0.3
								^{26}Al	2.86695$^{\#}$	0.0895	2.8238E-12	4.3000E-14	0.21%	**9.1319E+06**	**3.1778E+05**	a3376	
RC20-05*	-43.81415	-71.15841	1020	1.15	2.5	0.99999	20.0200	^{10}Be	0.23186	0.0005	1.8099E-12	3.4020E-14	1.10%	**1.3845E+06**	**2.6584E+04**	b12109	6.5 ± 0.3
								^{26}Al	2.03553$^{\#}$	0.0661	3.9912E-12	6.4770E-14	0.21%	**9.0374E+06**	**3.2871E+05**	a3377	
RC20-10*	-43.81509	-71.15717	1029	1.66	1.7	0.99999	10.5800	^{10}Be	0.23772	0.0005	5.1964E-13	9.4730E-15	3.73%	**7.4934E+05**	**1.4825E+04**	b12113	n/a
RC20-11*	-43.80433	-71.13924	1002	1.55	1.2	1.00000	19.8670	^{10}Be	0.23441	0.0005	1.2858E-12	2.4140E-14	1.53%	**9.9741E+05**	**1.9268E+04**	b12114	n/a
Blanks	Processed with																
RC20-BL	Δ samples	n/a	n/a	n/a	n/a	n/a	n/a	^{10}Be	0.44728	0.0005	1.9671E-15	3.0249E-16	n/a	n/a	n/a	IIDP	n/a
CB190421	* samples	n/a	n/a	n/a	n/a	n/a	n/a	^{10}Be	0.22855	0.0005	2.1105E-14	2.6590E-15	n/a	n/a	n/a	b12121-blk	n/a
								^{26}Al	2.97988$^{\#}$	0.1120	6.1162E-15	1.7660E-15	n/a	n/a	n/a	a3382	
EUTL9	Υ samples	n/a	n/a	n/a	n/a	n/a	n/a	^{10}Be	0.24843	0.0005	7.0592E-15	1.5050E-15	n/a	n/a	n/a	b11930	n/a

Table footnotes. All cobble samples were crushed whole, without prior cutting. Sample preparation and wet chemistry was conducted at three different laboratories: **Υ** samples: The University of Edinburgh's Cosmogenic Nuclide Laboratory (Edinburgh, UK), ***** samples: The Scottish Universities Environmental Research Centre (SUERC) (East Kilbride, UK), **Δ** samples: The French National Cosmogenic Nuclides Laboratory (LN2C) of the European Centre for Research and Teaching in Environmental Geosciences (CEREGE, Aix-en-Provence, France). Nuclide ratios in **Υ** and ***** samples were measured at the SUERC AMS facility (East Kilbride, UK), while Nuclide ratios in **Δ** samples were measured at the ASTER AMS facility (CEREGE, Aix-en-Provence, France). SiO_2 is the chemical formula of silica (quartz). # Total ^{27}Al mass from both carrier (^{27}Al concentration: 982 ± 0.1 µg g^{-1}) and sample, determined by ICP-OES. *Be* Carrier solution used at LN2C has a ^{9}Be concentration of 3025 ± 9 µg g^{-1} while carrier solutions used at SUERC and the University of Edinburgh's Cosmogenic Nuclide Laboratory have ^{9}Be concentrations of 849 ± 12 µg g^{-1} and 1000 µg g^{-1}, respectively. Conversions of isotope ratios to ^{10}Be and ^{26}Al concentrations were conducted following standard equations, as described by Balco (2006).

5.4.2 TCN exposure-age chronology

The exposure-age results for the 23 samples are presented in Table 5.2. Four of the five cobbles sampled on the outermost Tecka/RC 0 outwash surface (Fig. 5.1c) range from 252.0 ± 6.3 ka to 284.1 ± 7.0 ka and afford a mean ^{10}Be exposure age of 268.7 ± 14.4 ka (arithmetic mean ± 1σ standard deviation). One older age (19RHS12: 311.5 ± 8.1 ka) lies outside the remaining population's 95% (2σ) confidence level and is rejected as a statistical outlier. The remaining exposure-age population is relatively well-clustered given the landform age, but still displays a >1 mean square weighted deviation (MSWD) value of 4.38 (>k = 2.63). Such a MSWD value is indicative of greater exposure-age scatter than can be predicted by 1σ analytical uncertainties alone (Jones *et al*., 2019).

The five ^{10}Be ages from the RC I outwash surface cobbles range from 185.0 ± 3.0 ka to 257.4 ± 6.6 ka and afford a mean exposure age of 214.0 ± 29.5 ka. Although the age population presents no obvious statistical or stratigraphical outliers, the exposure ages are poorly clustered, and present a high MSWD value of 33.6 (> k = 2.41), indicating significantly more exposure-age scatter than solely predicted by analytical uncertainties. From the ^{26}Al measured in two samples (RC20-13 and RC20-15) from this population, the resulting $^{26}Al/^{10}Be$ concentration ratios are 6.4 ± 0.3 and 6.0 ± 0.6, respectively, and are consistent with a single, continuous exposure history post erosion (Granger and Muzikar, 2001; Balco and Rovey, 2008).

The ice-moulded bedrock surface (RC20-01), located inboard of the RC I moraine, yields a ^{10}Be exposure age of 185.7 ± 5.0 ka, an ^{26}Al exposure age of 181.1 ± 8.5 ka, and an $^{26}Al/^{10}Be$ concentration ratio of 6.8 ± 0.3, which is consistent with continuous exposure post erosion of the surface.

The six ^{10}Be ages from the RC II outwash surface cobbles range from 120.6 ± 2.0 ka to 146.6 ± 4.3 ka with a mean exposure age of 131.3 ± 11.1 ka. The age population is tightly clustered considering analytical uncertainties associated with TCN exposure dating of pre-LGC landforms, and thus features no obvious statistical or stratigraphical outliers. However, the population still

yields a MSWD value of 11.4 (> k = 2.26), diagnostic of some non-analytical exposure-age scatter in the ^{10}Be age distribution.

Three of the six ^{10}Be ages from the RC II moraine boulders range from 125.5 ± 3.4 ka to 161.9 ± 3.6 ka and afford a mean exposure age of 145.3 ± 18.4 ka. Younger ages from the remaining three boulders (RC20-03, 10, 11) plot outside the remaining boulder population's 95% confidence level and the 2σ envelope associated with the youngest RC II outwash cobble (RC20-07). We consider ^{10}Be inheritance an unlikely source of exposure-age scatter compared with the high potential for boulder exhumation causing young outliers. Moreover, the RC II outwash and RC II moraine belt are geomorphologically likely to represent the same glacier expansion event. Hence, these three younger boulder ages were rejected as stratigraphical and statistical outliers (Table 5.2). The three remaining moraine boulder ages still exhibit a high MSWD value of 28.7 (>k = 3.0), indicating that the remaining dataset displays substantially more exposure-age scatter than can be predicted solely by analytical uncertainties. The two oldest sampled boulders, RC20-04 (161.9 ± 3.6 ka) and RC20-05 (148.6 ± 3.0 ka), yielded ^{26}Al exposure ages of 143.6 ± 5.4 ka and 137.5 ± 5.4 ka, corresponding to $^{26}Al/^{10}Be$ concentration ratios of 6.3 ± 0.3 and 6.5 ± 0.3, respectively. Such ratios are consistent with continuous exposure post erosion.

Table 5.2. TCN exposure ages and summary statistics

Sample ID	Nuclide	LSDn			St			Lm			Outlier
		Age	Internal	External	Age	Internal	External	Age	Internal	External	
		Years BP			Years BP			Years BP			
Tecka drift outwash surface cobbles											
19RHS09	^{10}Be	276461	9267	25853	299616	10102	28347	278319	9333	26176	
19RHS10	^{10}Be	262261	9057	24545	283596	9847	26839	263892	9117	24837	
19RHS12	^{10}Be	311517	8053	28598	339128	8829	31545	313965	8121	29001	Yes
19RHS13	^{10}Be	284138	6979	25816	308209	7617	28348	286092	7030	26152	
19RHS15	^{10}Be	251988	6251	22738	272373	6791	24856	253561	6292	23017	
Mean (n = 5): 277.27 ka; 1σ std: 22.83 ka											
Mean (n = 4): 268.71 ka; 1σ std: 14.37 ka; 1σ internal: 15.99 ka; 1σ internal + PR%: 28.35 ka											
Oldest cobble (n=4): **284.14** ka; 1σ internal: 6.98 ka											
Uncertainty weighted mean (n = 4): 268.06 ka; 1σ std: 13.11 ka											
MSWD: 4.38 > *k* : 2.63 (n−4); Peak age (n−4): 281.26 ka											
RC I outwash surface cobbles											
RC20-12	^{10}Be	236643	8917	22310	258263	9785	24618	240146	9057	22775	
RC20-13	^{10}Be	208105	4584	18433	226933	5023	20322	211056	4653	18815	
	^{26}Al	191679	9487	20471	203478	10131	25523	189094	9347	21655	
RC20-14	^{10}Be	198062	6403	18118	215770	7007	19941	200857	6498	18484	
RC20-15	^{10}Be	184989	2957	16053	200289	3214	17559	187105	2993	16340	
	^{26}Al	157741	18142	23333	166261	19204	26863	155152	17821	23787	
RC20-16	^{10}Be	257360	6563	23302	281123	7213	25764	261214	6668	23806	
Mean (n = 5): 214.03 ka; 1σ std: 29.48 ka; 1σ internal: 13.90 ka; 1σ internal + PR%: 23.27 ka											
Oldest cobble (n=2): **257.36** ka; 1σ internal: 6.56 ka;											
Uncertainty weighted mean (n = 5): 209.46 ka; 1σ std: 25.91 ka											
MSWD: 33.57 > *k* : *2.41* (n=5); Peak age (n=5): 185.20 ka											
RC I-II ice-moulded bedrock surface											
RC20-01	^{10}Be	185674	4954	16596	201425	5395	18184	187977	5018	16904	
	^{26}Al	181079	8514	19053	191447	9049	23703	178385	8376	20151	
RC II outwash surface cobbles											
RC20-06	^{10}Be	124477	2532	10758	133895	2730	11671	125552	2554	10915	
RC20-07	^{10}Be	120592	2040	10323	129458	2195	11177	121543	2057	10467	
RC20-19	^{10}Be	122414	2428	10560	131578	2616	11448	123440	2449	10712	
RC20-20	^{10}Be	146616	4334	13121	158063	4686	14269	148078	4379	13328	
RC20-21	^{10}Be	142948	3935	12689	154172	4256	13805	144388	3976	12891	
RC20-22	^{10}Be	130620	2179	11202	140785	2354	12182	131858	2200	11378	
Mean (n = 6): 131.28 ka; 1σ std: 11.05 ka; 1σ internal: 7.45 ka; 1σ internal + PR%: 13.32 ka											
Oldest cobble (n=6): **146.62** ka; 1σ internal: 4.33 ka;											
Uncertainty weighted mean (n = 6): 128.88 ka; 1σ std: 9.03 ka											
MSWD: 11.36 > *k* : *2.26* (n=6); Peak age (n=6): 121.96 ka											
RC II moraine boulders											
RC20-02	^{10}Be	125486	3356	11064	135098	3622	12012	126630	3388	11230	
RC20-03	^{10}Be	108441	1630	9217	115730	1742	9917	109171	1641	9335	Yes
RC20-04	^{10}Be	161918	3593	14192	174602	3887	15448	163599	3632	14426	
	^{26}Al	143604	5367	14309	151277	5676	17887	141129	5268	15174	
RC20-05	^{10}Be	148589	2962	12902	160552	3210	14070	150344	2998	13134	
	^{26}Al	137464	5353	13743	145113	5673	17185	135316	5264	14587	
RC20-10	^{10}Be	79902	1613	6830	84106	1699	7241	80260	1620	6900	Yes
RC20-11	^{10}Be	107548	2134	9245	114817	2283	9949	108339	2151	9368	Yes
Mean (n = 6): 121.98 ka; 1σ std: 29.92 ka											
Mean (n = 3): **145.33** ka; 1σ std: **18.43** ka; 1σ internal: 5.74 ka; 1σ internal + PR%: 13.55 ka											
Uncertainty weighted mean (n = 3): 145.12 ka; 1σ std: 14.70 ka											
MSWD: 28.73 > *k* : *3.0* (n=3); Peak age (n=3): 148.61 ka											

Table footnotes. ^{10}Be and ^{26}Al exposure ages were calculated using "the online calculator formerly known as the CRONUS-Earth online calculator version 3" (Balco *et al*., 2008). Rock density is assumed to be 2.65 g cm^{-3} and elevation flag is STD. All samples were collected in 2020, thus considered the year of reference for "before present" (BP). ^{10}Be ages reported here are calculated using the central Patagonia production rate (Kaplan *et al*., 2011) while ^{26}Al ages are here calculated using the global ^{26}Al production rate of Borchers *et al*. (2016). AMS standardizations employed for calculator input data are NIST_27900 (^{10}Be) and Purdue Z92-0222 (^{26}Al). Scaling schemes: St is the time-independent version of Lal (1991) and Stone (2000), Lm is the time-dependent version of Lal (1991) and Stone (2000), and LSDn is the time-dependent scheme of Lifton *et al*. (2014). Ages are reported with 1σ analytical and external uncertainties, the latter including production rate and scaling uncertainties. Summary statistics were calculated for each dated landform using only ^{10}Be exposure ages and LSDn scaling. This includes arithmetic means with 1σ standard deviations (std), 1σ propagated (from individual ages) internal uncertainties, and propagated 1σ internal plus production rate uncertainty (PR%). Summary statistics for sets of outwash surface cobble ages also display the oldest cobble exposure age; here considered a better minimum-age estimate of outwash deposit formation. Summary statistics also include uncertainty-weighted means and 1σ standard deviations, MSWDs and Peak ages; calculated using standard equations as described by Jones *et al*. (2019). Ages in bold are here interpreted as the most appropriate summary ages per landform and are the ones used throughout the paper for discussion.

5.4.3 TCN exposure-age scatter sources

We consider post-depositional shielding of TCN exposure dating samples by vegetation and/or snow to be negligible given the semi-arid and windy conditions (annual 1970-2000 mean wind speed of ~5.3 m s^{-1}; WorldClim 2.1 data; Fick and Hijmans., 2017) that characterise the study site and more generally the Argentinian steppe foreland (Garreaud *et al*., 2013; Hein *et al*., 2009; 2017). Modern daily winter (June-August) precipitation is estimated at 2.2 mm near the sampling site (Fick and Hijmans, 2017), which would represent between 20 and 50 cm thick snowfalls given various snow densities. Snow covers of between 75-150 cm thick persisting for four months of the year are typically required to reduce nuclide production by ~5% (snow density range: 0.16-0.33 g cm^{-3}; Dunai, 2010). Snow accumulation at the study site is thus considered too low to impact exposure ages beyond analytical uncertainties on 10^5 yr timescales. Cosmogenic nuclide inheritance from previous exposure has been shown to be negligible in other eastern Patagonian valleys (*e.g*. Douglass *et al*., 2007; Hein *et al*., 2009) and is considered minimal for our samples based on the long (>80 km) distance separating glacial deposits and source regions. Such transport

distance should have enabled efficient glacial erosion of transported clasts. For moraine boulder samples, we expect the sources of exposure-age scatter to originate mainly from rock surface erosion and boulder exhumation through moraine surface deflation and lateral creep (Putkonen and Swanson, 2003; Briner *et al.*, 2005; Hein *et al.*, 2017). For all outwash surface cobbles sampled, total rock-surface erosion is considered negligible due to the fluvially-rounded nature of target samples. We do, however, expect exposure-age scatter to reflect cobble exhumation via a combination of outwash surface deflation (Hein *et al.*, 2009; Darvill *et al.*, 2015) and near surface turbation (*e.g.* cryoturbation) caused by possible local development of soil permafrost during cold intervals (Trombotto, 2008). We thus assume post-depositional disturbance to predominantly cause cobble exhumation and young apparent exposure ages (Phillips *et al.*, 1990; Hein *et al.*, 2011), and thus consider the oldest cobble exposure age a better minimum-age estimate of outwash-plain stabilisation following glacier-front retreat, with the exception of obvious statistical outliers (Table 5.2, Fig. 5.4).

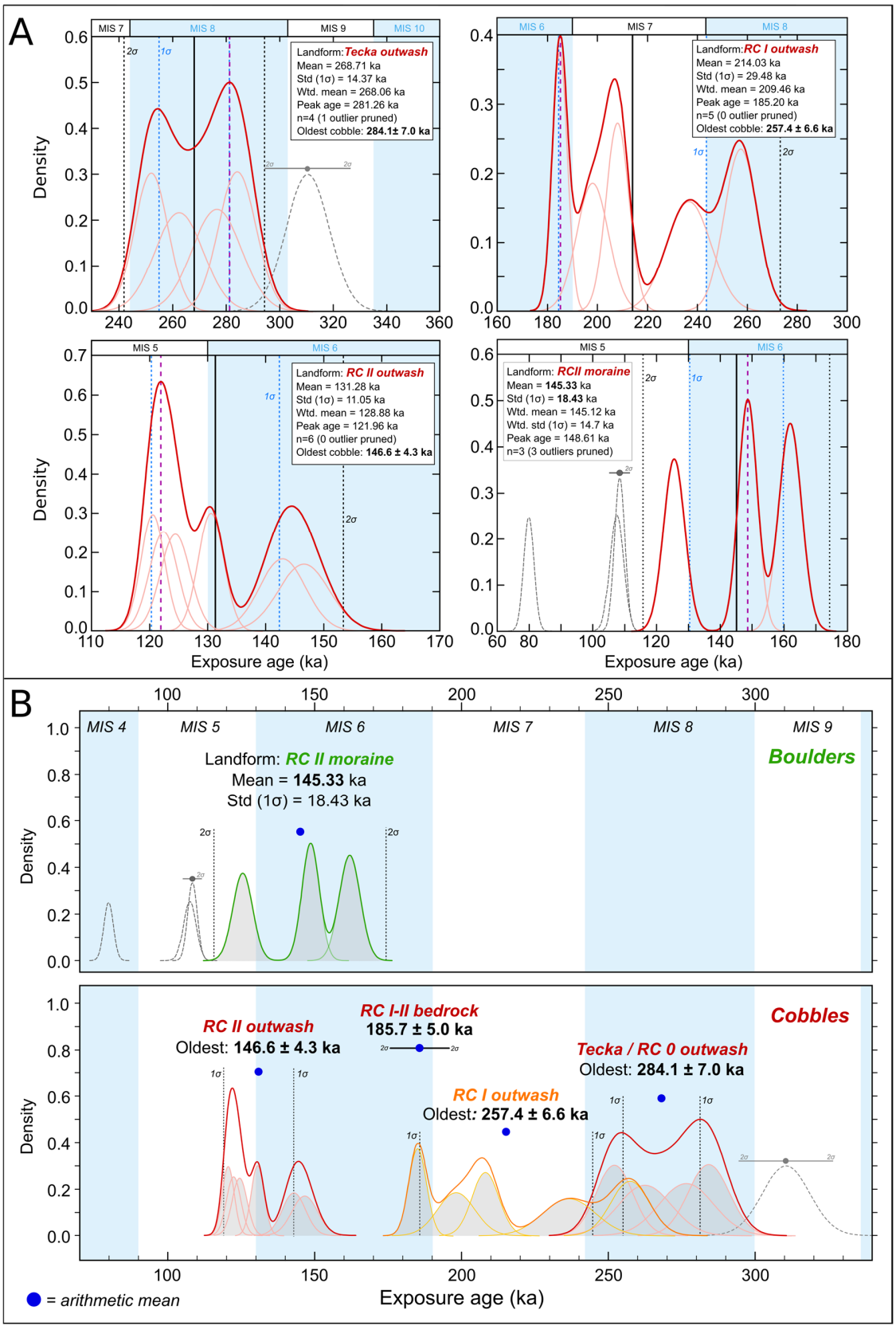
A
MIS 7
MIS 8
MIS 9
MIS 10
Landform: Tecka outwash
Mean = 268.71 ka
Std (1σ) = 14.37 ka
Wtd. mean = 268.06 ka
Peak age = 281.26 ka
n=4 (1 outlier pruned)
Oldest cobble: 284.1± 7.0 ka
MIS 6
MIS 7
MIS 8
Landform: RC I outwash
Mean = 214.03 ka
Std (1σ) = 29.48 ka
Wtd. mean = 209.46 ka
Peak age = 185.20 ka
n=5 (0 outlier pruned)
Oldest cobble: 257.4 ± 6.6 ka
MIS 5
MIS 6
Landform: RC II outwash
Mean = 131.28 ka
Std (1σ) = 11.05 ka
Wtd. mean = 128.88 ka
Peak age = 121.96 ka
n=6 (0 outlier pruned)
Oldest cobble: 146.6 ± 4.3 ka
MIS 5
MIS 6
Landform: RCII moraine
Mean = 145.33 ka
Std (1σ) = 18.43 ka
Wtd. mean = 145.12 ka
Wtd. std (1σ) = 14.7 ka
Peak age = 148.61 ka
n=3 (3 outliers pruned)
Density
Exposure age (ka)
B
MIS 4
MIS 5
MIS 6
MIS 7
MIS 8
MIS 9
Landform: RC II moraine
Mean = 145.33 ka
Std (1σ) = 18.43 ka
Boulders
RC II outwash
Oldest: 146.6 ± 4.3 ka
RC I-II bedrock
185.7 ± 5.0 ka
Tecka / RC 0 outwash
Oldest: 284.1 ± 7.0 ka
RC I outwash
Oldest: 257.4 ± 6.6 ka
Cobbles
Density
Exposure age (ka)
= arithmetic mean

Figure 5.4. (**A**): Kernel density plots, adapted from IceTEA tools for exposure dating outputs (Jones *et al.*, 2019) and summary statistics for dated landforms. Thick red curve represent the summed probability distribution for the exposure-age population, excluding outliers, while thin red curves depict Gaussian curves for individual samples. Outliers are denoted by grey dashed curves. Vertical black and purple dashed lines denote the population's arithmetic mean and peak ages, respectively. (**B**): Same kernel density plots as (**A**) but visualised on single time scale to enable better comparison of different landform ages and relative exposure-age scatter between surface outwash cobble and moraine boulder samples. On both panels, white and blue vertical bands differentiate Marine Isotope Stages (after Lisiecki and Raymo, 2005).

5.5 Discussion

5.5.1 TCN exposure-age interpretations

5.5.1.1. The Tecka/RC 0 outwash cobble exposure ages

Surface cobbles from the Tecka/RC 0 outwash (Fig. 5.1c) yield a mean exposure age of 268.7 ± 14.4 ka (n=4), excluding one statistical outlier with an age of 311.5 ± 8.1 ka, and display a discernible amount of exposure-age scatter (MSWD: 4.38 >*k*). Following the rationale outlined in section *5.4.3*., we consider the outwash's oldest cobble (284.1 ± 7.0 ka) as the closest minimum-age estimate for the RC 0 advance (Figs. 5.4, 5.5). The relatively tight cluster of remaining exposure ages (284 ± 7 - 252 ± 6 ka) supports this interpretation (Fig. 5.4).

Here, the outwash terrace sampled features preserved braided meltwater channels that demonstrate minimal outwash surface deflation post deposition. We therefore assess the possible impact of cryoturbation alone on exposure-age underestimation, and estimate broadly the potential magnitude of former cobble exhumation through soil. To do so, we model the constant exhumation of all sampled cobbles (excluding outliers) through a given soil horizon (density: 1.3 g cm^{-3}) and calculate the resulting exposure-age bias caused by cosmic-ray attenuation with depth (Gosse and Phillips, 2001; see supplementary materials). We acknowledge that cobble upfreezing is unlikely to have been continuous and of similar magnitude for all cobbles. We assume that some of this variability is considered by reporting a population mean exposure age post-simulation that matches

the original age of the oldest cobble, although this assumption undoubtedly yields uncertainties. Using such simulations, we calculated that a soil thickness of ~12 cm would have been required for the Tecka/ RC 0 cobbles to yield a mean ^{10}Be exposure age (283.1 ± 15.0 ka: +5.7%) that approximately matches that of the oldest original surface cobble. This estimated magnitude of cobble upfreezing is plausible given our observations of modern soil thicknesses (0-20 cm) near to the sampling locations. Therefore, despite local semi-arid conditions, cobble exhumation due to cryoturbation through a realistic soil thickness can potentially explain the observed exposure-age scatter (Fig. 5.5). Such results may also support the hypothesis that outwash surface erosion and deflation was minimal at this location.

In summary, our interpretations suggest that the exposure ages from the Tecka outwash place the timing of the RC 0 advance at around 290-270 ka, thus during the Marine Isotope Stage (MIS) 8 (300-243 ka; Lisiecki and Raymo, 2005) interval (Figs. 5.4, 5.6).

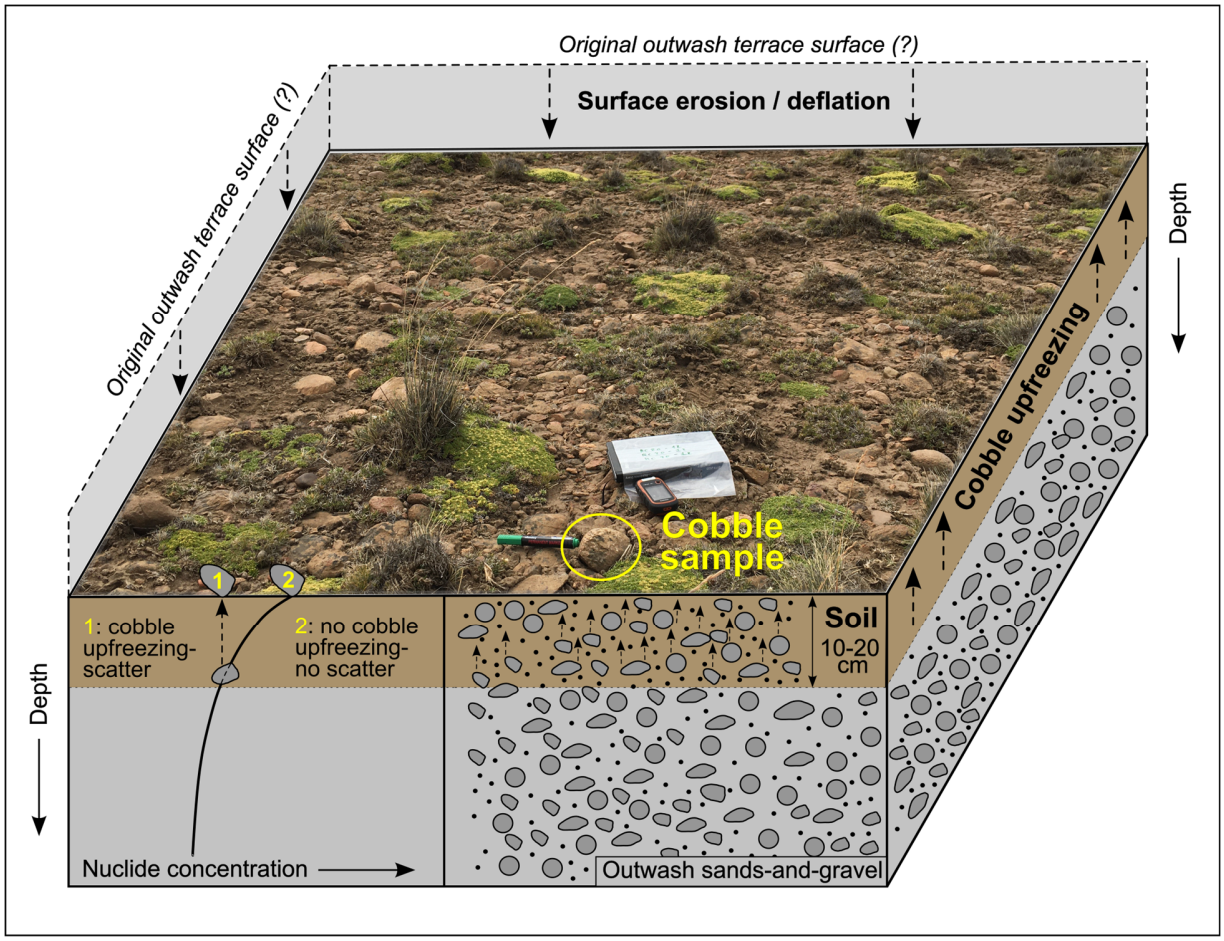

Figure 5.5. Illustration of the impact of combined outwash-plain surface deflation and near-surface turbation on exposure-age scatter for outwash surface cobbles sampled. The relationship between depth and nuclide concentration is illustrated by the decay curve (purely schematic) on the bottom left-hand corner of the diagram, which demonstrates that radionuclide production in rock minerals is reduced with depth below surface due to cosmic-ray attenuation. The attenuation effect causes cobbles that have experienced some exhumation post-deposition, due to the effect of upfreezing (dashed vertical arrows; scenario 1), to display exposure-age scatter causing landform deposition age underestimation. Cobbles that remained near the outwash surface since deposition (scenario 2) will display less/no scatter and better estimate the true minimum outwash deposition age. Cobble upfreezing is considered to mainly occur within the soil horizon (brown-coloured) due to the impact of potential permafrost formation. Soil thickness is locally estimated to reach a maximum of ~20 cm. The outwash surface photograph focuses on one of the surface cobble sampled (yellow circle), and enables the assessment of surface cobble density, roundness, size, vegetation type and cover density that are characteristic of outwash plain surfaces sampled within the context of this investigation.

5.5.1.2. The RC I outwash cobbles and timing of the RC I outermost advance

Surface cobbles from the RC I outwash are poorly clustered (MSWD: 33.6 > *k*) and afford a mean exposure age of 214.0 ± 29.5 ka and an oldest cobble age of 257.4 ± 6.6 ka (Table 5.2, Fig. 5.4). As previously justified (*section 5.4.3.*), we consider the population's oldest cobble (257.4 ± 6.6 ka) as the closest minimum-age estimate for the RC I outwash deposition. Simulations of constant cobble upfreezing through soil (section *5.5.1.1.*) demonstrate that a mean exposure age (257.2 ± 35.3 ka: + 20%) similar to that of the oldest original cobble is obtained when simulating constant exhumation through a ~39 cm-thick soil horizon. Although reasonable, this average soil thickness is greater than modern observations (0-20 cm). For these cobbles, three distinct outwash surface locations were sampled. They display near identical surface morphologies, vegetation cover and apparent modern soil thicknesses (Fig. 5.2d). It is thus challenging to assess whether spatially variable cryoturbation could have contributed to the observed scatter. This may indicate that, additionally to cobble upfreezing, outwash surface deflation played, in this instance, an important role in causing significant exhumation of certain RC I cobbles post deposition. This hypothesis is supported by the observation that RC I cobble exposure ages display three distinct age groups that correspond with the three different sampling locations (Table 5.1, Chapter 5 SM figure 3). The first group (sample RC20-16) yields an exposure age of 257.4 ± 6.6 ka, while the second (RC20-12 and 13) and third (RC20-14 and 15) groups display mean exposure ages of 222.4 ± 20.2 ka and 191.5 ± 9.3 ka, respectively. We note that the 1σ standard deviations associated with these age groups do not overlap. Thus, it seems plausible that outwash surface deflation was greater at the locations of the second and third sample groups and, combined with clast upfreezing, could therefore explain the substantial exposure-age scatter observed in the ^{10}Be age distribution of the RC I outwash cobbles.

An alternative hypothesis to explain the large RC I exposure-age scatter would be to argue that the RC I outwash could be a composite glaciofluvial deposit formed by meltwater runoff associated with numerous distinct RC outlet-glacier advances. While we commonly expect younger glaciofluvial sedimentation to bury previous deposits, certain cobbles associated with the oldest advances could have been remobilised by either meltwater or ice during younger advances and re-deposited towards the outwash surface. The overlap between the youngest RC I outwash

cobble age (185.0 ± 3.0 ka) and the deglacial ^{10}Be age (185.7 ± 5.0 ka) obtained from the ice-moulded bedrock surface sampled directly inboard of the RC I limit could support this hypothesis. Moreover, the RC I moraine belt is a wider (~4 km) complex constituted of more ice-contact hummocks and hummocky ridges suggestive of a greater glaciogenic sediment volume than the RC 0 and RC II moraine complexes (Fig. 5.6a). This geomorphological distinction could signal that a higher number of individual outlet-glacier advances have reached the RC I margin.

Establishing which of the previous hypotheses are more likely to be valid would require a more detailed chronological and sedimentological analysis through a depth profile of the RC I outwash deposit. However, regardless of which mechanism is responsible for the observed exposure-age scatter, we argue the oldest exposure age from the RC I outwash suggests a separate extensive advance of the RC outlet glacier occurred at around 270-245 ka, thus during the latest stage of the MIS 8 interval (Figs. 5.4, 5.6).

5.5.1.3. The RC I-II bedrock surface and timing of innermost RC I advances

The sampled ice-moulded bedrock's position and elevation (1026 m *a.s.l.*) suggests it was exposed after deglaciation from the RC I moraine-outwash complex, and prior to the RC II advance (Fig. 5.1c, 5.6a). Its ^{10}Be age of 185.7 ± 5.0 ka is thus interpreted as a minimum-age estimate of ice-front retreat following the innermost RC outlet-glacier advance reaching the RC I moraine complex. The older RC I outwash-cobble mean exposure age (214.0 ± 29.5 ka) brings further evidence for this stratigraphic relationship. The $^{26}Al/^{10}Be$ ratio (6.8 ± 0.3) from this surface bedrock sample does not indicate a complex exposure-burial history, thus suggesting the RC glacier did not advance beyond and bury the bedrock for any prolonged period (Chapter 5 SM Fig. 1). This ratio also demonstrates efficient subglacial erosion of the bedrock surface, which created a fresh surface free of inherited nuclides when last ice-covered.

Unlike other samples, we noticed signs of surface erosion on the bedrock outcrop (Fig. 5.2e). The surface demonstrated a lack of fluvio-glacial polish preservation and showed signs of homogeneous granular disintegration of a depth that proved challenging to quantify in the field.

We thus suspect a certain degree of exposure-age underestimation from this bedrock sample. Applying the rock-surface erosion rate of 0.2 mm ka^{-1} estimated for semi-arid central Patagonia (Douglass *et al*., 2007; Hein *et al*., 2017) increases its age by 3% to 191.3 ± 5.3 ka, which is within 1σ analytical uncertainty. Subsequently, this minimum deglacial exposure age suggests the youngest outlet-glacier advance to have reached the RC I moraine complex had to occur prior to ~190 ka. This interpretation is coherent with RC I outwash cobble exposure ages, and together indicate the RC I complex was most likely deposited prior to the MIS 6 (191-130 ka; Lisiecki and Raymo, 2005) cold interval. Because palaeo-climate proxy records such as Antarctic atmospheric temperature and global SST suggest a return to warmer, near-interglacial conditions between the MIS 7d interstadial (~220-230 ka) and ~190 ka (Fig. 5.8; Parrenin *et al*., 2013; Shakun *et al*., 2015), it is likely that the innermost RC I advance occurred during, or prior to the MIS 7d interstadial. In fact, the exposure age of the bedrock surface would date to peak MIS 7d Antarctic cooling (*i.e*. 225 ka, Fig. 5.8) if a surface erosion rate of 1.07 mm ka^{-1} was applied (LSDn age: 225.1 ± 7.5 ka), which lies within reasonable bounds for rock erosion rates in eastern Patagonia (maximum rate: 1.4 mm ka^{-1}; Kaplan *et al*., 2005).

To summarise, outwash cobble and bedrock ages suggest that outermost RC I glaciogenic deposits were likely deposited by a MIS 8 glacier advance (~270-245 ka), as portrayed by the oldest outwash cobble age (Figs. 5.6b, 5.7). On the other hand, the innermost and youngest outlet-glacier advance to have reached the multi-ridge, 4 km-wide RC I moraine complex (Fig. 5.1c, 5.6a) may have been significantly younger, and perhaps occurred during the MIS 7d interstadial. However, the latter part of this interpretation remains unclear, due to the lack of chronological data for the innermost RC I deposits combined with the analytical uncertainties and the large scatter displayed by outwash cobble exposure ages from this margin. More chronological constraints are thus required to test this hypothesis.

5.5.1.4. The RC II outwash cobble and moraine boulder exposure ages

As for the older RC I and Tecka outwash cobble samples, we argue the observed scatter (MSWD: 11.4 >*k*) in the RC II outwash cobbles exposure ages (mean: 131.3 ± 11.1 ka) likely originates from cobble exhumation and minor outwash-surface deflation (Fig. 5.5). This interpretation is reinforced by cobble ages displaying a younger mean age and a tighter cluster than moraine boulders from the stratigraphically -equivalent glacial margin (RC II; Table 5.2, Fig. 5.4). Consequently, the oldest surface cobble (146.7 ± 4.3 ka) is deemed a better minimum-age estimate for the RC II glacial advance. We find that a mean exposure age (145.5 ± 12.6 ka: + 11%) similar to that of the oldest cobble can be obtained when simulating constant exhumation of all cobbles (*see section 5.1.1.*) through a 24 cm-thick soil horizon. This estimate, although highly uncertain, is consistent with modern soil thickness observations near sampling locations (0-20 cm). This simulation suggests that, despite local semi-arid conditions, cobble upfreezing through a realistic soil thickness can cause the observed exposure-age scatter leading to the age underestimation of outwash plain formation. In summary, the RC II outwash cobble ages seem to suggest a minimum-age estimate of ~145 ka. Therefore, we argue the RC II limit reflects an extensive expansion of the local PIS outlet glacier occurring towards the latest stage of the MIS 6 cold interval (Figs. 5.4, 5.6, 5.7).

Following outlier removal (n = 3), the RC II moraine boulder mean exposure age (n = 3; 145.3 ± 18.4 ka) overlaps the RC II mean outwash cobble age within 1σ analytical uncertainties. The boulder population also displays two ages that are consistent with the set of outwash cobbles (125.5 ± 3.4 ka and 148.6 ± 3.0 ka). These results support our stratigraphic interpretation that these two landforms were deposited by the same outlet-glacier advance. Because we sampled rounded boulders and specifically targeted raised rock fragments presenting fluvioglacial polish, we here consider boulder surface erosion to be negligible, in contrast to the sampled ice-moulded bedrock surface, where granular disintegration was ubiquitous. The population's oldest boulder (RC20-04: 161.9 ± 3.6 ka) displays a ~15 ka older exposure age than the oldest RC II outwash surface cobble. Cosmogenic nuclide inheritance from pre-glacial-transport exposure is considered unlikely given the >80 km distance to source region and the sub-rounded morphology of the boulders sampled indicative of subglacial clast erosion (Fig. 5.3b,c). We instead propose this older boulder may

reflect at least one earlier glacial advance to the same terminal position, or may have been re-deposited during the RC II advance following exposure during previous glacier advances reaching proximal inboard ice-front positions. The $^{26}Al/^{10}Be$ concentration ratio from this sample (6.3 ± 0.3) does not suggest a prolonged period of boulder burial (Chapter 5 SM Fig. 1). We therefore hypothesise previous PIS advances might have locally occurred during earlier MIS 6 cold intervals (*e.g.* MIS 6c,e), while the youngest penultimate MIS 6 glacial maximum is more accurately dated by the RC II surface outwash cobbles, as the glaciofluvial terraces likely remained active until the end of the glaciation.

Overall, our results from the RC II limit (n = 12 ages) indicate that outwash surface cobble ages display less post-depositional scatter than moraine boulder ages, with MSWD values of ~11 vs ~30, respectively. This comparison thus agrees with results of Hein *et al*. (2009, 2017) suggesting that well-rounded cobbles sampled from the surface of former proglacial outwash plains are better-suited to numerically date pre-LGC glaciations in semi-arid, undisturbed environments such as the Argentinian steppe of Patagonia. However, even if semi-arid conditions usually limit soil thickness to <20 cm on outwash plains of the Argentinian steppe, our simulations show that potential cobble exhumation due to cryoturbation alone can cause meaningful landform-age underestimations for pre-LGC glacial deposits. This source of post-depositional exposure-age scatter is thus important to consider when interpreting outwash surface cobble exposure ages. Another advantage of targeting outwash cobbles is their abundance in formerly active glaciofluvial environments, while moraine boulders on pre-LGC margins are often sparse and where found, are highly eroded. This enables rigorous selection of cobbles that are most suitable to TCN exposure dating. On the other hand, obtaining exposure ages from both moraine boulders and outwash cobbles can provide additional insight on former glacier activity that may not be evident without the combined approach.

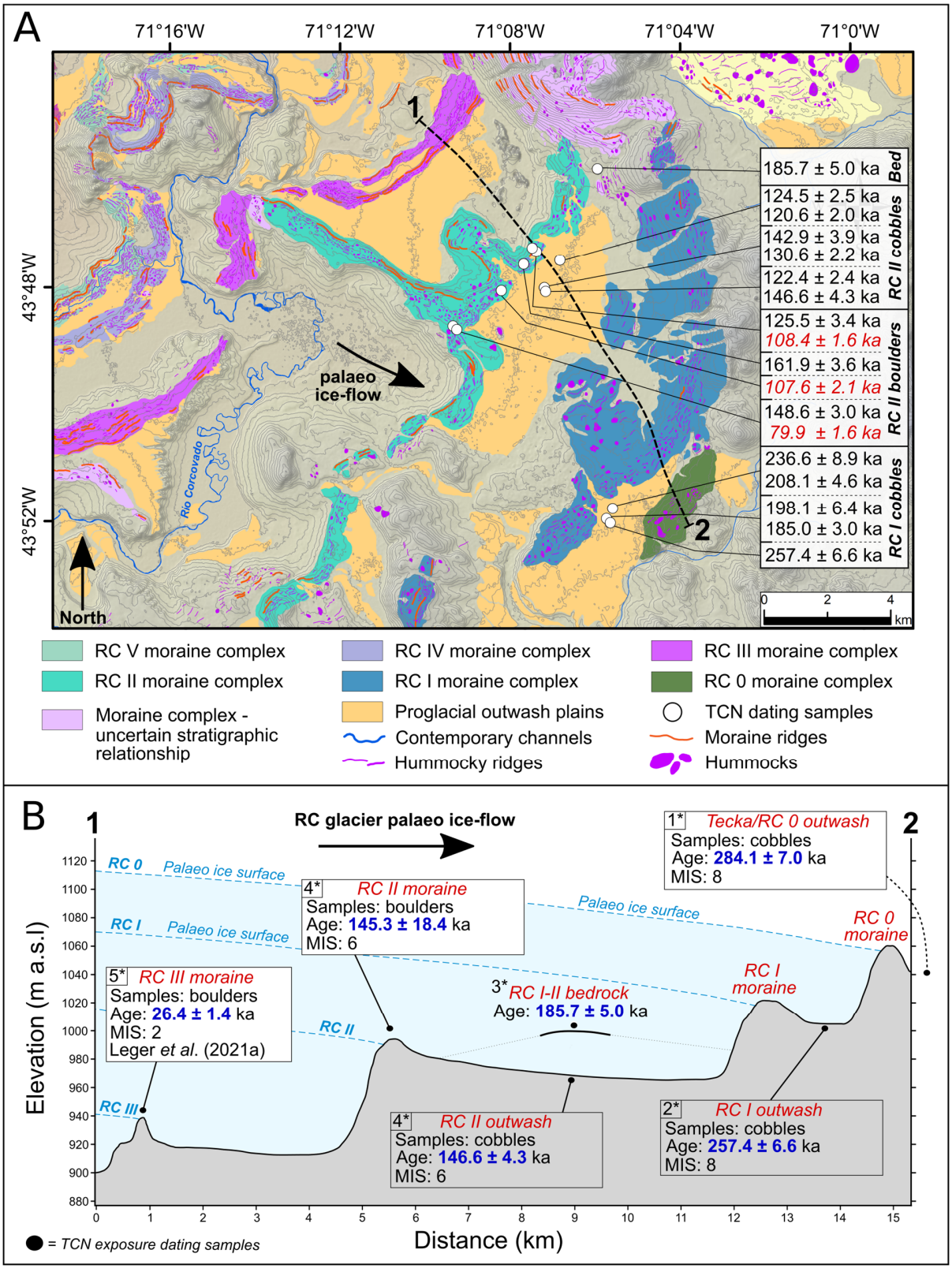
A
71°16'W
71°12'W
71°08'W
71°04'W
71°0'W
43°48'W
43°52'W
1
2
palaeo ice-flow
Río Corcovado
North
185.7 ± 5.0 ka
Bed
124.5 ± 2.5 ka
120.6 ± 2.0 ka
142.9 ± 3.9 ka
130.6 ± 2.2 ka
122.4 ± 2.4 ka
146.6 ± 4.3 ka
RC II cobbles
125.5 ± 3.4 ka
108.4 ± 1.6 ka
161.9 ± 3.6 ka
107.6 ± 2.1 ka
148.6 ± 3.0 ka
79.9 ± 1.6 ka
RC II boulders
236.6 ± 8.9 ka
208.1 ± 4.6 ka
198.1 ± 6.4 ka
185.0 ± 3.0 ka
257.4 ± 6.6 ka
RC I cobbles
0 2 4 km
RC V moraine complex
RC IV moraine complex
RC III moraine complex
RC II moraine complex
RC I moraine complex
RC 0 moraine complex
Moraine complex - uncertain stratigraphic relationship
Proglacial outwash plains
TCN dating samples
Contemporary channels
Moraine ridges
Hummocky ridges
Hummocks
B
1
2
RC glacier palaeo ice-flow
RC 0
Palaeo ice surface
RC I
Palaeo ice surface
RC II
RC III
4* RC II moraine
Samples: boulders
Age: 145.3 ± 18.4 ka
MIS: 6
5* RC III moraine
Samples: boulders
Age: 26.4 ± 1.4 ka
MIS: 2
Leger et al. (2021a)
1* Tecka/RC 0 outwash
Samples: cobbles
Age: 284.1 ± 7.0 ka
MIS: 8
Palaeo ice surface
RC 0 moraine
RC I moraine
3* RC I-II bedrock
Age: 185.7 ± 5.0 ka
4* RC II outwash
Samples: cobbles
Age: 146.6 ± 4.3 ka
MIS: 6
2* RC I outwash
Samples: cobbles
Age: 257.4 ± 6.6 ka
MIS: 8
Elevation (m a.s.l)
1120
1100
1080
1060
1040
1020
1000
980
960
940
920
900
880
0 1 2 3 4 5 6 7 8 9 10 11 12 13 14 15
Distance (km)
= TCN exposure dating samples

Figure 5.6. (**A**): Glacial geomorphological map focused on the RC 0 - RC II moraine-outwash sequence around the location of TCN exposure dating samples, highlighted by white dots (with the exception of Tecka/RC 0 outwash samples (Fig. 5.1c)). Exposure ages displayed are ^{10}Be ages ± 1σ analytical uncertainties, calibrated with LSDn scaling and central Patagonia production rate (Kapan *et al*., 2011). Ages in red were interpreted as outliers. "Bed" stands for "bedrock" and depicts the RC I – RC II ice moulded bedrock surface sampled. Elevation data is provided by the 30-m resolution DEM from the ALOS World 3D missions (AW3D30, version 2.2; JAXA; https://www.Eorc.jaxa.jp/ALOS/en/aw3d30/) with a shaded relief background and elevation contour lines at 15-m intervals. (**B**): Simplified and smoothed elevation profile graph (DEM data: AW3D30) drawn along the black line denoted in panel (A), with TCN exposure dating results (^{10}Be) from the RC 0 - III moraine-outwash dataset after interpretation of the best minimum-age estimate for each dated landform. Palaeo-ice surface elevation and slope gradients are hypothetical and purely schematic. *: Stratigraphic order of events (1: oldest, 5: youngest).

5.5.2. Comparisons with palaeo-climate and global cryosphere contexts

5.5.2.1. The MIS 8 glaciations

Our chronology suggests that two of the most extensive PIS advances preserved at the study site (RC 0 and RC I outermost) occurred during MIS 8, at around 290-270 ka, and 270-245 ka, respectively (Figs. 5.6, 5.7). These expansion events are coeval, within dating uncertainties, with glacial advances recorded by the two largest outlet glaciers of the former PIS in central Patagonia. There, the penultimate glacial advance in both the Lago Buenos Aires valley (46.5°S; Hein *et al*., 2017; Fig. 5.1) and the Lago Pueyrredón valley (47.5°S; Hein *et al*., 2009), are thought to have occurred during MIS 8. Altogether, these three pre-LGC Patagonian TCN chronologies indicate that the MIS 8 glacial events were some of the PIS's most extensive Pleistocene glaciations. These advances likely affected the former PIS across a large latitudinal range, as they can now be traced across multiple valleys from central to northern Patagonia. The geographical ubiquity of these events is diagnostic of a strong climatic forcing, while their timing coincides with some of the lowest middle Pleistocene δD values recorded over Antarctica at around 280-270 ka, associated with maximum MIS 8 Antarctic cooling of -8.5°C relative to pre-industrial modern temperatures (Parrenin *et al*., 2013; Fig. 5.8). The RC 0 advance may also be coeval with a severe peak in dust flux recorded in the EDC Antarctic ice core at ~270 ka (Lambert *et al*., 2008; Fig. 5.8). Isotopic composition analyses have demonstrated that Antarctic ice-core dust concentrations are positively

correlated to outwash-plain activity in southern Patagonia, and thus may directly reflect PIS outlet-glacier expansion events (Sugden *et al*., 2009; Koffman *et al*., 2021).

During MIS 8, Northern Hemisphere (NH) mid-latitude summer insolation intensity reached two distinct minima at 280 ka and 255 ka (Berger and Loutre, 1991; Fig. 5.8). These troughs are synchronous with peaks in the SH mid-latitude seasonality curve indicative of colder winters and warmer summers in Patagonia at those times (Darvill *et al*., 2016). Importantly, the signal of NH mid-latitude summer insolation intensity also mirrors orbitally-controlled SH seasonal duration (Denton *et al*., 2021). Hence, Patagonia was experiencing longer, colder winters and shorter, warmer summers around 280 ka and 255 ka. In contrast, SH mid-latitude summer insolation intensity reached maximum values at 280 ka and 255 ka, but minimum values at 292 ka and 268 ka, which are within exposure-age scatter and analytical uncertainties associated with dating of the RC 0 and outermost RC I advances (this study), and of the MIS 8 advances of the Lago Buenos Aires and Lago Pueyrredón outlet glaciers also (Hein *et al*., 2009; 2017). Therefore, due to current TCN exposure dating uncertainties, it remains a challenge to determine whether the MIS 8 Patagonian glaciation was coeval with a SH, or a NH mid-latitude summer insolation intensity minimum. However, more accurate dating of younger PIS outlet-glacier advances occurring during the global LGM (MIS 2; *e.g.* Peltier *et al*., 2021), including the RC outlet glacier (RC III-VII; Leger *et al*., 2021a), has shown that these later SH glacier advances, and also SSTs and Antarctic atmospheric temperature depressions, were anti-phased with SH summer insolation intensity, and were instead coeval with high SH seasonality and winter duration. Consequently, it is plausible that the PIS advanced at ~280 ka (RC 0) and ~255 ka (RC I), when SH summer insolation intensity was high, but when SH winters were cold and long. The proposed timing for the RC 0 advance is consistent with other SH palaeo-climate proxy records which suggest that peak MIS 8 cooling occurred relatively early during the glacial cycle (*i.e.* 280-270 ka; Fig. 5.8), in contrast with the later MIS 6 and MIS 5d to MIS 2 glaciations, which are characterised by maximum global cooling occurring just prior to sudden glacial terminations (Hughes *et al*., 2020).

Paradoxically, MIS 8 displays a relatively weak global cooling signal in several records such as benthic $\delta^{18}O$ (Hughes *et al*., 2020), and is thought to have been characterised by the lowest sea-level depression relative to other middle Pleistocene 100 ka glacial intervals (-93 m; Spratt and

Lisiecki, 2016). Moreover, glacial terrestrial records from different regions demonstrate contrasting ice-sheet and glacier behaviours during MIS 8. Indeed, although stratigraphic evidence for MIS 8 glaciations is often elusive, some has been reported for the Fennoscandian and British-Irish ice sheets (Beets *et al*., 2005; Davies *et al*., 2012; White *et al*., 2010; 2017), former ice sheets and glaciers overprinting Poland (Krznanian glaciations; Lindner and Marks; 1999), Siberia and Russia (Astakhov *et al*., 2011; 2016), Central and southern Europe (*e.g.* Preusser *et al*., 2011), and the West Coast Range of Tasmania (Colhoun and Barrows, 2011; Kiernan *et al*., 2010). In North America, chronological constraints for stratigraphic evidence of pre-MIS 6 glacial deposits are, in most cases, too imprecise to determine the marine isotope stage to which they relate (Hughes *et al*., 2020). The review by Hughes *et al*. (2020) concludes that robust chronological evidence of MIS 8 glaciations is rare, and, where it is found, is often characterised by margins located inboard of MIS 6 limits. In general, direct chronological evidence of MIS 8 glaciations more extensive than MIS 6-2 advances has only been found in Russia (east of the Urals; Astakhov *et al*., 2016) and Patagonia. Therefore, the extensive MIS 8 glaciation of Patagonia implies a strong regional cooling signal (Hein *et al*., 2017).

It has been noted in previous work that the major eastern Patagonian valleys, including the RC valley (Figs. 5.6, 5.7), feature records of progressively decreasing glacier extents as the glacier advances get younger (Singer *et al*., 2004; Kaplan *et al*., 2009; Cogez *et al*., 2018). This pattern may not be entirely climate-related. Instead, it might be caused by a combination of long-term erosion of the accumulation area and focused subglacial erosion along former glacial valleys that resulted in glacial overdeepening (Kaplan *et al*., 2009). During Quaternary glacial cycles, selective subglacial erosion, shown to be most effective along the flowlines of warm-based PIS outlet glaciers and near the centre of the ice sheet where ice was thickest (Clapperton, 1983), has caused rapid and zonally asymmetric overdeepening of main Patagonian valleys (Rabassa and Clapperton, 1990). In the past ~1.2 Ma, this erosive process has been estimated to cause >1000 m of bedrock elevation lowering in certain Patagonian valleys (Singer *et al*., 2004). Kaplan *et al*. (2009) argued that such overdeepening would likely have overcome the effects of tectonic- and glacial isostatic adjustment-related uplift. For a given location and identical climate forcing, erosion-driven bed lowering may have led to progressively more negative glacier mass balances during each major PIS expansion event, causing less extensive glacier advances with time. Moreover, if more

effective towards the former ice divide, subglacial erosion would also have increased retrograde basal slope gradients and thus augmented basal shear stress during subsequent glacier advances. These processes could therefore partly explain the observed pattern of decreasing outlet-glacier extent through time in eastern Patagonia (Fig. 5.6). Consequently, although the geographically widespread MIS 8 advances of the PIS were most likely the result of strong climate forcing, their outboard positions relative to MIS 6-2 deposits do not necessarily indicate colder regional conditions during MIS 8 than during the younger advances.

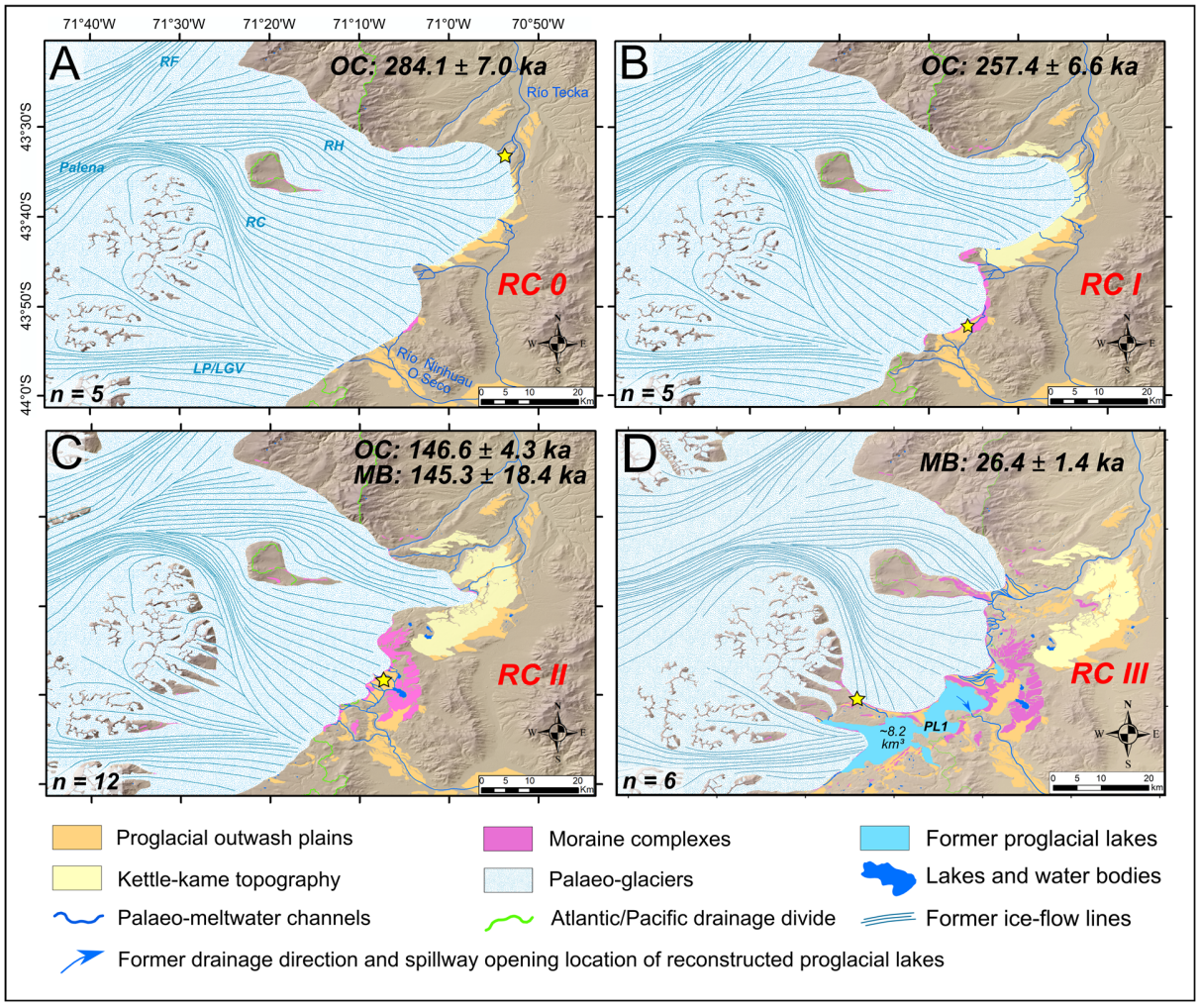

Figure 5.7. Palaeo-glacial reconstructions for the RC, RH, RF and Lago Palena/General Vintter (LP/LGV) valleys, for each advances/stillstands and deglacial events interpreted in this investigation (**A-C**). Panel **D** displays the ice extent associated with the RC III moraine complex, described in detail in companion publication (Leger *et al.*, 2021a). The latter reconstruction includes the formation of glaciolacustrine phase

one (here termed PL1; Leger *et al.*, 2021a). Ice-sheet and mountain glacier models were digitised manually in ArcGIS. Apart from when delineated by confidently-mapped moraine limits (*e.g.* the RC, RH and LP/LGV moraine sequences), the geographical location of ice margins are inferred from topography. Topographic data is from the AW3D30 DEM. "*OC"* and "*MB"* denote the type of rock samples used for TCN exposure dating of the represented event, and stand for "*outwash cobbles*", and "*moraine boulders*", respectively. Yellow stars indicate the approximate sample locations for TCN exposure dating of each represented event, while each panel features the number of ^{10}Be exposure ages produced (n = x) on the bottom left-hand corner (this excludes ^{26}Al ages). There are no previously published glacier chronologies in the RH, RF and LP/LGV valleys. Relative ice extents in those neighbouring valleys are thus inferred from our RC chronology and cross-valley comparisons of moraine set numbers, preservation and morphostratigraphy. Hence, these inferences yield some uncertainties. Proglacial lake volume estimates were computed from DEM data (AW3D30).

5.5.2.2. The MIS 7 glaciation

Our chronology provides inceptive evidence that the innermost and youngest advance to have reached the RC I moraine complex may have occurred during MIS 7 (243-191 ka; Lisiecki and Raymo, 2005). Although the resolution of our chronology is not sufficient to assert the following with confidence, we argue that this potential event might relate to interstadial MIS 7d (~235-225 ka), described in detail by Ruddiman and McIntyre (1982, p1273) as an event that "*bisected "interglacial" isotopic stage 7, lasted no more than 23,000 yr from inception to end, and resulted in a very large ice-volume build- up and a full-glacial climatic response of the North Atlantic Ocean*". Direct terrestrial evidence and robust dating of this event are currently non-existent in the southern mid-latitudes, and hence more empirical data from several locations are required to assess the geographical ubiquity of this glacial expansion event.

During the relatively brief MIS 7d interstadial, global atmospheric CO_2 concentrations are estimated to have diminished by ~75 ppm (Bereiter *et al.*, 2015), and the atmospheric temperature depression over Antarctica was of similar magnitude to that recorded during the MIS 8 and MIS 6 stadials (Fig. 5.8). These records indicate that a 20 ka-long Antarctic atmospheric cooling phase, with a peak cooling of approximately -7.5°C relative to pre-industrial modern temperatures, occurred at ~223 ka, 7 ka after NH mid-latitude summer insolation intensity reached the lowest

values of the past 1 Ma, at 230 ka (Fig. 5.8). Therefore, while interstadial MIS 7d was relatively short-lived, it was characterised by record-high winter duration and a peak in local seasonality (colder winters and warmer summers) at the SH mid-latitudes. Antarctic dust concentration records also indicate a significant maximum at 225-220 ka (Lambert *et al*., 2008; 2012). This implies the MIS 7d interstadial was likely associated with an expansion of the PIS inducing outwash-plain activity in southern Patagonia (Sugden *et al*., 2009).

5.5.2.3. The penultimate MIS 6 glaciation

Our interpretation of TCN exposure ages from the penultimate RC II margin suggests that a major expansion of the PIS occurred during MIS 6, and towards the latter part of the glacial interval, at around 140-150 ka (Figs. 5.4, 5.6, 5.7). Our chronology suggests that maximum PIS expansion occurred just prior to the rapid global warming leading to MIS 5e, one of the warmer middle-to-late Pleistocene interglacial periods (Fig. 5.8). This is consistent with global sea-level reconstructions suggesting that the second greatest global ice volume of the past 800 ka, associated with a sea-level minimum of -125 m, was reached towards the end of MIS 6, at ~140 – 135 ka (Spratt and Lisiecki, 2016). At that time, mean atmospheric temperatures over Antarctica are estimated to have reached their second lowest values of the past 800 ka (-9.3 °C relative to pre-industrial period; Fig. 5.8). Global cooling during MIS 6 was more persistent than during other middle Pleistocene glacial cycles. Indeed, this cycle is associated with four major minima in Antarctic atmospheric temperatures spread over ~50 ka, and occurring at around ~185, ~165, ~155 and ~140 ka (Parrenin *et al*., 2013; Fig. 5.8). As observed for the MIS 8 interval, these peaks in atmospheric cooling occurred a few ka after NH summer insolation intensity minima, associated with SH seasonality and winter duration maxima. Global SSTs and atmospheric CO_2 concentrations remained consistently low for the same 50 ka time-window, between ~190 and ~140 ka (Bereiter *et al*., 2015; Shakun *et al*., 2015). The persistence of the cold phase throughout MIS 6 may have facilitated multiple expansions of the PIS at this time. In our ^{10}Be chronology, this may be reflected by the potential recycling and re-deposition of one RC II moraine boulder sample, yielding a ^{10}Be exposure ages of 162 ± 4 ka, during the younger penultimate advance dated by the RC II outwash cobbles (~130-140 ka).

Evidence for several distinct MIS 6 glaciations has been reported from other regions of the world. For the European Ice Sheet, for instance, stratigraphic investigations have led to the dating, and naming, of two glaciations within MIS 6, respectively the Late Saalian Drenthe glaciation at 175-155 ka, and the Warthe Stadial between 150 ka and 135 ka (Toucanne *et al*., 2009; Margari *et al*., 2014). More generally, MIS 6 glacial deposits are ubiquitous near former glacial margins and are documented by a wider body of evidence than other pre-LGC glaciations (*e.g.* Putnam *et al*., 2013; Kiernan *et al*., 2014; Evans *et al*., 2019; Fernandes *et al*., 2021), suggesting that the greatest global ice volume of the middle Pleistocene was likely reached during that interval (Hughes *et al*., 2020). In Patagonia, however, our chronology is amongst the first published datasets, along with one other ongoing investigation (abstract: Peltier *et al*., 2017), offering direct and robust dating of a MIS 6 glacial expansion event. Indeed, the well-studied Lago Pueyrredón and Lago Buenos Aires pre-LGC moraine-outwash records do not provide clear chronological evidence for MIS 6 advances (Hein *et al*., 2009; 2017). However, this may just imply that the MIS 2 advances of the Lago Pueyrredón and Lago Buenos Aires outlet glaciers were more extensive than any MIS 6 glacial events. Therefore, as for the MIS 8 glaciation, MIS 6 expansions of outlet glaciers may have been ubiquitous through the former PIS. However, the current lack of robust pre-LGC glacier chronologies in Patagonia prevents this hypothesis from being tested adequately.

5.5.2.4. Synthesis: The timing of Patagonian glaciations

Along with companion publications focusing on the LGC (Leger *et al*., 2020; 2021a), our findings illustrate that the preserved sequence of moraine-outwash complexes in the RC valley system records a minimum of four major PIS expansion events occurring during MIS 8, 6, and 2; and possibly also during MIS 7. In Antarctic atmospheric paleo-temperature proxy records, global SST records, and global atmospheric CO_2 records, the strongest minima between today and 330 ka are all recorded by the RC moraine-outwash complexes, with the exception of the 70-60 ka (MIS 4) cold interval, for which no preserved moraine-outwash complex could be found at the study site. However, we note that a major advance of the PIS near this time did occur on the western side of the Andes at 42°S (García *et al*., 2021; Gómez *et al*., 2022). There, Garcia *et al*. (2021) dated glacial sediments on the Isle of Chiloe to 57.8 ± 4.7 ka, or early MIS 3, with a somewhat

smaller advance occurring during MIS 2 at 26.0 ± 2.9 ka. The lack of a corresponding MIS 3/4 moraine east of the mountains suggests that the PIS behaved asynchronously between its western and eastern margins at this time. In southeastern Patagonia, more-extensive-than MIS 2 advances were also dated to MIS 4 and 3 using TCN exposure dating (*e.g.* Darvill *et al*., 2016; García *et al*., 2018; Peltier *et al*., 2021). We argue that while the RC outlet glacier most likely advanced during the MIS 4 and 3 cooling events, these intervals were relatively short-lived, impeding the PIS from becoming locally thick enough to allow the RC outlet glacier to advance along its retrograde bed slope and generate an extensive advance. Very likely, in addition, all glaciogenic deposits associated with MIS 3/4 advances may have been eroded during the younger MIS 2 advances. This may suggest that steady cooling over periods >15-20 ka is an important pre-requisite for northeastern PIS outlet glaciers to reach a mass balance positive enough to enable highly extensive advances.

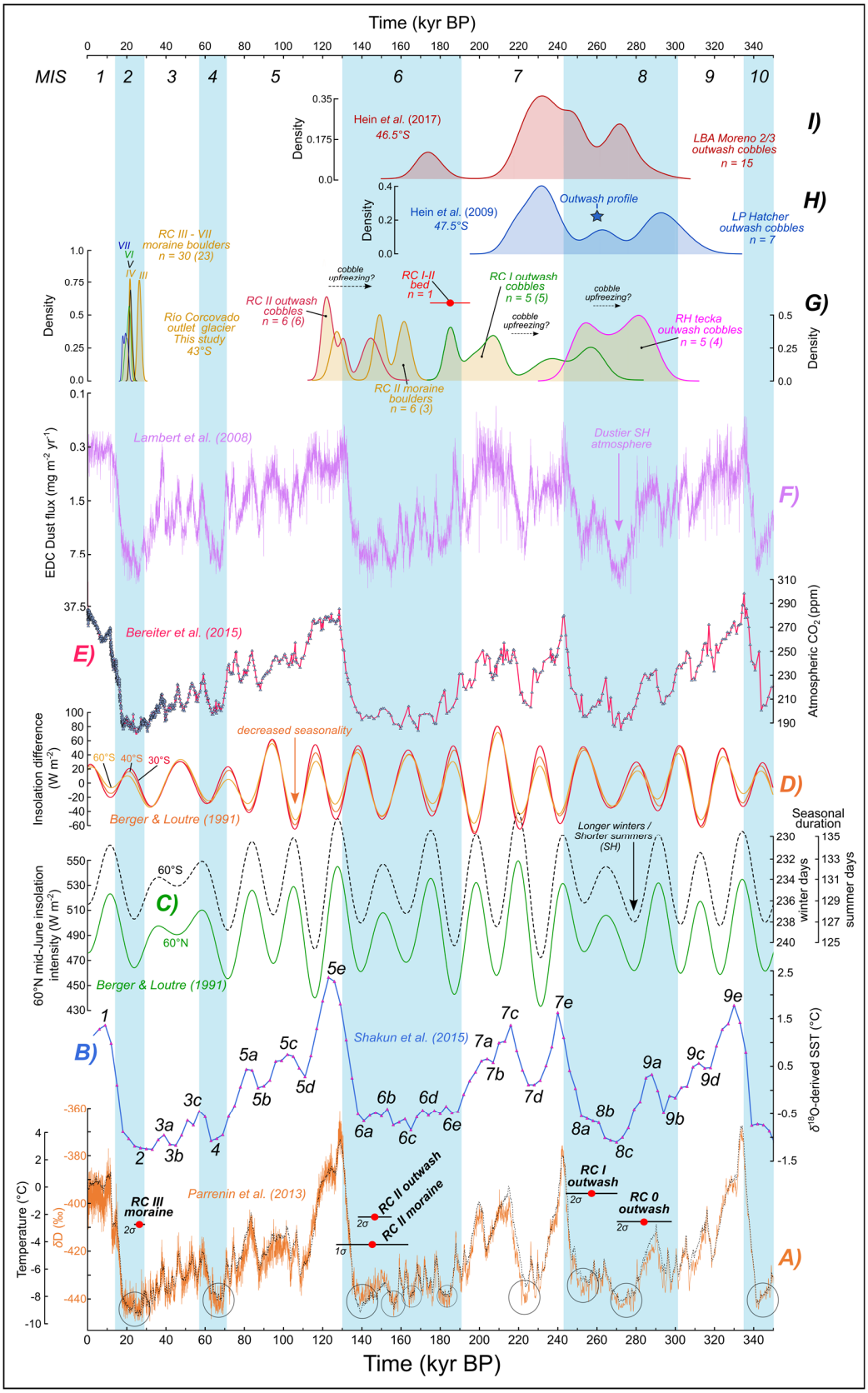
Time (kyr BP)
MIS
Hein et al. (2017)
46.5°S
LBA Moreno 2/3
outwash cobbles
n = 15
I)
Hein et al. (2009)
47.5°S
Outwash profile
LP Hatcher
outwash cobbles
n = 7
H)
RC III - VII
moraine boulders
n = 30 (23)
Río Corcovado
outlet glacier
This study
43°S
RC II outwash
cobbles
n = 6 (6)
RC I-II
bed
n = 1
RC I outwash
cobbles
n = 5 (5)
RH tecka
outwash cobbles
n = 5 (4)
RC II moraine
boulders
n = 6 (3)
cobble
upfreezing?
G)
Lambert et al. (2008)
Dustier SH
atmosphere
EDC Dust flux (mg m-2 yr-1)
F)
Bereiter et al. (2015)
E)
Atmospheric CO2 (ppm)
decreased seasonality
60°S
40°S
30°S
Insolation difference
(W m-2)
Berger & Loutre (1991)
D)
Longer winters /
Shorter summers
(SH)
Seasonal
duration
winter days
summer days
60°N mid-June insolation
intensity (W m-2)
C)
60°N
Shakun et al. (2015)
B)
δ18O-derived SST (°C)
Parrenin et al. (2013)
RC III
moraine
RC II outwash
RC II moraine
RC I
outwash
RC 0
outwash
2σ
1σ
Temperature (°C)
δD (‰)
A)
Time (kyr BP)

Figure 5.8. Vertical plot comparing this investigation's TCN ^{10}Be chronology to other Patagonian outlet-glacier TCN chronologies, to insolation intensity variations, and to palaeo-climate proxy records over the past 350 ka. (**A**) Stable isotope δ Deuterium record (orange curve) from the EPICA Dome C (EDC) ice core, 75°S, east-Antarctica and Antarctic atmospheric temperature (overlying dashed black curve) from a stack of isotopic temperature reconstructions from five different ice cores (EDC, Vostok, Dome Fuji, TALDICE, and EDML) (Parrenin *et al*., 2013), with most potent cooling events of the past 350 ka highlighted by black circles. TCN exposure ages from the RC valley interpreted as best minimum-age estimate for each reconstructed glacial event are displayed (red dots) with analytical uncertainty (black horizontal bars). (**B**): Global stack (n = 49 cores) of paired planktonic δ^{18}O-derived Sea Surface Temperature (SST) data with Marine Isotope Stage numbers indicated (Shakun *et al*., 2015). (**C**): Dark green line: summer (mid-June) insolation intensity for 60°N (Berger and Loutre, 1991). Dashed black curve: seasonal duration at 60°S (insolation threshold = 300 W m^{-2}) after Huybers and Denton (2008) and Denton *et al*. (2021). (**D**): Southern Hemisphere seasonality at 30°C, 40°S, and 60°S calculated by subtracting June from December insolation intensity values (Berger and Loutre, 1991), such that increasing seasonality indicates colder winters and warmer summers (after Darvill *et al*., 2016). (**E**): Atmospheric CO_2 concentrations composite record from several Antarctic ice cores including EDC, WAIS, Vostock, Siple Dome, TALDICE, EDML, and LAW Dome (Bereiter *et al*., 2015). (**F**): Dust flux record from the EDC ice core (Lambert *et al*., 2008). (**G-I**): Kernel density distribution curves (1σ) for TCN exposure ages from the RC O – RC II moraine-outwash records (this study: **G**), the Hatcher moraine-outwash complex, in the Lago Cochrane/Pueyrredón valley (Hein *et al*., 2009; **H**), and the Moreno 2/3 moraine-outwash limits, in the Lago General Carerra / Buenos Aires valley (Hein *et al*., 2017; **I**).

5.5.3. Climatic and orbital drivers of SH glaciations - hypotheses

Our chronology implies that the most extensive middle Pleistocene PIS expansion events preserved match the strongest minima in Antarctic atmospheric temperatures (Parrenin *et al*., 2013), global oceanic SSTs (Shakun *et al*., 2015), and global atmospheric CO_2 concentrations (Bereiter *et al*., 2015) (Fig. 5.8). They also often appear to occur a few ka after minima in NH summer insolation intensity (60°N) and maxima in SH seasonality, while being out-of-phase with mid-latitude SH summer insolation intensity (Fig. 5.8c). The first observations of the asynchrony between SH mid-latitude glacier advances/recessions and local summer insolation intensity (*e.g.* Mercer, 1976; Denton *et al*., 1999) encouraged the hypothesis that major glacial-termination-inducing warming signals were primarily controlled by NH summer insolation intensity driving NH glacial mass balance, and were propagated from the northern to the southern hemisphere through oceanic and atmospheric circulation shifts (*e.g.* Broecker, 1998; Denton *et al*., 2010).

Some of these interhemispheric climate-transmission mechanisms, such as the impact of the abrupt weakening of the Atlantic meridional overturning circulation in the north Atlantic following the last deglaciation, have been well documented (Barker *et al*., 2009; Denton *et al*., 2010). However, there is still a great deal of debate regarding the dominant trigger mechanisms responsible for global ice-sheet expansion/retreat cycles (Putnam *et al*., 2013). Indeed, the above hypothesis entails the dilemma that while NH summer insolation intensity would be a key driver of NH ice-sheet mass balance, it would instead have little impact on mass fluctuations of SH mid-latitude ice sheets and glaciers (Denton *et al*., 2021). This problem invites the consideration of alternative hypotheses, such as the potential roles of SH seasonality and seasonal duration on controlling global ice-sheet mass fluctuations.

García *et al*. (2018) noted that the extensive advances of the Torres del Paine (51°S) and the Última Esperanza (51.5°S) outlet glaciers at 48 ka (MIS 3) coincide with a minimum in obliquity-modulated high-latitude winter insolation intensity. The authors therefore hypothesise that colder SH winters during periods of high obliquity may favour SH mid-latitude glaciation by promoting local atmospheric cooling, Southern Ocean stratification and expanded Antarctic sea ice. Since we observe that middle-to-late Pleistocene PIS expansion events appear to occur during periods of longer, colder winters and shorter, warmer summers, we suggest that other PIS chronologies (including this study) may support García *et al*. (2018)'s hypothesis.

Alternatively, the "*Zealandia Switch*" hypothesis (Denton *et al*., 2021) focuses on the SH seasonal-duration aspect of orbitally-controlled insolation as a potential driver of late-Quaternary glaciation. By pacing the seasonal cycle of weakened and northward-migrated SWW during winter versus strengthened and southward-migrated SWW during summer, this hypothesis implies that SH seasonal duration might be a key driver of global climate change during middle-to-late Pleistocene glacial/interglacial cycles. Using global climate model simulations, the authors show that a reduced SH summer duration and increased SH winter duration could cause millennial-scale equatorward migrations of the SWW and its coupled Antarctic Circumpolar Current. Such zonal wind configuration would induce a northward migration of the subtropical front and a latitudinally-restricted subtropical gyre system in the Indo-Pacific Ocean basins (*ibid*). The bathymetry of the Australia/Zealandia continent is such that a restricted Indo-Pacific subtropical gyre could decrease

Indonesian Throughflow and restrict westward Agulhas Leakage into the South Atlantic Ocean (Lorrey and Bostock, 2017). A reduced Aghulhas Leakage has implications for the Atlantic salt input resulting in a potential weakening of Atlantic meridional overturning circulation (Caley *et al*., 2012). The authors thus argue that such a southern oceanic and atmospheric circulation configuration could promote a global glacial mode (Denton *et al*., 2021) that would greatly affect SH and thus Patagonian glacier mass balance.

Moreover, variations in the intensity and latitudinal position of the SWW influence Southern Ocean upwelling of deep-stored CO_2 and nutrients (Anderson *et al*., 2009; Ai *et al*., 2020). This mechanism is thought to represent a major contribution to variations in global atmospheric CO_2 concentrations over millennial timescales (Sarmiento and Toggweiler, 1984). Former equatorward shifts and weakening of the SWW could have decreased Southern Ocean upwelling and enhanced CO_2 storage in the deep ocean, thus causing delayed global cooling amplification (Sime *et al*., 2013). Conversely, a poleward migration and strengthening of the SWW is thought to amplify global warming via increasing Southern Ocean upwelling, CO_2 outgassing and increasing CO_2 atmospheric concentrations. This hypothetical CO_2 capacitor storage-and-release mechanism may explain the highly amplified warming observed during major glacial terminations (Anderson *et al*., 2009; Denton *et al*., 2021). This positive feedback mechanism may partly justify why middle-to-late Pleistocene global oceanic and atmospheric temperature variations often reached their most extreme values with some notable delay (a few ka) relative to NH mid-latitude summer insolation intensity.

To summarise, empirical data including this study suggest that major middle-to-late Pleistocene cycles of SH mid-latitude glaciers and ice sheets appear to be coeval with NH glaciers and ice sheets, but out-of-phase with local mid-latitude summer insolation intensity (Putnam *et al*., 2013; Peltier *et al*., 2021), traditionally thought to be the primary driver of middle-to-late Pleistocene glacial expansion/demise cycles (Mercer, 1984). However, recent hypotheses suggest that this paradox might be explained by the potentially more dominant climate-forcing effect of the seasonality and seasonal-duration expressions of SH insolation, through their impact on atmospheric temperature, the position of the SWW belt and Subtropical Front, Antarctic sea ice extent, and Southern Ocean stratification and CO_2 storage-and-release feedback mechanisms.

Testing the above hypotheses, and determining which of seasonality versus seasonal duration played a primary role in driving SH climate and glacial variations during the middle-to-late Pleistocene, represent key avenues for future research.

5.6. Conclusions

- We provide geomorphological and direct chronological evidence for at least three extensive, stratigraphically distinct pre-Last Glacial Cycle advances of the Río Corcovado glacier, a major outlet of the former northern Patagonian Ice Sheet. TCN surface exposure dating of outwash surface cobbles yields best minimum-age estimates for the RC 0, RC I and RC II advances of 284 ± 7 ka, 257 ± 7 ka, and 147 ± 4 ka, respectively.

- Together with evidence we have reported in Leger *et al*. (2021a, b), our complete chronology reveals a minimum of four distinct expansion events of northeastern Patagonian Ice Sheet outlet glaciers that occurred during the MIS 8, MIS 6, and MIS 2 intervals. Further results gathered from bedrock surface and moraine boulder exposure ages also provide inceptive evidence for another MIS 7 expansion event and at least another MIS 6 advance previously reaching a close extent to that of the penultimate RC II advance.

- Our dataset presents the first robust direct dating evidence of MIS 6 glaciations in Patagonia.

- We did not find evidence for MIS 4 and 3 deposits in the RC valley geomorphological record. However, extensive glaciations did occur at these times on the former western margin of the Ice Sheet, and in other, more southern Patagonian regions. This highlights longitudinal and latitudinal asynchronies in former Patagonian Ice Sheet mass balance during these stages. We suggest that MIS 4 and 3 outlet-glacier advances likely occurred in northeastern Patagonia, but were of relatively shorter extent, and their associated deposits were likely eroded by the younger, more extensive MIS 2 glaciation.

- We interpret that major middle-to-late Pleistocene Patagonian Ice Sheet expansions occurred in synchrony with the greatest cooling events recorded in global SST and Antarctic atmospheric temperatures, with the most prominent peaks in Antarctic ice-core dust concentrations, and with major minima in global CO_2 atmospheric concentrations. We observe a particularly good correlation between Antarctic atmospheric temperature signals and southern mid-latitude ice-sheet volume fluctuations, over several glacial cycles.

- Our results suggest that Patagonian glaciations were more extensive during MIS 8 than during MIS 6-2, while global ice volumes and sea level depression were not particularly high during MIS 8. This implies that there was interhemispheric asynchrony in the relative volume and extent of Earth's major ice sheets during MIS 8. However, we acknowledge that a larger MIS 8 eastern Patagonian Ice Sheet is not necessarily indicative of a more potent local climate-forcing event than during younger glaciations (MIS 6-2) as glacial erosion, which greatly influences the local topography, may play a role in controlling ice-sheet extent.

- Major middle-to-late Pleistocene advances of the Patagonian Ice Sheet appear to have occurred out-of-phase with local summer insolation intensity but in synchrony with orbitally-controlled periods of longer and colder winters. We hypothesise that seasonality and seasonal duration may exert more control over southern mid-latitude ice-sheet mass balance than mid-latitude summer insolation intensity over millennial timescales. This may be a consequence of the possible effect of seasonal duration variability on the strength and migration of the SWW, and the impact of these migrations on global climate and Southern Ocean circulation and CO_2 upwelling, as proposed by the "*Zealandia Switch*" hypothesis.

- Our findings corroborate work by Hein *et al*. (2009; 2017) and indicate that, in eastern Patagonia, pre-LGC outwash surface cobbles yield exposure ages displaying less post-depositional scatter than moraine boulders from the same margins, and hence facilitate more accurate estimations of the approximate timing of pre-LGC glacial advances.

Chapter VI

|

Conclusions

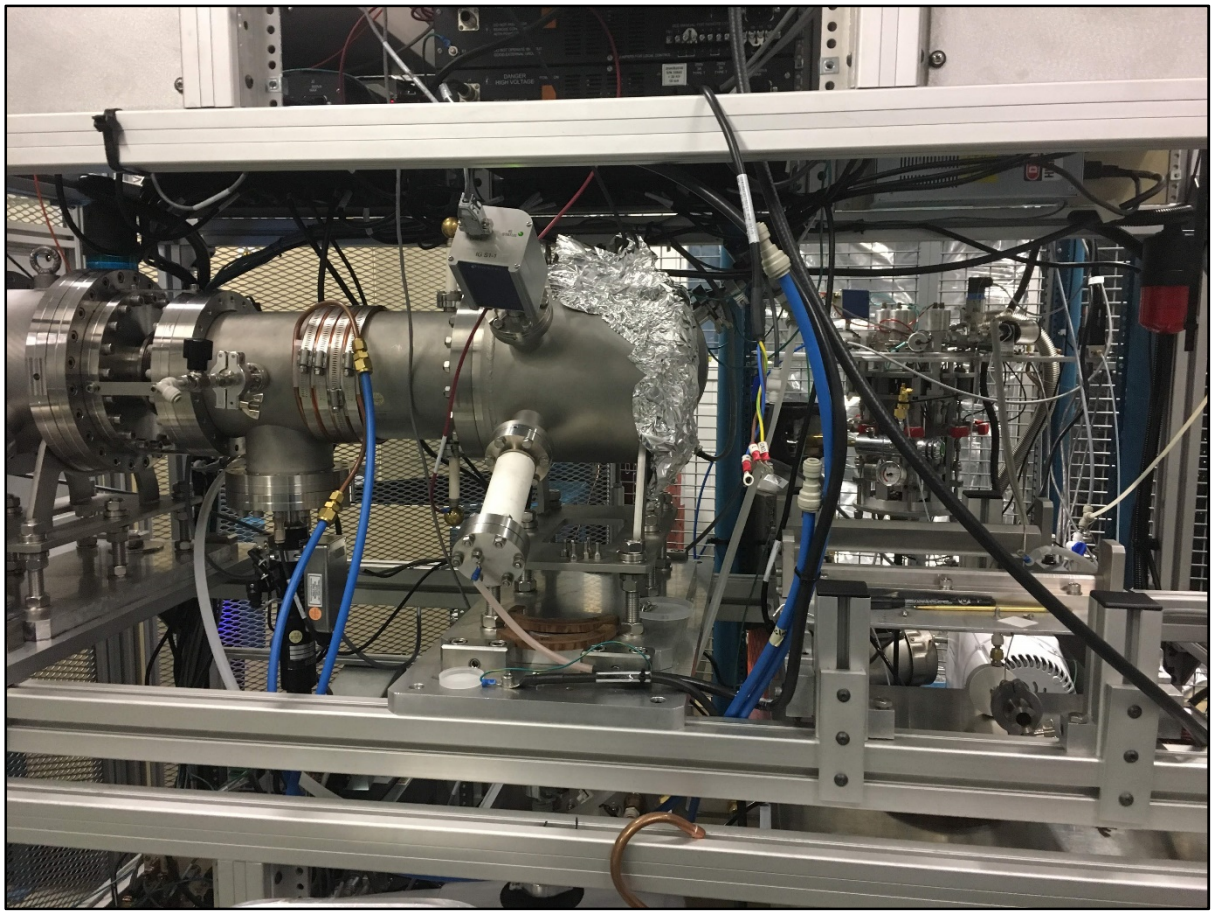

6.1 Main conclusions and implications

The principal aim of this Ph.D. investigation was to better constrain the late-Quaternary evolution of Patagonian Ice Sheet outlet glaciers in a largely under-studied region defined as the former ice-sheet's northeastern sector (aim 1.). This thesis also aimed at using this reconstruction to unravel former synchronous and/or asynchronous behaviour between outlet-glaciers of the former Patagonia Ice Sheet (aim 2.). Finally, the aim was also to gain further insights into the environmental mechanisms responsible for major outlet-glacier expansions at the study site and throughout the southern mid-latitudes (aim 3.). In an attempt to fulfil these aims, the thesis was structured around four main research objectives (section 1.4). I here summarise the thesis' findings by describing how each chapter address each of these four objectives.

6.1.1. Objective 1: Establishing a geomorphological and morphostratigraphic reconstruction of glacial dynamics at the study site

Glacial geomorphological mapping presented in Chapter 2 has led to the identification of 25 landform types associated with former ice-contact glaciogenic, glaciofluvial, glaciolacustrine and subglacial activity of three distinct PIS outlet glaciers at the study site: The Río Corcovado, Río Huemul and Lago Palena/General Vintter glaciers (5300 km^2). Our investigation has enabled to produce the first detailed glacial geomorphological map of these valley systems. As well as representing the framework underpinning further geomorphological and geochronological reconstructions conducted at the study site (Chapters 3-5), this map has enabled us to constrain, for the first time, the detailed morphostratigraphy of former glacial events associated with the PIS activity in this region. For instance, mapping has allowed us to establish that: 1) A minimum of eight distinct glacial expansion events of the former Río Corcovado outlet glacier are preserved locally under the form of terminal moraine belts. 2) Sets of palaeo-shorelines inform that a minimum of three former proglacial lake phases occurred in the studied valleys during the last glacial expansion and retreat cycle of the PIS. 3) Resurgences of local mountain glaciers occurred following the onset of PIS deglaciation, as evidenced by lateral moraines of the El Loro valley cross-cutting inner moraines formed by the RC palaeo-glacier. These three examples, along with numerous other findings, highlight that our

geomorphological map is the foundation for all morphostratigraphic interpretations of glacial dynamics presented in this thesis. Moreover, the map enables us to identify empirical ice-extent boundaries that can prove essential to future work including palaeo-ice-sheet numerical modelling investigations. Our mapping work also has implications for future studies aiming at reconstructing former fluvial and lacustrine drainage activity in the region.

6.1.2. Objective 2: Establishing a detailed geochronological reconstruction of local glacial and proglacial events during the local LGM and the last deglaciation

Our results from ^{10}Be TCN exposure dating of moraine boulders from the RC III – RC VII moraines combined with Bayesian age modelling has enabled us to establish a detailed chronology of local LGM glacial expansion events in the understudied northeastern sector of the former PIS. This detailed chronology (n = 30 ages) has revealed that 5 distinct advances/stillstands of the Río Corcovado have occurred between 26.4 ± 1.4 ka and 19.9 ± 1.1 ka, thus during MIS 2 and the global LGM. While this reconstruction corroborates that the PIS was highly sensitive to global cooling during MIS 2, a major finding is also that no advances dating to the LGC and more extensive than those that occurred during the global LGM could be found at the study site. Because some outlet glaciers of the southern PIS and of other southern mid-latitude mountainous locations have reached maximum ice extent during MIS 3 (*e.g.* Darvill *et al*., 2015), MIS 4 (*e.g.* Schaefer *et al*., 2015) and MIS 5 (*e.g.* Mendelová et al., 2020) rather than during the global LGM, the implication of our finding is that the PIS experienced large latitudinal and longitudinal asynchronies in the magnitude and timing of its outlet glacier expansions during the LGC. Our findings also confirm that the ubiquitous MIS 2 southern mid-latitude glaciation was out-of-phase with local summer insolation intensity and synchronous with Northern Hemisphere ice masses, thus suggesting that local summer insolation intensity had little impact on glacier SMB during these events (as previously shown: *e.g.* Doughty *et al*., 2015). Our LGM – focused geochronological reconstruction also enabled to reconstruct the timing of the onset of local PIS deglacation, here estimated to have occurred between 19 and 20 ka, thus ~1 ka prior to northwestern and more southern outlet glaciers. These findings thus suggest that the PIS was particularly sensitive to warming and drying during the Varas insterstade (~22.5-19.5 ka) in its northeastern sector. Finally, this

investigation has implications for better understanding the palaeo-lake history of the study site, associated with the local palaeo-glacial activity during the global LGM and deglaciation phases. By dating palaeo-shoreline outwash cobbles and ice-moulded bedrok surfaces, at least three distinct local glaciolacustrine phases were reconstructed. They occurred at 26.4 ± 1.4 ka (~990 m a.s.l. level), between ~22 and ~20.5 ka (~790 m a.s.l. level), and between ~19 and ~16 ka (~680 m a.s.l. level), respectively. Our dating of final glaciolacustrine phase three lake drainage at 16.3 ± 0.3 ka enables us to imply that local ice retreat lead to the desintegration of the PIS by ~16 ka in the Río Palena valley system. Constraining the timing of PIS desintegration is critical, as it caused an ice-dam breach and a westward drainage of the large ~680 m proglacial lake (~273 km^3 of freshwater). This sudden Atlantic/Pacific reversal of freshwater drainage has undoubtedly had major implications for both terrestrial and oceanic ecosystems of the region.

To summarise, the results produced within the context of this investigation (Chapter 3) have implications for better constraining both the magnitude and timing of former glacial events, former glaciolacustrine bodies and former glacier-climate interaction mechanisms, during a key ~10-ka-long period of the LGC when environmental changes of rare magnitudes occurred.

6.1.3. Objective 3: Establishing a reconstruction of paleoclimate dynamics by combining geochronology and glacier numerical modelling

The main implications of the study/paper presented in Chapter 4 are threefold. Firstly, the glacial geomorphological and geochronological analyses of this investigation have revealed that, at the study site, former advances/still-stands of mountain glaciers younger than the innermost local LGM resurgence of the RC outlet glacier have occurred. The timing of this glacial event (18.0 ± 1.15 ka) in the EL valley suggests that climate-sensitive mountain glaciers re-advanced/stabilized during the late-LGM, between ~19.5 and ~18 ka. This glacier resurgence signal does not appear in the geomorphological record associated with local PIS outlet glaciers, most likely due to their early initial deglaciation (~19-20 ka) and the enhanced ablation factor associated with the formation of large proglacial lakes in main overdeepened valleys. This additional study of independent mountain glaciers was thus crucial here, as it revealed that the late-LGM 1.5 kyr-long cold and wet episode (~19.5-18 ka) reported in other

Patagonian regions (*e.g.* Moreno *et al.*, 2018) also had a positive impact on glacier mass balance in northeastern Patagonia.

Secondly, the combination of the previous findings with our coupled ice-flow and SMB model analyses have enabled to provide quantitative estimations of both former glacier geometries and likely palaeo-climate conditions during late-LGM glacial event at the study site. For instance, this approach enabled to estimate that, during its late-LGM advance/still-stand (18.0 ± 1.15 ka), the EL glacier reached a steady-state volume of between 0.614 and 0.769 km^3, while atmospheric surface temperatures were likely to range between -1.9 °C and -2.8 °C relative to a 1970-2000 AD average. Unlike palaeo-climate reconstructions that rely exclusively on the analysis of glacier ELA depressions, an interesting feature of our approach was also to assess the role of precipitation change in promoting glacier expansion/stabilization. This component has proven crucial for this study, as all model simulations conducted suggested a positive precipitation anomaly during this late-LGM glacier advance, thus supporting the previously posed hypothesis of equatorward-migrated SWW at this time.

Thirdly, our ice-flow model -derived palaeo-temperature and palaeo-ELA estimations required a correction for regional surface elevation change associated with post-LGM uplift caused by GIA. This analysis revealed that the site-specific cumulative surface uplift approximated ~130 m between 18 ka and today. Because such amount of surface uplift equates to a significant atmospheric surface temperature adjustment (0.85 °C with an ALR of 6.5 °C km^{-1}), this finding has important implications for future investigation using palaeo-glacier SMB to reconstruct climate dynamics. It shows that estimating and taking into account post-event surface elevation change is, in some specific cases, an important requirement when employing palaeo-glacier reconstructions as climate proxies.

Therefore, this investigation, by combining results from glacial geomorphology, geochronology, and glacier and GIA numerical modelling, has addressed research objective 3 accordingly and contributed to the scientific exercise of studying past glaciers to reconstruct former climate change in Patagonia.

6.1.4. Objective 4: Establishing a reconstruction of major pre-LGM and pre-Last Glacial Cycle glaciations at the study site and assess palaeo-climatic context

The study/paper presented in Chapter 5 features a detailed TCN exposure dating chronology of the preserved moraine-outwash complexes deposited by major middle-to-late Pleistocene glaciations pre-dating the LGC at the study site. Due to the local preservation and suitability of proglacial outwash sediment to TCN exposure dating, this additional dataset enabled us to reveal the full potential of the study site's glacial geomorphological record by compiling a multi-glacial-cycle geochronological reconstruction of local PIS expansion events. This complete chronology has implications for discerning longitudinal and latitudinal a/synchronies in PIS outlet glacier behaviour, such as the lack of extensive MIS 3 and MIS 4 advances in northeastern Patagonia, for instance. The discovery that the highly extensive MIS 8 expansion of the PIS did also occur at the study site and was ubiquitous throughout central (Hein *et al*., 2017), northern (this study), and likely other regions of Patagonia, is another example of the implications that this additional pre-LGC dataset entails. Moreover, this chronology enabled to provide the first (to this day) numerically-dated evidence of an MIS 6 glaciation in Patagonia. By enabling to understand the timing of major Patagonian glaciations over several glacial cycles, which can be compared with other glacial chronologies, palaeo-climate records, and orbital signals of insolation, this dataset also has implications for better isolating the natural and climatic mechanisms responsible for southern mid-latitude glaciations. For instance, similarly to observations made with the MIS 2 glacial maximum in the southern mid-latitudes (*e.g.* Doughty *et al*., 2015), the timing of the PIS MIS 6 advance discovered in this study (146.6 ± 4.3 ka) suggests major Patagonian glaciations systematically occurred out-of-phase with local summer insolation intensity. However these advances seem to have been coeval with the expansion of NH ice sheets and with major cooling signals recorded in Antarctica and global SST. Consequently, such findings address objective 4 and provide further evidence for Mercer's paradox (Denton *et al*., 2021), thus allowing us to explore new hypotheses including the role of other expressions of orbitally-controlled insolation and southern circulation in promoting globally synchronous glaciations at the mid-latitudes.

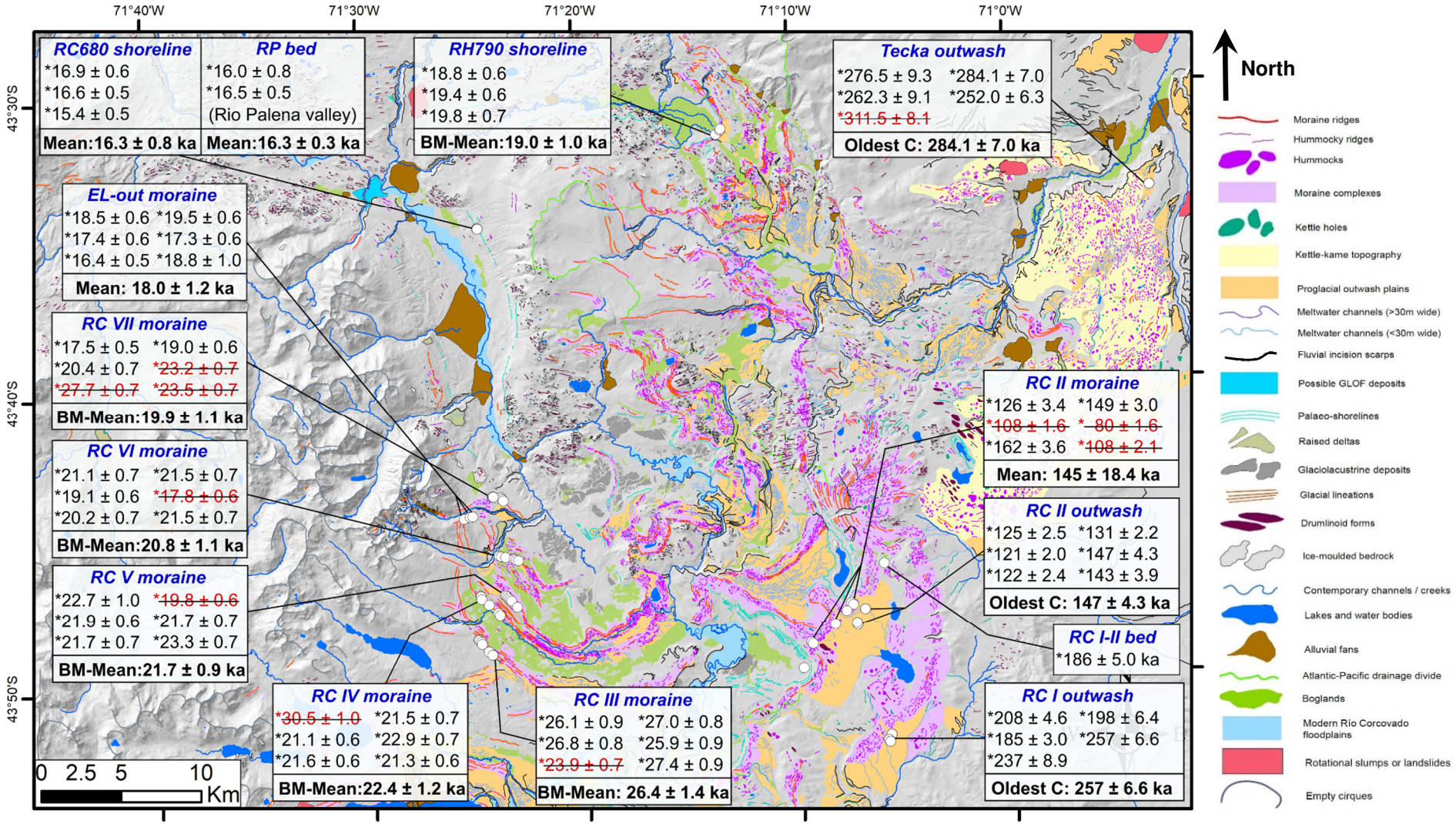

Figure 6.1. Glacial geomorphological map of the study site over DEM hillshade: focusing on the Río Corcovado and Río Huemul valleys. All ^{10}Be surface exposure ages produced within the context of this Ph.D. investigation, including outliers (in red), are displayed. Sampling locations are denoted by white dots. "Mean", "BM-Mean" and "Oldest C" stand for arithmetic mean, arithmetic mean after Bayesian age-model corrections, and oldest cobble age of the dataset.

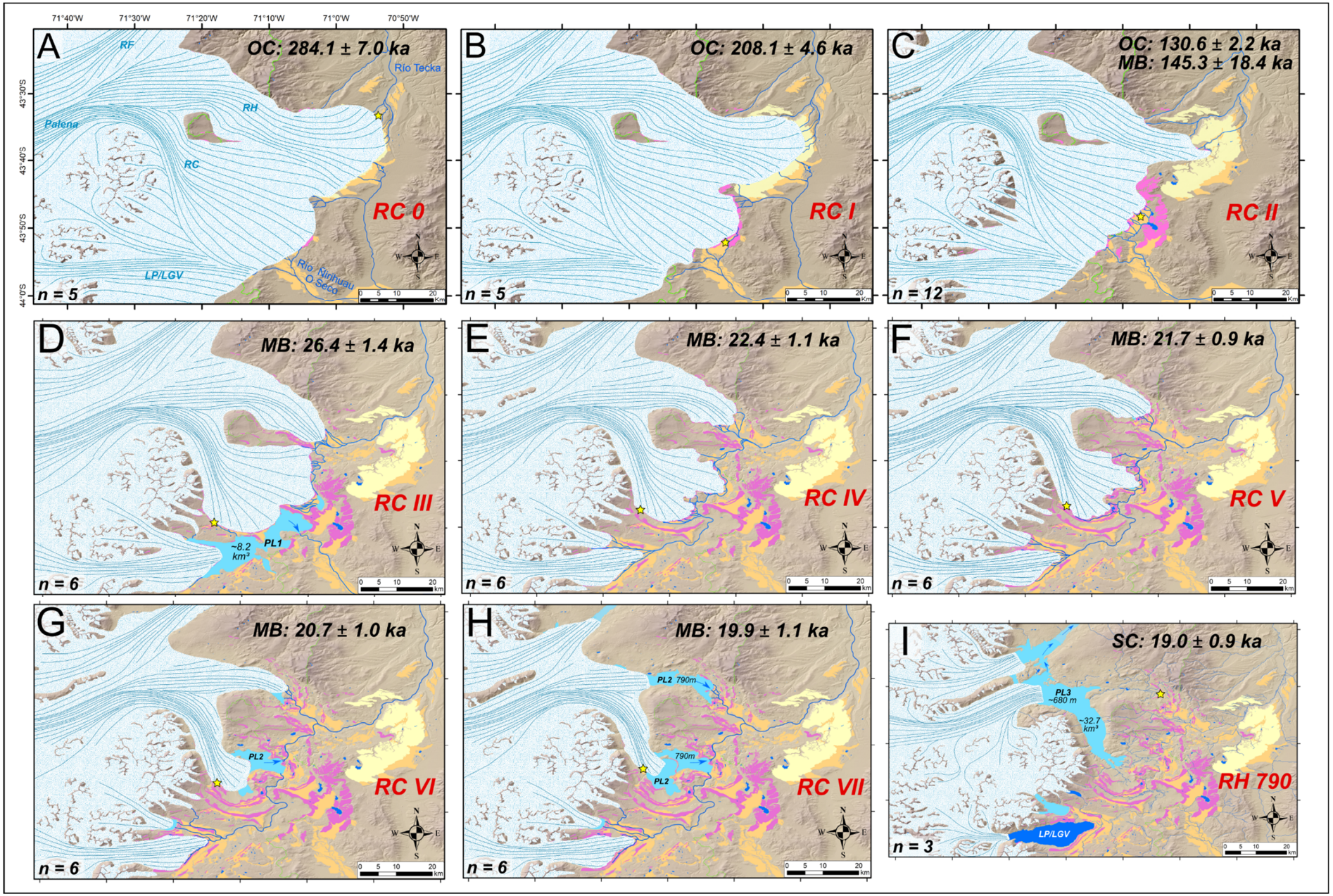
71°40'W
71°30'W
71°20'W
71°10'W
71°0'W
70°50'W
43°30'S
43°40'S
43°50'S
44°0'S
A
OC: 284.1 ± 7.0 ka
RF
Río Tecka
RH
Palena
RC
RC 0
LP/LGV
Río Kinhuau O Seco
n = 5
B
OC: 208.1 ± 4.6 ka
RC I
n = 5
C
OC: 130.6 ± 2.2 ka
MB: 145.3 ± 18.4 ka
RC II
n = 12
D
MB: 26.4 ± 1.4 ka
RC III
~8.2 km³
PL1
n = 6
E
MB: 22.4 ± 1.1 ka
RC IV
n = 6
F
MB: 21.7 ± 0.9 ka
RC V
n = 6
G
MB: 20.7 ± 1.0 ka
PL2
RC VI
n = 6
H
MB: 19.9 ± 1.1 ka
PL2 790m
790m
PL2
RC VII
n = 6
I
SC: 19.0 ± 0.9 ka
PL3 ~680 m
~32.7 km³
RH 790
LP/LGV
n = 3
0 5 10 20 Km

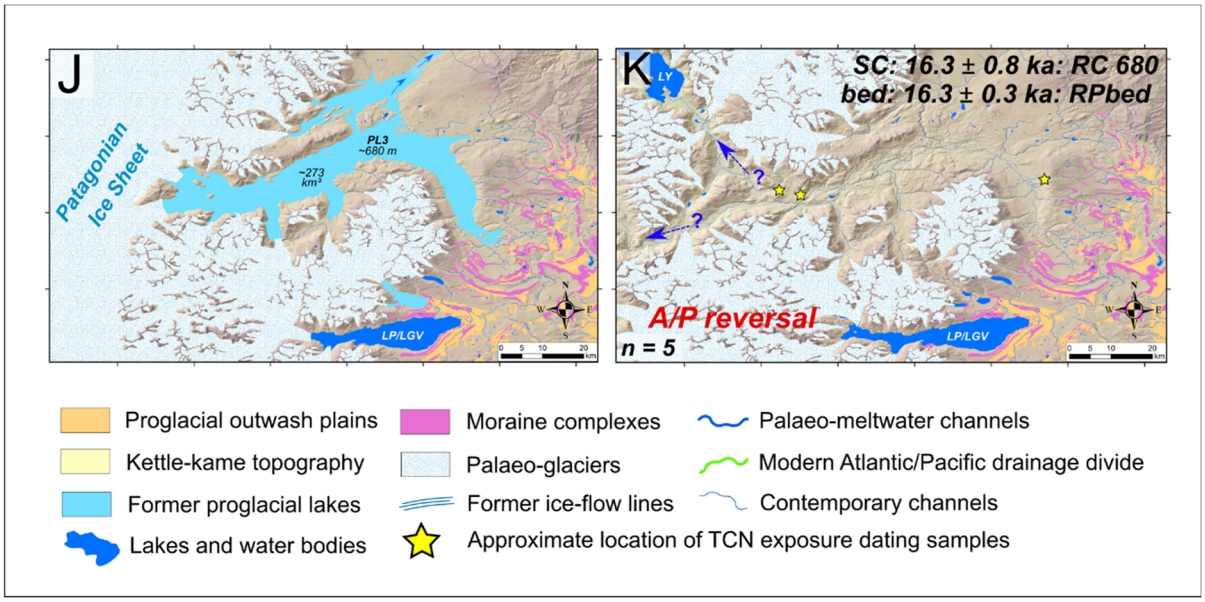

Figure 6.2. Palaeoglacial and palaeolake reconstructions for the RC, RH, RF and Lago Palena/General Vintter valleys, for advances/stillstands and deglacial events interpreted in this investigation (**A-C**) as well as companion publications (Leger *et al*., 2020, 2021a,). Ice-sheet and mountain glacier models were digitised manually in ArcGIS. Except when delineated by confidently mapped moraine limits (*e.g.* the RC, RH and LP/LGV moraine sequences), the geographical location of ice margins are inferred from topography. *OC*, *MB*, *SC*, and *bed* denote the type of rock samples used for TCN exposure dating of the represented event, and stand for "*outwash cobbles*", "*moraine boulders*", "*shoreline cobbles*", and "*bedrock*", respectively. Yellow stars indicate the approximate sample locations for TCN exposure dating of each represented event, while each panel features the number of exposure ages produced (n = x) towards the bottom left-hand corner. (**A-H**): Ice extents associated with the RC 0 to RC VII moraine complexes. This includes the formation of glaciolacustrine phase one and two (here termed PL1 and PL2, respectively). There are no previously published numerical chronologies in the RH, RF and LP/LGV valleys. The relative ice extent in those neighbouring valleys is thus inferred based on our RC chronology and cross-valley comparisons of moraine numbers, preservation and morphostratigraphy. Hence, these inferences yield some uncertainties. (**I**): Reconstruction of the opening of the RF valley scenario and the subsequent RC proglacial lake lowering to 680 m (dated with shoreline surface cobbles from the RH_{790} shoreline), marking the onset of glaciolacsutrine phase 3 (here denoted: PL3), according to our geomorphic interpretation. (**J**): Reconstruction of the westward retreat of the RP outlet glacier towards the core of the Andes and the associated expansion of the 680 m proglacial lake. (**K**): Reconstruction of the onset of PIS disintegration, enabling ice-dam collapse and the Pacific-directed, final drainage of the 680 m proglacial lake (PL3). Proglacial lake volume estimates were computed from DEM data (AW3D30). Panel **K** question marks relate to the uncertainty regarding the former drainage pathway(s) employed during the local Atlantic/Pacific drainage reversal event. Location of ice fronts for panels **I**, **J**, **K** are hypothetical as not correlated to specific geomorphic limits, but are aimed at representing specific events/scenarios.

6.2 Future work

6.2.1 Empirical ice thickness constraints in Patagonia

The palaeo-glacial reconstruction conducted within the context of this thesis contributes to a growing body of geomorphological and geochronological evidence that provides empirical constraints on former outlet glacier and ice-sheet extent evolution through time in Patagonia (Davies *et al*., 2020). However, these investigations do not enable reconstructing thickness and volume fluctuations of the former PIS and its outlet glaciers empirically. Indeed, in Patagonia, the empirical assessment of former ice-sheet thickness evolution has been more challenging to constrain chronologically than lateral glacier extents, and only one published study (Boex *et al*., 2013) has produced a palaeo-ice thickness reconstruction with a direct chronology (n = 18 ages) that establishes the thinning history of the former Pueyrredón outlet glacier (North Patagonian Icefield) between 120 ka and 16 ka. Reconstructions of deglacial, Late-Glacial and Holocene ice-sheet thinning histories in Patagonia, for instance by using the cosmogenic nuclide dipstick model, are thus needed. Such empirical data would moreover be valuable to numerical modelling investigations that wish to calibrate simulated palaeo-ice-thickness and isostatic loading against observations.

6.2.2 Numerical modelling of the PIS

The last published investigation to have modelled the entire former PIS was produced by Hulton *et al*. (2002). Since then, our understanding of the timing and extent of former PIS outlet-glacier advances has increased significantly, and this thesis, for instance, contributes to bridging some of the remaining geographical gaps in our knowledge of former PIS evolution. Moreover, extensive work has been conducted in that time to improve the physical basis of numerical glacier and ice-sheet models. Improvements in computer power enable to formulate more complex, continental scale models that can be coupled and run over longer timescales (*e.g.* Larour *et al*., 2012). Therefore, there is a need to use high-order or full Stokes ice-sheet models (*e.g.* PISM, Elmer/Ice) at relatively high spatial resolution, which would require the use of supercomputers, to simulate the entire former PIS and its evolution during the late Quaternary. Because a large number of eastern Patagonian outlet glaciers terminated into

voluminous proglacial lakes during former PIS build-up and retreat phases (Davies *et al*., 2020), it is critical that future modelling investigations implement modules able to simulate floating ice and frontal ablation and take into account both calving and subaqueous melting (*e.g.* Sutherland *et al*., 2020). Investigations using such improved numerical ice-sheet models to reconstruct the former Quaternary evolution of the PIS have implications for better estimating past climate change, past sea-level contributions of Patagonian glaciers, past GIA-related surface elevation change and future cryosphere dynamics in response to ongoing climate change.

6.2.3 Dating pre-LGC glacial deposits in Patagonia

Previous work by Hein *et al*. (2009, 2011, 2017) along with the investigation presented in Chapter 5 of this thesis has shown that detailed pre-LGC chronologies could be produced in eastern Patagonia through direct TCN exposure dating of proglacial outwash sediment. However, such approach is still quite novel and has so far been conducted in a limited number of sites. Numerous Patagonian valleys currently featuring robust chronologies of LGC glacial expansion events (*e.g.* García et al., 2018) could benefit from the addition of early-to-middle Pleistocene chronologies targeting deposits located further into the Argentine foreland. Due to the high erosion potential of these older pre-LGC deposits, a high number of geographically widespread datasets would be required to generate a fuller picture of the various glaciations that occurred in Patagonia during the Pleistocene. Generating robust glacier chronologies covering several glacial cycles are powerful tools to resolve long-lasting conundrums on orbital-scale regional and inter-hemispheric linkages of climate change. It thus seems critical to generate more empirical data of this kind in Patagonia in the coming years.

6.2.4 The study of glaciolacustrine deposits in the Río Corcovado valley system

The work conducted within the context of this thesis has revealed that fine, laminated glaciolacustrine sediment deposits associated with the former occurrence of several proglacial lake phases formed during and following the local LGM are geographically widespread across the Río Corcovado, Río Huemul and Río Frío valleys. While I targeted some of these deposits

for OSL dating, this investigation did not attempt to produce a high-resolution varve chronology of former glacial and deglacial activity at the study site. Such reconstructions are highly informative and have been produced successfully in other Patagonian valleys (*e.g.* Bendle *et al.*, 2017a). Thereby, there is undoubtedly a high potential for this type of geochronological reconstruction to be conducted within the studied valleys, along with the analysis and discovery of numerous tephra layers that are undoubtedly preserved within many sediment outcrops of the studied valleys.

6.2.5 The deglacial Atlantic/Pacific drainage reversal event in the Palena region

Our geochronological reconstruction of LGM and deglacial events presented in chapter 3 of this thesis includes an estimation of the timing of the final Atlantic/Pacific drainage reversal event that marks the full drainage of the extensive ~680 m proglacial lake that filled the Río Palena, Río Corcovado, Río Huemul and Río Frío valley system during PIS retreat following the LGT (*section 3.4.2.4*). Using TCN exposure dating of ice-moulded bedrock surfaces and palaeo-shoreline cobbles, I propose that the drainage reversal occurred around 16.3 ± 0.3 ka. However, our investigation does not enable to assert whether the estimated ~273 km^3 of freshwater that this palaeo-lake represented drained progressively towards the Pacific as the PIS slowly disintegrated and thinned, or whether it drained suddenly via an ice-dam breaching and GLOF event. The latter scenario would have caused highly disturbing consequences on the environment, local biodiversity and water chemistry of the Golfo Corcovado. Moreover, local valley topographies are such that two possible and distinct drainage routes could have been employed during this event. Resolving the accurate former drainage patterns, magnitude and speed of this major event would require a detailed geomorphological and sedimentological analysis of the fluvial and lacustrine records in the Lago Yelcho and Río Palena valleys, but also within the Golfo Corcovado basal sediments, offshore of the coastal towns of Chaitén (42°55'2 S; 72°42'5 W) and Puerto Raúl Balmaceda (43°46'4 S; 72°57'5 W).

Reference list

Ackert, R. P., Becker, R. A., Singer, B. S., Kurz, M. D., Caffee, M. W., & Mickelson, D. M. (2008). Patagonian glacier response during the Late Glacial–Holocene transition. *Science*, 321(5887), 392-395. Doi: https://doi.org/10.1126/science.1157215

Adhikari, S., & Marshall, S. J. (2012). Glacier volume-area relation for high-order mechanics and transient glacier states. *Geophysical Research Letters*, 39(16). Doi: https://doi.org/10.1029/2012GL052712

Ai, X.E., Studer, A.S., Sigman, D.M., Martínez-García, A., Fripiat, F., Thöle, L. M., Michel, E., Gottschalk, J., Arnold, L., Moretti, S., Schmitt, M., Oleynik, S., Jaccard, S.L., and Haug, G.H., 2020, Southern Ocean upwelling, Earth's obliquity, and glacial-interglacial atmospheric CO2 change: Science, v. 370(6522), p. 1348-1352, doi: https://doi.org/10.1126/science.abd2115.

Anderson, L. S., Roe, G. H., & Anderson, R. S. (2014). The effects of interannual climate variability on the moraine record. *Geology*, *42*(1), 55-58. Doi: https://doi.org/10.1130/G34791.1

Anderson, R. F., Ali, S., Bradtmiller, L. I., Nielsen, S. H. H., Fleisher, M. Q., Anderson, B. E., and Burckle, L. H., (2009). Wind-driven upwelling in the Southern Ocean and the deglacial rise in atmospheric CO2: *Science*, v. 323(5920), p. 1443-1448, doi: https://doi.org/10.1126/science.1167441.

Aitken, M. J. (1985). Thermoluminescence dating: past progress and future trends. *Nuclear Tracks and Radiation Measurements*, 10(1-2), 3-6. Doi: https://doi.org/10.1016/0735-245X(85)90003-1

Alexanderson, H., & Murray, A. S. (2012). Problems and potential of OSL dating Weichselian and Holocene sediments in Sweden. *Quaternary Science Reviews*, 44, 37-50. Doi: https://doi.org/10.1016/j.quascirev.2009.09.020

Allen, C. S., Pike, J., & Pudsey, C. J. (2011). Last glacial–interglacial sea-ice cover in the SW Atlantic and its potential role in global deglaciation. *Quaternary Science Reviews*, *30*(19-20), 2446-2458. Doi: https://doi.org/10.1016/j.quascirev.2011.04.002

Alloway, B. V., Almond, P. C., Moreno, P. I., Sagredo, E., Kaplan, M. R., Kubik, P. W., & Tonkin, P. J. (2018). Mid-latitude trans-Pacific reconstructions and comparisons of coupled glacial/interglacial climate cycles based on soil stratigraphy of cover-beds. *Quaternary Science Reviews*, *189*, 57-75. Doi: 10.1016/j.quascirev.2018.04.005

Andrada de Palomera, R. P. (2002). Geomorfología del valle de Esquel y alrededores de las lagunas Willimanco, Zeta y Carao, noroeste del Chubut. Actas del XV Congreso Geológico Argentino El Calafate. CD-ROM. Artículo No. 052, 6pp.

Applegate, P. J., Urban, N. M., Laabs, B. J. C., Keller, K., & Alley, R. B. (2010). Modelling the statistical distributions of cosmogenic exposure dates from moraines. *Geoscientific Model Development*, *3*(1), 293. Doi: https://doi.org/10.5194/gmd-3-293-2010

Aravena, J. C., & Luckman, B. H. (2009). Spatio-temporal rainfall patterns in southern South America. *International Journal of Climatology: A Journal of the Royal Meteorological Society*, *29*(14), 2106-2120. Doi: https://doi.org/10.1002/joc.1761

Arnold, M., Merchel, S., Bourlès, D. L., Braucher, R., Benedetti, L., Finkel, R. C., Aumaître, G., Gottdang, A., Klein, M. (2010). The French accelerator mass spectrometry facility ASTER: improved performance and developments. *Nuclear Instruments and Methods in Physics Research Section B: Beam Interactions with Materials and Atoms*, 268(11-12), 1954-1959. Doi: https://doi.org/10.1016/j.nimb.2010.02.107

Astakhov, V., 2011. Ice margins of northern Russia revisited. In: Ehlers, J., Gibbard, P.L., Hughes, P.D. (Eds.), Quaternary Glaciations - Extent and Chronology: A Closer Look. Developments in Quaternary Sciences 15. Elsevier, Amsterdam, pp. 1–14.

Astakhov, V., Shkatova, V., Zastrozhnov, A., and Chuyko, M., 2016, Glaciomorphological map of the Russian Federation: Quaternary International, v. 420, p. 4-14, doi: https://doi.org/10.1016/j.quaint.2015.09.024.

Auer, V., 1956. The Pleistocene of Fuego-Patagonia. Part I: the Ice and Interglacial Ages. Annales Academia Scientiarum Fennicae, Series A, III 45, 1-22.

Augustinus, P., Fink, D., Fletcher, M. S., and Thomas, I., 2017, Re-assessment of the mid to late Quaternary glacial and environmental history of the Boco Plain, western Tasmania: Quaternary Science Reviews, v. 160, p. 31-44, doi: https://doi.org/10.1016/j.quascirev.2017.01.015.

Balco, G., 2006, Converting Al and Be isotope ratio measurements to nuclide concentrations in quartz, Documentation—Be-10/26-Al exposure age calculator.

Balco, G., and Rovey, C. W., 2008, An isochron method for cosmogenic-nuclide dating of buried soils and sediments. American Journal of Science, v. 308(10), p. 1083-1114, doi: https://doi.org/10.2475/10.2008.02.

Balco, G., Stone, J. O., Lifton, N. A., & Dunai, T. J. (2008). A complete and easily accessible means of calculating surface exposure ages or erosion rates from 10Be and 26Al measurements. *Quaternary geochronology*, *3*(3), 174-195. Doi: https://doi.org/10.1016/j.quageo.2007.12.001

Balco, G. (2011). Contributions and unrealized potential contributions of cosmogenic-nuclide exposure dating to glacier chronology, 1990–2010. Quaternary Science Reviews, v. 30(1-2), p. 3-27, doi: https://doi.org/10.1016/j.quascirev.2010.11.003.

Balescu, S., Lamothe, M., (1993). Thermoluminescence dating of the Holsteinian marine formation of Herzeele, northern France. *Journal of Quaternary Science*, 8(2), 117-124. Doi: https://doi.org/10.1002/jqs.3390080204

Banerjee, A., & Shankar, R. (2013). On the response of Himalayan glaciers to climate change. *Journal of Glaciology*, 59(215), 480-490. Doi: https://doi.org/10.3189/2013JoG12J130

Barker, S., Diz, P., Vautravers, M. J., Pike, J., Knorr, G., Hall, I. R., & Broecker, W. S. (2009). Interhemispheric Atlantic seesaw response during the last deglaciation. *Nature*, 457(7233), 1097-1102. Doi: https://doi.org/10.1038/nature07770

Barrows, T. T., Stone, J. O., Fifield, L. K., and Cresswell, R. G., (2002). The timing of the last glacial maximum in Australia: Quaternary Science Reviews, v. 21(1-3), p. 159-173: doi: https://doi.org/10.1016/S0277-3791(01)00109-3.

Barrows, T. T., Juggins, S., De Deckker, P., Calvo, E., & Pelejero, C. (2007). Long-term sea surface temperature and climate change in the Australian–New Zealand region. *Paleoceanography*, *22*(2). Doi: https://doi.org/10.1029/2006PA001328

Barrows, T. T., Almond, P., Rose, R., Fifield, L. K., Mills, S. C., & Tims, S. G. (2013). Late Pleistocene glacial stratigraphy of the Kumara-Moana region, west coast of South Island, New Zealand. *Quaternary Science Reviews*, *74*, 139-159. Doi: https://doi.org/10.1016/j.quascirev.2013.04.010

Beets, D.J., Meijer, T., Beets, C.J., Cleveringa, P., Laban, C., and Van der Spek, A.J.F., (2005). Evidence for a Middle Pleistocene glaciation of MIS 8 age in the southern North Sea: Quaternary International, v. 133, p. 7-19, doi: https://doi.org/10.1016/j.quaint.2004.10.002.

Bell, W.T. 1980. Alpha dose attenuation in quartz grains for thermoluminescence dating. Ancient TL, 12, 4 – 8.

Bell, C. M. (2008). Punctuated drainage of an ice-dammed Quaternary lake in southern South America. *Geografiska Annaler: Series A, Physical Geography*, *90*(1), 1-17. Doi: https://doi.org/10.1111/j.1468-0459.2008.00330.x

Bendle, J. M., Palmer, A. P., Thorndycraft, V. R., & Matthews, I. P. (2017 A). High-resolution chronology for deglaciation of the Patagonian Ice Sheet at Lago Buenos Aires (46.5 S) revealed through varve chronology and Bayesian age modelling. Quaternary Science Reviews, 177, 314-339. Doi: https://doi.org/10.1016/j.quascirev.2017.10.013

Bendle, J. M., Thorndycraft, V. R., & Palmer, A. P. (2017 B). The glacial geomorphology of the Lago Buenos Aires and Lago Pueyrredón ice lobes of central Patagonia. *Journal of Maps*, *13*(2), 654-673. Doi: https://doi.org/10.1080/17445647.2017.1351908

Benn, D. I., & Ballantyne, C. K. (1993). The description and representation of particle shape. *Earth Surface Processes and Landforms*, *18*(7), 665-672. Doi: https://doi.org/10.1093/oxfordjournals.humrep.a137463

Benn, D. I., & Clapperton, C. M. (2000). Pleistocene glacitectonic landforms and sediments around central Magellan Strait, southernmost Chile: evidence for fast outlet glaciers with cold-based margins. *Quaternary Science Reviews*, *19*(6), 591-612. Doi: 10.1016/S0277-3791(99)00012-8

Benn, D. I., Kirkbride, M. P., Owen, L. A., & Brazier, V. (2003). Glaciated valley landsystems. *Glacial landsystems*, chapter 15, pp 372-406.

Benn, D. I., Owen, L. A., Osmaston, H. A., Seltzer, G. O., Porter, S. C., & Mark, B. (2005). Reconstruction of equilibrium-line altitudes for tropical and sub-tropical glaciers. *Quaternary International*, 138, 8-21. Doi: https://doi.org/10.1016/j.quaint.2005.02.003

Benn, D. I., Warren, C. R., & Mottram, R. H. (2007). Calving processes and the dynamics of calving glaciers. *Earth-Science Reviews*, *82*(3-4), 143-179. Doi: 10.1016/j.earscirev.2007.02.002

Benn, D. I., & Evans, D. J. (2014). *Glaciers and glaciation*. Routledge.

Bentley, M. J., Sugden, D. E., Hulton, N. R., & McCulloch, R. D. (2005). The landforms and pattern of deglaciation in the Strait of Magellan and Bahía Inútil, southernmost South America. *Geografiska Annaler: Series A, Physical Geography*, *87*(2), 313-333. Doi: 10.1111/j.0435-3676.2005.00261.x

Bereiter, B., Eggleston, S., Schmitt, J., Nehrbass-Ahles, C., Stocker, T. F., Fischer, H., Kipfstuhl, S., Chappellaz, J., 2015, Revision of the EPICA Dome C CO2 record from 800 to 600 kyr before present: Geophysical Research Letters, v. 42(2), p. 542-549, doi: https://doi.org/10.1002/2014GL061957.

Berger, A., & Loutre, M. F. (1991). Insolation values for the climate of the last 10 million years. *Quaternary Science Reviews*, *10*(4), 297-317.

Berman, A. L., Silvestri, G. E., & Tonello, M. S. (2016). Differences between Last Glacial Maximum and present-day temperature and precipitation in southern South America. Quaternary Science Reviews, 150, 221-233. Doi: https://doi.org/10.1016/j.quascirev.2016.08.025

Bindschadler, R. (1983). The importance of pressurized subglacial water in separation and sliding at the glacier bed. *Journal of Glaciology*, 29(101), 3-19. Doi: https://doi.org/10.3189/S0022143000005104

Bingham, R. G., Vaughan, D. G., King, E. C., Davies, D., Cornford, S. L., Smith, A. M., Arthern, R. J., Brisbourne, A. M., Jan De Rydt, Graham, A. G. C., Spagnolo, M., Marsh, O. J., Shean, D. E. (2017). Diverse landscapes beneath Pine Island Glacier influence ice flow. *Nature communications*, *8*(1), 1-9. Doi: 10.1038/s41467-017-01597-y

Blair, T. C. (2002). Alluvial-fan sedimentation from a glacial-outburst flood, Lone Pine, California, and contrasts with meteorological flood deposits. *Flood and Megaflood Processes and Deposits: Recent and Ancient Examples*, 111-140. Doi: https://doi.org/10.1002/9781444304299.ch8

Blake, W., Fischer, U. H., Bentley, C. R., & Clarke, G. K. (1994). Instruments and methods: Direct measurement of sliding at the glacier bed. *Journal of Glaciology*, 40(136), 595-599. Doi: https://doi.org/10.3189/S002214300001248X

Boex, J., Fogwill, C., Harrison, S., Glasser, N. F., Hein, A., Schnabel, C., & Xu, S. (2013). Rapid thinning of the late Pleistocene Patagonian Ice Sheet followed migration of the Southern Westerlies. *Scientific reports*, *3*, 2118. Doi: https://doi.org/10.1038/srep02118

Borchers, B., Marrero, S., Balco, G., Caffee, M., Goehring, B., Lifton, N., Nishiizumi, K., Phillips, F., Schaefer, J., Stone, J. (2016). Geological calibration of spallation production rates in the CRONUS-Earth project. *Quaternary Geochronology*, *31*, 188-198. Doi: https://doi.org/10.1016/j.quageo.2015.01.009

Bøtter-Jensen, L., Andersen, C.E., Duller, G.A.T., Murray, A.S. (2003). Developments in radiation, stimulation and observation facilities in luminescence measurements. Radiation Measurements, 37(4-5), 535-541. Doi : https://doi.org/10.1016/S1350-4487(03)00020-9

Boulton, G. S., & Clark, C. D. (1990). The Laurentide ice sheet through the last glacial cycle: the topology of drift lineations as a key to the dynamic behaviour of former ice sheets. *Earth and Environmental Science Transactions of The Royal Society of Edinburgh*, *81*(4), 327-347. Doi: 10.1017/S0263593300020836

Bourlès, D. Etude de la géochimies de l'isotope cosmogénique ^{10}Be et de son isotope stable ^{9}Be en milieu océanique. Application à la datation des sédiments marins (1988). Ph.D. thesis, Univ. Paris XI

Braithwaite, R. J., & Müller, F. (1980). On the parameterization of glacier equilibrium line altitude. *IAHS Publ*, *126*, 263-271.

Braithwaite, R. J., & Zhang, Y. (2000). Sensitivity of mass balance of five Swiss glaciers to temperature changes assessed by tuning a degree-day model. *Journal of Glaciology*, 46(152), 7-14. Doi: https://doi.org/10.3189/172756500781833511

Braucher, R., Guillou, V., Bourlès, D. L., Arnold, M., Aumaître, G., Keddadouche, K., & Nottoli, E. (2015). Preparation of ASTER in-house 10Be/9Be standard solutions. *Nuclear Instruments and Methods in Physics Research Section B: Beam Interactions with Materials and Atoms*, 361, 335-340. Doi: https://doi.org/10.1016/j.nimb.2015.06.012

Briner, J. P., Kaufman, D. S., Manley, W. F., Finkel, R. C., and Caffee, M. W., 2005, Cosmogenic exposure dating of late Pleistocene moraine stabilization in Alaska: Geological Society of America Bulletin, v. 117(7-8), p. 1108-1120, doi: https://doi.org/10.1130/B25649.1.

Broecker, W. S. (1998). Paleocean circulation during the last deglaciation: a bipolar seesaw? *Paleoceanography*, *13*(2), 119-121. Doi: https://doi.org/10.1029/97PA03707

Bronk Ramsey, C. (2008). Deposition models for chronological records. *Quaternary Science Reviews*, 27(1-2), 42-60. Doi: https://doi.org/10.1016/j.quascirev.2007.01.019

Bronk Ramsey, C., 2017. OxCal 4.3. https://c14.arch.ox.ac.uk/oxcal/OxCal.html.

Budd, W. F., Keage, P. L., & Blundy, N. A. (1979). Empirical studies of ice sliding. *Journal of glaciology*, 23(89), 157-170. Doi: https://doi.org/10.3189/S0022143000029804

Buizert, C., Sigl, M., Severi, M., Markle, B. R., Wettstein, J. J., McConnell, J. R., Pedro, J. B., Sodemann, H., Goto-Azuma, K., Kawamura, K., Fujita, S., Motoyama, H., Hirabayashi, M., Uemura, R., Stenni, B., Parrenin, F., Ha, F., Fudge, T. J., & Steig, E. J. (2018). Abrupt ice-age shifts in southern westerly winds and Antarctic climate forced from the north. *Nature*, 563(7733), 681-685. Doi: https://doi.org/10.1130/G36477.1

Caldenius, C. C. Z. (1932). Las glaciaciones cuaternarias en la patagonia y tierra del fuego. *Geografiska Annaler*, 14, 1–164. Doi: https://doi.org/10.1080/20014422.1932.11880545

Caniupán, M., Lamy, F., Lange, C. B., Kaiser, J., Arz, H., Kilian, R., Baeza Urrea, O., Aracena, C., Hebbeln, D., Kissel, C., Laj, C., Mollenhauer, G., Tiedemann, R. (2011). Millennial-scale sea surface temperature and Patagonian Ice Sheet changes off southernmost Chile (53 S) over the past∼ 60 kyr. *Paleoceanography*, *26*(3). Doi: https://doi.org/10.1029/2010PA002049.

Carrivick, J. L., Davies, B. J., James, W. H., Quincey, D. J., & Glasser, N. F. (2016). Distributed ice thickness and glacier volume in southern South America. Global and Planetary Change, v. 146, p. 122-132, doi: https://doi.org/10.1016/j.gloplacha.2016.09.010.

Carter, L., McCave, I.N., Williams, M.J.M., (2008). Circulation and water masses of the Southern Ocean: a review. In: Fabio, F., Martin, S. (Eds.), *Developments in Earth and Environmental Sciences*, 8, 85-114. Doi: https://doi.org/10.1016/S1571-9197(08)00004-9

Cartwright, A., Quade, J., Stine, S., Adams, K. D., Broecker, W., & Cheng, H. (2011). Chronostratigraphy and lake-level changes of Laguna Cari-Laufquén, Río Negro, Argentina. *Quaternary Research*, 76(3), 430-440. Doi: https://doi.org/10.1016/j.yqres.2011.07.002

Chandler, B.M., Lovell, H., Boston, C.M., Lukas, S., Barr, I.D., Benediktsson, Í.Ö., Benn, D.I., Clark, C.D., Darvill, C.M., Evans, D.J. and Ewertowski, M.W. (2018). Glacial geomorphological mapping:

A review of approaches and frameworks for best practice. *Earth-Science Reviews*, *185*, 806-846. Doi: 10.1016/j.earscirev.2018.07.015

Chiverrell, R. C., Thrasher, I. M., Thomas, G. S., Lang, A., Scourse, J. D., Van Landeghem, K. J. J, McCarroll, D., Clark, C. D., Cofaigh, C. Ó., Evans, D. J. A., Ballantyne, C. K. (2013). Bayesian modelling the retreat of the Irish Sea Ice Stream. *Journal of Quaternary Science*, *28*(2), 200-209. Doi: https://doi.org/10.1002/jqs.2616

Chmeleff, J., von Blanckenburg, F., Kossert, K., & Jakob, D. (2010). Determination of the 10Be half-life by multicollector ICP-MS and liquid scintillation counting. *Nuclear Instruments and Methods in Physics Research Section B: Beam Interactions with Materials and Atoms*, 268(2), 192-199. Doi: https://doi.org/10.1016/j.nimb.2009.09.012

Clapperton, C. M. (1990). Quaternary glaciations in the Southern Hemisphere: an overview. *Quaternary Science Reviews*, 9(2-3), 299-304. Doi: https://doi.org/10.1016/0277-3791(90)90024-5

Clapperton, C.M., 1993, Quaternary geology and geomorphology of South America: Amsterdam, Elsevier Science Publishers B.V., 779 p.

Clapperton, C. M., Sugden, D. E., Kaufman, D. S., & McCulloch, R. D. (1995). The last glaciation in central Magellan Strait, southernmost Chile. *Quaternary Research*, 44(2), 133-148. doi:10.1006/qres.1995.1058

Clark, P. U., Dyke, A. S., Shakun, J. D., Carlson, A. E., Clark, J., Wohlfarth, B., Mitrovica, J. X., Hostetler, S. W., & McCabe, A. M. (2009). The last glacial maximum. *Science*, *325*(5941), 710-714. Doi: https://doi.org/10.1126/science.1172873

Clark, C.D., Ely, J.C., Greenwood, S.L., Hughes, A.L., Meehan, R., Barr, I.D., Bateman, M.D., Bradwell, T., Doole, J., Evans, D.J. and Jordan, C.J. (2018). BRITICE Glacial Map, version 2: a map and GIS database of glacial landforms of the last British–Irish Ice Sheet. *Boreas*, *47*(1), 11-e8. Doi: 10.1111/bor.12273

Cogez, A., Herman, F., Pelt, É., Reuschlé, T., Morvan, G., Darvill, C. M., Norton, K. P., Christl, M., Märki, L., Chabaux, F., 2018, U–Th and 10 Be constraints on sediment recycling in proglacial settings, Lago Buenos Aires, Patagonia: Earth Surface Dynamics, v. 6(1), p. 121-140, doi: https://doi.org/10.5194/esurf-6-121-2018.

Cohen, D., Hooke, R. L., Iverson, N. R., & Kohler, J. (2000). Sliding of ice past an obstacle at Engabreen, Norway. *Journal of Glaciology*, 46(155), 599-610. Doi: https://doi.org/10.3189/172756500781832747

Cohen, D., Iverson, N. R., Hooyer, T. S., Fischer, U. H., Jackson, M., & Moore, P. L. (2005). Debris-bed friction of hard-bedded glaciers. *Journal of Geophysical Research: Earth Surface*, 110(F2). Doi: https://doi.org/10.1029/2004JF000228

Colhoun, E.A., Barrows, T.T., 2011. The glaciation of Australia. In: Ehlers, J., Gibbard, P.L., Hughes, P.D. (Eds.), Quaternary Glaciations - Extent and Chronology: A Closer Look. Developments in Quaternary Sciences 15. Elsevier, Amsterdam, pp. 1037–1045.

Coronato, A., Ercolano, B., Corbella, H., & Tiberi, P. (2013). Glacial, fluvial and volcanic landscape evolution in the Laguna Potrok Aike maar area, Southern Patagonia, Argentina. *Quaternary Science Reviews*, *71*, 13-26. Doi: 10.1016/j.quascirev.2012.06.019

Cuffey, K. and Paterson, W. S. B. (2010). The Physics of Glaciers, Elsevier, Butterworth-Heineman, Burlington, MA, USA.

Darvill, C. M., Stokes, C. R., Bentley, M. J., & Lovell, H. (2014). A glacial geomorphological map of the southernmost ice lobes of Patagonia: the Bahía Inútil–San Sebastián, Magellan, Otway, Skyring and Río Gallegos lobes. *Journal of Maps*, *10*(3), 500-520. Doi: https://doi.org/10.1080/17445647.2014.890134

Darvill, C. M., Bentley, M. J., Stokes, C. R., Hein, A. S., & Rodés, Á. (2015). Extensive MIS 3 glaciation in southernmost Patagonia revealed by cosmogenic nuclide dating of outwash sediments. *Earth and Planetary Science Letters*, *429*, 157-169. Doi: https://doi.org/10.1016/j.epsl.2015.07.030

Darvill, C. M., Bentley, M. J., Stokes, C. R., & Shulmeister, J. (2016). The timing and cause of glacial advances in the southern mid-latitudes during the last glacial cycle based on a synthesis of exposure ages from Patagonia and New Zealand. *Quaternary Science Reviews*, *149*, 200-214. Doi: https://doi.org/10.1016/j.quascirev.2016.07.024

Darvill, C. M., Stokes, C. R., Bentley, M. J., Evans, D. J., & Lovell, H. (2017). Dynamics of former ice lobes of the southernmost Patagonian Ice Sheet based on a glacial landsystems approach. *Journal of Quaternary Science*, *32*(6), 857-876. Doi: 10.1002/jqs.2890

Davies, B. J., Roberts, D.H., Bridgland, D.R., Cofaigh, C.Ó., Riding, J.B., Demarchi, B., Penkman, K.E.H., and Pawley, S. M., 2012, Timing and depositional environments of a Middle Pleistocene glaciation of northeast England: New evidence from Warren House Gill, County Durham: Quaternary Science Reviews, v. 44, p. 180-212. https://doi.org/10.1016/j.quascirev.2010.02.003.

Davies, B. J., Thorndycraft, V. R., Fabel, D., & Martin, J. R. V. (2018). Asynchronous glacier dynamics during the Antarctic Cold Reversal in central Patagonia. *Quaternary Science Reviews*, *200*, 287-312. Doi: 10.1016/J.QUASCIREV.2018.09.025

Davies, B. J., Darvill, C. M., Lovell, H., Bendle, J. M., Dowdeswell, J. A., Fabel, D., Garcia, J-L., Geiger, A., Glasser, N. F., Gheorghiu, D. M., Harrison, S., Hein, A. S., Kaplan, M. R., Martin, J. R. V., Mendelova, M., Palmer, A., Pelto, M., Rodes, A., Sagredo, E. A., Smedley, R., Smellie, J. L., Thorndycraft, V. R. (2020). The evolution of the Patagonian Ice Sheet from 35 ka to the Present Day (PATICE). *Earth-Science Reviews*, 103152. Doi: https://doi.org/10.1016/j.earscirev.2020.103152

De Angelis, H. (2014). Hypsometry and sensitivity of the mass balance to changes in equilibrium-line altitude: the case of the Southern Patagonia Icefield. *Journal of Glaciology*, 60(219), 14-28. Doi: https://doi.org/10.3189/2014JoG13J127

De Deckker, P., Arnold, L. J., van der Kaars, S., Bayon, G., Stuut, J. B. W., Perner, K., Lopes dos Santos, R., Uemura, R., & Demuro, M. (2019). Marine Isotope Stage 4 in Australasia: A full glacial culminating 65,000 years ago – Global connections and implications for human dispersal. *Quaternary Science Reviews*, *204*, 187-207. Doi: https://doi.org/10.1016/j.quascirev.2018.11.017

Denton, G. H., Lowell, T. V., Heusser, C. J., Schlüchter, C., Andersen, B. G., Heusser, L. E., Moreno, P.I., Marchant, D. R. (1999). Geomorphology, stratigraphy, and radiocarbon chronology of Llanquihue Drift in the area of the Southern Lake District, Seno Reloncaví, and Isla Grande de Chiloé, Chile. *Geografiska Annaler: Series A, Physical Geography*, *81*(2), 167-229. Doi: https://doi.org/10.1111/j.0435-3676.1999.00057.x

Denton, G.H., Anderson, R.F., Toggweiler, J.R., Edwards, R.L., Schaefer, J.M., and Putnam, A.E., 2010, The last glacial termination: Science, v. 328, p. 1652-1656, doi: https://doi.org/10.1126/science.1184119.

Denton, G. H., Putnam, A. E., Russell, J. L., Barrell, D. J., Schaefer, J. M., Kaplan, M. R., & Strand, P. D. (2021). The Zealandia Switch: Ice age climate shifts viewed from Southern Hemisphere moraines. *Quaternary Science Reviews*, 257, 106771. Doi: https://doi.org/10.1016/j.quascirev.2020.106771

De Porras, M.E., Maldonado, A., Abarzúa, A.M., Cárdenas, M., Francois, J.P., Martel-Cea, A., Stern, C.R., Méndez, C., Reyes, O., 2012. Postglacial vegetation, fire and climate dynamics at Central Chilean Patagonia (Lake Shaman, 44°S), Chile. Quaternary Science Reviews 50, 71–85. Doi: https://doi.org/10.1017/qua.2018.93

De Porras, M. E., Maldonado, A., Quintana, F. A., Martel-Cea, A., Reyes, O., & Méndez, C. (2014). Environmental and climatic changes in central Chilean Patagonia since the late glacial (Mallín El Embudo, 44 S). *Climate of the Past*, 10(3), 1063-1078. Doi: https://doi.org/10.5194/cp-10-1063-2014

Doughty, A. M., Schaefer, J. M., Putnam, A. E., Denton, G. H., Kaplan, M. R., Barrell, D. J., Andersen, B. G., Kelley, S. E., Finkel, R. C., Schwartz, R. (2015). Mismatch of glacier extent and summer insolation in Southern Hemisphere mid-latitudes. *Geology*, *43*(5), 407-410. Doi: https://doi.org/10.1130/G36477.1

Doughty, A. M., Schaefer, J. M., Putnam, A. E., Denton, G. H., Kaplan, M. R., Barrell, D. J., Andersen, B. G., Kelley, S. E., Finkel, R. C., Schwartz, R. (2015). Mismatch of glacier extent and summer insolation in Southern Hemisphere mid-latitudes. *Geology*, *43*(5), 407-410. Doi: https://doi.org/10.1130/G36477.1

Douglass, D. C., Singer, B. S., Kaplan, M. R., Mickelson, D. M., & Caffee, M. W. (2006). Cosmogenic nuclide surface exposure dating of boulders on last-glacial and late-glacial moraines, Lago Buenos Aires, Argentina: interpretive strategies and paleoclimate implications. *Quaternary Geochronology*, *1*(1), 43-58. Doi: https://doi.org/10.1016/j.quageo.2006.06.001

Douglass, D. C., Singer, B., Ackert, R. P., Kaplan, M. R., & Caffee, M. W. (2007). Constraining Boulder Erosion Rates and Ages of Mid-Pleistocene Moraines in Lago Buenos Aires, Argentina. *GSA Abstracts and Programs Northeastern Section, 42nd Annual Meeting*.

Dunai, T. J. (2010). *Cosmogenic Nuclides: Principles, concepts and applications in the Earth surface sciences*. Cambridge University Press.

Durcan, J. A., King, G.E., Duller, G.A.T. (2015). DRAC: Dose Rate and Age Calculator for trapped charge dating. *Quaternary Geochronology*, 28, 54 – 61. Doi : https://doi.org/10.1016/j.quageo.2015.03.012

Engelhardt, H. F., Harrison, W. D., & Kamb, B. (1978). Basal sliding and conditions at the glacier bed as revealed by bore-hole photography. *Journal of Glaciology*, 20(84), 469-508. Doi: https://doi.org/10.3189/S002214300002089X

EPICA Community Members. (2006). One-to-one coupling of glacial climate variability in Greenland and Antarctica. *Nature*, *444*(7116), 195.

Evans, D. J. A., & Benn, D. I. (Eds.). (2004). *A practical guide to the study of glacial sediments*. Arnold, London (266 pp.).

Evans, D. J. A. (2014). *Glacial landsystems*. Routledge.

Evans, D. J. A. & Orton, C. (2015). Heinabergsjökull and Skalafellsjökull, Iceland: active temperate piedmont lobe and outwash head glacial landsystem. *Journal of Maps*, *11*(3), 415-431. Doi: 10.1080/17445647.2014.919617

Evans, D.J.A., Roberts, D.H., Bateman, M.D., Ely, J., Medialdea, A., Burke, M.J., Chiverrell, R.C., Clark, C.D., Fabel, D., 2019, A chronology for North Sea Lobe advance and recession on the Lincolnshire and Norfolk coasts during MIS 2 and 6: Proceedings of the Geologists' Association, v.130, p. 523–540, doi: https://doi.org/10.1016/j.pgeola.2018.10.004.

Eyles, N., Boyce, J. I., & Barendregt, R. W. (1999). Hummocky moraine: sedimentary record of stagnant Laurentide Ice Sheet lobes resting on soft beds. *Sedimentary Geology*, 123(3-4), 163-174. Doi: 10.1016/S0037-0738(98)00129-8

Fabel, D., Small, D., Miguens-Rodriguez, M., & Freeman, S. P. (2010). Cosmogenic nuclide exposure ages from the 'Parallel Roads' of Glen Roy, Scotland. *Journal of Quaternary Science: Published for the Quaternary Research Association*, *25*(4), 597-603. Doi: https://doi.org/10.1002/jqs.1318

Fernandes, M., Oliva, M., Vieira, G., Palacios, D., Fernández-Fernández, J. M., Delmas, M., García-Oteyza, J., Schimmelpfennig, I., Ventura, J., ASTER Team., 2021, Maximum glacier extent of the Penultimate Glacial Cycle in the Upper Garonne Basin (Pyrenees): new chronological evidence: Environmental Earth Sciences, v. 80(24), p. 1-20, doi: https://doi.org/10.1007/s12665-021-10022-z.

Fick, S. E., & Hijmans, R. J. (2017). WorldClim 2: new 1-km spatial resolution climate surfaces for global land areas. *International journal of climatology*, *37*(12), 4302-4315. Doi: https://doi.org/10.1002/joc.5086

Fogwill, C. J., Turney, C. S. M., Hutchinson, D. K., Taschetto, A. S., & England, M. H. (2015). Obliquity control on southern hemisphere climate during the last glacial. *Scientific Reports*, *5*(1), 1-10. Doi: https://doi.org/10.1038/srep11673

Galbraith, R.F. and Laslett, G.M. (1993). Statistical models for mixed fission track ages. International Journal of Radiation Applications and Instrumentation. Part D. *Nuclear Tracks and Radiation Measurements*, 21, 459-470. Doi : https://doi.org/10.1016/1359-0189(93)90185-C

Galbraith, R.F., Roberts, R. G., Laslett, G.M., Yoshida, H. and Olley, J.M. (1999). Optical dating of single and multiple grains of quartz from Jinmium rock shelter, northern Austrailia: part I, experimental design and statistical models. *Archaeometry*, 41, 339 – 364. Doi : https://doi.org/10.1111/j.1475-4754.1999.tb00987.x

Galloway, R. W., Markgraf, V., & Bradbury, J. P. (1988). Dating shorelines of lakes in Patagonia, Argentina. *Journal of South American Earth Sciences*, 1(2), 195-198. Doi: https://doi.org/10.1016/0895-9811(88)90037-5

García, J. L. (2012). Late Pleistocene ice fluctuations and glacial geomorphology of the Archipiélago de Chiloé, southern Chile. *Geografiska Annaler: series A, Physical Geography*, 94(4), 459-479. Doi: https://doi.org/10.1111/j.1468-0459.2012.00471.x

García, J. L., Kaplan, M. R., Hall, B. L., Schaefer, J. M., Vega, R. M., Schwartz, R., & Finkel, R. (2012). Glacier expansion in southern Patagonia throughout the Antarctic cold reversal. *Geology*, 40(9), 859-862. Doi: https://doi.org/10.1130/G33164.1

García, J. L., Hein, A. S., Binnie, S. A., Gómez, G. A., González, M. A., & Dunai, T. J. (2018). The MIS 3 maximum of the Torres del Paine and Última Esperanza ice lobes in Patagonia and the pacing of southern mountain glaciation. *Quaternary Science Reviews*, *185*, 9-26. Doi: https://doi.org/10.1016/j.quascirev.2018.01.013

García, J. L., Maldonado, A., de Porras, M. E., Delaunay, A. N., Reyes, O., Ebensperger, C. A., Binnie, S.A., Lüthgens, C., Méndez, C. (2019). Early deglaciation and paleolake history of Río Cisnes glacier, Patagonian ice sheet (44° S). *Quaternary Research*, *91*(1), 194-217. Doi: https://doi.org/10.1017/qua.2018.93

García, J. L., Lüthgens, C., Vega, R. M., Rodés, Á., Hein, A. S., Binnie, S. (2021). A composite ^{10}Be, IR-50 and ^{14}C chronology of the pre-LGM full ice extent of the western Patagonian Ice Sheet in the Isla de Chiloé, south Chile (42°S). *E&G Quaternary Science Journal,* 70, 105–128. Doi: https://doi.org/10.5194/egqsj-70-105-2021

Garreaud, R., Lopez, P., Minvielle, M., & Rojas, M. (2013). Large-scale control on the Patagonian climate. *Journal of Climate*, *26*(1), 215-230. Doi: https://doi.org/10.1175/JCLI-D-12-00001.1

Glasser, N. F., Jansson, K. N., Harrison, S., & Kleman, J. (2008). The glacial geomorphology and Pleistocene history of South America between 38°S and 56°S. *Quaternary Science Reviews*, *27*(3-4), 365-390. Doi: https://doi.org/10.1016/j.quascirev.2007.11.011

Glasser, N., & Jansson, K. (2008). The glacial map of southern South America. *Journal of Maps*, *4*(1), 175-196. Doi: https://doi.org/10.4113/jom.2008.1020

Glasser, N. F., Jansson, K. N., Goodfellow, B. W., De Angelis, H., Rodnight, H., & Rood, D. H. (2011). Cosmogenic nuclide exposure ages for moraines in the Lago San Martin Valley, Argentina. Quaternary Research, 75(3), 636-646. Doi: https://doi.org/10.1016/j.yqres.2010.11.005

Glasser, N. F., Jansson, K. N., Duller, G. A., Singarayer, J., Holloway, M., & Harrison, S. (2016). Glacial lake drainage in Patagonia (13-8 kyr) and response of the adjacent Pacific Ocean. *Scientific reports*, *6*, 21064. Doi: https://doi.org/10.1038/srep21064

Gómez, G. A., García, J. L., Villagrán, C., Lüthgens, C., Abarzúa, A. M., 2022, Vegetation, glacier, and climate changes before the global last glacial maximum in the Isla Grande de Chiloé, southern Chile (42° S): Quaternary Science Reviews, v. 276, 107301, doi: https://doi.org/10.1016/j.quascirev.2021.107301.

Gosse, J. C., & Phillips, F. M. (2001). Terrestrial in situ cosmogenic nuclides: theory and application. *Quaternary Science Reviews*, *20*(14), 1475-1560. Doi: https://doi.org/10.1016/S0277-3791(00)00171-2

Gowan, E. J., Zhang, X., Khosravi, S., Rovere, A., Stocchi, P., Hughes, A. L., Gyllencreutz, R., Mangerud, J., Svendsen, J-I., Lohmann, G. (2021). A new global ice sheet reconstruction for the past 80 000 years. *Nature communications*, 12(1), 1-9. Doi: https://doi.org/10.1038/s41467-021-21469-w

Guerin, G., Mercier, N., Adamiec, G. (2011). Dose-rate conversion factors: update. *Ancient TL* 29, 5-8.

Granger, D. E., and Muzikar, P. F., 2001, Dating sediment burial with in situ-produced cosmogenic nuclides: theory, techniques, and limitations. Earth and Planetary Science Letters, v. 188(1-2), p. 269-281, doi: https://doi.org/10.1016/S0012-821X(01)00309-0.

Hall, B. L., Porter, C. T., Denton, G. H., Lowell, T. V., & Bromley, G. R. (2013). Extensive recession of Cordillera Darwin glaciers in southernmost South America during Heinrich stadial 1. *Quaternary Science Reviews*, *62*, 49-55. Doi: https://doi.org/10.1016/j.quascirev.2012.11.026

Hall, B. L., Lowell, T. V., & Brickle, P. (2020). Multiple glacial maxima of similar extent at~ 20–45 ka on Mt. Usborne, East Falkland, South Atlantic region. *Quaternary Science Reviews*, 250, 106677. Doi: https://doi.org/10.1016/j.quascirev.2020.106677

Haller, M., Lech, R.R., Martinez, O.A., Meister, C.M., Page, S.M., (2003). Hoja Geologica 4373IV/III, Trevelin, Provincia del Chubut. Programa Nacional de Cartas Geologicas de la Republica Argentina, 1:250.000. Servicio Geologico Nacional, Buenos Aires.

Hein, A. S., Hulton, N. R., Dunai, T. J., Schnabel, C., Kaplan, M. R., Naylor, M., & Xu, S. (2009). Middle Pleistocene glaciation in Patagonia dated by cosmogenic-nuclide measurements on outwash gravels. *Earth and Planetary Science Letters*, *286*(1-2), 184-197. Doi: https://doi.org/10.1016/j.epsl.2009.06.026

Hein, A. S., Hulton, N. R., Dunai, T. J., Sugden, D. E., Kaplan, M. R., & Xu, S. (2010). The chronology of the Last Glacial Maximum and deglacial events in central Argentine Patagonia. *Quaternary Science Reviews*, *29*(9-10), 1212-1227. Doi: https://doi.org/10.1016/j.quascirev.2010.01.020

Hein, A. S., Dunai, T. J., Hulton, N. R., & Xu, S. (2011). Exposure dating outwash gravels to determine the age of the greatest Patagonian glaciations. *Geology*, *39*(2), 103-106. Doi: https://doi.org/10.1130/G31215.1

Hein, A. S., Cogez, A., Darvill, C. M., Mendelová, M., Kaplan, M. R., Herman, F., Dunai, T.J., Norton, K., Xu, S., Christl, M., Rodés, Á. (2017). Regional mid-Pleistocene glaciation in central Patagonia. *Quaternary Science Reviews*, *164*, 77-94. Doi: https://doi.org/10.1016/j.quascirev.2017.03.023

Hemming, S. R. (2004). Heinrich events: Massive late Pleistocene detritus layers of the North Atlantic and their global climate imprint. *Reviews of Geophysics*, 42(1). Doi: https://doi.org/10.1029/2003RG000128

Henríquez, W. I., Villa-Martínez, R., Vilanova, I., Pol-Holz, R. D., & Moreno, P. I. (2017). The Last Glacial Termination on the eastern flank of the central Patagonian Andes (47°S). *Climate of the Past*, *13*(7), 879-895. Doi: 10.5194/cp-13-879-2017

Herber, L. J. (1969). Separation of feldspar from quartz by flotation. *American Mineralogist: Journal of Earth and Planetary Materials*, *54*(7-8), 1212-1215.

Hervé, F., Fuentes, F., Calderón, M., Fanning, M., Quezada, P., Pankhurst, R., & Rapela, C. (2017). Ultramafic rocks in the North Patagonian Andes: is their emplacement associated with the Neogene tectonics of the Liquiñe-Ofqui Fault Zone?. *Andean Geology*, *44*(1), 1-16. Doi: https://doi.org/10.5027/andgeoV44n1-a01

Heusser, C. J. (1983). Quaternary pollen record from laguna de Tagua Tagua, Chile. *Science*, 219(4591), 1429-1432. URL: https://www.jstor.org/stable/1689979

Heusser, C. J. (1989). Late Quaternary vegetation and climate of southern Tierra del Fuego. Quaternary Research, v. 31(3), p. 396-406, doi: https://doi.org/10.1016/0033-5894(89)90047-1.

Heusser, C.J., Heusser, L.E., Lowell, T.V., (1999). Paleoecology of the Southern Chilean Lake District-Isla Grande de Chiloé during middle–late Llanquihue glaciation and deglaciation. Geografiska Annaler: Series A, *Physical Geography*, 81A, 231–284. http://www.jstor.com/stable/521343

Heyman, J., Stroeven, A. P., Harbor, J. M., & Caffee, M. W. (2011). Too young or too old: evaluating cosmogenic exposure dating based on an analysis of compiled boulder exposure ages. *Earth and Planetary Science Letters*, *302*(1-2), 71-80. Doi: https://doi.org/10.1016/j.epsl.2010.11.040

Heyman, J., Applegate, P. J., Blomdin, R., Gribenski, N., Harbor, J. M., & Stroeven, A. P. (2016). Boulder height–exposure age relationships from a global glacial ^{10}Be compilation. *Quaternary Geochronology*, *34*, 1-11. Doi: https://doi.org/10.1016/j.quageo.2016.03.002

Hock, R. (2003). Temperature index melt modelling in mountain areas. *Journal of hydrology*, 282(1-4), 104-115. Doi: https://doi.org/10.1016/S0022-1694(03)00257-9

Hubbard, A., Hein, A. S., Kaplan, M. R., Hulton, N. R., & Glasser, N. (2005). A modelling reconstruction of the last glacial maximum ice sheet and its deglaciation in the vicinity of the Northern Patagonian Icefield, South America. *Geografiska Annaler: Series A, Physical Geography*, 87(2), 375-391. Doi: https://doi.org/10.1111/j.0435-3676.2005.00264.x

Hughes, P. D., Gibbard, P. L., and Ehlers, J, (2020). The "missing glaciations" of the Middle Pleistocene. *Quaternary Research*, v. 96, p. 161-183, doi: https://doi.org/10.1017/qua.2019.76

Hulton, N. R., Purves, R. S., McCulloch, R. D., Sugden, D. E., & Bentley, M. J. (2002). The last glacial maximum and deglaciation in southern South America. *Quaternary Science Reviews*, 21(1-3), 233-241. Doi: https://doi.org/10.1016/S0277-3791(01)00103-2

Huntley, D.J., Lamothe, M. (2001). Ubiquity of anomalous fading in K-feldspars and the measurement and correction for it in optical dating. *Canadian Journal of Earth Sciences*, 38(7), 1093-1106. Doi : https://doi.org/10.1139/e01-013

Huss, M., Sugiyama, S., Bauder, A., & Funk, M. (2007). Retreat scenarios of Unteraargletscher, Switzerland, using a combined ice-flow mass-balance model. *Arctic, Antarctic, and Alpine Research*, 39(3), 422-431. Doi: https://doi.org/10.1657/1523-0430(06-036)

Hutchinson, M.F., 1989. A new procedure for gridding elevation and stream line data with automatic removal of spurious pits. *Journal of Hydrology*, 106(3-4), 211–232. Doi: https://doi.org/10.1016/0022-1694(89)90073-5

Hutter, K. (1983). Theoretical glaciology: material science of ice and the mechanics of glaciers and ice sheets. *Kluwer Academic Publishers, Dordrecht, Netherlands*.

Huybers, P., and Denton, G. (2008) Antarctic temperature at orbital timescales controlled by local summer duration. *Nature Geoscience*. v. 1, p.787-792. Doi: https://doi.org/10.1038/ngeo311.

Iglesias, V., Markgraf, V., & Whitlock, C. (2016). 17,000 years of vegetation, fire and climate change in the eastern foothills of the Andes (lat. 44 S). *Palaeogeography, Palaeoclimatology, Palaeoecology*, 457, 195-208. Doi: 10.1016/j.palaeo.2016.06.008

Ivins, E. R., & James, T. S. (2004). Bedrock response to Llanquihue Holocene and present-day glaciation in southernmost South America. *Geophysical Research Letters*, 31(24). Doi: https://doi.org/10.1029/2004GL021500

Jackson, R. H., Nash, J. D., Kienholz, C., Sutherland, D. A., Amundson, J. M., Motyka, R. J., Skyllingstad, E., Pettit, E. C. (2020). Meltwater intrusions reveal mechanisms for rapid submarine melt at a tidewater glacier. *Geophysical Research Letters*, 47(2), e2019GL085335. Doi: https://doi.org/10.1029/2019GL085335

Johnsen, T. F., Olsen, L., & Murray, A. (2012). OSL ages in central Norway support a MIS 2 interstadial (25–20 ka) and a dynamic Scandinavian ice sheet. *Quaternary Science Reviews*, *44*, 96-111. Doi: https://doi.org/10.1016/j.quascirev.2010.10.007

Jomelli, V., Mokadem, F., Schimmelpfennig, I., Chapron, E., Rinterknecht, V., Favier, V., Verfaillie, D., Brunstein, D., Legentil, C., Michel, E., Swingedouw, D., Jaouen, A., Aumaitre, G., Bourlès, D. L., Keddadouche, K. (2017). Sub-Antarctic glacier extensions in the Kerguelen region (49 S, Indian Ocean) over the past 24,000 years constrained by 36Cl moraine dating. Quaternary Science Reviews, 162, 128-144. Doi: https://doi.org/10.1016/j.quascirev.2017.03.010

Jones, R. S., Small, D., Cahill, N., Bentley, M. J., & Whitehouse, P. L. (2019a). iceTEA: Tools for plotting and analysing cosmogenic-nuclide surface-exposure data from former ice margins. *Quaternary Geochronology*, *51*, 72-86. Doi: https://doi.org/10.1016/j.quageo.2019.01.001

Jones, R. S., Whitehouse, P. L., Bentley, M. J., Small, D., & Dalton, A. S. (2019b). Impact of glacial isostatic adjustment on cosmogenic surface-exposure dating. *Quaternary Science Reviews*, 212, 206-212. Doi: https://doi.org/10.1016/j.quascirev.2019.03.012

Jouvet, G., & Funk, M. (2014). Modelling the trajectory of the corpses of mountaineers who disappeared in 1926 on Aletschgletscher, Switzerland. *Journal of Glaciology*, 60(220), 255-261. Doi: https://doi.org/10.3189/2014JoG13J156

Kaiser, J., Lamy, F., & Hebbeln, D. (2005). A 70-kyr sea surface temperature record off southern Chile (Ocean Drilling Program Site 1233). *Paleoceanography*, *20*(4). Doi: https://doi.org/10.1029/2005PA001146

Kaiser, J., Lamy, F., Arz, H. W., & Hebbeln, D. (2007). Dynamics of the millennial-scale sea surface temperature and Patagonian Ice Sheet fluctuations in southern Chile during the last 70 kyr (ODP Site 1233). *Quaternary International*, *161*(1), 77-89. Doi: https://doi.org/10.1016/j.quaint.2006.10.024

Kaplan, M. R., Ackert, R. P., Singer, B. S., Douglass, D. C., & Kurz, M. D. (2004). Cosmogenic nuclide chronology of millennial-scale glacial advances during O-isotope stage 2 in Patagonia. *GSA Bulletin*, *116*(3-4), 308-321. Doi: https://doi.org/10.1130/B25178.1

Kaplan, M. R., Douglass, D. C., Singer, B. S., Ackert, R. P., & Caffee, M. W. (2005). Cosmogenic nuclide chronology of pre-last glacial maximum moraines at Lago Buenos Aires, 46°S, Argentina. *Quaternary Research*, *63*(3), 301-315. Doi: https://doi.org/10.1016/j.yqres.2004.12.003

Kaplan, M. R., Coronato, A., Hulton, N. R. J., Rabassa, J. O., Kubik, P. W., & Freeman, S. P. H. T. (2007). Cosmogenic nuclide measurements in southernmost South America and implications for

landscape change. *Geomorphology*, *87*(4), 284-301. Doi: https://doi.org/10.1016/j.geomorph.2006.10.005

Kaplan, M. R., Fogwill, C. J., Sugden, D. E., Hulton, N. R. J., Kubik, P. W., & Freeman, S. P. H. T. (2008). Southern Patagonian glacial chronology for the Last Glacial period and implications for Southern Ocean climate. *Quaternary Science Reviews*, *27*(3-4), 284-294. Doi: 10.1016/j.quascirev.2007.09.013

Kaplan, M. R., Hein, A. S., Hubbard, A., & Lax, S. M. (2009). Can glacial erosion limit the extent of glaciation?. *Geomorphology*, 103(2), 172-179. Doi: https://doi.org/10.1016/j.geomorph.2008.04.020

Kaplan, M.R., Schaefer, J.M., Denton, G.H., Barrell, D.J., Chinn, T.J., Putnam, A.E., Andersen, B.G., Finkel, R.C., Schwartz, R., and Doughty, A.M. (2010). Glacier retreat in New Zealand during the Younger Dryas stadial. *Nature*. v. 467(7312), p. 194-197. Doi: https://doi.org/10.1038/nature09313.

Kaplan, M. R., Strelin, J. A., Schaefer, J. M., Denton, G. H., Finkel, R. C., Schwartz, R., Putnam, A. E., Vandergoes, M. J., Goehring, B. M., Travis, S. G. (2011). In-situ cosmogenic 10Be production rate at Lago Argentino, Patagonia: implications for late-glacial climate chronology. *Earth and Planetary Science Letters*, *309*(1-2), 21-32. Doi: https://doi.org/10.1016/j.epsl.2011.06.018

Kawamura, K., Parrenin, F., Lisiecki, L., Uemura, R., Vimeux, F., Severinghaus, J. P., Hutterli, M. A., Nakazawa, T., Aoki, S., Jouzel, J., Raymo, M. E., Matsumoto, K., Nakata, H., Motoyama, H., Fujita, S., Goto-Azuma, K., Fujii, Y., Watanabe, O. (2007). Northern Hemisphere forcing of climatic cycles in Antarctica over the past 360,000 years. *Nature*, *448*(7156), 912-916. Doi: https://doi.org/10.1038/nature06015

Kelley, S. E., Kaplan, M. R., Schaefer, J. M., Andersen, B. G., Barrell, D. J., Putnam, A. E., Denton, G. H., Schwartz, R., Finkel, R. C., Doughty, A. M. (2014). High-precision 10Be chronology of moraines in the Southern Alps indicates synchronous cooling in Antarctica and New Zealand 42,000 years ago. *Earth and Planetary Science Letters*, *405*, 194-206. Doi: https://doi.org/10.1016/j.epsl.2014.07.031

Kern, Z., & László, P. (2010). Size specific steady-state accumulation-area ratio: an improvement for equilibrium-line estimation of small palaeoglaciers. *Quaternary Science Reviews*, *29*(19-20), 2781-2787. Doi: https://doi.org/10.1016/j.quascirev.2010.06.033

Kiernan, K., Fifield, L. K., & Chappell, J. (2004). Cosmogenic nuclide ages for last glacial maximum moraine at Schnells Ridge, southwest Tasmania. *Quaternary Research*. v. 61(3), p. 335-338. Doi: https://doi.org/10.1016/j.yqres.2004.02.004.

Kiernan, K., Fink, D., Greig, D., & Mifud, C. (2010). Cosmogenic radionuclide chronology of pre-last glacial cycle moraines in the Western Arthur range, Southwest Tasmania. *Quaternary Science Reviews*. v. 29(23-24), p. 3286-3297. Doi: https://doi.org/10.1016/j.quascirev.2010.07.023.

Kiernan, K., McMinn, M. S., and Fink, D. (2014). Topographic and microclimatic impacts on glaciation of the Denison Range, southwest Tasmania. *Quaternary Science Reviews*. v. 97, p. 136-147. Doi: https://doi.org/10.1016/j.quascirev.2014.05.008.

Kiernan, K., Fink, D., & McConnell, A. (2017) Cosmogenic 10Be and 26Al exposure ages of glaciations in the Frankland Range, southwest Tasmania reveal a limited MIS-2 ice advance. *Quaternary Science Reviews*. v. 157, p. 141-151. Doi: https://doi.org/10.1016/j.quascirev.2016.12.008.

Knight, J. (1997). Morphological and morphometric analyses of drumlin bedforms in the Omagh Basin, north central Ireland. *Geografiska Annaler: Series A, Physical Geography*, *79*(4), 255-266. Doi: 10.1111/j.0435-3676.1997.00021.x

Knight, J. (2011). Uses and limitations of field mapping of lowland glaciated landscapes. In *Developments in Earth Surface Processes* (Vol. 15, pp. 533-550). Elsevier. Doi: 10.1016/B978-0-444-53446-0.00021-5

Koffman, B. G., Goldstein, S. L., Winckler, G., Borunda, A., Kaplan, M. R., Bolge, L., Cai, Y., Recasens, C., Koffman, T.N.B., and Vallelonga, P. (2021). New Zealand as a source of mineral dust to the atmosphere and ocean. *Quaternary Science Reviews*. v. 251, 106659. Doi: https://doi.org/10.1016/j.quascirev.2020.106659.

Kolb, T., Fuchs, M. (2018). Luminescence dating of pre-Eemian (pre-MIS 5e) fluvial terraces in Northern Bavaria (Germany) – Benefits and limitations of applying a pIRIR225-approach. *Geomorphology*, 321, 16-32. Doi : https://doi.org/10.1016/j.geomorph.2018.08.009

Kohl, C. P., & Nishiizumi, K. (1992). Chemical isolation of quartz for measurement of in-situ-produced cosmogenic nuclides. Geochimica et Cosmochimica Acta, v. 56(9), p. 3583-3587, doi: https://doi.org/10.1016/0016-7037(92)90401-4.

Korschinek, G., Bergmaier, A., Faestermann, T., Gerstmann, U. C., Knie, K., Rugel, G., Wallner, A., Dillmann, I., Dollinger, G., Lierse von Gostomski, Ch., Kossert, K., Maiti, M., Poutivtsev, M., Remmert, A. (2010). A new value for the half-life of 10Be by heavy-ion elastic recoil detection and liquid scintillation counting. *Nuclear Instruments and Methods in Physics Research Section B: Beam Interactions with Materials and Atoms*, 268(2), 187-191. Doi: https://doi.org/10.1016/j.nimb.2009.09.020

Lal, D. (1991). Cosmic ray labeling of erosion surfaces: *in situ* nuclide production. *Earth and Planetary Science Letters*, *104*, 424-439. Doi: https://doi.org/10.1016/0012-821X(91)90220-C

Lambeck, K., Rouby, H., Purcell, A., Sun, Y., & Sambridge, M. (2014). Sea level and global ice volumes from the Last Glacial Maximum to the Holocene. *Proceedings of the National Academy of Sciences*, 111(43), 15296-15303. Doi: 10.1073/pnas.1411762111

Lambert, F., Delmonte, B., Petit, J.R., Bigler, M., Kaufmann, P.R., Hutterli, M.A., Stocker, T.F., Ruth, U., Steffensen, J.P., Maggi, V. (2008) Dust-climate couplings over the past 800,000 years from the EPICA Dome C ice core. *Nature*. v. 452(7187), p. 616-619. Doi: https://doi.org/10.1038/nature06763.

Lambert, F., Bigler, M., Steffensen, J.P., Hutterli, M., Fischer, H. (2012). Centennial mineral dust variability in high-resolution ice core data from Dome C, Antarctica. *Climate of the Past*. v. 8, p. 609–623. Doi: https://doi.org/10.5194/cp-8-609-2012.

Lamy, F., Kaiser, J., Ninnemann, U., Hebbeln, D., Arz, H. W., & Stoner, J. (2004). Antarctic timing of surface water changes off Chile and Patagonian ice sheet response. *Science*, *304*(5679), 1959-1962. Doi: https://doi.org/10.1126/science.1097863

Lamy, F., Kaiser, J., Arz, H.W., Hebbeln, D., Ninnemann, U., Timm, O., Timmermann, A., Toggweiler, J.R., (2007). Modulation of the bipolar seesaw in the southeast Pacific during Termination 1. *Earth and Planetary Science Letters*, 259, 400–413. Doi: https://doi.org/10.1016/j.epsl.2007.04.040

Lamy, F., Arz, H. W., Kilian, R., Lange, C. B., Lembke-Jene, L., Wengler, M., Kaiser, J., Baeza-Urrea, O., Hall, I. R., Harada, N., Tiedemann, R. (2015). Glacial reduction and millennial-scale variations in Drake Passage throughflow. *Proceedings of the National Academy of Sciences*, *112*(44), 13496-13501. Doi: https://doi.org/10.1073/pnas.1509203112.

Lange, D., Cembrano, J., Rietbrock, A., Haberland, C., Dahm, T., & Bataille, K. (2008). First seismic record for intra-arc strike-slip tectonics along the Liquiñe-Ofqui fault zone at the obliquely convergent plate margin of the southern Andes. *Tectonophysics*, *455*(1-4), 14-24. Doi: https://doi.org/10.1016/j.tecto.2008.04.014

Lange, H., Casassa, G., Ivins, E. R., Schröder, L., Fritsche, M., Richter, A., Groh, A., Dietrich, R. (2014). Observed crustal uplift near the Southern Patagonian Icefield constrains improved viscoelastic Earth models. *Geophysical Research Letters*, 41(3), 805-812. Doi: https://doi.org/10.1002/2013GL058419

Lapido, O. (1990). Glacial deposits on the Patagonian Cordillera at latitude 43°30′ South. *Quaternary of South America and Antarctic Peninsula*, *6*, 257-266.

Larour, E., Seroussi, H., Morlighem, M., and Rignot, E. (2012). Continental scale, high order, high spatial resolution, ice sheet modeling using the Ice Sheet System Model (ISSM). *Journal of Geophysical Research: Earth Surface*, v. 117(F1). Doi: https://doi.org/10.1029/2011JF002140.

Leger, T. P. M., Hein, A. S., Bingham, R. G., Martini, M. A., Rodrigo, L. S., Sagredo, E. A., Martínez, O. A. (2020). The glacial geomorphology of the Río Corcovado, Río Huemul and Lago Palena/General Vintter valleys, northeastern Patagonia (43°S, 71°W). *Journal of Maps*, *16*(2), 651-668. Doi: https://doi.org/10.1080/17445647.2020.1794990

Leger, T.P.M., Hein, A.S., Bingham, R.G., Rodés, Á., Fabel, D., and Smedley, R., 2021a, Geomorphology and ^{10}Be chronology of the Last Glacial Maximum and deglaciation in northeastern Patagonia, 43°S-71°W: Quaternary Science Reviews, v. 272, doi: https://doi.org/10.1016/j.quascirev.2021.107194.

Leger, T.P.M., Hein, A.S., Goldberg, D., Schimmelpfennig, I., Van Wyk de Vries, M.S., Bingham, R.G., and ASTER Team, 2021b, Northeastern Patagonian Glacier Advances (43°S) Reflect Northward Migration of the Southern Westerlies Towards the End of the Last Glaciation: Frontiers in Earth Science, v. 9, 751987, doi: https://doi.org/10.3389/feart.2021.751987.

Lenaerts, J. T., Van Den Broeke, M. R., van Wessem, J. M., van de Berg, W. J., van Meijgaard, E., van Ulft, L. H., & Schaefer, M. (2014). Extreme precipitation and climate gradients in Patagonia revealed by high-resolution regional atmospheric climate modeling. *Journal of climate*, *27*(12), 4607-4621. Doi: https://doi.org/10.1175/JCLI-D-14-00660.1

Lifton, N. A., Jull, A. T., & Quade, J. (2001). A new extraction technique and production rate estimate for in situ cosmogenic 14C in quartz. *Geochimica et Cosmochimica Acta*, *65*(12), 1953-1969. Doi: https://doi.org/10.1016/S0016-7037(01)00566-X

Lifton, N., Sato, T., & Dunai, T. J. (2014). Scaling in situ cosmogenic nuclide production rates using analytical approximations to atmospheric cosmic-ray fluxes. *Earth and Planetary Science Letters*, *386*, 149-160. Doi: https://doi.org/10.1016/j.epsl.2013.10.052

Lifton, N., Caffee, M., Finkel, R., Marrero, S., Nishiizumi, K., Phillips, F. M., Goehring, B., Gosse, J., Stone, J., Schaefer, J., Theriault, B., Timothy Jull, A. J., Fifield. K. (2015). In situ cosmogenic nuclide production rate calibration for the CRONUS-Earth project from Lake Bonneville, Utah,

shoreline features. *Quaternary Geochronology*, *26*, 56-69. Doi: https://doi.org/10.1016/j.quageo.2014.11.002

Lindner, L., and Marks, L. (1999). New approach to stratigraphy of palaeolake and glacial sediments of the younger Middle Pleistocene in mid-eastern Poland. *Geological Quarterly*. v. 43(1), p. 1-8.

Lisiecki, L. E., and Raymo, M. E. (2005). A Pliocene-Pleistocene stack of 57 globally distributed benthic δ18O records. *Paleoceanography*, v. 20(1). Doi, https://doi.org/10.1029/2004PA001071.

Lopes dos Santos, R. A., Spooner, M. I., Barrows, T. T., De Deckker, P., Sinninghe Damsté, J. S., & Schouten, S. (2013). Comparison of organic (UK'37, TEXH86, LDI) and faunal proxies (foraminiferal assemblages) for reconstruction of late Quaternary sea surface temperature variability from offshore southeastern Australia. *Paleoceanography*, *28*(3), 377-387. Doi: https://doi.org/10.1002/palo.20035

Lorrey, A.M., Bostock, H., 2017, The Quaternary climate of New Zealand. Advances in Quaternary Science - the New Zealand Landscape. Springer-Verlag, pp. 67-139.

Mashiotta, T. A., Lea, D. W., & Spero, H. J. (1999). Glacial–interglacial changes in Subantarctic sea surface temperature and δ18O-water using foraminiferal Mg. *Earth and Planetary Science Letters*, *170*(4), 417-432. Doi: https://doi.org/10.1016/S0012-821X(99)00116-8

Margari, V., Skinner, L.C., Hodell, D.A., Martrat, B., Toucanne, S., Grimalt, J.O., Gibbard, P.L., Lunkka, J.P., and Tzedakis, P.C., 2014, Land-ocean changes on orbital and millennial time scales and the penultimate glaciation: Geology, v. 42, p. 183–186, doi: https://doi.org/10.1130/G35070.1.

Martin, L. C. P., Blard, P. H., Balco, G., Lavé, J., Delunel, R., Lifton, N., and Laurent, V., 2017, The CREp program and the ICE-D production rate calibration database: A fully parameterizable and updated online tool to compute cosmic-ray exposure ages: Quaternary geochronology, v. 38, p. 25-49, doi: https://doi.org/10.1016/j.quageo.2016.11.006.

Martin, J. R., Davies, B. J., & Thorndycraft, V. R. (2019). Glacier dynamics during a phase of Late Quaternary warming in Patagonia reconstructed from sediment landform associations. *Geomorphology*, *337*, 111-133. Doi: https://doi.org/10.1016/j.geomorph.2019.03.007

Martínez, O., 2002. Geomorfología y geología de los depositós glaciarios y periglaciarios de la región comprendida entre los 43° y 44° lat. Sur y 70°30’ y 72° long. Oeste, Chubut, República Argentina. Universidad Nacional de la Patagonia-San Juan Bosco, unpublished doctoral thesis, Comodoro Rivadavia and Esquel.

Martínez, O., Coronato, A., & Rabassa, J. (2011). Pleistocene glaciations in northern Patagonia, Argentina: an updated review. In *Developments in Quaternary Sciences* (Vol. 15, pp. 729-734). Elsevier. Doi: https://doi.org/10.1016/j.quaint.2009.06.019

McCulloch, R. D., Fogwill, C. J., Sugden, D. E., Bentley, M. J., & Kubik, P. W. (2005). Chronology of the last glaciation in central Strait of Magellan and Bahía Inútil, southernmost South America. *Geografiska Annaler: Series A, Physical Geography*, *87*(2), 289-312. Doi: https://doi.org/10.1111/j.0435-3676.2005.00260.x

Meglioli, A., 1992, Glacial geology and chronology of southernmost Patagonia and Tierra del Fuego, Argentina and Chile [Ph.D. thesis]: Bethlehem, Pennsylvania, Lehigh University, 216 p.

Mendelová, M., Hein, A. S., McCulloch, R., & Davies, B. (2017). The last glacial maximum and deglaciation in central Patagonia, 44° S–49° S. *Cuadernos de Investigación Geográfica*, *43*(2), 719-750. Doi: https://doi.org/10.18172/cig.3263

Mendelová, M., Hein, A. S., Rodés, Á., & Xu, S. (2020a). Extensive mountain glaciation in central Patagonia during Marine Isotope Stage 5. *Quaternary Science Reviews*, *227*, 105996. Doi: https://doi.org/10.1016/j.quascirev.2019.105996

Mendelová, M., Hein, A. S., Rodés, Á., Smedley, R. K., & Xu, S. (2020b). Glacier expansion in central Patagonia during the Antarctic Cold Reversal followed by retreat and stabilisation during the Younger Dryas. *Quaternary Science Reviews*, *227*, 106047. Doi: https://doi.org/10.1016/j.quascirev.2019.106047

Mercer, J. H. (1972). Chilean glacial chronology 20,000 to 11,000 carbon-14 years ago: some global comparisons. *Science*, *176*(4039), 1118-1120. Doi: https://doi.org/10.1210/jcem-10-10-1361

Mercer, J. H. (1976). Glacial history of Southernmost South America. *Quaternary Research*, *6*(2), 125-166. Doi: https://doi.org/10.1016/0033-5894(76)90047-8

Mercer, J. H. (1984). Simultaneous climatic change in both hemispheres and similar bipolar interglacial warming: Evidence and implications. *Climate processes and climate sensitivity*, 29, 307-313. Doi: https://doi.org/10.1029/GM029p0307

Millan, R., Mouginot, J., Rabatel, A., Jeong, S., Cusicanqui, D., Derkacheva, A., & Chekki, M. (2019). Mapping surface flow velocity of glaciers at regional scale using a multiple sensors approach. *Remote Sensing*, 11(21), 2498. Doi: https://doi.org/10.3390/rs11212498

Montade, V., Combourieu Nebout, N., Kissel, C., Haberle, S.G., Siani, G., Michel, E. (2013). Vegetation and climate changes during the last 22,000yr from a marine core near Taitao Peninsula, southern Chile. *Palaeogeography, Palaeoclimatology, Palaeoecology,* 369, 335- 348. Doi: http://doi.org/10.1016/j.palaeo.2012.11.001

Moreiras, S. M., Páez, M. S., Lauro, C., & Jeanneret, P. (2017). First cosmogenic ages for glacial deposits from the Plata range (33°S): New inferences for Quaternary landscape evolution in the Central Andes. Quaternary international, 438, 50-64. Doi: 10.1016/j.quaint.2016.08.041

Moreno, F. P. (1899). Explorations in Patagonia. The Geographical Journal, v. 14(3), p. 241-269, doi: https://doi.org/1774365.

Moreno, P. I., Denton, G. H., Moreno, H., Lowell, T. V., Putnam, A. E., & Kaplan, M. R. (2015). Radiocarbon chronology of the last glacial maximum and its termination in northwestern Patagonia. *Quaternary Science Reviews*, *122*, 233-249. Doi: https://doi.org/10.1016/j.quascirev.2015.05.027

Moreno, P. I., Videla, J., Valero-Garcés, B., Alloway, B. V., & Heusser, L. E. (2018). A continuous record of vegetation, fire-regime and climatic changes in northwestern Patagonia spanning the last 25,000 years. *Quaternary Science Reviews*, *198*, 15-36. Doi: https://doi.org/10.1016/j.quascirev.2018.08.013

Moreno, P. I., Simi, E., Villa-Martínez, R. P., & Vilanova, I. (2019). Early arboreal colonization, postglacial resilience of deciduous Nothofagus forests, and the Southern Westerly Wind influence in central-east Andean Patagonia. *Quaternary Science Reviews*, 218, 61-74. Doi: https://doi.org/10.1016/j.quascirev.2019.06.004

Mouginot, J., and Rignot, E. (2015). Ice motion of the Patagonian icefields of South America: 1984–2014. Geophysical Research Letters, v. 42(5), p. 1441-1449. Doi: https://doi.org/10.1002/2014GL062661.

Murray, A.S., Thomsen, K.J., Masuda, N., Buylaert, J.P., Jain, M. (2012). Identifying well-bleached quartz using the different bleaching rates of quartz and feldspar luminescence signals. *Radiation Measurements*, 47(9), 688-695. Doi : https://doi.org/10.1016/j.radmeas.2012.05.006

Murray, D. S., Carlson, A. E., Singer, B. S., Anslow, F. S., He, F., Caffee, M., Marcott, S. A., Liu, Z., Otto-Bliesner, B. L. (2012). Northern Hemisphere forcing of the last deglaciation in southern Patagonia. *Geology*, *40*(7), 631-634. Doi: https://doi.org/10.1130/G32836.1

NGRIP Members. (2004). High-resolution record of the Northern Hemisphere climate extending into the last interglacial period. *Nature*, *431*, 147-151. Doi: https://doi.org/10.1038/nature02805

Nimick, D. A., McGrath, D., Mahan, S. A., Friesen, B. A., & Leidich, J. (2016). Latest pleistocene and Holocene glacial events in the Colonia valley, northern Patagonia icefield, southern Chile. *Journal of Quaternary Science*, 31(6), 551-564. Doi: https://doi.org/10.1002/jqs.2847

Nishiizumi, K. (2004) Preparation of 26Al AMS standards: Nuclear Instruments and Methods in Physics Research Section B. *Beam Interactions with Materials and Atoms*. v. 223, p. 388-392. Doi: https://doi.org/10.1016/j.nimb.2004.04.075.

Nishiizumi, K., Imamura, M., Caffee, M. W., Southon, J. R., Finkel, R. C., & McAninch, J. (2007). Absolute calibration of 10Be AMS standards. *Nuclear Instruments and Methods in Physics Research Section B: Beam Interactions with Materials and Atoms*, 258(2), 403-413. Doi: https://doi.org/10.1016/j.nimb.2007.01.297

Nordenskjöld, O. (1897). Algunos datos sobre la naturaleza de la región magallánica. In Anales de la Sociedad Científica Argentina, v. 44, p. 190-197.

Nordenskjöld, O. (1899). Geological map of the Magellan territories with explanatory notes. Kungl. Boktryckeriet. PA Norstedt & Söner.

Oerlemans, J., & Fortuin, J. P. F. (1992). Sensitivity of glaciers and small ice caps to greenhouse warming. Science, v. 258(5079), p. 115-117. Doi: https://doi.org/10.1126/science.258.5079.115.

Olszak, J. (2011). Evolution of fluvial terraces in response to climate change and tectonic uplift during the Pleistocene: Evidence from Kamienica and Ochotnica River valleys (Polish Outer Carpathians). *Geomorphology*, *129*(1-2), 71-78. Doi: 10.1016/j.geomorph.2011.01.014

Orsi, A. H., Whitworth III, T., & Nowlin Jr, W. D. (1995). On the meridional extent and fronts of the Antarctic Circumpolar Current. *Deep Sea Research Part I: Oceanographic Research Papers*, *42*(5), 641-673. Doi: https://doi.org/10.1016/0967-0637(95)00021-W

Osmaston, H. (2005). Estimates of glacier equilibrium line altitudes by the Area × Altitude, the Area × Altitude Balance Ratio and the Area × Altitude Balance Index methods and their validation. *Quaternary International*, 138, 22-31. Doi: https://doi.org/10.1016/j.quaint.2005.02.004

Pahnke, K., Zahn, R., Elderfield, H., & Schulz, M. (2003). 340,000-year centennial-scale marine record of Southern Hemisphere climatic oscillation. *Science*, *301*(5635), 948-952. Doi: https://doi.org/10.1126/science.1084451

Pankhurst, R. J., Hervé, F., Rojas, L., & Cembrano, J. (1992). Magmatism and tectonics in continental Chiloé, Chile (42–42 30′ S). *Tectonophysics*, *205*(1-3), 283-294. Doi: https://doi.org/10.1016/0040-1951(92)90431-5

Parrenin, F., Masson-Delmotte, V., Köhler, P., Raynaud, D., Paillard, D., Schwander, J., Barbante, C., Landais, A., Wegner, A., and Jouzel, J. (2013). Synchronous change of atmospheric CO2 and Antarctic temperature during the last deglacial warming. *Science*. v. 339(6123), p. 1060-1063. Doi: https://doi.org/10.1126/science.1226368.

Paterson, W.S.B., 1994. The Physics of Glaciers, 3rd Edition Pergamon/Elsevier, London.

Pedro, J. B., Bostock, H. C., Bitz, C. M., He, F., Vandergoes, M. J., Steig, E. J., Chase, B. M., Krause, C. E., Rasmussen, S. O., Markle, B. R., Cortese, G. (2016). The spatial extent and dynamics of the Antarctic Cold Reversal. *Nature Geoscience*, 9(1), 51-55. Doi: https://doi.org/10.1038/ngeo2580

Pedro, J. B., Jochum, M., Buizert, C., He, F., Barker, S., & Rasmussen, S. O. (2018). Beyond the bipolar seesaw: Toward a process understanding of interhemispheric coupling. *Quaternary Science Reviews*, *192*, 27-46. Doi: https://doi.org/10.1016/j.quascirev.2018.05.005

Pellitero, R., Rea, B. R., Spagnolo, M., Bakke, J., Hughes, P., Ivy-Ochs, S., Lukas, S., Ribolini, A. (2015). A GIS tool for automatic calculation of glacier equilibrium-line altitudes. *Computers & Geosciences*, 82, 55-62. Doi: https://doi.org/10.1016/j.cageo.2015.05.005

Pellitero, R., Rea, B. R., Spagnolo, M., Bakke, J., Ivy-Ochs, S., Frew, C. R., Hughes, P., Ribolini, A., Lukas, S., & Renssen, H. (2016). GlaRe, a GIS tool to reconstruct the 3D surface of palaeoglaciers. *Computers & Geosciences*, 94, 77-85. Doi: https://doi.org/10.1016/j.cageo.2016.06.008

Peltier, W. R., Argus, D. F., & Drummond, R. (2015). Space geodesy constrains ice age terminal deglaciation: The global ICE-6G_C (VM5a) model. Journal of Geophysical Research: Solid Earth, 120(1), 450-487. Doi: https://doi.org/10.1002/2014JB011176

Peltier, C., Kaplan, M. R., Schaefer, J. M., Araos, J., Sagredo, E. A., and Schwartz, R., 2017 (December), Glacier-Climate Change in Southern South America over Multiple Glacial Cycles and Implications for Glacial to Interglacial Shifts in the Westerly Winds: In 2017 AGU Fall Meeting. AGU, Bibcode: 2017AGUFMPP43B1349P

Peltier, C., Kaplan, M. R., Birkel, S. D., Soteres, R. L., Sagredo, E. A., Aravena, J. C., Araos, J., Moreno, P. I., Schwartz, R., Schaefer, J. M. (2021). A large MIS 4 and long MIS 2 glacier maximum on the southern tip of South America. *Quaternary Science Reviews*, 262, 106858. Doi: https://doi.org/10.1016/j.quascirev.2021.106858

Phillips, F.M., Zreda, M.G., Smith, S.S., Elmore, D., Kubik, P.W., and Sharma, P., 1990, Cosmogenic chlorine-36 chronology for glacial deposits at Bloody Canyon, eastern Sierra Nevada: Science, v. 248, p. 1529–1532, doi: https://doi.org/10.1126/science.248.4962.1529.

Prescott, J.R., Hutton, J.T., 1994. Cosmic ray and gamma ray dosimetry for TL and ESR. *International Journal of Radiation Applications and Instrumentation. Part D. Nuclear Tracks and Radiation Measurements,* 14(1-2), 223-227. Doi : https://doi.org/10.1016/1359-0189(88)90069-6

Preusser, F., Graf, H. R., Keller, O., Krayss, E., & Schlüchter, C., 2011, Quaternary glaciation history of northern Switzerland: E&G Quaternary Science Journal, v. 60(2/3), p. 282-305, doi: https://doi.org/10.3285/eg.60.2-3.06.

Price, R. J. (1969). Moraines, sandar, kames and eskers near Breidamerkurjökull, Iceland. *Transactions of the Institute of British Geographers*, 17-43. Doi: 10.2307/621406

Putkonen, J., & Swanson, T. (2003). Accuracy of cosmogenic ages for moraines. *Quaternary Research*, *59*(2), 255-261. Doi: https://doi.org/10.1016/S0033-5894(03)00006-1

Putnam, A. E., Schaefer, J. M., Barrell, D. J. A., Vandergoes, M., Denton, G. H., Kaplan, M. R., Finkel, R. C., Schwartz, R., Goehring. B. M., Kelley, S. E. (2010). In situ cosmogenic 10Be production-rate calibration from the Southern Alps, New Zealand. *Quaternary Geochronology*, *5*(4), 392-409. Doi: https://doi.org/10.1016/j.quageo.2009.12.001

Putnam, A. E., Schaefer, J. M., Denton, G. H., Barrell, D. J., Andersen, B. G., Koffman, T. N., Rowan, A. V., Finkel, R. C., Rood, D. H., Schwartz, R., Vandergoes, M. J., Plummer, M. A., Brocklehurst, S. H., Kelley, S. E., Ladig, K. L. (2013). Warming and glacier recession in the Rakaia valley, Southern Alps of New Zealand, during Heinrich Stadial 1. *Earth and Planetary Science Letters*, *382*, 98-110. Doi: 10.1016/j.epsl.2013.09.005

Putnam, A.E., Schaefer, J.M., Denton, G.H., Barrell, D.J.A., Birkel, S.D., Andersen, B.G., Kaplan, M.R., Finkel, R.C., Schwartz, R., and Doughty, A.M. (2013). The Last Glacial Maximum at 44°S documented by a 10Be moraine chronology at Lake Ohau, Southern Alps of New Zealand. *Quaternary Science Reviews*, v. 62, 114e141. Doi: https://doi.org/10.1016/j.quascirev.2012.10.034.

Rabassa, J., and Clapperton, C. M. (1990) Quaternary glaciations of the southern Andes. *Quaternary Science Reviews*, v. 9(2-3), p. 153-174. Doi: https://doi.org/10.1016/0277-3791(90)90016-4.

Rabassa, J., Coronato, A., Bujalesky, G., Salemme, M., Roig, C., Meglioli, A., Heusser, C., Gordillo, S., Roig, F., Borromei, A., Quattrocchio, M. (2000). Quaternary of Tierra del Fuego, southernmost South America: an updated review. *Quaternary International*, *68*, 217-240. Doi: 10.1016/S1040-6182(00)00046-X

Rabassa, J., and Coronato, A. (2009) Glaciations in Patagonia and Tierra del Fuego during the Ensenadan stage/age (early Pleistocene–earliest middle Pleistocene). *Quaternary International*, v. 210(1-2), p. 18-36. Doi: https://doi.org/10.1016/j.quaint.2009.06.019.

Raedeke, L. D. (1978). Formas del terreno y depósitos cuaternarios, Tierra del Fuego Central, Chile. *Revista geológica de Chile: An international journal on andean geology*, (5), 3-31.

Rapela, C. W., & Pankhurst, R. J. (1992). The granites of northern Patagonia and the Gastre Fault System in relation to the break-up of Gondwana. *Geological Society, London, Special Publications*, *68*(1), 209-220. Doi: https://doi.org/10.1144/GSL.SP.1992.068.01.13

Reynhout, S. A., Sagredo, E. A., Kaplan, M. R., Aravena, J. C., Martini, M. A., Moreno, P. I., Rojas, M., Schwartz, R., Schaefer, J. M. (2019). Holocene glacier fluctuations in Patagonia are modulated by summer insolation intensity and paced by Southern Annular Mode-like variability. *Quaternary Science Reviews*, 220, 178-187. Doi: https://doi.org/10.1016/j.quascirev.2019.05.029

Richter, A., Ivins, E., Lange, H., Mendoza, L., Schröder, L., Hormaechea, J. L., Casassa, G., Marderwald, E., Fritsche, M., Perdomo, R., Horwath, M., Dietrich, R. (2016). Crustal deformation across the Southern Patagonian Icefield observed by GNSS. *Earth and Planetary Science Letters,* 452, 206-215. Doi: https://doi.org/10.1016/j.epsl.2016.07.042

Rignot, E., Mouginot, J., Scheuchl, B., van den Broeke, M., van Wessem, M. J., & Morlighem, M. (2019). Four decades of Antarctic Ice Sheet mass balance from 1979–2017. *Proceedings of the National Academy of Sciences*, *116*(4), 1095-1103. Doi: https://doi.org/10.1073/pnas.1812883116

Rivera, A., Bown, F., Carrión, D., & Zenteno, P. (2012). Glacier responses to recent volcanic activity in Southern Chile. *Environmental Research Letters*, 7(1), 014036. Doi: https://doi.org/10.1088/1748-9326/7/1/014036

Roberts, H.M. (2012). Testing post-IR IRSL protocols for minimising fading in feldspars, using Alaskan loess with independent chronological control. *Radiation Measurements*, 47(9), 716-724. Doi : https://doi.org/10.1016/j.radmeas.2012.03.022

Roe, G. H., & O'Neal, M. A. (2009). The response of glaciers to intrinsic climate variability: observations and models of late-Holocene variations in the Pacific Northwest. *Journal of Glaciology*, 55(193), 839-854. Doi: https://doi.org/10.3189/002214309790152438

Roe, G. H. (2011). What do glaciers tell us about climate variability and climate change? *Journal of Glaciology*, *57*(203), 567-578. Doi: https://doi.org/10.3189/002214311796905640

Rother, H., Shulmeister, J., Fink, D., Alexander, D., & Bell, D. (2015). Surface exposure chronology of the Waimakariri glacial sequence in the Southern Alps of New Zealand: Implications for MIS-2 ice extent and LGM glacial mass balance. *Earth and Planetary Science Letters*, *429*, 69-81. Doi: https://doi.org/10.1016/j.epsl.2015.07.033

Rosenau, M., Melnick, D., & Echtler, H. (2006). Kinematic constraints on intra-arc shear and strain partitioning in the southern Andes between 38°S and 42°S latitude. *Tectonics*, *25*(4). Doi: https://doi.org/10.1029/2005TC001943

Russell, A. J., Roberts, M. J., Fay, H., Marren, P. M., Cassidy, N. J., Tweed, F. S., & Harris, T. (2006). Icelandic jökulhlaup impacts: implications for ice-sheet hydrology, sediment transfer and geomorphology. *Geomorphology*, *75*(1-2), 33-64. Doi: 10.1016/j.geomorph.2005.05.018

Sagredo, E. A., Moreno, P. I., Villa-Martínez, R., Kaplan, M. R., Kubik, P. W., & Stern, C. R. (2011). Fluctuations of the Última Esperanza ice lobe (52 S), Chilean Patagonia, during the last glacial maximum and termination 1. *Geomorphology*, *125*(1), 92-108. Doi: https://doi.org/10.1016/j.geomorph.2010.09.007

Sagredo, E. A., Kaplan, M. R., Araya, P. S., Lowell, T. V., Aravena, J. C., Moreno, P. I., Kelly, M. A., Schaefer, J. M. (2018). Trans-pacific glacial response to the Antarctic Cold Reversal in the southern mid-latitudes. *Quaternary Science Reviews*, 188, 160-166. Doi: https://doi.org/10.1016/j.quascirev.2018.01.011

Sato, T., Yasuda, H., Niita, K., Endo, A., and Sihver, L. (2008) Development of PARMA: PHITS-based analytical radiation model in the atmosphere. *Radiation research*. v. 170(2), p. 244-259. Doi, https://doi.org/10.1667/RR1094.1.

Sarmiento, J. L., and Toggweiler, J. R. (1984). A new model for the role of the oceans in determining atmospheric p CO2: Nature, v. 308(5960), p. 621-624, doi: https://doi.org/10.1038/308621a0.

Schaefer, J. M., Putnam, A. E., Denton, G. H., Kaplan, M. R., Birkel, S., Doughty, A. M., Kelley, S. E., Barrell, D. J. A., Finkel, R. C., Winckler, G., Anderson, R. F., Ninneman, U. S., Barker, S., Schwartz, R., Andersen, B. J., Schluechter, C. (2015). The southern glacial maximum 65,000 years

ago and its unfinished termination. *Quaternary Science Reviews*, *114*, 52-60. Doi: https://doi.org/10.1016/j.quascirev.2015.02.009

Shakun, J.D., Lea, D.W., Lisiecki, L.E., and Raymo, M. E. (2015). An 800-kyr record of global surface ocean δ18O and implications for ice volume-temperature coupling. *Earth and Planetary Science Letters*. v. 426, p. 58-68. Doi: https://doi.org/10.1016/j.epsl.2015.05.042.

Shilling, D.H., Hollin, J.T., (1981). Numerical reconstructions of valley glaciers and small ice caps. In: Denton, G.H., Hughes, T.J. (Eds.), *The Last Great Ice Sheets*. Wiley, New York, pp. 207-220.

Shulmeister, J., Fink, D., Hyatt, O. M., Thackray, G. D., & Rother, H. (2010). Cosmogenic ^{10}Be and ^{26}Al exposure ages of moraines in the Rakaia Valley, New Zealand and the nature of the last termination in New Zealand glacial systems. *Earth and Planetary Science Letters*, *297*(3-4), 558-566. Doi: https://doi.org/10.1016/j.epsl.2010.07.007

Shulmeister, J., Thackray, G. D., Rittenour, T. M., Fink, D., & Patton, N. R. (2019). The timing and nature of the last glacial cycle in New Zealand. *Quaternary Science Reviews*, *206*, 1-20. Doi: https://doi.org/10.1016/j.quascirev.2018.12.020

Siani, G., Colin, C., Michel, E., Carel, M., Richter, T., Kissel, C., Dewilde, F. (2010). Late Glacial to Holocene terrigenous sediment record in the Northern Patagonian margin: Paleoclimate implications. *Palaeogeography, Palaeoclimatology, Palaeoecology* 297 (1), 26-36. Doi: http://doi.org/10.1016/j.palaeo.2010.07.011

Sime, L. C., Kohfeld, K. E., Le Quéré, C., Wolff, E. W., de Boer, A. M., Graham, R. M., & Bopp, L. (2013). Southern Hemisphere westerly wind changes during the Last Glacial Maximum: model-data comparison. *Quaternary Science Reviews*, *64*, 104-120. Doi: https://doi.org/10.1016/j.quascirev.2012.12.008

Singer, B. S., Laurie, L. B., Rabassa, J. O., & Guillou, H. (2004). ^{40}Ar/^{39}Ar Chronology of Late Pliocene and Early Pleistocene Geomagnetic and Glacial Events in Southern Argentina. *Geophysical Monograph Series, 145*, 175-190. Doi: https://doi.org/10.1029/145GM13

Sissons, J. B. (1978). The parallel roads of Glen Roy and adjacent glens, Scotland. *Boreas*, *7*(4), 229-244. Doi: https://doi.org/10.1111/j.1502-3885.1978.tb00281.x

Skirrow, G. K., Smedley, K., Chiverrell, R. C., & Hooke, J. M. (2021). Planform change of the Río Chubut (~ 42° S,~ 70° W, Argentina) in response to climate drivers in the southern Andes. *Geomorphology*, 107924. Doi: https://doi.org/10.1016/j.geomorph.2021.107924

Small, D., Bentley, M. J., Jones, R. S., Pittard, M. L., & Whitehouse, P. L. (2019). Antarctic ice sheet palaeo-thinning rates from vertical transects of cosmogenic exposure ages. *Quaternary Science Reviews*, 206, 65-80. Doi: https://doi.org/10.1016/j.quascirev.2018.12.024

Smedley, R.K., Duller, G.A.T., Pearce, N.J.G., Roberts, H.M. (2012). Determining the K- content of single-grains of feldspar for luminescence dating. *Radiation Measurements*, 47(9), 790-796. Doi : https://doi.org/10.1016/j.radmeas.2012.01.014

Smedley, R.K., Duller, G.A.T. (2013). Optimising the reproducibility of measurements of the post-IR IRSL signal from single-grains of feldspar for dating. *Ancient TL*, 31(2), 49-58. URL : hdl.handle.net/2160/28754

Smedley, R.K., Pearce, N.J. G. (2016). Internal U and Th concentrations of K-feldspar grains: implications for luminescence dating. *Quaternary Geochronology*, 35, 16 – 25.

Smedley, R. K., Glasser, N. F., & Duller, G. A. T. (2016). Luminescence dating of glacial advances at Lago Buenos Aires (~46°S), Patagonia. *Quaternary Science Reviews*, *134*, 59-73. Doi: https://doi.org/10.1016/j.quascirev.2015.12.010

Smedley, R. K., & Skirrow, G. K. (2020). Luminescence dating in fluvial settings: overcoming the challenge of partial bleaching. In *Palaeohydrology* (pp. 155-168). Springer, Cham.

Smith, M. J., Knight, J., Field, K. S., & Harrison, S. (2008). Glacial striae observations for Ireland compiled from historic records. *Journal of Maps*, *4*(1), 378-398. Doi: 10.4113/jom.2008.1035

Sneed, E. D., & Folk, R. L. (1958). Pebbles in the lower Colorado River, Texas a study in particle morphogenesis. *The Journal of Geology*, *66*(2), 114-150. Doi: https://doi.org/10.1086/626490

Soteres, R. L., Peltier, C., Kaplan, M. R., & Sagredo, E. A. (2020). Glacial geomorphology of the Strait of Magellan ice lobe, southernmost Patagonia, South America. *Journal of Maps*, 16(2), 299-312. Doi: https://doi.org/10.1080/17445647.2020.1736197

Spagnolo, M., Clark, C. D., & Hughes, A. L. (2012). Drumlin relief. *Geomorphology*, *153*, 179-191. Doi: 10.1016/j.geomorph.2012.02.023

Spencer, C. J., Yakymchuk, C., & Ghaznavi, M. (2017). Visualising data distributions with kernel density estimation and reduced chi-squared statistic. *Geoscience Frontiers*, *8*(6), 1247-1252. Doi: https://doi.org/10.1016/j.gsf.2017.05.002

Spratt, R.M., and Lisiecki, L.E. (2016). A Late Pleistocene sea level stack. *Climate of the Past*, v. 12(4), p. 1079-1092. Doi: https://doi.org/10.5194/cp-12-1079-2016.

Stenni, B., Buiron, D., Frezzotti, M., Albani, S., Barbante, C., Bard, E., Barnola, J.M., Baroni, M., Baumgartner, M., Bonazza, M., Capron, E., Castellano, E., Chappellaz, J., Delmonte, B., Falourd, S., Genoni, L., Iacumin, P., Jouzel, J., Kipfstuhl, S., Landais, A., Lemieux-Dudon, B., Maggi, V., Masson-Delmotte, V., Mazzola, C., Minster, B., Montagnat, M., Mulvaney, R., Narcisi, B., Oerter, H., Parrenin, F., Petit, J.R., Ritz, C., Scarchilli, C., Schilt, A., Schüpbach, S., Schwander, J., Selmo, E., Severi, M., Stocker, T. F., and Udisti, R. (2011). Expression of the bipolar see-saw in Antarctic climate records during the last deglaciation. *Nature Geoscience*, *4*(1), 46-49. Doi: https://doi.org/10.1038/ngeo1026

Stern, C. R., de Porras, M. E., & Maldonado, A. (2015). Tephrochronology of the upper Río Cisnes valley (44°S), southern Chile. *Andean geology*, *42*(2), 173-189. Doi: https://doi.org/10.5027/andgeoV42n2-a02

Stone, J. O. (2000). Air pressure and cosmogenic isotope production. *Journal of Geophysical Research: Solid Earth*, 105(B10), 23753-23759. Doi: https://doi.org/10.1029/2000jb900181

Strand, P. D., Schaefer, J. M., Putnam, A. E., Denton, G. H., Barrell, D. J., Koffman, T. N., & Schwartz, R. (2019). Millennial-scale pulsebeat of glaciation in the Southern Alps of New Zealand. *Quaternary Science Reviews*, *220*, 165-177. Doi: https://doi.org/10.1016/j.quascirev.2019.07.022

Sugden, D. E., Bentley, M. J., Fogwill, C. J., Hulton, N. R. J., McCulloch, R. D., & Purves, R. S. (2005). Late-glacial glacier events in southernmost south america: a blend of 'northern' and

'southern' hemispheric climatic signals?. *Geografiska Annaler: Series A, Physical Geography*, *87*(2), 273-288. Doi: https://doi.org/10.1111/j.0435-3676.2005.00259.x

Sugden, D.E., McCulloch, R.D., Bory, A.J.M., and Hein, A.S. (2009). Influence of Patagonian glaciers on Antarctic dust deposition during the last glacial period. *Nature Geoscience*. v. 2(4), p. 281-285. Doi: https://doi.org/10.1038/ngeo474.

Sun, Y., Xu, X., Zhang, L., Liu, J., Zhang, X., Li, J., & Pan, B. (2020). Numerical Reconstruction of Three Holocene Glacial Events in Qiangyong Valley, Southern Tibetan Plateau and Their Implication for Holocene Climate Changes. *Water*, 12(11), 3205. Doi: https://doi.org/10.3390/w12113205

Sutherland, J. L., Carrivick, J. L., Gandy, N., Shulmeister, J., Quincey, D. J., & Cornford, S. L. (2020). Proglacial lakes control glacier geometry and behavior during recession. *Geophysical Research Letters*, 47, e2020GL088865. Doi: https://doi.org/10.1029/2020gl088865.

Sylwan, C., Beraza, L., and Caselli, A. (1991). Magnetoestratigrafi a de la secuencia morenica en el valle del Lago Pueyrredon, provincia de Santa Cruz. *Revista de la Asociación Geológica Argentina*, v. 46, p. 235–238.

Tarolli, P., & Mudd, S. M. (2019). Remote Sensing of Geomorphology (Vol. 23). *Elsevier*.

Terrizzano, C. M., Morabito, E. G., Christl, M., Likerman, J., Tobal, J., Yamin, M., & Zech, R. (2017) Climatic and Tectonic forcing on alluvial fans in the Southern Central Andes. *Quaternary science reviews*, v. 172, p. 131-141. Doi: https://doi.org/10.1016/j.quascirev.2017.08.002.

Thomsen, K.J., Murray, A.S., Jain, M., Bøtter-Jensen, L. (2008). Laboratory fading rates of various luminescence signals from feldspar-rich sediment extracts. *Radiation measurements*, 43(9-10), 1474-1486. Doi : https://doi.org/10.1016/j.radmeas.2008.06.002

Thomson, S. N., & Herve, F. (2002). New time constraints for the age of metamorphism at the ancestral Pacific Gondwana margin of southern Chile (42-52 S). *Revista geológica de Chile*, *29*(2), 255-271. Doi: https://doi.org/10.4067/S0716-02082002000200007

Thorndycraft, V. R., Bendle, J. M., Benito, G., Davies, B. J., Sancho, C., Palmer, A. P., Fabel, D., Medialdea, A., Martin, J. R. (2019). Glacial lake evolution and Atlantic-Pacific drainage reversals during deglaciation of the Patagonian Ice Sheet. *Quaternary Science Reviews*, 203, 102-127. Doi: https://doi.org/10.1016/J.QUASCIREV.2018.10.036

Toggweiler, J. R. (2009). Shifting westerlies. Science, v. 323(5920), p. 1434-1435, doi: DOI: https://doi.org/10.1126/science.1169823.

Toucanne, S., Zaragosi, S., Bourillet, J.F., Cremer, M., Eynaud, F.,Van Vliet-Lanoe, B., Penaud, A., Fontanier, C., Turon, J.L., Cortijo, E., and Gibbard, P.L. (2009). Timing of massive "Fleuve Manche" discharges over the last 350 kyr: insights into the European ice-sheet oscillations and the European drainage network from MIS 10 to 2. *Quaternary Science Reviews*. v. 28, p. 1238–1256. Doi: https://doi.org/10.1016/j.quascirev.2009.01.006.

Trauerstein, M., Lowick, S.E., Preusser, F., Schlunegger, F. (2014). Small aliquot and single-grain IRSL and post-IR IRSL dating of fluvial and alluvial sediments from the Pativilca valley, Peru. *Quaternary Geochronology*, 22, 163-174. Doi : https://doi.org/10.1016/j.quageo.2013.12.004

Trombotto, D. (2008) Geocryology of southern South America, in Rabassa, J., ed., The late Cenozoic of Patagonia and Tierra del Fuego: Developments in Quaternary Sciences Volume 11: Amsterdam, Elsevier, p. 255–268, doi: https://doi.org/10.1016/S1571-0866(07)10012-9.

Turner, K. J., Fogwill, C. J., McCulloch, R. D., & Sugden, D. E. (2005). Deglaciation of the eastern flank of the North Patagonian Icefield and associated continental-scale lake diversions. Geografiska Annaler: Series A, Physical Geography, 87(2), 363-374. Doi: https://doi.org/10.1111/j.0435-3676.2005.00263.x

Van Daele, M., Bertrand, S., Meyer, I., Moernaut, J., Vandoorne, W., Siani, G., Tanghe, N., Ghazoui, Z., Pino, M., Urrutia, R., De Batist, M. (2016). Late Quaternary evolution of Lago Castor (Chile, 45.6°S): Timing of the deglaciation in northern Patagonia and evolution of the southern westerlies during the last 17 kyr. *Quaternary Science Reviews*, *133*, 130-146. Doi: https://doi.org/10.1016/j.quascirev.2015.12.021

Vilanova, I., Moreno, P. I., Miranda, C. G., & Villa-Martínez, R. P. (2019). The last glacial termination in the Coyhaique sector of central Patagonia. *Quaternary Science Reviews*, *224*, 105976. Doi: https://doi.org/10.1016/j.quascirev.2019.105976

Villa-Martínez, R., Moreno, P. I., & Valenzuela, M. A. (2012). Deglacial and postglacial vegetation changes on the eastern slopes of the central Patagonian Andes (47 S). *Quaternary Science Reviews*, 32, 86-99. Doi: https://doi.org/10.1016/j.quascirev.2011.11.008

Vivian, R. (1967). Le glacier Blanc. *Revue de géographie alpine*, *55*(4), 729-732. URL: https://www.persee.fr/doc/rga_0035-1121_1967_num_55_4_3351

Vivian, R., & Volle, L. (1967). Le glacier d'Arsine. *Revue de Géographie Alpine*, *55*(2), 396-400. URL: https://www.persee.fr/doc/rga_0035-1121_1967_num_55_2_3325

Ward, G. K., & Wilson, S. R. (1978). Procedures for comparing and combining radiocarbon age determinations: a critique. *Archaeometry*, 20(1), 19-31. Doi: https://doi.org/10.1111/j.1475-4754.1978.tb00208.x

WAIS Divide Project Members. (2013). Onset of deglacial warming in West Antarctica driven by local orbital forcing. *Nature*, *500*(7463), 440-444. Doi: https://doi.org/10.1038/nature12376

WAIS Divide Project Members. (2015). Precise interpolar phasing of abrupt climate change during the last ice age. *Nature*, *520*(7549), 661. Doi: https://doi.org/10.1038/nature14401

Wallace, J. M., & Hobbs, P. V. (2006). Atmospheric science: an introductory survey (Vol. 92). *Elsevier*.

Wallinga, J. (2002). On the detection of OSL age overestimation using single-aliquot techniques. *Geochronometria: Journal on Methods & Applications of Absolute Chronology*, *21*.

Weertman, J. (1957). On the sliding of glaciers. *Journal of glaciology*, *3*(21), 33-38.

Wendt, I., & Carl, C. (1991). The statistical distribution of the mean squared weighted deviation. *Chemical Geology: Isotope Geoscience Section*, *86*(4), 275-285. Doi: https://doi.org/10.1016/0168-9622(91)90010-T

White, T.S., Bridgland, D.R., Howard, A.J., Westaway, R., and White, M.J., 2010, Evidence from the Trent terrace archive, Lin- colnshire, UK, for lowland glaciation of Britain during the Middle and Late Pleistocene: Proceedings ofthe Geologists' Association, v. 121, p. 141–153, doi: https://doi.org/10.1016/j.pgeola.2010.05.001.

White, T.S., Bridgland, D.R., Westaway, R., and Straw, A., 2017, Evidence for late Middle Pleistocene glaciation of the British margin of the southern North Sea: Journal of Quaternary Science, v. 32(2), p. 261-275, doi: https://doi.org/10.1002/jqs.2826.

Whittaker, T. E., Hendy, C. H., & Hellstrom, J. C. (2011). Abrupt millennial-scale changes in intensity of Southern Hemisphere westerly winds during marine isotope stages 2–4. *Geology*, *39*(5), 455-458. Doi: https://doi.org/10.1130/G31827.1

Wickert, A. D. (2015). Open-source modular solutions for flexural isostasy: gFlex v1. 0. Geoscientific Model Development Discussions, 8(6). Doi: https://doi.org/10.5194/gmd-9-997-2016

Wijngaard, R. R., Steiner, J. F., Kraaijenbrink, P. D., Klug, C., Adhikari, S., Banerjee, A., Pellicciotti, F., van Beek, L. P. H., Bierkens, M. F. P., Lutz, A. F., Immerzeel, W. W. (2019). Modeling the Response of the Langtang Glacier and the Hintereisferner to a Changing Climate Since the Little Ice Age. *Frontiers in Earth Science*, 7, 143. Doi: https://doi.org/10.3389/feart.2019.00143

Zech, J., Terrizzano, C. M., Garcia Morabito, E., Veit, H., and Zech, R. (2017). Timing and extent of late Pleistocene glaciation in the arid Central Andes of Argentina and Chile (22-41 S). *Cuadernos de Investigación Geográphica*, v. 43 (2), p. 697-718, doi: https://doi.org/10.18172/cig.3235.

Appendix

|



7.1 Chapter 2 supplementary materials

Geomorphological mapping through polyline and polygon shapefile digitization was conducted using ArcGIS 10.6 software. Final map and figure editing was produced using Adobe Illustrator CC 2020 and Inkscape 0.92.4.

The study area presented within this map is located between these coordinates:
70°44'0"W - 71°40'0"W ; 43°24'0"S - 44°2'0"S

The data produced for this map are freely available online, as long as original publication is cited when used and/or referred to. This includes the original geomorphological map: which can be downloaded under this link:
https://www.tandfonline.com/doi/suppl/10.1080/17445647.2020.1794990?scroll=top
It also includes all twenty-six shapefiles (.shp) necessary for visualising and analysing the data on a geographical information system such as ArcGIS software. The data are deposited in a Mendeley Data online repository, accessible using this Doi:
https://data.mendeley.com/datasets/c2hy8rkbyd/1.
This data comprises 26 polyline and polygon shapefiles georeferenced in the WGS84 geographic reference coordinate system. Multi-polygon shapefiles have been merged to enable better visualisation. For optimum visualisation of all features mapped using a geographical information software we recommend to symbolise all polygon layers without outlines and to modify the layer order of the shapefiles according to the numbering system (1 to 25) provided in the shapefile folder and file names: with 01 representing the bottom layer and 25 the topmost layer. We here provide a table with RGB colour recommendations for each shapefile for better visualisation (see table below).

Chapter 2 Supplementary Table 1. RGB colour recommendations for shapefile visualisation

Shapefile	R	G	B	Transparency (%)
01_Atlantic_Pacific_drainage_divide	85	255	0	0
02_Boglands	140	212	0	50
03_Modern_Río_Corcovado_floodplain	153	219	255	10
04_Kettle_kame_topography	255	255	190	10
05_Moraine_complexes	232	190	255	0
06_Moraine_ridges	255	85	0	0
07_Hummocky_ridges	197	0	255	0
08_Hummocks	197	0	255	0
09_Proglacial_outwash_plains	255	211	127	0
10_Lakes_and_water_bodies	0	112	255	0
11_Kettle_holes	0	168	132	0
12_Glaciolacustrine_deposits	156	156	156	0
13_Raised_deltas	199	204	150	0
14_Palaeo_shorelines	0	219	197	0
15_Ice_moulded_bedrock	225	225	225	0
16_Drumlinoid_forms	115	0	76	0
17_Glacial_lineations	168	87	20	0
18_Rotational_slumps_or_landslides	247	89	112	10
19_Meltwater_channels_(30m_wide_or_above)	107	117	196	0
20_Meltwater_channels_(less_than_30m_wide)	143	181	235	0
21_Fluvial_incision_scarps	0	0	0	0
22_Alluvial_fans	168	112	0	0
23_Possible_GLOF_deposits	0	214	255	0
24_Contemporary_channels_and_creeks	0	92	230	0
25_Empty_cirques	112	127	140	0

7.2 Chapter 3 supplementary materials

7.2.1 Study site former glaciolacustrine phases: additional geomorphological evidence and interpretation

7.2.1.1 Glaciolacustrine phase one

Handheld GPS elevation transects revealed the preservation of at least five notched terraces running parallel to each other over tens of kilometres on the northeastern, eastern and southern slopes of the palaeolake basin. These features range in elevation from 910 ± 5 m to 990 ± 5 m, where the most prominent platform lies, and were interpreted as wave-cut palaeo-shorelines (SM Table 1). On the southwestern edge of the palaeolake basin, a well-preserved, low-gradient (mean slope: 0.8°) outwash plain deposit progrades from both arcuate terminal moraines of the RC III complex to the north and Lago Palena/General Vintter terminal moraines to the west (43°51'S, 71°16'W). This outwash plain lies at elevations of between ~980 and ~965 m, and appears to be raised ~100 m above the modern valley floor (880 m). It was thus interpreted as a raised outwash deposit formed by glaciofluvial sediment aggradation during proglacial lake residence. On the palaeolake basin's southern slopes, at 43°50'59"S, 71°11'13"W, the palaeo-shorelines bend southward into a 230 m-wide gorge, which acts as a breach through RC II glaciogenic deposits. This breach reaches a maximum basal elevation of 980 m, leads southward to a 100 m-wide palaeo meltwater channel incised into RC II-related outwash deposits, and is indicative of southeast-directed palaeolake drainage towards the contemporary Río Ñirihuau O Seco. It was interpreted as the main proglacial lake spillway. At this location, the RC II deposits mark the local Atlantic-Pacific drainage divide, and thus represent the southeastern limit of the RC valley over-deepening.

7.2.1.2 Glaciolacustrine phase two

The second glaciolacustrine phase identified is associated with the retreat of the RC and RH outlet glaciers from intermediate LGM margins into their respective over-deepened, westward-dipping valleys. Remote sensing and field observations uncovered the relatively widespread occurrence of preserved palaeo-shorelines nested at the elevation of ~790-800 m in both the RC and RH valleys (Leger *et al.*, 2020, main map). In the RC valley, the palaeo-shoreline can be discerned across the RC eastern sub-basin, notched on the ice-proximal slopes of the RC V moraine complex (Chapter 3 SM

Table 1). Such evidence suggests that initial lake formation for this second phase occurred following ice-front retreat from the RC VI and RC V moraines. Remote sensing analysis reveals that this basin is characterised by a low gradient bed (~0.5° average slope), and the noticeable occurrence of incised, white to light grey deposits interpreted and mapped as glaciolacustrine sediment accumulations (Leger et al., 2020; nearby 43°42'S, 71°16'W). We propose that the 790 m proglacial lake's main spillway occurred at 43°42'S, 71°13'W, where the prominent shoreline bends eastwards into a 200 m-wide gorge breaching RC V and RC IV moraine complexes, leading to the Atlantic/Pacific drainage divide and a large, 215 m-wide palaeo-channel heading northward, towards Río Tecka (SM Table 1).

~10 km to the northwest, in the more topographically-constrained RC trough, isolated patches of the 790 m palaeo-shoreline can be discerned on the eastern hillslope (Figure 3.5a), while evidence of this shoreline disappears north of 43°37'S. This suggests that this proglacial lake might have expanded and persisted during the early stages of local deglaciation, when the RC calving front progressively retreated northward. This is supported by the finding of fine, sand to clay-sized sediment deposits exposed through sections of the valley's main road (RP44), at elevations of 686 m (43°42'7.2"S), 709 m (43°42'15.2"S) and 720 m (43°42'11.7"S). In each cases, these exposures exhibit laminations and varves, represent the topmost unit below soil, and were interpreted as glaciolacustrine deposits. Rippled sands from the 709 m exposure and varves from the 686 m exposure were sampled for OSL dating (see chapter 3 main text).

In the RH valley, field mapping revealed the instance of a prominent bench running over tens of kilometres on the southern valley slopes, perched at an elevation of ~790 m, and nested on the ice-proximal side of the innermost preserved terminal RH moraine, forming a clear step 15 m below the moraine crest (Figure 3.2, 3.4c, d). This landform was interpreted as a former proglacial lake shoreline and was sampled for TCN dating using polished granite surface cobbles (Figure 3.4d, e). DEM elevation profiles and approximate palaeo-surface reconstructions based on hillside and backing cliff slope angles revealed, on average, a maximum shoreline excavation of ~4 m around the location of sampling. Risk of shoreline post-formation burial is regarded as minimal due to the limited height (<15m) and slope gradient (7°) of overlying moraine (Figure 3.4d). This landform thus indicates the formation of a separate, isolated proglacial lake in the RH valley, formed as the RH glacier retreated westward. However, the comparable elevation of shorelines in both the RC and RH valleys suggests that both RC and RH proglacial lakes could have been connected during phase two, following northward/westward retreat of both ice-fronts beyond Corcovado (43°32'S, 71°27'W). The main spillway draining the RH palaeolake towards the Atlantic occurs at 43°31'42.S, 71°13'26.W, where a central, 130 m-wide breach through the innermost RH moraine complex reaches a maximum basal

elevation of 780 m (Figure 3.6b). The breach leads to a 250 m-wide southward-directed palaeo-channel, which reaches the Atlantic/Pacific drainage divide 2.5 km to the southeast and heads towards Río Tecka.

7.2.1.3 Glaciolacustrine phase three

The eastern, windier hillslope of the RC valley displays a second, easily discernible platform cutting through the entire north-to-south extent (over 15 km) of the 16-19° sloped hillside, at the elevation of ~680 m (Figure 3.4a, 3.6c). It was studied in the field, interpreted as a wave-cut proglacial lake shoreline, and was sampled for TCN dating using polished granite surface cobbles (Figure 3.4b, 3.6c). Twenty-seven terrace cross-section elevation profiles were drawn from DEM in locations exhibiting a preserved platform. They revealed, on average, a maximum shoreline excavation of ~6 m. At the location of sampling, maximum excavation appears to be closer to 7 m. This shoreline roughly matches the elevations of numerous other shorelines, raised deltas and raised outwash deposits located in the RC, RH, RF and RP valleys (Chapter 3 SM Table 1). Such geomorphic evidences suggest the formation of a geographically widespread proglacial lake connecting all valleys of the studied region during the last glacial termination (Figure 3.9g). This is further evidenced by field observations of uppermost (below soil) units of fine, sand to clay-sized and occasionally laminated, varved sediments exposed along several road-cut sections across the RC, RP and RF valley floors (Chapter 3 SM Table 1). However, observed elevations of different landforms associated with glaciolacustrine phase three fluctuate between 675 and 695 m. We attribute this variation to a combination of 1) DEM and GPS vertical measurement error, and 2) asymmetrical local isostatic rebound and tectonic activity since landform stabilization. Subsequently, we interpret this third glaciolacustrine phase to have started with the ~100 m lake level drop from 790 m (phase two) to ~680 m (Figure 3.9f).

We argue that this proglacial lake lowering to phase three is likely due to the continued northward, westward and southward retreats of the RC, RH and RF ice fronts into the RP valley during the last glacial termination. In doing so, the northern RF ice-dam was breached, and proglacial lake waters from both RC and RH valleys were able to flow northward into the narrow, low-gradient (average slope: 0.5°) and over-deepened RF valley. By modelling a hypothetical ice front of maximum eastward extent while enabling proglacial lake connection of all three RC, RH and RF valleys, the reconstructed 680 m lake approximates 266 km^2 in surface area and 32.7 km^3 in volume (computed from DEM; Figure 3.9f).

In the RF valley, the lowest potential spillway towards the northeast lies at approximately 750 m. Such spillway would enable waters to drain towards contemporary Lago Rosario (aerial cover; 9.6 km^2), which in turn drains towards the Trevelin basin to the north, and the Pacific Ocean via Río Futaleufú. Work by Andrada de Palomera (2002) and Martínez *et al.* (2011) suggest the former occurrence of yet another large proglacial lake in the Trevelin and Esquel over-deepened valleys following local glacier recession, with a lowest possible spillway nested at ~650 m through terminal moraines located east of Laguna Suñica (43°05'57"S, 71°02'48"W). We thus propose, during glaciolacustrine phase three, a complex hypothetical network of connected, extensive palaeolakes enabling meltwater drainage from the former RC, RH and RF-connected lake (~680 m) into the current Lago Rosario (665m), and into a former Trevelin basin proglacial lake (~650m), which eventually spilled eastward towards Río Tecka and the Atlantic Ocean. The RF palaeolake-connection hypothesis is further evidenced by the ~680 m elevation of raised deltas and palaeo-shorelines observed in the RF valley, and the lack of raised landforms above this elevation (Chapter 3 SM Table 1). However, in modern times, such lake connection would be impossible due to 60-70 m of localised excess land surface in the RF valley impeding a ~680 m lake connection towards Lago Rosario. We here hypothesise that this land-elevation mismatch can be attributed to the accretion of a large (~5 km^2) arcuate alluvial fan into a narrow col located between the RF and Lago Rosario basins (43°17"S; 71°24"W).

The alluvial fan is formed at the bottom of the steep RF upland catchment, where the RF channel discharges water and sediment from the mountain front to the main, lower-gradient valley. It exhibits an average radial slope gradient of 1.95°, and a maximum radial length of 4.5 km towards the south-west. The upper mountain catchment displays 900 m of vertical relief, a maximum elevation of ~1800 m, and some geomorphological evidence of slope instabilities. Our geomorphological mapping reveals small, empty cirques around the catchment summit indicating the former occurrence of topographically constrained mountain glaciers. No sedimentological analyses were conducted due to a lack of access to fan sediment exposures. Using 70 m of material aggradation and bracketing ages of 16.3 ± 0.8 ka (minimum age for phase three lake lowering, Figure 3.8) and 19.9 ka ± 1.1 ka (RC VII age, onset of glacial retreat in RC valley, Figure 3.8) as the potential onsets of alluvial fan accretion, we obtain sedimentation rates ranging between 3.4 and 4.5 mm $.yr^{-1}$. Such high sedimentation rates suggest a dominating contribution of infrequent, high-magnitude flood and/or mass-wasting events to fan aggradation (Blair & McPherson, 2009). Possible events of sporadic high-material/water discharge include rapid spring snow/glacial melt and non-cohesive sediment-gravity flows caused by 1) moraine and/or ice dam failure or 2) large-scale slope failure such as rock-slope failures, rotational slumps and other landslides, sometimes triggered during earthquakes. The latter

hypothesis could possibly be supported by the observation (from DEM) of a large and heavily incised oversteepening resembling a series of steep scarps running for ~4 km across the RF upper catchment, with upper break-in-slopes nested between 1350 m and 1500 m. Such slope failure events are not unusual on tectonically active and formerly glaciated, steep mountain slopes with substantial volumes of poorly sorted till and lateral moraine deposits mantling the catchments (Blair, 2009).

For the ~680 m proglacial lake to exploit a lower spillway col and drain further, the western Palena ice dam had to retreat 45 km west of Corcovado, towards the eastern foothills of Macizo Nevado (Figure 3.9g). We expect such extensive retreat to cause the disintegration of the local PIS into smaller, separate mountain ice caps, causing ice-free conditions in low-lying (100-150 m) local valley floors, and enabling the ~680 m proglacial lake to drain westward between or beneath shrinking ice-masses (Figure 3.9h). Such event would have caused proglacial lake drainage reversal from the Atlantic to the Pacific Ocean (Figure 3.9h), similarly to other over-deepened eastern Patagonian valleys (Thorndycraft *et al*., 2019). Depending on the configuration and extent of local glaciers at the time of ice-dam breach, glaciolacustrine waters could have either drained westward using; 1) a northwest-directed pathway towards the modern Lago Yelcho (115 km^2), elevated at ~40 m, or 2) a valley narrowing (~2 km-wide) located to the south of Macizo Nevado (43°43'S; 72°13'W) and exploited by the modern Río Palena. The latter drainage route heads south using the prominent LOFZ valley to eventually drain into Golfo Corcovado at Puerto Rául Marín Balmaceda (43°46'S; 72°57'W). Resolving the former pathways of final lake drainage would require more detailed sedimentological and geomorphological investigations in these regions. Such work could also reveal whether the Atlantic/Pacific drainage reversal was a progressive or catastrophic event in this region. In both cases, the ~680 m proglacial lake would have drained into the Golfo Corcovado. Using an approximate PIS configuration associated with a maximum proglacial lake extent prior to western ice-dam breach, the reconstructed 680 m proglacial lake approximates 950 km^2 in area and 273 km^3 in volume (Figure 3.9g, computed from DEM). These estimates yield significant uncertainties, however, as they were computed using a hypothetical ice-dam location near the foothills of Macizo Nevado (Figure 3.9g), under the assumption that any further westward retreat of the ice front would likely cause ice-dam breach.

Chapter 3 Supplementary Table 1: Summary of geomorphological and sedimentological field-based evidence for former glaciolacustrine activity across the study site

Feature type	Latitude (DD)	Longitude (DD)	Valley / basin	Elevation (m a.s.l)	Feature geomorphological / sedimentological description	Interpretation & hypothesised geomorphological significance	Glaciolacustrine phase-association	Suggested formation / deposition age
Landform	-43.793199	-71.234376	RC valley		Two raised terraces nested on ice-distal slope of RC III moraine.	Interpreted as raised outwash deposits associated with RC III meltwater drainage into proglacial lake, representing two distinc lake levels.	Phase 1	≥26.4 ± 1.4 ka
Landform	-43.930778	-71.166394	RC valley	~910	Prominent terrace protruding from surrounding terrain, with surface clasts dominated by sands and rounded to subrounded pebbles.	Interpreted as beach deposit drapping a wave-cut platform associated with former proglacial lake surface.	Phase 1	>22.4 ± 1.2 ka and < 26.6 ka
Landform	-43.794059	-71.234099	RC valley	~960	Prominent terrace running across the ice-distal slope of the RC3 moraine at a single elevation.	Interpreted as palaeo-shoreline, suggests stabilisation of former proglacial lake at ~960 m.	Phase 1	≥26.4 ± 1.4 ka
Landform	-43.823247	-71.163322	RC valley	~960	Prominent terrace feature nested on the eastern slopes of the RC western sub-basin at single evelation.	Interpreted as palaeo-shoreline, suggests a former proglacial lake stabilized at ~960 m.	Phase 1	≥26.4 ± 1.4 ka
Landform	-43.824091	-71.154785	RC valley	~990	Prominent terrace feature nested on the northeastern slopes of the RC western sub-basin at single evelation.	Interpreted as palaeo-shoreline, suggests a former proglacial lake stabilized at ~990 m.	Phase 1	≥26.4 ± 1.4 ka
Landform	-43.618186	-71.381267	RC valley	~790	Terrace feature running at single elevation across the eastern mountain slope of the RC trough.	Interpreted as palaeo-shoreline, suggests a former proglacial lake stabilised at ~790 m.	Phase 2	> 19.0 ± 0.9 ka < 21.7 ± 0.9 ka
Landform	-43.731778	-71.258657	RC, northern sub-basin	~790	Series of terraces running across the northern slopes of the mid-valley 300 m-high bedrock step separating the northern and southern RC sub-basins.	Interpreted as palaeo-shorelines, suggests a former proglacial lake stabilised at ~790 m.	Phase 2	> 19.0 ± 0.9 ka < 21.7 ± 0.9 ka
Landform	-43.704880	-71.225869	RC, northern sub-basin	~790	200 m-wide and 20 m-deep gorge cutting through RC V and RC IV moraine complexes, with a maximum basal elevation of ~795 m, and associated with a northward bending and confluence of mapped palaeo-shorelines.	Interpreted as former proglacial lake spillway opening, indicating the location, elevation, and downflow direction of proglacial lacustrine water drainage.	Phase 2	> 19.0 ± 0.9 ka < 21.7 ± 0.9 ka
Lanform	-43.746482	-71.395796	RC valley	~790-800	Low-gradient fan-shaped terrace prograding from the mouth of the Río Comisario tributary river, "raised" as further incised by modern river located ~30 m below terrace.	Elevation of raised terrace matches former elevation of RC proglacial lake during phase two (~790 m). This landform was thus possibly formed as a fan deposit when the Río Comisario flowed into the proglacial lake and could be interpreted as a raised delta. Alternatively, the matching elevation could be a coincidence and this landform could simply relate to fluvial and/or glaciofluvial terrace aggradation.	Phase 2	> 19.0 ± 0.9 ka < 21.7 ± 0.9 ka

Landform	-43.73818	-71.223582	RC, northern sub-basin	~790	Series of large terraces with clear incision scarps nested on the northern slopes of the RC mid-valley bedrock step: where the Río Corcovado flows out of narrow gorge to reach the low-gradient eastern sub-basin. The teraces are raised by ~50 m above modern river and located on both sides of the channel.	Those fluvial terraces match the elevation of former RC proglacial lake during phase 2 (790-800 m) and are raised by up to 50 m. These landforms were thus possibly formed as fan deposits when the Río Corcovado flowed into the 790m proglacial lake located in the eastern sub-basin. They could potentially be interpreted as raised deltas.	Phase 2	> 19.0 ± 0.9 ka < 21.7 ± 0.9 ka
Landform	-43.697673	-71.216309	RC, northern sub-basin	~800	Low-gradient, 200 m wide palaeo-channel located directly to the northeast of spillway opening associated with proglacial lake phase 2, with a basal elevation of ~800 m and gently prograding towards the north: and Río Tecka.	This palaeo-channel can be linked to the location and elevation of the proglaical lake phase 2 spillway opening: and represents a substantially larger discharge regime than modern runoff can enable (by several orders of magnitude). We thus interpret this landform as the location of glaciolactustrine water drainage during proglacial lake phase 2.	Phase 2	> 19.0 ± 0.9 ka < 21.7 ± 0.9 ka
Landform	-43.728158	-71.397497	RC valley	~790	Terrace feature running at single elevation across the northern, ice-proximal slope of the RCVII moraine. The notched platform was revealed through DEM cross-moraine elevation profiles and demonstrates an average excavation height of ~7 m.	Interpreted as palaeo-shoreline, sugests stabilisation of former proglacial lake at ~790 m in the RC valley	Phase 2	> 19.0 ± 0.9 ka < 21.7 ± 0.9 ka
Sediment exposure	-43.703130	-71.41177	RC valley	709	Section with top-most (below soil) unit of undistrubed and homogeneous sands with cross-beddings and asymmetrical ripples. 1 m below surface, sands make place for homogeneous laminated and alternating silt and clay sediment layers (varves)	We interpret these sediments as glaciolacustrine varve deposits overlaid by shallow lake beach deposits.	Phase 2	> 19.0 ± 0.9 ka < 21.7 ± 0.9 ka OSL age: 34.9 ± 2.9 ka
Sediment exposure	-43.702222	-71.411556	RC valley	690	Road-cut section with top-most (below soil) unit (2 m tall exposure) of undisturbed, homogeneous laminated and alternating silt and clay sediment layers (varves).	We interpret these sediments as glaciolacustrine varve deposits.	Phase 2	> 19.0 ± 0.9 ka < 21.7 ± 0.9 ka OSL age: 52.1 ± 4.4 ka
Sediment exposure	-43.704190	-71.411740	RC valley	720	Road-cut section with top-most (below soil) unit (1 m tall exposure) of compacted and laminated sands and clay sediment layers	We interpret these sediments as shallow-water glaciolacustrine deposits.	Phase 2	> 19.0 ± 0.9 ka < 21.7 ± 0.9 ka
Landform	-43.519162	-71.219524	RH valley	~790	Very prominent terrace running at single elevation across the ice-proximal slope of the innermost preserved moraine complex of the RH valley. The terrace is preserved and continuous for over five km	Interpreted as palaeo-shoreline, suggests stabilisation of former proglacial lake at ~790 m in the RH valley	Phase 2: RH and RC connected proglacial lake?	> 19.0 ± 0.9 ka < 21.7 ± 0.9 ka
Landform	-43.514188	-71.305366	RH valley	~790	Very prominent terrace running at single elevation across the southern slopes of the RH valley. The terrace is preserved and continuous for over eight km	Interpreted as palaeo-shoreline, suggests stabilisation of former proglacial lake at ~790 m in the RH valley	Phase 2: RH and RC connected proglacial lake?	> 19.0 ± 0.9 ka < 21.7 ± 0.9 ka

Landform / deposit	-43.679770	-71.428771	RC valley	~740 - 690	Fan shaped, 1.1 km2 platform prograding eastward (average slope: 3°) from the mouth of the Río Poncho Moro western tributary and towards the RC valley centre. The plain deposit displays well-preserved surface braided channels visible from imagery and is located on the southern side of the modern tributary river. The plain is raised ~230 m above the modern RC valley floor and its lower, eastern margin matches the phase three proglacial lake elevation of ~680 m.	We interpret this fan-shaped platform as a "raised delta" formed by fluvial depostion related to the Río Poncho Moro tributary drainage into the former ~680 m proglacial lake residing in the RC trough.	Phase 3: RC, RP and RF connected proglacial lake	> 16.3 ± 0.3 ka < 19.0 ± 0.9 ka
Landform	-43.572829	-71.412454	RC valley	~680	The most prominent terrace feature observed at the field site. The well-preserved, easily discernable terrace is nested at the single elevation of ~680 m on the eastern slope of the RC valley trough, and runs along the valley side discontinuously for ~15 km. Cross-platform DEM elevation profiles reveal an average excavation height of ~6 m.	Interpreted as palaeo-shoreline, suggests stabilisation of former proglacial lake at ~680 m and causing significant wave erosion and platform notching on its former, wind-exposed eastern shore	Phase 3: RC, RP and RF connected proglacial lake	> 16.3 ± 0.3 ka < 19.0 ± 0.9 ka
Landform / deposit	-43.653278	-71.437611	RC valley	~685	Terrace feature runing along the western slope of the RC valley at the maximum elevation of proglacial lake phase three (~680 m). Less prominent than the eastern palaeo-shoreline, this platform was observed on the field at one particular location. The platform is there characterized by a low relief (1-2 m), gently curving ridge with sand- and gravel-sized surface sediments resembling a beach deposit.	Interpreted as palaeo-shoreline, indicating stabilisation of former proglacial lake at ~680 m and causing beach deposition on its former western shore	Phase 3: RC, RP and RF connected proglacial lake	> 16.3 ± 0.3 ka < 19.0 ± 0.9 ka
Sediment exposure	-43.525710	-71.510960	RC valley	393	Road-cut section with top-most (below soil) unit of homogeneous laminated and alternating silt and clay sediment layers (varves).	We interpret these sediments as glaciolacustrine varve deposits.	Phase 3: RC, RP and RF connected proglacial lake	> 16.3 ± 0.3 ka < 19.0 ± 0.9 ka
Sediment exposure	-43.697306	-71.406222	RC valley	544	Quarried section with top-most (below soil) unit (3.5 m of exposure) of homogeneous laminated and alternating silt and clay sediment layers (varves).	We interpret these sediments as glaciolacustrine varve deposits.	Phase 3: RC, RP and RF connected proglacial lake	> 16.3 ± 0.3 ka < 19.0 ± 0.9 ka OSL age: 65.4 ± 7.1 ka
Sediment exposure	-43.534590	-71.486460	RC valley	414	Quarried section with top-most (below soil) 1.7 m thick unit of matrix-supported silt and clay sediments with occasional alternating laminations (varves). The unit also features some embedded larger sub-angular and unsorted gravel, cobbles and boulders of varied lithologies.	We interpret these sediments as glaciolacustrine varve deposits interspersed with ice-rafted debris	Phase 3: RC, RP and RF connected proglacial lake	> 16.3 ± 0.3 ka < 19.0 ± 0.9 ka

Landform / deposit	-43.687121	-71.704755	Río Tigre valley	~710 - 690	Fan-shaped, flat outwash plain with evidence of glaciofluvial deposition (sands and gravel with large polished rounded cobbles, well sorted sediments) located at the mouth of the Río Tigre tributary valley, to the south of the RP valley, and raised 50 m above the modern river elevation. The plain elevation is approximately 10-15 m above the reconstructed maximum elevation of proglacial lake phase three. The plain's northern margin leads to steep, heavily incised slopes displaying a grey/white coloration on imagery suggestive of softer, perhaps glaciolacustrine sediments.	Interpreted as a raised outwash surface/raised delta deposited by glacial meltwater from the Río Tigre flowing northward towards the RP valley during residence of the ~680 m proglacial lake.	Phase 3: RC, RP and RF connected proglacial lake	> 16.3 ± 0.3 ka < 19.0 ± 0.9 ka
Landform	-43.333880	-71.488080	RF valley	~680 - 700	Two raised terraces notched on northwestern slope of RF valley.	Interpreted as palaeo-shorelines, suggests stabilisation of former proglacial lake at ~700-680 m in the narrow RF valley.	Phase 3: RC, RP and RF connected proglacial lake	> 16.3 ± 0.3 ka < 19.0 ± 0.9 ka
Landform	-43.353210	-71.503900	RF valley	~690 - 700	Prominent, well preserved terrace running across the southeastern slope of the RF valley at single elevation for approximately 1 km. Approximate feature elevation was measured using a Laser Range Finder.	Interpreted as palaeo-shoreline, suggests stabilisation of former proglacial lake at ~700-680 m in the narrow RF valley.	Phase 3: RC, RP and RF connected proglacial lake	> 16.3 ± 0.3 ka < 19.0 ± 0.9 ka
Landform / deposit	-43.326520	-71.479690	RF valley	~680 - 700	Two prominent, well preserved, fan-shaped terraces prograding from the mouth of a southern tributary channel of the Río Frío (name unknown) and towards the RF valley. The two terraces are raised 15-20 m above the modern tributary.	We interpret these fan-shaped terraces as "raised deltas" formed by fluvial depostion related to a southern tributary of the RF while draining into the former ~680 m proglacial lake residing in the narrow and shallow RF trough.	Phase 3: RC, RP and RF connected proglacial lake	> 16.3 ± 0.3 ka < 19.0 ± 0.9 ka
Landform	-43.369300	-71.512290	RF valley	683	Prominent, well preserved terrace running across the southeastern slope of the RF valley at single elevation. Lanform proximity to road enabled platform elevation GPS measurement. Landform displays a well-preserved convex lower break-in slope and is raised above modern RF valley floor at this location by ~8 m.	Interpreted as palaeo-shoreline, indicating stabilization of former proglacial lake at ~700-680 m in the narrow RF valley.	Phase 3: RC, RP and RF connected proglacial lake	> 16.3 ± 0.3 ka < 19.0 ± 0.9 ka
Sediment exposure	-43.315990	-71.458250	RF valley	683	Road-cut section with top-most (below soil) unit of homogeneous clay with occasional evidence of lamination.	We interpret these sediments as lacustrine clay deposits suggesting a former lake system in the narrow RF valley	Phase 3: RC, RP and RF connected proglacial lake	> 16.3 ± 0.3 ka < 19.0 ± 0.9 ka
Sediment exposure	-43.52413	-71.57738	RP valley	337	Road-cut section with top-most (below soil) unit of undisturbed, homogeneous laminated and alternating silt and clay sediment layers (varves).	We interpret these sediments as glaciolacustrine varve deposits.	Phase 3: RC, RP and RF connected proglacial lake	> 16.3 ± 0.3 ka < 19.0 ± 0.9 ka

Sediment exposure	-43.531810	-71.571400	RP valley	371	Road-cut section with top-most (below soil) unit of undisturbed, homogeneous laminated and alternating silt and clay sediment layers (varves).	We interpret these sediments as glaciolacustrine varve deposits.	Phase 3: RC, RP and RF connected proglacial lake	> 16.3 ± 0.3 ka < 19.0 ± 0.9 ka
Sediment exposure	-43.53614	-71.61917	RP valley	436	Road-cut section with top-most (below soil) unit of undisturbed, homogeneous laminated clay sediment layers.	We interpret these sediments as lacustrine clay deposits.	Phase 3: RC, RP and RF connected proglacial lake	> 16.3 ± 0.3 ka < 19.0 ± 0.9 ka
Sediment exposure	-43.56483	-71.73346	RP valley	329	Road-cut section with top-most (below soil) unit of undisturbed, homogeneous laminated clay sediment layers.	We interpret these sediments as lacustrine clay deposits.	Phase 3: RC, RP and RF connected proglacial lake	> 16.3 ± 0.3 ka < 19.0 ± 0.9 ka
Sediment exposure	-43.58182	-71.70596	RP valley	404	Road-cut section with top-most (below soil) unit of undisturbed, homogeneous laminated and alternating silt and clay sediment layers (varves).	We interpret these sediments as glaciolacustrine varve deposits.	Phase 3: RC, RP and RF connected proglacial lake	> 16.3 ± 0.3 ka < 19.0 ± 0.9 ka
Sediment exposure	-43.59210	-71.70546	RP valley	375	Quarried section with top-most (below soil) unit (3.5 m of exposure) of laminated sand and silt sediment layers and some occasional clay sediment layers. The unit also displays well dispersed, sub-angular, cobble- and boulder-sized embedded clasts of varied lithologies.	We interpret these sediments as glaciolacustrine deposits with some occasional embedded dropstones.	Phase 3: RC, RP and RF connected proglacial lake	> 16.3 ± 0.3 ka < 19.0 ± 0.9 ka

7.2.2 OSL dating samples details and lab methodology

Samples for luminescence dating were collected in opaque tubes and prepared for analysis under subdued lighting conditions. To calculate the environmental dose-rate throughout burial for each sample, *U*, *Th* and *K* concentrations were measured for ca. 80 g of the bulk sediment sample using high-resolution gamma spectrometry. Water contents of 5 ± 2 % were estimated considering the field and saturated water contents, and the environmental history for each sample. Cosmic dose-rates were calculated after Prescott and Hutton (1994). Environmental dose-rates determined for all samples are shown in Chapter 3 SM Table 2.

To determine equivalent doses (D_e), grains of *K*-feldspar were used to determine equivalent doses (D_e). Samples were first treated with a 10 % v/v dilution of 37 % *HCl* and with 20 % v/v of H_2O_2 to remove carbonates and organics, respectively. Dry sieving then isolated the grainsize used for analysis, which was then subject to density separation using sodium polytungstate (< 2.58 g cm^{-3} *K*-feldspar dominated) and not etched using hydrofluoric acid. Finally, grains of *K*-feldspar were mounted on a 9.8 mm diameter aluminium single-grain disc for analysis, which contained a 10 by 10 grid of 200 μm (150 - 180 μm grainsize) or 300 μm (180 – 250 μm grainsize) diameter holes to ensure each hole contained only one grain.

All luminescence measurements were performed using a Risø TL/OSL DA-15 automated single-grain system equipped with a $^{90}Sr/^{90}Y$ beta source (Bøtter-Jensen *et al*. 2003) fitted with a blue filter pack (BG39, Coring 7-59) in front of the photomultiplier tube. Single aliquot regenerative dose (SAR) protocols (Murray and Wintle, 2000) were used for the post-IR IRSL analyses performed at 225 °C (Thomsen *et al*. 2008), termed the $pIRIR_{225}$ signal. A preheat temperature of 250 °C for 60 s was used prior to stimulations of 2 s using the infra-red laser at 225 °C. The IRSL signal measured performed at 50 °C prior to the $pIRIR^{225}$ measurement and the elevated temperature bleach of 330 °C for 200 s at the end of each L_x/T_x cycle were performed using the IR LEDs. The location of the single-grain discs was performed at room temperature, rather than elevated temperatures to prevent thermal annealing of the IRSL signal (after Smedley and Duller, 2013). The first 0.3 s and final 0.6 s of stimulation were summed to calculate the initial and background IRSL signals, respectively. The grains were accepted after applying the following screening criteria and accounting for the associated uncertainties: (1) whether the test dose response was greater than three sigma above the background, (2) whether the test dose uncertainty was less than 10 %, (3) whether the recycling and OSL-IR depletion

ratios were within the range of ratios 0.9 to 1.1, and (4) whether recuperation was less than 5 % of the response from the largest regenerative dose.

Grains from sample RC19S03 were used for dose-recovery experiments and successfully recovered a given dose within 10 % using the $pIRIR_{225}$ signal. Fading rates (*g*-values, Aitken, 1985) were determined for three aliquots of each sample and normalised to a t_c of two days (Huntley and Lamothe 2001; Fig. 6). The large uncertainties on the individual *g*-values measured were derived from the uncertainty in the fit of the data, which is typical of fading measurements for the pIRIR signal (e.g. Smedley *et al*. 2016). To derive a more reliable estimate of the fading rate, the weighted mean and standard error for all the samples was calculated for $pIRIR_{225}$ signals (-0.9 ± 0.8 %/decade). Given that the $pIRIR_{225}$ fading rate is low with large uncertainties for each sample (SM Table 2) and in line with previous $pIRIR_{225}$ studies (e.g. Roberts, 2012; Trauerstein *et al*. 2014; Kolb and Fuchs 2018), we did not correct the $pIRIR_{225}$ ages for fading.

D_e values were calculated from all grains passing all the screening criteria. The minimum age model (MAM; Galbraith and Laslett, 1993; Galbraith *et al*. 1999) was applied to determine an age for the samples as the asymmetrical D_e distributions suggested the samples were partially bleached prior to burial (Fig. 1). The scatter in the D_e distribution arising from intrinsic and extrinsic sources were combined in quadrature to determine σ_b for the MAM (SM Table 2). The overdispersion values arising from intrinsic sources for sample RC19S03 (13 ± 1 %) were derived from the dose-recovery experiments, while the over-dispersion arising from variability in the internal dose-rates of *K*-feldspar grains for both samples was assumed to be 10 % (after Smedley and Pearce, 2016). Additional over-dispersion (20 %) was incorporated to account for the variability in single-grain D_e distributions caused by external microdosimetry (after Smedley *et al*. 2020). The D_e values were then divided by the environmental dose-rates to determine an age for each sample (SM Table 2).

Chapter 3 Supplementary Table 2. Luminescence dating results for samples RC19S01, RC19S02 (180-250 µm) and RC19S03 (150-180 µm) from Río Corcovado. Environmental dose-rates were determined using high-resolution gamma spectrometry. The dose-rates were calculated using the conversion factors of Guerin *et al*. (2011) and alpha (Bell, 1980) and beta (Guerin *et al*. 2012) dose-rate attenuation factors. Water contents (5 ± 5 %) were estimated considering the field water contents, and the environmental history for each sample; these values are expressed as a percentage of the mass of dry sediment. An internal K-content of 10 ± 2 % (Smedley *et al*. 2012) were used to determine the internal dose-rates. An a-value of 0.10 ± 0.02 (Balescu & Lamothe, 1993) was used to calculate the alpha dose-rates. Cosmic dose-rates were determined after Prescott & Hutton (1994). Dose-rates were calculated using the Dose Rate and Age Calculator (DRAC; Durcan *et al*. 2015). The *g*-values (%/decade) were measured using the pIRIR225 signal for three aliquots of K-feldspar for each sample, normalised to 2 days and are presented as weighted means and standard errors. The number of grains that were used to determine a *De* value (n) are shown as a proportion of the total grains measured (N). The MAM was used to determine the *De* for age calculating, applying a σb value of 0.25 for all samples.

Sample	U (ppm)	Th (ppm)	K (%)	Internal dose-rate (Gy/ka)	External alpha dose-rate (Gy/ka)	External beta dose-rate (Gy/ka)	External gamma dose-rate (Gy/ka)	Cosmic dose-rate (Gy/ka)	Total dose-rate (Gy/ka)	*g*-value (%/dec.)	n/N	OD (%)	D_e (Gy)	Age (ka)
RC19S01	1.98±0.22	8.25±0.22	1.09±0.22	0.72±0.16	0.12±0.02	1.16±0.16	0.84±0.06	0.27±0.03	3.11±0.24	1.5±4.8	141/4400	53	203.3±15.8	65.4±7.1
RC19S02	2.24±0.25	8.53±0.24	1.20±0.24	0.72±0.16	0.13±0.03	1.28±0.17	0.91±0.07	0.29±0.03	3.31±0.25	0.5±1.5	523/1900	46	172.7±6.4	52.1±4.4
RC19S03	1.69±0.19	6.46±0.25	1.54±0.26	0.56±0.10	0.13±0.02	1.44±0.19	0.83±0.07	0.23±0.02	3.18±0.23	-1.5±0.9	569/2100	47	111.1±4.8	34.9±2.9

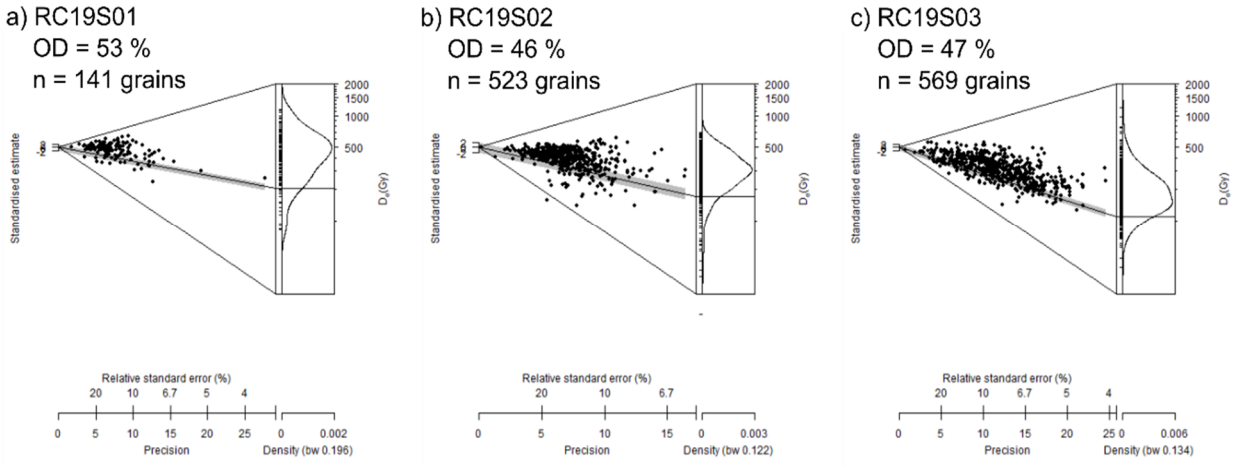

Chapter 3 Supplementary Figure. 1. Abanico plots of the D_e values determined for OSL dating, where the grey shading shows the MAM D_e for each distribution.

7.2.3 ^{10}Be TCN dating wet chemistry lab methodology

The 125-250 μm and 250-500 μm grain fractions were cleaned and oven-dried to remove non-mineralic grains, prior to being magnetically separated. Non-magnetic fractions were recovered. To remove feldspar and mica minerals, the samples were treated with eucalyptus oil and a carbonated surfactant solution of water and dodecylamine to enable froth floatation (Herber, 1969). Non-floating quartz grains were recovered while floating minerals were stored. The samples were then etched a minimum of three times (24 h each) in 1000 ml of pure water, 40% *HF* and 68% HNO_3 (150:2:1) to isolate the quartz grain cores, thus removing meteoric ^{10}Be. An aliquot of the final quartz sample was dissolved and its purity tested for *Al*; *Be*; *Fe*; *Ca* and *Ti* by ICP-OES. Samples containing *Al* concentrations higher than 300 ppm were re-etched. The samples were dissolved in 40% *HF* and each sample and processed blank (n =3) were spiked with between 0.23 and 0.25 mg of ^{9}Be, using an in-house carrier solution obtained from phenakite. After dissolution, the *HF* was evaporated and replaced by *HCl*. The solutions were first passed through anion exchange chromatography columns to remove *Fe*. The *Fe*-free fractions were then evaporated and the *HCl* was replaced by dilute H_2SO_4. The sulphate solutions were then passed through cation exchange chromatography columns to remove *Ti* and *B*, and to isolate *Be* and *Al* fractions, eluted using *HCl* solutions. The *Be* fractions were precipitated as hydroxides and oxidised at ~900 °C. Resulting *BeO* samples were mixed with *Nb* (1:6) and pressed into copper cathodes for AMS measurements. $^{10}Be/^{9}Be$ ratios were determined with a 5MV Tandem Pelletron (NEC Model 15SDH-2). All $^{10}Be/^{9}Be$ ratios were normalised to NIST SRM4325 with a nominal $^{10}Be/^{9}Be$ ratio of $2.79 .10^{-11}$ (Nishiizumi *et al*., 2007), corresponding to a ^{10}Be half-life of 1.36 Ma. Processed blank corrections ranged between 1.4% and 4.5% of the sample $^{10}Be/^{9}Be$ ratios.

7.2.4 Vertical plot of published LGM TCN exposure ages from glacial deposits in Patagonia

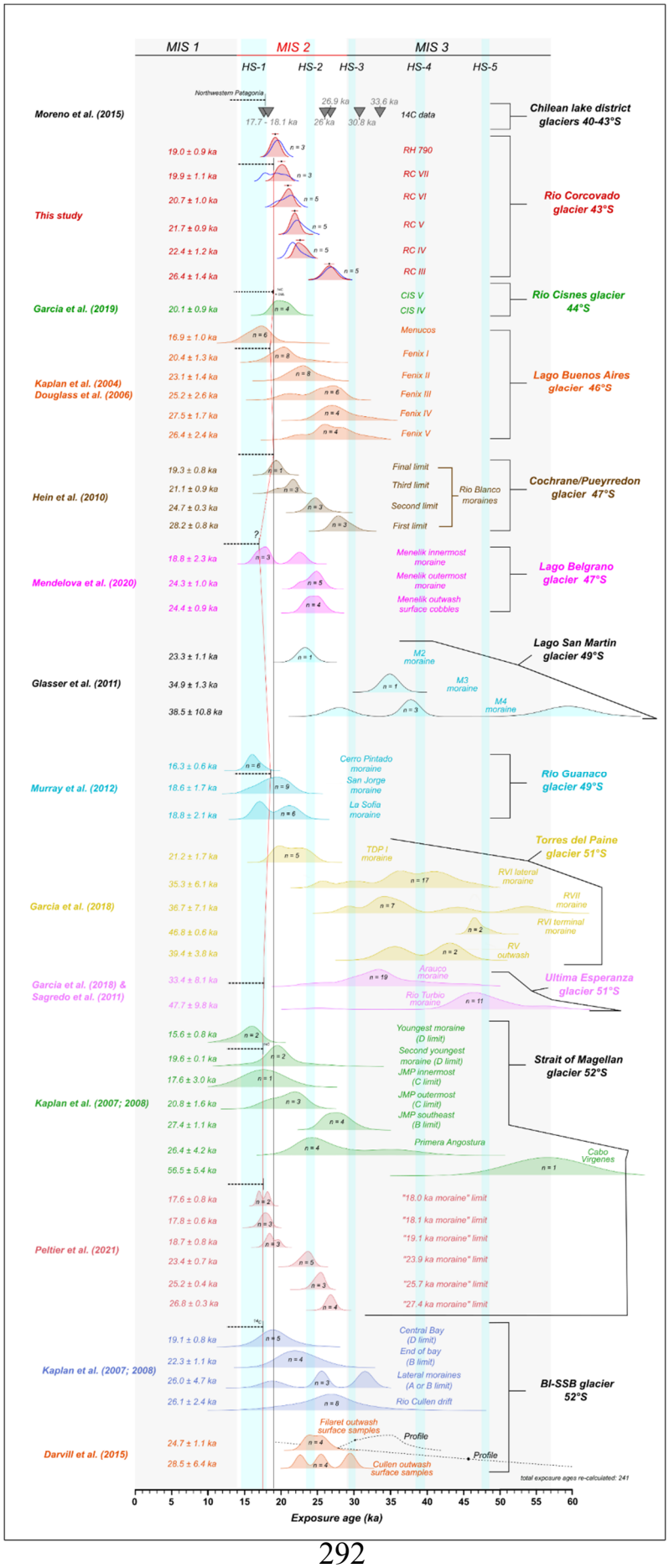

Chapter 3 Supplementary Figure 2. Vertical plot of published exposure ages dating local LGM advances of the PIS over the last 60 ka, from north to south, including the RC III – RC VII record (this study). MIS intervals are illustrated by light grey bars (from Lisiecki & Raymo, 2005) while the Heinrich Stadial (HS) 1-5 events are designated by a light blue bars (from Hemming, 2004). Apart from the Chilean Lake District record (^{14}C dates), ^{10}*Be* exposure ages (n = 241) are displayed as cumulative kernel density plots (adapted from iceTEA tools for exposure dating plots; Jones *et al*., 2019) using 1σ ranges and internal analytical uncertainties from individual ages. All exposure ages (n=241) have been re-calculated using the Patagonian production rate (Kaplan *et al*., 2011) obtained from the ICE-D online database (http://calibration.ice-d.org/) and the LSDn-time-dependent scaling scheme of Lifton *et al*. (2014). All ages assume no surface erosion and no correction for shielding by snow, soil and/or vegetation. Outliers identified as such by original publications were manually removed. Dashed horizontal black bars with vertical bars on right-hand extremities indicate the possible onset of local deglaciation proposed by the original publications, after taking into account landform-age re-calculation. Note that the number of samples per landform varies significantly between study-sites / publications. Subsequently, not all records displayed here present comparable levels of dating robustness.

7.2.5 ^{10}Be TCN exposure dating kernel density plots per landform

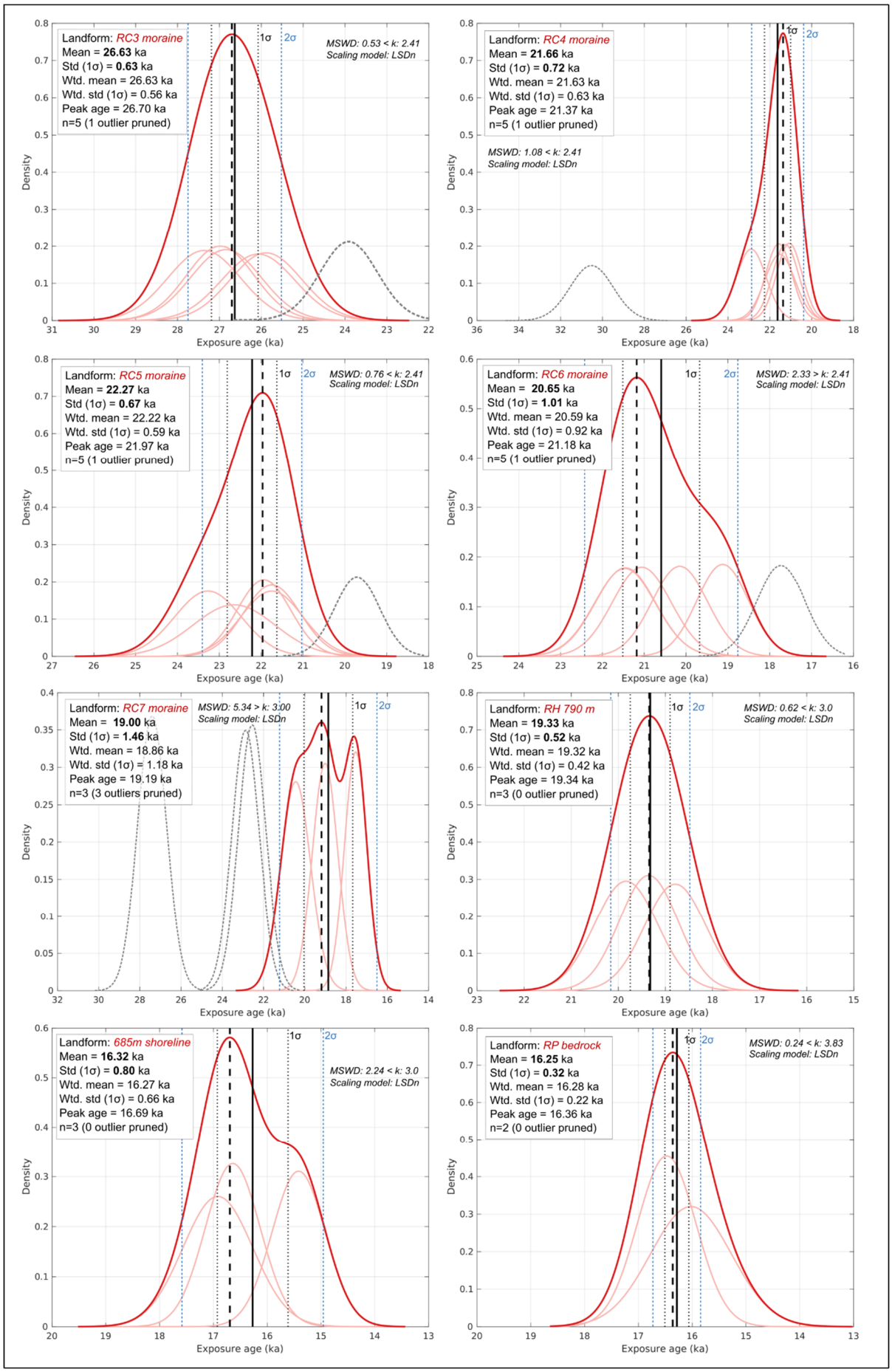

Chapter 3 Supplementary Figure 3. Kernel density plots, adapted from plots produced using the IceTEA tools for exposure dating (Jones *et al*., 2019; http://ice-tea.org/en/) and TCN dating summary statistics for the RC III-VII, RH_{790}, RC_{680} and RPbed dated landforms. Thick red curve represent the summed probability distribution for the age population, excluding outliers, while thin red curves depict Gaussian curves for individual samples. Outliers are denoted by grey dashed curves. Vertical black lines denote the arithmetic mean, while thin black and blue vertical dashed lines denote the 1σ and 2σ confidence intervals of the mean, respectively. Thick black and dashed vertical line highlights the peak age associated with the summed probability distribution. Std: standard deviation, Wtd. mean: uncertainty-weighted mean, Wtd. std: uncertainty-weighted standard deviation.

7.2.6 Cosmo-Ages Sequence Calculator (CASC) – Bayesian age model

This programme was employed to produce age probability distributions for each dated landform using a Bayesian statistical approach that takes into account the relative stratigraphic order of events.

Programmer: Dr. Ángel Rodés (Scottish Universities Environmental Research Centre, Scottish Enterprise Technology Park, East Kilbride, G75 OQF, Glasgow, Scotland, United Kingdom of Great Britain and Northern Ireland)

Coding language: MATLAB

Code URL: https://github.com/angelrodes/CASC

Input filename: data.csv

Input data format:

Column A (Sample) = Sample ID

Column B (Age) = Sample exposure age (ka)

Column C (Uncert.) = Internal analytical uncertainty (ka)

Column D (Moraine) = Landform name

Column E (Sequence) = Stratigraphic order of sequences: with "1" being the oldest event, "2" the second oldest etc… (see example below).

Sample	Age	Uncert.	Moraine	Sequence
19RCS21	26.075	0.877	RC3	1
19RCS23	XXXXX	YYYY	RC3	1
19RCS25	XXXXX	YYYY	RC3	1
19RCS27	XXXXX	YYYY	RC3	1
19RCS28	XXXXX	YYYY	RC3	1
19RCS15	XXXXX	YYYY	RC4	2
19RCS16	XXXXX	YYYY	RC4	2
19RCS17	XXXXX	YYYY	RC4	2
19RCS51	XXXXX	YYYY	RC4	2
19RCS52	XXXXX	YYYY	RC4	2

7.3 Chapter 4 supplementary materials

7.3.1 Ice-flow model output comparison with GlaRe flowline model

7.3.1.1 GlaRe methods

To compare our model outputs to the more commonly-used method of land-terminating glacier surface reconstruction using a simple flowline model (e.g. Huss *et al*., 2007; Banerjee & Shankar, 2009), we also conducted simulations using GlaRe, a GIS-based toolbox enabling the estimation of ice-thickness distribution and palaeo-glacier geometry using user-defined bed elevations, flowline network and maximum ice-extent polygon constraints (Pellitero *et al*., 2016). We drew a flowline network manually using ice-surface topographic contour lines from ice-elevation outputs from our ice-flow model, while we determined ice-extent constraints using the EL terminal and lateral moraines and following mountain ridges characteristic of the EL drainage basin. We used GlaRe to calculate ice thickness values along the central glacier flowline at regular step intervals by iteratively solving the following equation, which assumes no basal sliding and glacier ice that has a perfectly plastic rheology (Shilling & Hollin, 1981; Paterson, 1994, p. 240; Pellitero *et al*., 2016):

$$h^2{}_{i+1} - h_{i+1}\,(bed_i + bed_{i+1}) + h_i\,(bed_{i+1} - H_i) - \frac{2\Delta x \tau_{av}}{Fg} = 0 \qquad (1)$$

where h is ice surface elevation (m a.s.l), bed is bed elevation (m a.s.l), H is ice thickness (m), Δx is step length, here set to 20 m, τ_{av} is average basal shear stress (Pa) over a 20 m interval, g is gravity acceleration (9.81 m s^{-2}), ρ is ice density (~900 kg m^{-3}), F is a shape factor, and i represents the iteration (step) number (Pellitero *et al*., 2016). We tuned basal shear stress manually between 70 and 150 kPa along several sections of the central glacier flowline until the simulated palaeo-glacier tongue width and thickness matched the EL lateral moraine record. In the accumulation zone, a higher basal shear stress value of up to 200 kPa was assigned to tributary flowlines, thereby simulating topographically-controlled feeding glaciers draining cirques with higher surface roughness. The 2D ice-thickness data were then extrapolated to a 3D ice-surface DEM using the *Topo to Raster* tool (Hutchinson, 1989; Pellitero *et al*., 2016), which was found to produce a more satisfactory result than the *IDW*, *Kriging*, or *Trend* methods available. The simulated palaeo-glacier ELA, relative to present-day sea level, was then

automatically estimated with the AAR method for a given ratio using the GlaRe glacier DEM output and a GIS toolbox developed by Pellitero *et al*. (2015). Although this analysis provides a mean of comparing different modelling methods and palaeo-glacier reconstructions, GlaRe does not take into account dynamic glacier evolution in response to SMB and requires glacier outline input constraints for satisfactory results. Therefore, it does not represent a substitute to a SMB driven ice-flow model for the purpose of our investigation.

7.3.1.2 GlaRe results and comparisons

Using the GlaRe flow-line model (Pellitero *et al*., 2016), the simulated EL-out palaeo-glacier surface exhibiting the best fit with lateral and terminal moraines yielded an ELA of 1516 m a.s.l when calculated with an AAR of 0.65. Including correction for GIA-related uplift decreases this palaeo-ELA to 1385 m a.s.l (AAR 0.7-0.6 range = 1340 – 1425 m a.s.l). The reconstructed glacier SMB profile matches relatively well our spatially-distributed ice-flow model outputs (1384-1473 m a.s.l), despite employing quite different physical modelling assumptions. However, the simulated steady-state glacier volume (0.453 km^3), surface area (6.710 km^2) and maximum ice thickness (246 m) were all lower when simulated with GlaRe than our coupled glacier mass balance and ice-flow model. These differences in ice-thickness estimations originate from glacier DEM outputs from GlaRe being the product of an iterative grid-calculation method enabling three-dimensional interpolation of two-dimensional ice-thickness data (Pellitero *et al*., 2016), while ice-flow models provide spatially- and vertically-distributed calculations of ice flux instead (Wijngaard *et al*., 2019).

7.3.2 Ice-flow model source code

The Matlab© source code for the ice-flow model used in this study is provided under the "Source_code.zip" compressed document, under this link:
https://www.frontiersin.org/articles/10.3389/feart.2021.751987/full#supplementary-material

The "domain.dat" and "mask.dat" files it contains are example domain and ocean mask files (from DEM) used for EL glacier simulations. If any queries appear regarding the use of the source code, please email corresponding author.

7.3.3 Supplementary Figures and Tables

7.3.3.1 Supplementary Figures

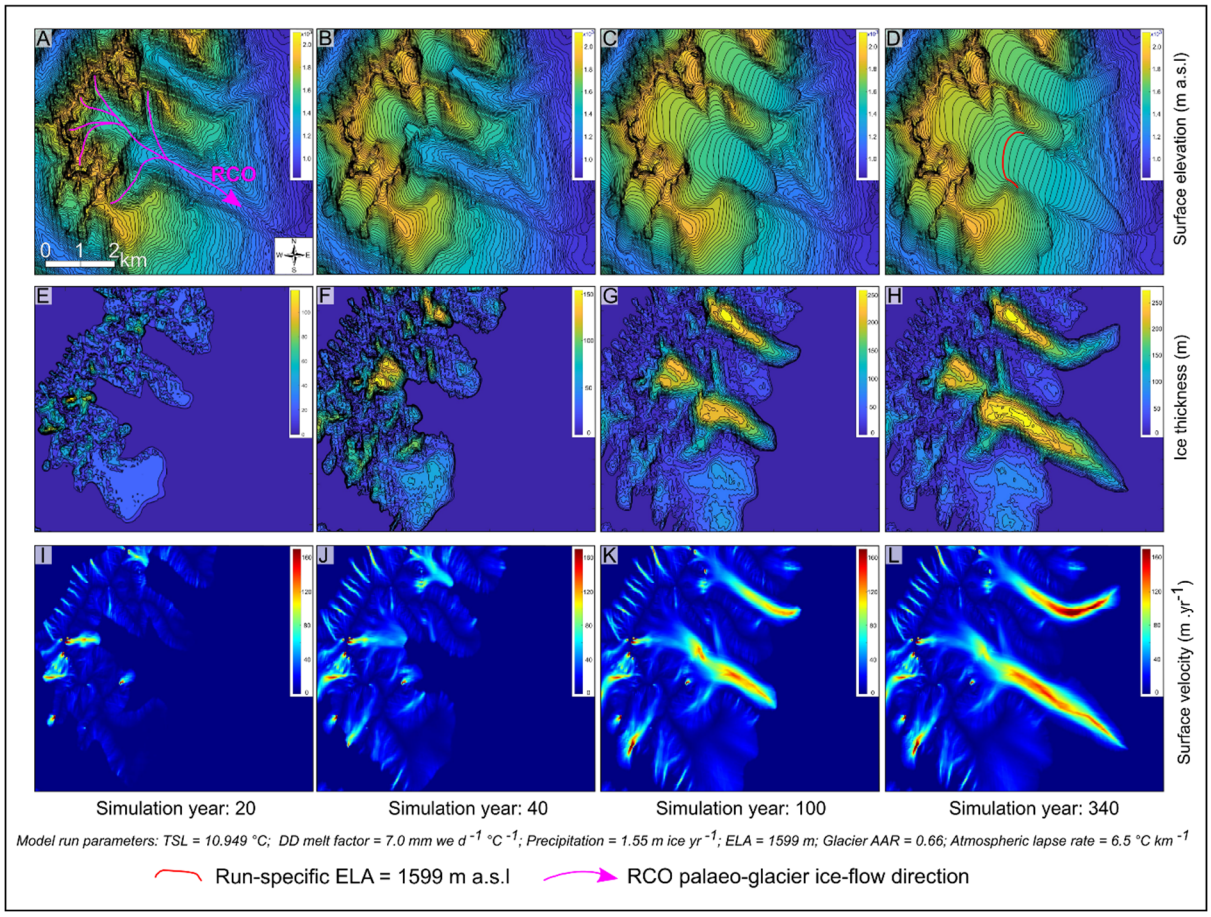

Chapter 4 Supplementary Figure 1. Ice-flow model output data (~30 x ~30 m grid-cell spatial resolution) for one selected model simulation of the RCO-out advance. (**A-D**) Surface elevation data (m a.s.l.) including AW3D30 DEM data plus simulated ice thickness, (**E-H**) ice thickness data (m), and (**I-L**) ice-surface velocity data (m yr^{-1}); for simulation years 20 (panels A, E, I), 40 (panels B, F, J), 100 (panels C, G, K) and 340 (steady-state volume, panels D, H, L). Note that colorbar values and scaling are panel-specific.

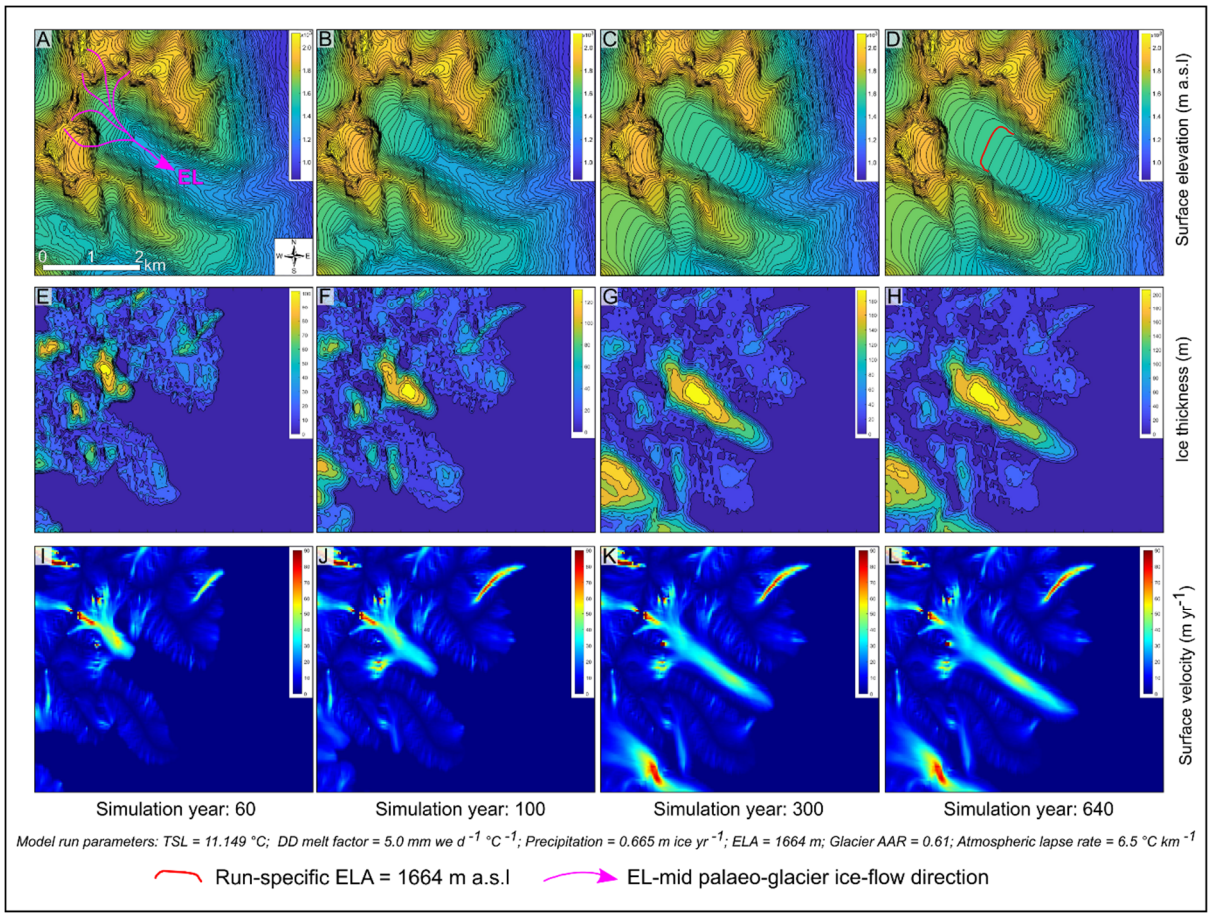

Chapter 4 Supplementary Figure 2. Ice-flow model output data (~30 x ~30 m grid-cell spatial resolution) for one selected model simulation of the EL-mid advance/still-stand. (**A-D**) Surface elevation data (m a.s.l.) including AW3D30 DEM data plus simulated ice thickness, (**E-H**) ice thickness data (m), and (**I-L**) ice-surface velocity data (m yr^{-1}); for simulation years 60 (panels A, E, I), 100 (panels B, F, J), 300 (panels C, G, K) and 640 (steady-state volume, panels D, H, L). Note that colorbar values and scaling are panel-specific.

7.4 Chapter 5 supplementary materials

7.4.1 Rock sample preparation, wet chemistry and exposure-age calculations

7.4.1.1 SUERC cosmogenic isotopes analysis laboratory methodology

Thirteen samples were processed at the Scottish Universities Environmental Research Centre (SUERC) cosmogenic isotope analysis facility (Glasgow, Scotland) (main paper Table 1). Following rock sample crushing and sieving, the 125-250 μm and 250-500 μm grain fractions were cleaned and oven-dried to remove non-mineralic grains, prior to being magnetically separated. Non-magnetic fractions were recovered. To remove feldspar and mica minerals, the samples were treated with 1% *HF*, eucalyptus oil and a carbonated surfactant solution of water and dodecylamine to enable froth floatation (Herber, 1969). Non-floating quartz grains were recovered while floating minerals were stored. The samples were then etched in high-power ultrasonic baths a minimum of three times (24 h each) in 1000 ml of pure water, 40% *HF* and 68% HNO_3 (150:2:1) to isolate the quartz grain cores, thus removing meteoric ^{10}Be (Kohl and Nishiizumi, 1992). A 0.4 g aliquot of the final quartz sample was dissolved and its purity tested for *Al*; *Be*; *Fe*; *Ca* and *Ti* by Inductively Coupled Plasma - Optical Emission Spectrometry. Samples containing higher-than-300 ppm *Al* concentrations were re-etched. Purified samples were dissolved in 40% *HF* and each sample and process blank were spiked with between 0.27 and 0.29 mg of ^{9}Be, using an in-house carrier solution obtained from phenakite (< 2 x10^{-15} $^{10}Be/^{9}Be$). After dissolution, the *HF* was evaporated and replaced by *HCl*. The solutions were first passed through anion exchange chromatography columns to remove *Fe*. The *Fe*-free fractions were then evaporated and the *HCl* was replaced by dilute H_2SO_4. The sulphate solutions were then passed through cation exchange chromatography columns to remove *Ti* and *B*, and to isolate *Be* and *Al* fractions, eluted using *HCl* solutions. The *Be* and *Al* fractions were precipitated as hydroxides and oxidised at ~900 °C. Resulting *BeO* and Al_2O_3 samples were mixed with *Nb* (1:6 ratio) and *Ag* (1:2 ratio), respectively, and pressed into copper cathodes for AMS measurements. $^{10}Be/^{9}Be$ and $^{26}Al/^{27}Al$ ratios were determined with a 5MV Tandem Pelletron (NEC Model 15SDH-2). All $^{10}Be/^{9}Be$ ratios were normalised to NIST SRM4325 with a nominal $^{10}Be/^{9}Be$ ratio of 2.79 x10^{-11} (Nishiizumi *et al*., 2007), corresponding to a ^{10}Be half-life of 1.36 Ma. Sample $^{10}Be/^{9}Be$ AMS measurement uncertainties ranged between 1.4% and 2.5%. Processed blank corrections for ^{10}Be concentrations ranged

between 0.9% and 4.1% of the sample $^{10}Be/^{9}Be$ ratios. $^{26}Al/^{27}Al$ ratios were normalised to the Purdue Z92-0222 standard, with a nominal $^{26}Al/^{27}Al$ ratio of 4.11 $x10^{-11}$, equivalent to standardisation of ^{26}Al concentrations using the KNSTD standard (Nishiizumi, 2004). Processed blank corrections for ^{26}Al concentrations ranged between 0.2% and 0.4% of the sample $^{26}Al/^{27}Al$ ratios. The uncertainty of this correction is included in the stated standard uncertainties. The standard uncertainties also include between 3% and 11% for the uncertainty of stable ^{27}Al determination.

7.4.1.2 CEREGE LN_2C laboratory methodology

Five samples (RC20-12, 14, 16, 20, and 21) presenting low quartz yields were processed at the French National Laboratory for Cosmogenic Nuclides (LN_2C) of CEREGE, Aix-en-Provence, France (Table 5.1). Following rock sample crushing and sieving, one to three treatments in *HCl*, H_2SiF_6 and *HF* on a shaker table for 48 hours per treatment was performed to reduce/remove non-quartz minerals (inspired by Bourlès, 1988). Feldspar and other remaining non-quartz minerals were further reduced by magnetic separation after addition of magnetite powder. Pure quartz was obtained by repeated etching in a *HF* solution (*HF* 48%) diluted with ultrapure water (resistivity of 18.2 MΩ. cm^{-1} at 25°C) for 24 hours in a heated ultrasonic bath, with a variable sample-to-acid ratio dependent on sample mass and mass conservation goals. At least 30% of pre-etching sample mass was dissolved, thus ensuring efficient removal of atmospheric ^{10}Be (Kohl and Nishiizumi, 1992). The purified quartz samples were dissolved in concentrated *HF* (48%) and each sample and one process blank were spiked with between 0.439 and 0.456 mg of ^{9}Be, in the form of an in-house carrier solution made from phenakite. After dissolution, the *HF* was evaporated and the solid residue was dissolved in *HCl* (10.2 mol L^{-1}) followed by $Be(OH)_2$ precipitation at pH ~9 through the addition of NH_3, and re-dissolution in *HCl* (10.2 mol L^{-1}). The solutions were first passed through anion exchange chromatography columns to remove *Fe*, *Ti* and *Mn*. After another evaporation and $Be(OH)_2$ precipitation step, *HCl* of lower concentration (1 mol L^{-1}) was added to dissolve the *Be* prior to passing the solution through cation exchange chromatography columns to isolate *Be* from *B* and *Al*. The *Be* fractions were then precipitated again as hydroxides (pH ~9), prior to dissolution in 200 µL of HNO_3 (65%) and oxidation for 1 hour at ~700 °C. The resulting *BeO* samples were mixed with *Nb* powder (1:1 ratio) and pressed into

nickel cathodes for AMS measurements at the ASTER AMS facility. $^{10}Be/^{9}Be$ ratio measurements are based on the in-house standard *STD-11* (equivalent to NIST SRM4325 and the 07KNSTD standards) with a $^{10}Be/^{9}Be$ ratio of (1.191 ± 0.013) x10^{-11} (Braucher *et al*., 2015) and a ^{10}Be half-life of (1.387 ± 0.0012) x10^{6} years (Chmeleff *et al*., 2010; Korschinek *et al*., 2010). Analytical uncertainties include ASTER counting statistics and stability (the latter being ~0.5%; Arnold *et al*., 2010) and machine blank correction. $^{10}Be/^{9}Be$ AMS measurement uncertainties ranged between 2.4% and 3.5%. Process blank corrections ranged between 0.6% and 1.5% of calculated sample ^{10}Be atoms.

7.4.1.3 University of Edinburgh Cosmogenic Nuclide Laboratory methodology

Five samples (RHS09, 10, 12, 13, 15) were processed for wet chemistry at the University of Edinburgh Cosmogenic Nuclide Laboratory (main paper Table 1). The ~1 kg samples were crushed whole and sieved to isolate the 250-500 μm grain fractions. One to three treatments in *HCl* and H_2SiF_6 on a shaker table for up to seven days per treatment was performed to reduce/remove non-quartz minerals (Bourlès, 1988). Pure quartz was obtained by repeated etching in a 2% *HF* and 1% HNO_3 solution for 24 hours in a heated ultrasonic bath, with a sample to acid ratio of about 12 g L^{-1}. At least three etches were then performed to remove atmospheric ^{10}Be. Between 0.248 and 0.250 mg of ^{9}Be carrier was added to quartz separates prior to dissolution in concentrated HF (48%). The dissolved samples were fumed in $HClO_4$ and passed through anion exchange chromatography columns to remove *Fe* and other contaminants. Precipitation to remove *Ti* was followed by separation of *Be* from *Al* by cation exchange chromatography. These were precipitated and fumed in $HClO_4$ to reduce Boron levels. Hydroxide gels were rinsed with ultra-pure water, dried, fired in a furnace, mixed with *Nb* and pressed into cathodes for AMS measurements at SUERC (section 7.4.1.1.).

7.4.2 ^{10}Be and ^{26}Al concentrations ratio analysis

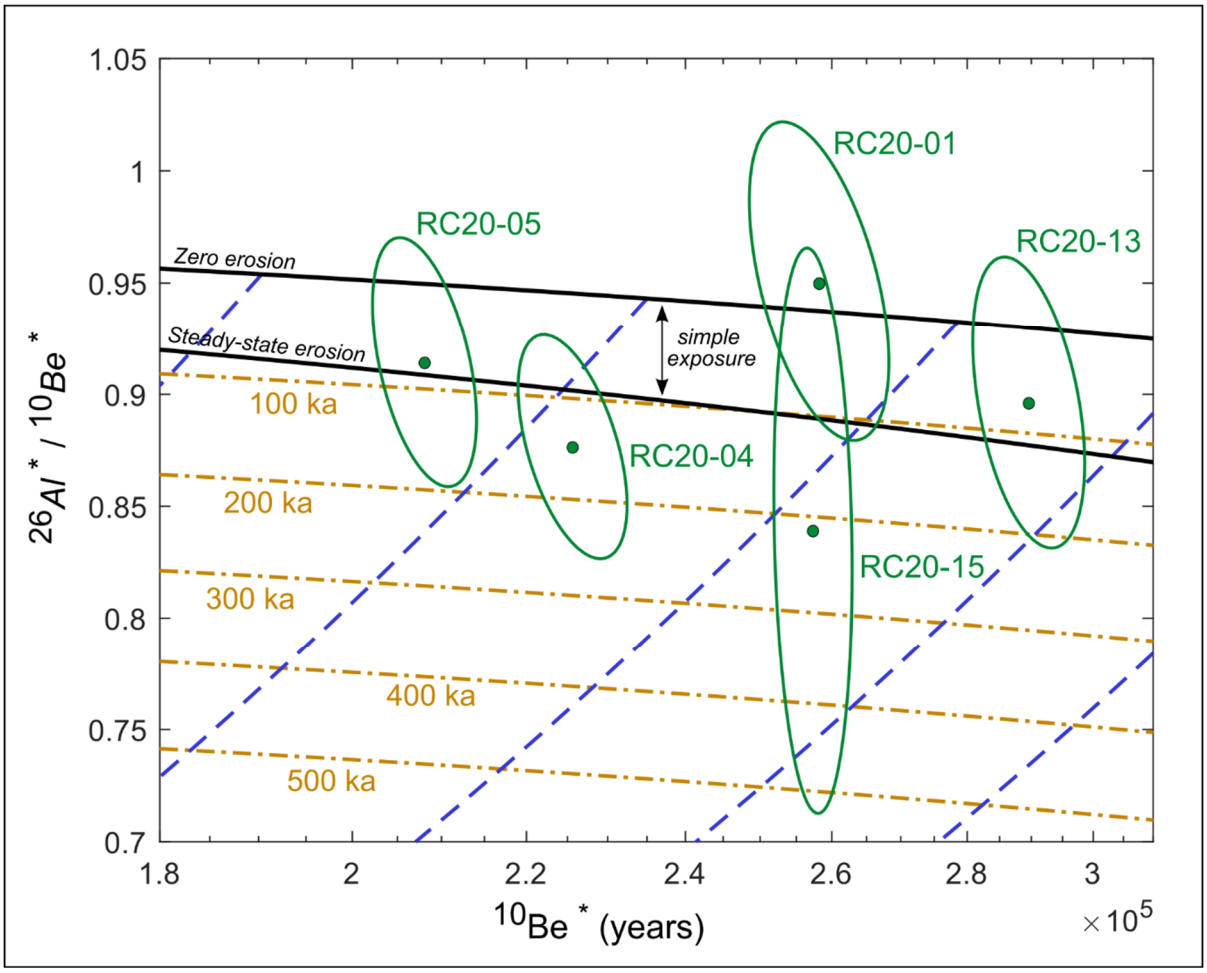

Chapter 5 Supplementary materials figure 1. Two-isotope diagram of the five samples for which both ^{10}Be and ^{26}Al concentrations in quartz were determined. This plot was adapted from plots produced using the iceTEA tools for exposure ages Matlab© code (Jones *et al.*, 2019). The diagram features ^{10}Be and ^{26}Al concentrations normalised at SLHL by the global production rate of Borchers *et al.* (2016). The thick black lines highlight the simple exposure region. Sample point means and uncertainty ellipses (1σ uncertainties) are symbolised in green. Isochrones indicate lines of equal burial time (orange dot-dashed lines) and equal exposure time (blue dashed lines). The data shows that within 1σ analytical uncertainties (green ellipses), all sample nuclide concentrations fall inside the simple exposure region, thus suggesting all samples underwent a simple, single exposure and erosion history (Dunai, 2010). If samples fall below the simple exposure region within analytical uncertainties, $^{26}Al/^{10}Be$ ratios would instead indicate that samples experienced periods of burial and thus a complex exposure history. RC20-04,05 are moraine boulders from the RC II margin, RC20-01 is an ice-moulded bedrock surface sample located between the RC I and RC II margins, and RC20-13,15 are outwash surface cobbles from the RC I margin (main paper Table 1 and 2).

7.4.3 Sample location maps

7.4.3.1 RC II moraine-outwash complex samples & RC I-II ice-moulded bedrock sample

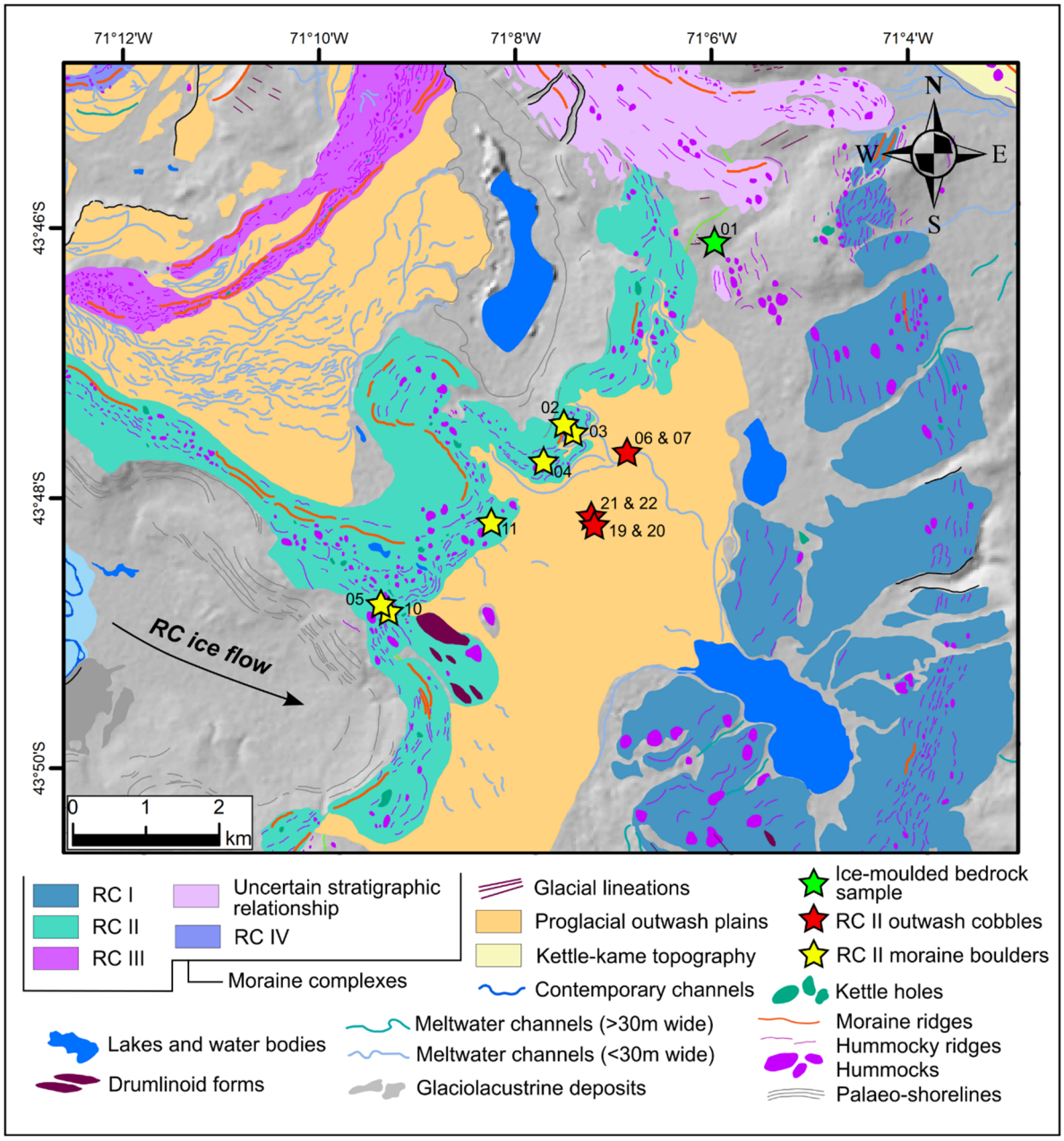

Chapter 5 Supplementary materials figure 2. Glacial geomorphological mapping (hillshade from ALOS WORLD 3D 30m DEM) focused on sampling locations of the RC II moraine-outwash complex. The locations of RC II outwash surface cobbles and RC II moraine boulders sampled for TCN exposure dating are denoted by red and yellow stars, respectively.

7.4.3.2 RC I moraine-outwash complex samples

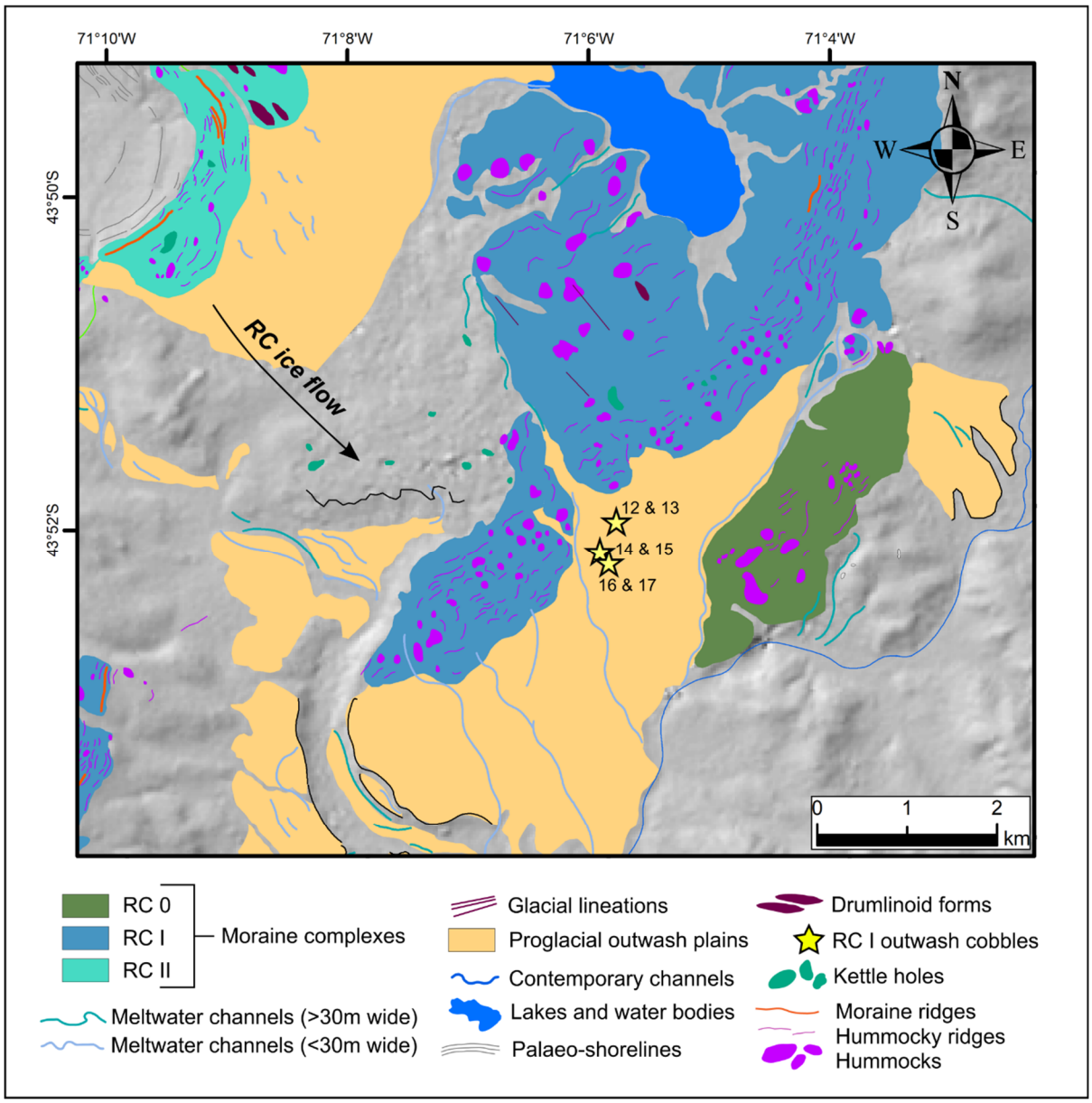

Chapter 5 Supplementary materials figure 3. Glacial geomorphological mapping (hillshade from ALOS WORLD 3D 30m DEM) focused on the sampling location of the RC I moraine-outwash complex. The locations of RC I outwash surface cobbles sampled for TCN exposure dating are denoted by yellow stars.

7.4.3.3 Tecka / RC 0 outwash samples

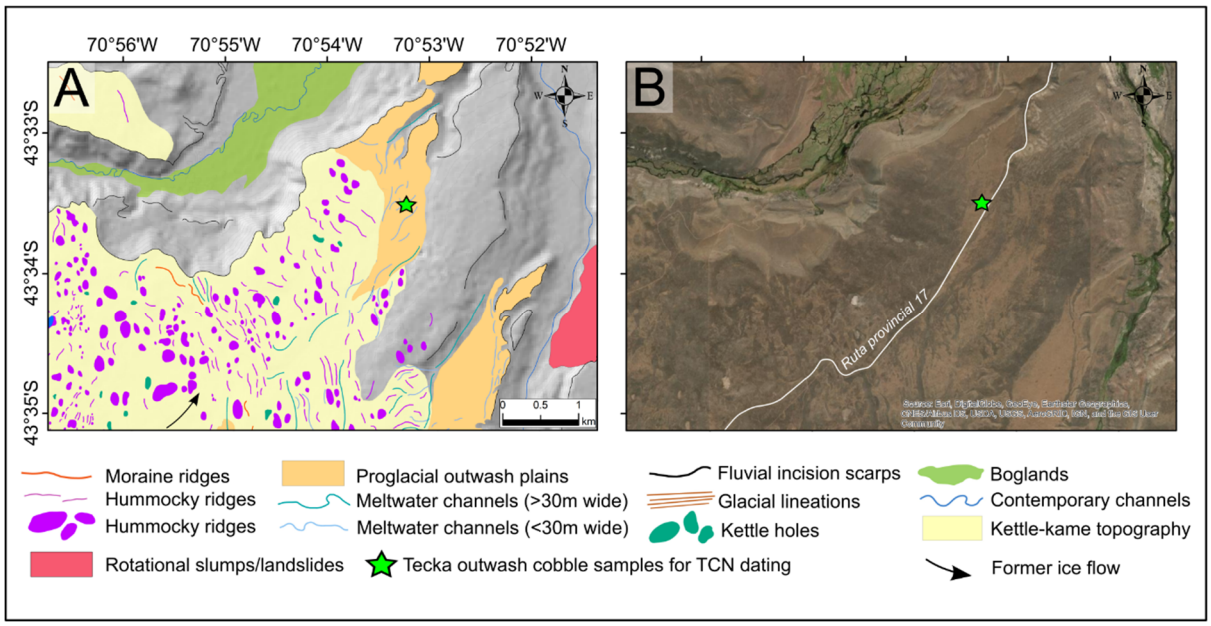

Chapter 5 Supplementary materials figure 4. A) Glacial geomorphological mapping (hillshade from ALOS WORLD 3D 30m DEM) and **B**) Satellite imagery (ESRI™, DigitalGlobe) comparison of the outermost belt of ice-contact glaciogenic kettle-kame deposit located to the east of the Río Huemul valley, and also termed the Tecka Drift (Haller *et al*., 2003). The northeastern edge of this deposit makes way to a proglacial outwash plain that was sampled for TCN exposure dating of surface cobbles (n=5, green star). We interpret this deposit as stratigraphically corresponding to the outermost moraine belt preserved in the Río Corcovado valley, here termed the RC 0 moraine.

7.4.4 Sample photographs

RC20-01





RC20-02





RC20-03



RC20-04



RC20-05



RC20-10



RC20-11



RC20-06



RC20-07



RC20-19



RC20-22



RC20-20



RC20-21





RC20-12



RC20-14



RC20-13





RC20-15





RC20-16



7.4.5 Method: estimating potential impact of outwash-cobble exhumation on exposure-age scatter

To estimate the possible impact of cobble exhumation through a soil horizon (*e.g.* via cryoturbation) on post-depositional exposure-age scatter and landform formation age underestimation, we conducted simulations of constant-rate cobble exhumation through soil columns of various thicknesses. Because the spallation-dominated production of cosmogenic ^{10}Be in quartz is reduced with depth below surface due to cosmic-ray attenuation (Gosse & Phillips, 2001), taking into account sample cover since deposition will result in older exposure ages than calculated if assuming a constant exposure history. Our approach is based on the assumption that, for depths <25 cm and relative to a simple exposure history, ^{10}Be concentration attenuation for a cobble exhumed at a constant-rate through a given soil depth is approximately equivalent to the ^{10}Be concentration attenuation for a cobble that is constantly buried below that given depth / 2. This mathematical simplification is based on the negligible curvature (relationship considered close to linear) of the theoretical cosmic-ray attenuation trajectory at such shallow depths, especially given the relatively low density (~1.3 g cm^{-3}) of soil material. We use the IceTEA tools for exposure ages[1] (Jones *et al.*, 2019) to calculate new sample shielding factors after taking into account a correction for constant sample cover by soil, prior to re-calculating exposure ages using the new shielding factor and the online calculator formerly known as the CRONUS-Earth online calculator version 3 (Balco *et al.*, 2008). The time-averaged surface shielding factor (*Ss*) is calculated from:

$$Ss = St\ exp\left(-\frac{Zcover\ \ Pcover}{\Delta s}\right) \quad (1)$$

Where *St* is the field-measured topographic shielding factor, *Zcover* is the given depth of sample cover below surface (cm), *Pcover* is the given average cover-material density (g cm^{-3}) and Δs is the attenuation length (g cm^{-2}), calculated from sample location (Sato *et al.*, 2008). Throughout our simulations, we use an average dry mineral soil density of 1.3 g cm^{-3}. Note that a more site-specific value could be obtained by conducting soil moisture-content

[1] http://ice-tea.org/en/tools/correct-surface-cover/

measurements in the field. We conducted a series of calculations using variable soil depths until the sample population (*e.g.* RC II outwash cobbles) mean exposure age post-simulation was similar to the population's oldest cobble's original exposure age. This is considered a better minimum age-estimate for the timing of landform deposition due to post-depositional age scatter causing young apparent ages. For these exposure ages to match, the estimated soil depth through which all cobbles hypothetically exhumed at a constant rate was ~12 cm and ~24 cm (equivalent to constant burial below ~6 and ~12 cm-thick soil covers) for the Tecka outwash and the RC II outwash cobble sample populations, respectively. Resulting mean exposure ages were increased by 5.7% and 10.8% for the Tecka and RC II outwash samples, respectively.